T2GGM Version 3.2: Gas Generation and Transport Code

P. Suckling[1], J. Avis[2], N. Calder[2], O. Nasir[2], P. Humphreys[3], F. King[4] and R. Walsh[2]

[1]Quintessa Ltd., [2]Geofirma Engineering Ltd., [3]University of Huddersfield, [4]Integrity Corrosion Consulting Ltd.

nwmo

NUCLEAR WASTE MANAGEMENT ORGANIZATION

SOCIÉTÉ DE GESTION DES DÉCHETS NUCLÉAIRES

T2GGM Version 3.2: Gas Generation and Transport Code

NWMO-TR-2015-13

November 2015

P. Suckling[1], J. Avis[2], N. Calder[2], O. Nasir[2], P. Humphreys[3], F. King[4] and R. Walsh[2]
[1]Quintessa Ltd., [2]Geofirma Engineering Ltd., [3]University of Huddersfield, [4]Integrity Corrosion Consulting Ltd.

Document History

Title:	T2GGM Version 3.2: Gas Generation and Transport Code		
Report Number:	NWMO-TR-2015-13		
Revision:	R000	Date:	November 2015
[1]Quintessa Ltd., [2]Geofirma Engineering Ltd., [3]University of Huddersfield, [4]Integrity Corrosion Consulting Ltd.			
Authored by:	P. Suckling[1], J. Avis[2], N. Calder[2], O. Nasir[2], P. Humphreys[3], F. King[4] and R. Walsh[2]		
Verified by:	P. Suckling[1], J. Avis[2], N. Calder[2], O. Nasir[2], R. Walsh[2]		
Approved by:	J. Avis[2]		
Nuclear Waste Management Organization			
Reviewed by:	J. Chen E. Kremer H. Leung		
Accepted by:	N. Hunt		

ABSTRACT

Title: **T2GGM Version 3.2: Gas Generation and Transport Code**
Report No.: **NWMO-TR-2015-13**
Author(s): P. Suckling[1], J. Avis[2], N. Calder[2], O. Nasir[2], P. Humphreys[3], F. King[4], R. Walsh[2]
Company: [1]Quintessa Ltd., [2]Geofirma Engineering Ltd., [3]University of Huddersfield, [4]Integrity Corrosion Consulting Ltd.
Date: November 2015

Abstract
T2GGM is a software package that can be used to analyze the generation and transport of gases and groundwater in a deep geologic repository. The current version is Version 3.2. It includes gas generation from low and intermediate level waste, and gas generation from the corrosion of used fuel containers under relevant conditions.

This report provides a reference manual for the T2GGM software. It includes the theory for the gas generation model, the user guide with descriptions of the software inputs and outputs, a summary of the verification that the software has undergone and software validation.

T2GGM includes the following capabilities:

- Corrosion product and hydrogen gas generation from corrosion of steels and other alloys under aerobic and anaerobic conditions;
- CO_2 and CH_4 gas generation from degradation of organic materials under aerobic and anaerobic conditions;
- H_2 gas reactions, including methanogenesis with CO_2;
- Biomass generation, decay and recycling;
- Exchange of gas and water between the repository and the surrounding geosphere; and
- Two-phase flow of water and gas within the geosphere.

Key results include the gas pressure and water saturation levels within a repository, as well as flow rates of water and gas within the geosphere. T2GGM does not include radionuclide transport and decay.

T2GGM is comprised of two coupled models: a Gas Generation Model (GGM) used to model the generation of gas within a repository due to corrosion and microbial degradation of the various materials present, and a TOUGH2 model for gas-water transport from the repository through the geosphere.

TABLE OF CONTENTS

LIST OF TABLES

LIST OF FIGURES

1.   INTRODUCTION

The long-term safety assessment of deep geological repositories may involve the analysis of behaviour of gases within and from the repository. This assessment requires the calculation of the generation and build-up of gas in the repository and the movement of gas from the repository to the surface environment. The gas generation and movement needs to be coupled with the availability and movement of groundwater.

T2GGM has been developed to undertake these calculations. It is comprised of two coupled models: a Gas Generation Model (GGM) used to model the generation of gas within a repository due to corrosion and microbial degradation of the various materials present, and the TOUGH2 model (Pruess et al., 1999) for gas and water transport from the repository and within the geosphere (Figure 1-1). Key outputs from this software are the peak repository pressure, repository saturation, and total flux of gases from the geosphere to surface.
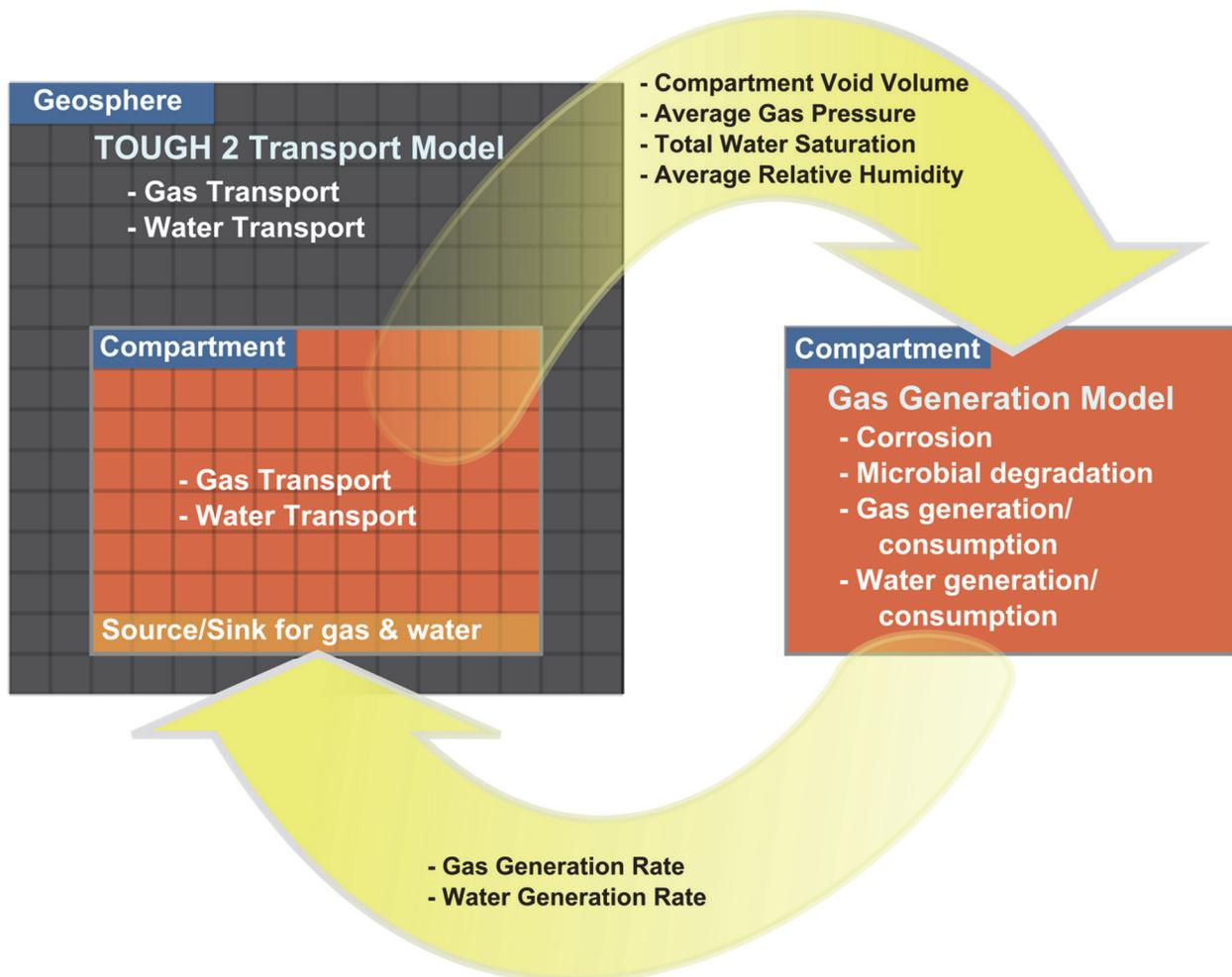
Figure 1-1: Coupling Gas Generation and Transport in T2GGM

This reference manual includes the following documentation for T2GGM:

- Program Abstract (Section 2);
- GGM Theory (Section 3);
- TOUGH2 Theory (Section 4);
- Verification (Section 5);
- Validation (Section 6); and
- User Manual (Section 7).

2.   PROGRAM ABSTRACT

T2GGM Version 3.2 is comprised of two coupled models: a gas generation model (GGM Version 3.2) used to model the generation of gas within a repository due to corrosion and microbial degradation of the various materials or waste streams present, and the TOUGH2 Version 2.0 model for gas transport from the repository through the geosphere. Key output parameters from this software are the peak repository pressure, repository saturation, and total flux of gases from or to the geosphere.

GGM Version 3.2 is implemented as a FORTRAN module that is used by TOUGH2 in its own gas generation and repository saturation calculations. GGM includes a kinetic description of the various microbial and corrosion processes that lead to the generation and consumption of various gases. Mass-balance equations are given for each of the species included in the model, including three forms of organic waste (cellulose, ion-exchange (IX) resins, and plastics and rubbers), four metallic waste forms and container materials (carbon and galvanized steel, passivated carbon steel, stainless steel and nickel-based alloys, and zirconium alloys), six different gases (CO_2, N_2, O_2, H_2, H_2S, and CH_4), five terminal electron acceptors (O_2, NO_3^-, Fe(III), SO_4^{2-}, and CO_2), five forms of biomass (aerobes, denitrifiers, iron reducers, sulphate reducers, and methanogens), five types of corrosion product (FeOOH, $FeCO_3$, Fe_3O_4, Fe_2O_3 and FeS), water, and MgO, which could be added to the repository to mitigate the effects of CO_2 generation.

TOUGH2 is a multi-phase flow and heat transport program for fluid mixtures. TOUGH2 is the collective name for a family of numeric models that simulate multi-phase flow and transport developed and maintained by the Earth Sciences Division of Lawrence Berkeley National Laboratory. TOUGH2 uses different Equations-of-State (EOS) modules to simulate different combinations of liquids and gases. T2GGM Version 3.2 includes TOUGH2 Version 2.0 with the EOS3 V1.01 equation-of-state module (ideal gas - air and water) (Pruess et al., 1999). T2GGM-MP Version 3.2 is a version of T2GGM that couples GGM with TOUGH2-MP Version 2.0. TOUGH2-MP uses multiple processors to undertake its calculations in order to improve run times. The majority of this documentation covers both the single and multiple processor versions of T2GGM. Sections that relate to single- or multi-processor functionality only are indicated as such.   Several modifications have been implemented in TOUGH2 (both single and multi-processor versions) providing the user with a greater range of capabilities, including:

- The option to use the modified van Genuchten model provided in iTOUGH2 (Finsterle 1999), a set of capillary pressure and relative permeability equations that are widely used in modeling two-phase flow in low-permeability media;

- User specification of gas (air, CH_4, CO_2, H_2, Ne or user-specified) and the option to use non-ideal gas compressibility factors in the ideal gas equations;

- 1D hydromechanical capability, to provide the ability to assess the effects of an applied glacial stress;

- Integration with FLAC3D to calculate stress fields for poro-elastic coupling or damage-permeability coupling;

- Time-varying permeability, useful in cases of degraded or evolving engineered materials or excavated damage zone (EDZ);

- Time-varying Dirichlet boundary conditions;

- The ability to link and simultaneously solve two different models at identified boundary junction points;

- Saturation-dependent intrinsic permeability and capillary pressure to represent bentonite materials; and

- Pressure dependent permeability and capillary pressure to represent dilatant flow.

While the version of T2GGM documented here (i.e., Version 3.2) uses the TOUGH2 EOS3 module that is limited to two components (gas and water), it should be noted that TOUGH2 has several modules available. For example, EOS7R models water, brine, air and two radionuclides. Replacing EOS3 with one of these modules is relatively straightforward.

2.1   CAPABILITIES

T2GGM Version 3.2 includes the following capabilities:

- Corrosion product and hydrogen gas generation from corrosion of steels and other alloys under aerobic and anaerobic conditions suitable for application to an L&ILW repository;
- Corrosion product and hydrogen gas generation from the high temperature corrosion of steel containers in the presence of a bentonite buffer suitable for application to a repository for used fuel;
- CO_2-enhanced corrosion of carbon steel and passive alloys;
- CO_2 and CH_4 gas generation from degradation of organic materials under aerobic and anaerobic conditions;
- Degradation of cellulose, IX resins, and plastics and rubbers at different rates based on the terminal electron acceptor;
- H_2 gas reactions, including methanogenesis with CO_2;
- Biomass generation, decay and recycling;
- Limitation of both microbial and corrosion reactions by the availability of water;
- Carbon, iron and water are mass balanced within repository reactions;
- Exchange of gas and water between the repository and the surrounding geosphere;
- The ability to subdivide the volume within which gas generation takes place into multiple compartments, each of which can be allocated its own associated inventory and evolved independently with coupling provided through gas and water transport;
- Calculation of the generation and build-up of gas in each repository volume;
- Two-phase flow of water and gas within the geosphere with gas dissolution according to Henry's law;
- Heat flow coupled to two-phase flow of water and gas.
- The ability to assess the use of magnesium oxide as a gas-mitigation method, and other strategies that may affect the consumption of gas in the repository;
- 1D hydro-mechanical model to assess the effects of an applied glacial stress;
- Time-variable permeability, allowing the permeability properties of certain materials, such as engineered materials or EDZ, to evolve or degrade with time.
- Time-variable Dirichlet boundary conditions;

- The ability to stop and restart the simulations;
- Automatically restart simulations with modified convergence parameters when incipient failure is detected;
- Use of a consistent compressibility factor with the equations of state for gases across the TOUGH2 and GGM components of T2GGM;
- Link and simultaneously solve two different models at identified boundary junction points. This approach prevents incongruent boundary conditions in nested models.

- Use GPU matrix solvers to improve computational performance;
- Integrate with FLAC3D to calculate stress fields for poro-elastic coupling or damage-permeability coupling;
- Pressure-dependent permeability and capillary pressure to represent dilatant flow; and,
- Saturation-dependent intrinsic permeability and capillary pressure to represent bentonite materials.

2.2   LIMITATIONS

T2GGM Version 3.2 is subject to the following limitations:

- Heat generation can only be modelled as a TOUGH2 input source or sink;
- T2GGM does not model radionuclide transport and decay;
- Repository corrosion and gas reaction rates are first order in a primary reactant, and in particular are not dependent on the amount of microbial biomass;
- Metal corrosion and organic decomposition is described by a constant or temperature dependent corrosion rate for the relevant conditions (aerobic/anaerobic, saturated/unsaturated);
- Organics are modelled as either cellulose or styrene;
- Oxygen, nitrates and sulphates can be depleted from an initial supply only (with the initial inventory of sulphates and Fe(III) being defined by the initial volume of water and a user-specified initial concentration), and O, N and S may not be strictly conserved. It is assumed that any long-term fluxes of nitrates, sulphates and Fe(III) into/out of the repository do not have significant impacts on gas processes;
- All gas in the geosphere is modelled as a single gas (either air, CH_4, CO_2 or H_2); all gases released from the repository are converted into this gas on an equivalent molar basis (e.g., if GGM calculates a generation rate of 1 mol s^{-1} of H_2 and 2 mol s^{-1} of CH_4, then it is converted into 3 mol s^{-1} of the selected gas, and then converted to a mass rate at the selected gas molecular weight for use by TOUGH2); and
- Groundwater in the geosphere is modelled as freshwater. Saline water will affect water flow due to differences in the viscosity and density of the water, and the impact of these differences must be evaluated on a case by case basis.
- The terminal electron acceptor processes are expected to dominate in a fixed sequence of stages. This is appropriate for closed systems, but may not be appropriate when there are long-term net fluxes of TEAs (sulphates/nitrates/iron-based species) from/to the repository.
- Advection and diffusion of dissolved species (dissolved gases, nitrates, sulphates) into or out of the repository is not modelled by GGM. The model may not be suitable if the

host rock maintains large concentrations of sulphates/nitrates and this is coupled with large water inflow to the repository.

- For H_2 and He, non-ideal gas behaviour is only strictly applicable for pure gas (i.e. no water vapour). At low temperatures, neglecting water vapour is typically negligible; at high temperatures, hydrogen and helium non-ideal gas calculations should be used with caution.

3.   THEORY – GGM

3.1   INTRODUCTION

Gas generation within the repository may be important to both operational and post-closure safety. During the operational phase, when air is still present, care must be taken to avoid the formation of flammable gas mixtures in closed spaces. Following closure and consumption of O_2, the build-up of gas within the sealed repository affects the resaturation time and can lead to the release of gaseous radionuclides. Gas is generated and consumed by various microbial and corrosion processes. For example, microbial degradation of organic components of the waste or other materials left in the repository produces CO_2 and CH_4. Corrosion of metallic waste forms and container materials consumes O_2 and CO_2, and produces H_2 under anaerobic[1] conditions.

This section describes GGM Version 3.2, the gas generation model for the T2GGM Version 3.2. The model incorporates a detailed description of the kinetics of microbial degradation of the organic wastes and accounts for the possible limitation of both microbial and corrosion processes due to the availability of water. In addition, GGM can be used to assess the effect of different gas-mitigation methods and other processes that may lead to the consumption of gas in the repository.

This theory section provides a detailed specification of all the equations solved by GGM Version 3.2. The microbial processes and corrosion processes described in Section 3.2 and Section 3.3, respectively, have been chosen for application to a deep geologic repository (DGR) for L&ILW, for which repository temperatures are expected to be relatively constant at around 20 °C. Thus for these processes, reaction rates are constant and do not contain any explicit temperature dependence. In Section 3.4, corrosion processes are presented that have been chosen for application to a clay-backfilled repository for used fuel. For this application, high initial temperatures are expected and so the corrosion rates have temperature dependence built in explicitly, and the model includes a staged representation of the breakthrough of water to the container through a bentonite buffer. It is not intended for L&ILW processes and used fuel processes to be used simultaneously[2]. Additional processes that can be relevant to both L&ILW and used fuel repositories (e.g., gas mitigation) are presented in Section 3.5, and general model and coding information is provided in Section 3.6. Section 3.7 describes the approach taken to modelling the partitioning of gas between the water-unsaturated and water-saturated phases. Section 3.8 describes the approach taken to modelling relative humidity. Section 3.9 describes the approach taken to modelling water-limited conditions.

A detailed list of the model parameters referenced throughout this section is given in Table 3-1.

---

[1] Here, the term anaerobic is used to describe not only the absence of air (oxygen), but also more generally to describe environments in which one or more redox couples control the redox potential at relatively negative values of Eh.

[2] Processes can be disabled by setting relevant reaction rates to zero.

3.2   MICROBIAL GAS GENERATION PROCESSES FOR APPLICATION TO L&ILW

3.2.1   Degradation of Organic Waste Components

GGM considers three classes of organic wastes that may be present in a repository containing low and intermediate level waste:

1. Cellulosic materials;
2. IX resins; and
3. Plastics and rubbers.

All three of these groups represent polymeric organic materials. The microbial degradation of polymeric organics follows a generic sequence of events (Figure 3-1) (Rittmann and McCarty 2001). Firstly, the polymer is converted into soluble intermediates, which are then subject to microbial oxidation reactions, the exact nature of which depends on the prevailing geochemical conditions. Microbes either couple the oxidation of these soluble intermediates to the reduction of Terminal Electron Acceptors (TEAs) or subject them to fermentation (Barlaz 1997, Pedersen 2000, Rittmann and McCarty 2001). Under ideal conditions, microbial systems employ a range of TEAs in oxidation-reduction reactions that are consumed in a well-defined order depending on the amount of energy provided by each reaction (Zehnder and Stumm 1988). This order is outlined below:

- Oxygen followed by;
- Nitrate followed by;
- Ferric ion (Fe III) followed by;
- Manganese (Mn IV) followed by;
- Sulphate followed by; and
- Carbon dioxide.

In subsurface environments the simultaneous consumption of terminal electron acceptors does occur due to local heterogeneity and the presence of microbial microsites. However, the general trend of sequential terminal electron consumption is seen in subsurface environments' pollution plumes, for example Williams et al. (2001). Consequently, the sequential consumption of terminal electron acceptors within the model is justifiable on the basis of reaction thermodynamics (Zehnder and Stumm 1988) and environmental observations (e.g., Williams et al., 2001).
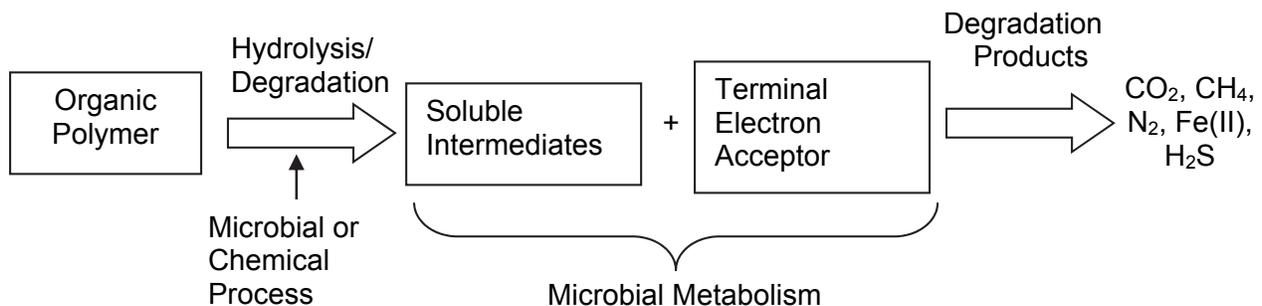
Figure 3-1: Microbial Degradation of Polymeric Substrates

Under oxidizing conditions when oxygen, and to a lesser extent nitrate, is used as a terminal electron acceptor, the degradation of polymeric substrates such as cellulose progresses to completion (Equations (3.1) and (3.2)). When oxygen is depleted and anaerobic conditions are established, polymeric substrates tend to undergo fermentation first, with the fermentation end products then being oxidized by TEA processes (Equations (3.3) and (3.4)) (Leschine 1995, Pedersen 2000). Fermentation is carried out by a varied group of microbes and consequently a wide range of fermentation end products (carboxylic acids and alcohols) are possible (Leschine 1995, Barlaz 1997, Rittmann and McCarty 2001), with Equation (3.3) showing the fermentation of glucose to acetic acid. The consumption of these fermentation end products during iron reduction is illustrated in Equation (3.4).

$$(C_6H_{10}O_5)_n + nH_2O \rightarrow nC_6H_{12}O_6 \qquad \text{cellulose hydrolysis} \qquad (3.1)$$

$$C_6H_{12}O_6 + 6O_2 \rightarrow 6CO_2 + 6H_2O \qquad \text{aerobic glucose degradation} \qquad (3.2)$$

$$C_6H_{12}O_6 + 4H_2O \rightarrow CH_3COOH + 8H_2 + 4CO_2$$

$$\text{glucose fermentation to acetic acid} \qquad (3.3)$$

$$CH_3COOH + 8H_2 + 24Fe(III) + 2H_2O \rightarrow 24Fe(II) + 2CO_2 + 24H^+$$

$$\text{iron reduction of glucose fermentation products} \quad (3.4)$$
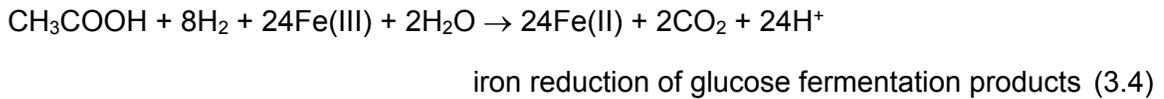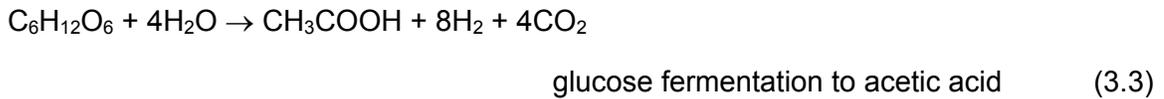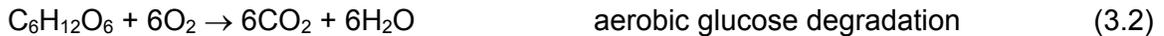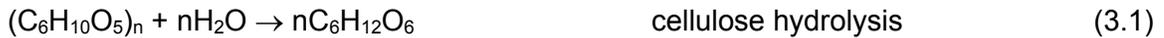
3.2.1.1 Modelling Organic Waste Degradation

The microbial degradation of polymeric substrates and the subsequent generation of gas is a complex multistage process involving a large array of microbial species (Pedersen 2000, Grant et al., 1997). However, for modelling purposes, this can be simplified by the fact that the conversion of polymeric substrates such as cellulose to their soluble intermediates is often the rate-limiting step in the gas generation process (Rittmann and McCarty 2001). This allows the microbial oxidation of polymeric substrates to be coupled directly to the reduction of the relevant TEA. The degradation of polymeric substrates then becomes a single-stage process with the consumption of TEAs being instantaneous and controlled by the rate of polymer degradation. This partial-equilibrium approach has been applied in other modelling studies (McNab and Narasimhan 1994, Postma and Jakobsen 1996), since it significantly simplifies the modelling of microbially driven systems and reduces the number of kinetic parameters required to run the model. The application of this approach to gas generation modelling can be justified on the basis that it is conservative from a gas generation perspective, since it maximizes gas generation by preventing the accumulation of intermediate products and ensuring gas generating processes proceed to completion.

Balanced reactions coupling the oxidation of organic waste components to the reduction of TEAs can be constructed using the approach outlined by Rittmann and McCarty (2001). Taking cellulose as an example, its hydrolysis to glucose is outlined in Equation (3.1) with its oxidation under aerobic conditions being outlined in Equation (3.2). However, if the rate of glucose oxidation is taken to be instantaneous when compared to the rate of cellulose hydrolysis then the overall reaction can be written as:

$$(C_6H_{10}O_5)_n + 6nO_2 \rightarrow 6nCO_2 + 5nH_2O$$
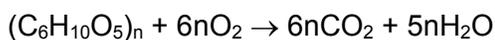
or   complete oxidation of cellulose   (3.5)

$$C_6H_{10}O_5 + 6O_2 \rightarrow 6CO_2 + 5H_2O$$
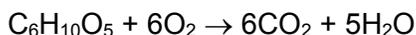
where the controlling reaction rate is that for cellulose hydrolysis, Equation (3.1).

Note that the rate of hydrolysis (and of the degradation of polystyrene into styrene) is redox dependent and so an aerobic rate and an anaerobic rate are considered.

The above approach closely resembles microbial cellulose degradation under oxidizing conditions where the polymer is completely degraded to carbon dioxide and water (Leschine 1995). However, under anaerobic conditions when fermentation occurs, the instantaneous consumption of fermentation end products is not always observed, resulting in the accumulation of carboxylic acids such as acetic acid and butyric acid. This accumulation generally occurs because the microbes responsible for the degradation of these products are inhibited by low pH, a process known as acid souring in landfill sites (p. 62, EA 2004). In anaerobic hypersaline environment the accumulation of volatile fatty acids has also been observed (Ollivier et al., 1994). The accumulation of fermentation end products such as acetic acid is not included in the model, allowing the degradation of polymeric organics to be modelled as a series of single-stage processes. As before, this approach is justified on the basis that it is conservative since it maximizes gas generation by preventing the accumulation of soluble organic intermediates.

Employing this approach, the metabolism of cellulose degradation (oxidation) under iron-reducing conditions, which is described in Equations (3.1), (3.3), and (3.4), can be simplified to:

$$C_6H_{10}O_5 + 24Fe(III) + 7H_2O \rightarrow 6CO_2 + 24Fe(II) + 24H^+$$

degradation of cellulose under iron-reducing conditions   (3.6)

where again the controlling reaction rate is that for cellulose hydrolysis, Equation (3.1).

Origins of Microbes

The model assumes that all microbial groups required to catalyze the processes modelled are present within the repository. This assumption is justified on the basis that it is conservative from a gas generation perspective, since it ensures gas generation processes proceed to completion. In reality, microbes are ubiquitous in terrestrial, man-made and subsurface environments (Pedersen 2000). Microbes will enter the repository during the construction and operational phases on vehicles, materials, people and in the air. In addition, the waste will carry its own microbial load. Microbial gas generation in stored and disposed wastes has been reported by a number of authors (Molnar et al., 2006, Molnar et al., 2000, Kannen and Muller 1999). Groundwater entering the repository could also carry a microbial load compatible with the saline conditions at depth.

Terminal Electron Acceptors

The model includes oxygen, nitrate, ferric iron, sulphate, and carbon dioxide as terminal electron acceptors. Oxygen is included, since it will be present in the repository atmosphere

postclosure. Sources of nitrate are less obvious, but may include blast explosive residue from repository construction, the groundwater, and also a chemical used in the nuclear industry and present in the wastes. Ferric iron is included, since it is a product of aerobic corrosion and sulphate is included since it may be present in the local groundwater. The inclusion of sulphate also allows gas mitigation options involving the precipitation of metal sulphides to be investigated. Finally, carbon dioxide is included since it is a major gaseous product of microbial degradation processes. With the exception of carbon dioxide, any or all of the processes associated with these terminal electron acceptors within the model can be turned off by setting the relevant input concentration to zero.

Terminal electron acceptors are theoretically consumed in a defined sequence (Section 3.2.1) starting with oxygen and finishing with carbon dioxide. This sequence is reflected in the model with a given TEA only being consumed once the previous one has been depleted. Finally, when all the competing TEAs have been depleted, carbon dioxide consumption and methane production will occur. The removal of TEAs is not modelled kinetically, but is controlled by the rate of organic waste degradation and the stoichiometry of the relevant reaction in a partial equilibrium approach similar to that employed by McNab and Narasimhan (1994) and Postma and Jakobsen (1996).

Degradation of Cellulose

The degradation of cellulosic materials has been extensively studied (Leschine 1995) and modelled (Rittmann and McCarty 2001). Consequently the degradation pathways are well established (Leschine 1995, Barlaz 1997). Taking the approach outlined in Section 3.2.1.1, cellulose degradation is modelled via the following equations constructed using the approach outlined by Rittmann and McCarty (2001):

$$C_6H_{10}O_5 + 6O_2 \rightarrow 6CO_2 + 5H_2O \qquad \text{oxidation of cellulose by molecular oxygen} \qquad (3.7)$$

$$5C_6H_{10}O_5 + 24NO_3^- + 24H^+ \rightarrow 30CO_2 + 12N_2 + 37H_2O$$

$$\text{oxidation of cellulose by nitrate reduction} \qquad (3.8)$$

$$C_6H_{10}O_5 + 24Fe(III) + 7H_2O \rightarrow 6CO_2 + 24Fe(II) + 24H^+$$

$$\text{oxidation of cellulose by ferric iron reduction} \qquad (3.9)$$

$$C_6H_{10}O_5 + 3SO_4^{2-} + 6H^+ \rightarrow 6CO_2 + 5H_2O + 3H_2S$$

$$\text{oxidation of cellulose by sulphate reduction} \qquad (3.10)$$

$$C_6H_{10}O_5 + H_2O \rightarrow 3CO_2 + 3CH_4 \qquad \text{methane generation from cellulose} \qquad (3.11)$$
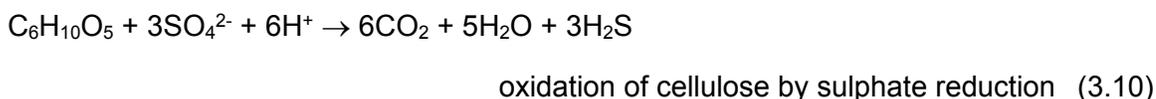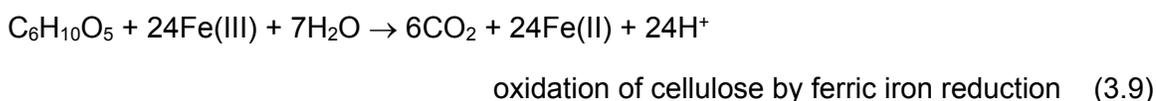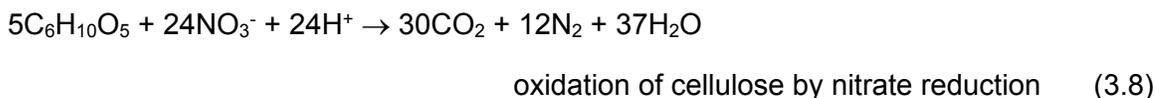
where the reaction rate for all these is that for cellulose hydrolysis, Equation (3.1).

Degradation of IX Resins

There may be significant amounts of IX resins in the intermediate-level waste inventory, and as such, these resins are potentially a significant source of biogenic gases. However, there is disagreement as to the biodegradability of these materials. For example, Grant et al. (1997) listed IX resins as being recalcitrant under repository conditions. However, a number of authors have suggested that these resins are subject to microbial degradation and subsequent gas

generation. For example, Bracke et al. (2003, 2004) report gas generation rates from resin wastes in interim storage and attribute a microbial gas generation rate to the degradation of these wastes. Bowerman et al. (1988) investigated the biodegradation of IX media using a mixed microbial culture isolated from resin waste samples, and found microbial growth under various conditions, although it is noted that the work appear to have been carried out under aerobic conditions. EPRI investigated biogas generation from IX resins in the late 1990's, and found that the gas was being generated from cellulose fibres contaminating the resins rather than microbial degradation of the resins themselves (EPRI 1998).

Although the chemical nature of IX resins suggests that they would not be biodegradable, particularly under anaerobic conditions, data from waste resins indicate that degradation is possible. There are a number of scenarios that explain the observed data:

- Organic contaminants adsorbed on the resins and corrosion hydrogen are supporting the gas generation and microbial communities rather than direct biodegradation of the resins;
- Radiolytic and/or chemical degradation is generating soluble intermediates which are subject to biodegradation; and
- The resins are subject to microbial degradation.

There are insufficient data to determine which of these options is correct and it is possible that all three are operating simultaneously. For generality, IX resin degradation is included in the model.

Water coolant IX resins are typically cross-linked polystyrene based, with various functional groups and water attached. The resins are therefore modelled via the degradation of polystyrene with bound water $(C_8H_8.mH_2O)_n$ to styrene with bound water $(C_8H_8.mH_2O)$ as in Figure 3-2, and then to final degradation products. The initial degradation is considered to be the rate-limiting step. This is comparable to the cellulose degradation model. This assumption is justified on the basis that it maximizes the amount of gas generated from this component of the waste inventory and is compatible with a mechanistic approach to the modelling of a water balance.
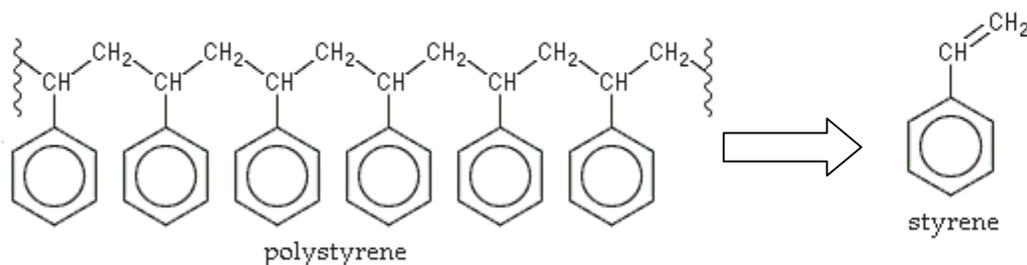
Figure 3-2: Polystyrene Degradation

The degradation of styrene is coupled to the reduction of the relevant TEAs in the same manner as outlined for cellulose. The microbial degradation of styrene under oxidizing conditions has been extensively investigated (Mooney et al., 2006) but there is little information regarding its degradation in reducing environments. The anaerobic degradation of other aromatic compounds has been reported (Lovely 2000, Spormann and Widdel 2000, Karthikeyan and

Bhandari 2001) but only where terminal electron acceptors such as ferric iron and sulphate are available.

The degradation of IX resins is modelled using a set of degradation pathways constructed using the approach outlined by Rittmann and McCarty (2001), but with the release of bound water. These pathways are outlined below:

$$C_8H_8.mH_2O + 10O_2 \rightarrow 8CO_2 + (4+m)H_2O$$

oxidation of styrene by molecular oxygen   (3.12)

$$C_8H_8.mH_2O + 8NO_3^- + 8H^+ \rightarrow 8CO_2 + 4N_2 + (8+m)H_2O$$

oxidation of styrene by nitrate reduction   (3.13)

$$C_8H_8.mH_2O + 40Fe(III) + 16H_2O \rightarrow 8CO_2 + 40Fe(II) + 40H^+ + mH_2O$$

oxidation of styrene by ferric iron reduction   (3.14)

$$C_8H_8.mH_2O + 5SO_4^{2-} + 10H^+ \rightarrow 8CO_2 + (4+m)H_2O + 5H_2S$$

oxidation of styrene by sulphate reduction   (3.15)

$$C_8H_8.mH_2O + 6H_2O \rightarrow 3CO_2 + 5CH_4 + mH_2O$$ methane generation from styrene   (3.16)

where the reaction rates for all these are that for polystyrene degradation and m represents the number of moles of bound water per mole of styrene monomer in the initial resin material.

Note that resins typically consist of anion and/or cation functional groups on the polystyrene divinylbenzene backbone, in addition to the bound water. These functional groups comprise a significant fraction of the mass of the resins, but do not usually contain much carbon and therefore do not contribute significantly to potential gas generation. In the GGM model, the presence of these mass components is taken into account when determining the number of moles of polystyrene divinylbenzene backbone per unit mass of dry resin so as to obtain a good estimate of the gas generating potential.

Degradation of Plastics and Rubber

The plastic and rubber components of radioactive waste represent a heterogeneous mix of materials such as PVC, polyethylene, neoprene, nitrile, and latex. The heterogeneous nature of this waste category makes it difficult to model since the degradation of each material would have to be modelled explicitly with an individual inventory and reaction scheme for each component.

A number of authors have suggested that plastic waste components such as polythene, PVC and polyurethane are recalcitrant under repository conditions (Grant et al., 1997; BNFL, 2002). British Nuclear Fuels Limited (BNFL 2002) stated in documentation supporting the 2002 Drigg safety case that: "*The current available information would suggest that the majority of the higher molecular weight polymers would remain undegraded for a considerable length of time, particularly addition polymers.*" This position is supported by the work of Francis et al. (1997) who found no evidence of biodegradation of electron beam irradiated plastic and rubber.

A more recent review by Cohen (2006) for the Waste Isolation Pilot Plant (WIPP) project concluded that some degradation of plastics and rubbers "*may occur over 10,000 years in the WIPP repository*." This conclusion appears to be based on the fact that oxidation and radiation damage may enhance biodegradation of these materials or generate soluble intermediates amenable to microbial attack. The authors point out that much of the evidence for the microbial degradation of these materials comes from aerobic systems. However, they do not rule out the possibility of anaerobic microbial degradation.

In order to assess the impact of potential plastic and rubber degradation on the overall gas generation in the repository these components are modelled in the same manner as IX resins, i.e., as polystyrene, but with a separate initial inventory and rate constants.

3.2.1.2 Microbial Hydrogen Metabolism

In radioactive waste disposal sites, significant amounts of hydrogen may be produced via anaerobic corrosion of metals. Hydrogen is also a common product of anaerobic microbial metabolism and consequently there are a large number of microbial processes able to process hydrogen (Grant et al., 1997; Pedersen, 2000). The oxidation of hydrogen takes place under anaerobic conditions and is therefore coupled with the reduction of ferric iron, sulphate and carbon dioxide:

$$H_2 + 2Fe(III) \rightarrow 2Fe(II) + 2H^+$$
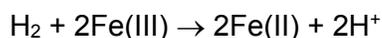
$$\text{hydrogen oxidation via iron reduction} \quad (3.17)$$

$$4H_2 + SO_4^{2-} + 2H^+ \rightarrow H_2S + 4H_2O$$
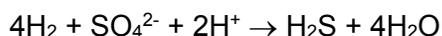
$$\text{hydrogen oxidation via sulphate reduction} \quad (3.18)$$

$$4H_2 + CO_2 \rightarrow CH_4 + 2H_2O$$
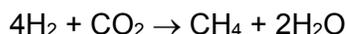
$$\text{methane generation from hydrogen oxidation} \quad (3.19)$$

where the corresponding rate constants are expressed in terms of the rate of consumption of H_2.

The ferric ion Fe(III) is assumed primarily present as FeOOH within the saturated region. The sulphate reaction also only occurs in the saturated region. The methane generation can occur anywhere within the system, if there is enough humidity to support microbial processes.

The corrosion hydrogen generation and microbial hydrogen consumption are independent of each other, each having independent rates of reaction. The accumulation of hydrogen within the system is controlled by the relative rates of anaerobic corrosion and microbial hydrogen consumption. If the rate of microbial hydrogen consumption is higher than that of corrosion and associated hydrogen generation, then the rate of corrosion becomes the rate-limiting step in the process. Consequently hydrogen consumption progresses instantaneously as long as sufficient TEA capacity is present. This case reflects the low levels of hydrogen detected in radioactive waste degradation experiments where significant amounts of corrodible metal are present (Beadle et al., 2001; Grey, 2002; Small et al., 2005).

3.2.1.3   Microbial Biomass

Biomass Production

When microbes degrade materials, some of the feed material is used to produce new biomass. Biological systems require more water than that required for the reactions they catalyze, since cells are typically 80 wt% water. Therefore, any attempt to model water within microbially active systems needs to account for the amount of water required to maintain microbial cells. This means that biomass production and degradation has to be modelled since significant amounts of water may be held up in microbial biomass. Consequently, although there may be sufficient water to complete the oxidation-reduction reactions, there may be insufficient water to support the production of microbial cells (Wang and Francis 2005).

The amount of water needed to support microbial biomass can be calculated using an empirical formula for microbial dry biomass such as $C_5H_7O_2N$ (Rittmann and McCarty 2001), which indicates that 1 mole of biomass would weigh 113 g. Since biomass is 80 wt% water then each mole of biomass also requires approximately 25 moles of water[3]. This requirement for water can then be integrated into the biomass generation reactions outlined below (in the model, we conservatively assume that there is always sufficient NH_3 to support these reactions):

$$5C_6H_{10}O_5 + 6NH_3 + 137H_2O \rightarrow 6C_5H_7O_2N{\cdot}25H_2O$$

<div align="right">biomass generation from cellulose   (3.20)</div>

$$C_8H_8 + 2NH_3 + 2CO_2 + 50H_2O \rightarrow 2C_5H_7O_2N{\cdot}25H_2O$$

<div align="right">biomass generation from styrene   (3.21)</div>

$$5CO_2 + 10H_2 + NH_3 + 17H_2O \rightarrow C_5H_7O_2N{\cdot}25H_2O$$

<div align="right">biomass generation from hydrogen   (3.22)</div>
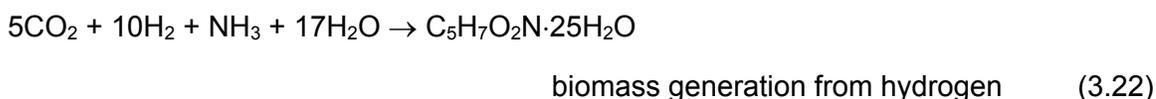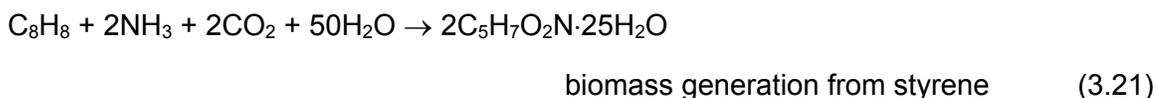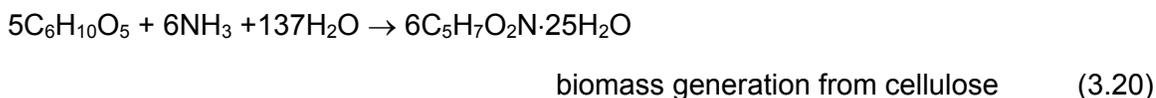
Cellulose degradation will involve both degradation products as outlined in Equations (3.7) to (3.11), as well as production of biomass as per Equation (3.20) using the energy from the degradation reactions (and CO_2 per Equation (3.21)). The overall reaction rate is described by the effective cellulose degradation rate, but with the cellulose mass divided between biomass and degradation products according to an empirical yield coefficient, Y:

<div align="center">Cellulose $\rightarrow$ Y (biomass) + (1-Y) (degradation products)</div>
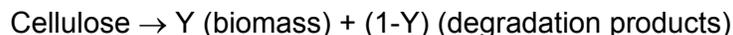
The rate of production of biomass is controlled, as with the degradation products, by the degradation rate of cellulose or styrene, or the rate of the methane-generation reaction Equation (3.19).

Biomass Decay

Microbial biomass is subject to natural turnover since cells have finite lifetimes. Biomass contains a range of compounds, which have different degradabilities. Some microbial cell components are recalcitrant to further degradation and accumulate in the environment. In the

---

[3] The molar mass of dry biomass is approximately 113 g mol^{-1}. Since the 113 g represents 20% of the whole, the remaining 80% which is water is equivalent to 452 g, which is 25.1 moles of water.

present model, two classes of biomass compounds are considered – easily recycled and recalcitrant.

The fraction K_R of dead <u>hydrated</u> biomass that is readily recycled is modelled according to the reverse of Equation (3.20):

$$6C_5H_7O_2N{\cdot}25H_2O \rightarrow 5C_6H_{10}O_5 + 6NH_3 + 137H_2O \qquad (3.23)$$

It is assumed that the recycled biomass can be represented as cellulose, with each mole of biomass ($C_5H_7O_2N$) producing 5/6 mol of cellulose ($C_6H_{10}O_5$). The energy to drive this process comes from the oxidation of the organic material itself. This approach to biomass recycling is adopted since it is considered conservative with respect to gas generation.

The remaining fraction of biomass is recalcitrant ($1 - K_R$) and does not degrade further, except that upon death, the cells will release the water they hold - 25 mol H_2O are released per mol recalcitrant dead biomass.

Threshold for Biomass Activity

Water activity (A_w) is the ratio of the vapour pressure of water in a material to the vapour pressure of pure water at the same temperature. Relative humidity of air (RH) is the ratio of the vapour pressure of water in air to the water saturation vapour pressure. When vapour and temperature are at equilibrium, the water activity of a material is equal to the relative humidity of the surrounding air:

$$RH = A_w \qquad (3.24)$$

A_w is important because biological activity ceases at an A_w below 0.6[4] with the lower limit for bacteria being 0.75 (Brown 1976, Wang and Francis 2005). Consequently, to model microbially driven reactions in the repository, it is necessary to check the water activity or RH. Microbial processes should be allowed to proceed within the vapour phase for sufficiently high RH. Rate constants for all the biomass generation reactions and microbial processes that normally occur only under saturated conditions are ramped smoothly down to zero as the RH drops from 0.8 to 0.6. If the rate of water consumption is rapid compared with the rate of water ingress, it is feasible that the relative humidity, or water activity, could fall below that required to sustain microbial activity.

3.2.2   Reaction Kinetics

The degradation of polymeric organic substrates is modelled as being first order with respect to their amounts (Equation (3.25)):

$$-\frac{dQ_i}{dt} = V_{i,j}.Q_i \qquad \text{degradation of polymeric substrates} \qquad (3.25)$$

---

[4] Note that some fungi can live at an A_w close to 0.6. Fungi are generally considered to be better adapted to low water availability. However fungi are generally aerobic organisms and would not be expected to play an important role in an anaerobic deep geologic environment.

where Q_i [mol] is the amount of substrate i (i = C, R, P for cellulose, IX resins, and plastics and rubbers, respectively) and $V_{i,j}$ [s⁻¹] is the degradation rate constant for substrate i under conditions j (j = a, b, c, d, e for aerobic respiration, denitrification, iron reduction, sulphate reduction, and methanogenesis, respectively). $V_{i,j} = V_i$ if substrate j is being consumed, and 0 otherwise, where V_i [s⁻¹] is the degradation rate of cellulose, IX resin, or plastics and rubbers.

This is an approach commonly applied to the modelling of the degradation of polymeric organic substrates (Pavlostathis and Giraldo-Gomez 1991, Rittmann and McCarty 2001, IWA 2002). The rates of all the microbial reactions modelled are determined by the rate of polymer degradation. This constrains the number of input kinetic parameters required to run the model to an aerobic and an anaerobic rate for each of the three polymeric substrates modelled.

The model is set up to allow the polymer degradation rates to be modified depending on the prevailing environmental conditions. Generally speaking, as the system moves from oxidizing to reducing conditions, degradation rates slow down. The model simulates this by having independent polymer degradation rates for when specific TEAs dominate. This is not the same as having the removal of the TEAs being kinetically controlled.

Biomass generation is coupled to polymer degradation via a yield coefficient that determines how organic carbon is partitioned between energy generation and biomass production, Equation (3.26). This yield coefficient depends on the TEA consumed since the yield decreases as the available energy generation decreases.

$$\frac{dX}{dt} = Y_j \frac{dQ_i}{dt} - XD \qquad\qquad \text{biomass generation} \qquad\qquad (3.26)$$

where X [mol] is the quantity of biomass, Y_j [-] is the biomass yield coefficient for condition j, and D [s⁻¹] is the biomass decay rate.

The production and consumption of gaseous products is also coupled to polymer degradation via the yield coefficient and a stoichiometric coefficient relevant to that product

$$\frac{dQ_k}{dt} = J_{ki}(1 - Y_j)\frac{dQ_i}{dt} \qquad\qquad \text{product generation} \qquad\qquad (3.27)$$

where Q_k [mol] is the number of moles of product k (k = CO_2, H_2, N_2, H_2S, CH_4) and J_{ki} [-] is the stoichiometric coefficient for product k formed from organic substrate i.

3.2.3   Summary of Microbial Modelling

The modelling of the microbial reactions includes the following features:

1. A mechanistic basis for treatment of microbial processes;
2. The inclusion of different rates of degradation of organic substrates based on either oxidizing or reducing conditions;
3. The possible limitation of microbial processes by the availability of water;
4. Separate treatment of cellulose, IX resins, and plastics and rubbers;
5. The inclusion of H_2-mediated microbial processes; and
6. The recycling of dead biomass.

3.3 CORROSION GAS GENERATION PROCESSES FOR APPLICATION TO L&ILW

3.3.1 Corrosion Reactions

The various metallic waste forms and container materials considered in the model are: carbon and galvanized steels, passivated carbon steel, stainless steel and nickel alloys, and zirconium alloys.

Corrosion of the metallic wastes and container materials occurs under both aerobic and anaerobic conditions and in unsaturated (i.e., humid) and saturated (i.e., submerged) environments. Under aerobic conditions, corrosion is generally supported by the cathodic reduction of dissolved O_2, although simultaneous reduction of O_2 and H_2O is possible for some materials. Once the initially trapped atmospheric O_2 has been consumed, corrosion is supported by the reduction of H_2O only. The effect of oxidizing radiolysis products is not included, as the radiation fields for the various low and intermediate level wastes are insignificant.

Aqueous corrosion processes are possible in humid atmospheres provided the relative humidity is sufficiently high. The relevant vapour phase rate constants are ramped smoothly down to zero between 80% and 60% relative humidity.

3.3.1.1 Carbon and Galvanized Steels

The inventory of carbon and galvanized steels in the repository will comprise various carbon steel wastes, as well as carbon and galvanized steel waste containers. Galvanized and carbon steels are treated as a single metallic source. Although the short-term rate of atmospheric corrosion of galvanized steel is lower than that of carbon steel, the thickness of the zinc layer on galvanized steel represents only a small fraction of the overall container wall thickness. Furthermore, there is little difference in the corrosion rate of these two materials under saturated conditions. Therefore, the corrosion of both materials is represented by the corrosion of Fe as carbon steel (C-steel).

The aerobic corrosion of C-steel under saturated and unsaturated conditions is given by the reaction:

$$4Fe + 2H_2O + 3O_2 \rightarrow 4 \text{ “FeOOH”} \tag{3.28}$$
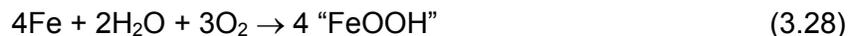
where "FeOOH" represents an un-specified ferric oxyhydroxide species, which may also contain groundwater species (Cl^-, SO_4^{2-}, CO_3^{2-}) in various forms of green rust (King and Stroes-Gascoyne 2000). Since FeOOH is only an intermediate species, the degree of hydration of the corrosion product need not be specified for the overall water mass-balance calculation (see below).

As the environment becomes anaerobic, the Fe(III) corrosion product is converted to Fe(II) via

$$2FeOOH + Fe + 2H_2O \rightarrow 3Fe(OH)_2 \tag{3.29}$$

Under anaerobic conditions, the corrosion of C-steel is supported by the reduction of H_2O

$$Fe + 2H_2O \rightarrow Fe(OH)_2 + H_2 \tag{3.30}$$

Ferrous hydroxide may also convert to magnetite via the Schikkor reaction (Shreir 1976)

$$3Fe(OH)_2 \rightarrow Fe_3O_4 + 2H_2O + H_2 \qquad (3.31)$$
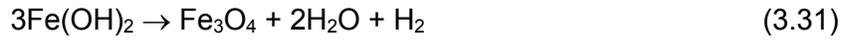
with the formation of additional H_2.

The nature of the long-term stable anaerobic corrosion product, $Fe(OH)_2$ or Fe_3O_4, determines the maximum amount of H_2 that can be produced from the corrosion of carbon steel. If $Fe(OH)_2$ is the stable corrosion product, then 1 mole of H_2 is produced for each mole of Fe corroded. Conversely, if Fe_3O_4 is the stable corrosion product, then 1.33 moles of H_2 are produced for each mole of Fe corroded.

King and Stroes-Gascoyne (2000) reviewed the nature of corrosion products formed during the corrosion of carbon steel in natural waters. Figure 3-3 shows an overall reaction scheme that accounts for the majority of observations reported in the literature[5]. Ferrous hydroxide ($Fe(OH)_2$) is generally an intermediate species in the aerobic and anaerobic oxidation of carbon steel, even at temperatures <80°C where the conversion of $Fe(OH)_2$ to Fe_3O_4 via the Schikkor reaction is generally regarded as slow. There is no evidence in the literature for the formation of $Fe(OH)_2$ as the main end product of the reduction of Fe(III) corrosion products.
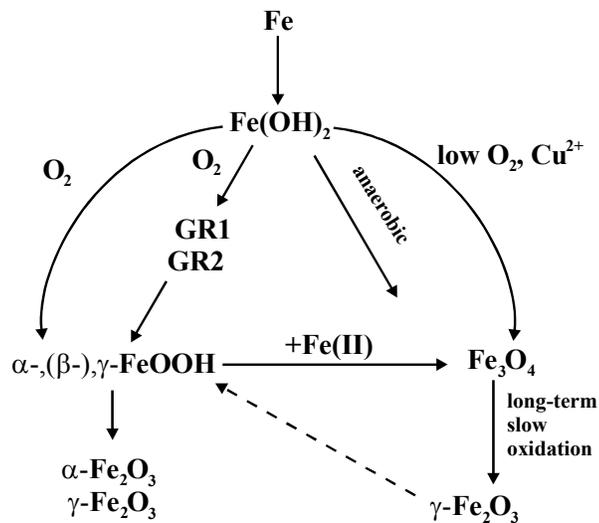
Figure 3-3: Generalized Reaction Scheme for the Formation and Transformation of Corrosion Product Films on C-steel[6]

---

[5] Not all the details in the figure are applicable to corrosion in a DGR, but the entire mechanism is shown for completeness, and to demonstrate the depth of understanding of the corrosion of steels in natural waters.

[6] GR1 and GR2 stand for Green Rust 1 and Green Rust 2, two forms of Fe(III) oxyhydroxide that contain varying amounts of Cl^-, SO_4^{2-}, and CO_3^{2-}. The α, β and γ variants correspond to different crystal structures: α-FeOOH is goethite; β-FeOOH is akaganeite; γ-FeOOH is lepidocrocite; α-Fe$_2$O$_3$ is haematite; and γ-Fe$_2$O$_3$ is magnetite.

Therefore, based on the evidence summarized above, the stable product of the corrosion of carbon steel is taken to be Fe_3O_4 rather than $Fe(OH)_2$. The overall reaction for the anaerobic corrosion of C-steel (Equations (3.30) and (3.31)) can then be written as

$$3Fe + 4H_2O \rightarrow Fe_3O_4 + 4H_2 \qquad (3.32)$$

and the overall reduction of FeOOH under anaerobic conditions can be written as

$$2FeOOH + Fe \rightarrow Fe_3O_4 + H_2 \qquad (3.33)$$
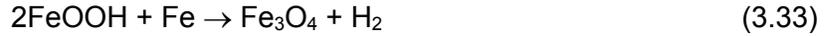
In GGM, the aerobic corrosion of C-steel is represented by Equation (3.28), the conversion of FeOOH under anaerobic conditions by Equation (3.33), and the anaerobic corrosion of C-steel by Equation (3.32).

These latter two processes represent a conservative approach to the calculation of the quantity of H_2 generated since, if $Fe(OH)_2$ rather than Fe_3O_4 is the stable long-term anaerobic corrosion product, less H_2 will be generated.

Carbon steel undergoes accelerated corrosion in the presence of high CO_2 partial pressures (de Waard and Milliams 1976). The enhanced corrosion rate is primarily a consequence of the decrease in pH that accompanies the dissolution of CO_2 in water to form carbonic acid (H_2CO_3). However, because of the high HCO_3^- concentration, the stable corrosion product is $FeCO_3$ rather than Fe_3O_4. The corrosion of carbon steel in CO_2-containing environments is given by

$$Fe + H_2CO_3 \rightarrow FeCO_3 + H_2 \qquad (3.34)$$

Because of the importance of this process in the oil and gas industry, there have been a large number of studies to determine the effect of the CO_2 partial pressure, P_{CO2}, on the corrosion rate of carbon steel (ASM 1987, 2003, 2005). Many of these studies have been performed under conditions of high rates of mass transport such as might be encountered in pipelines, and the absolute corrosion rates reported are not relevant to the environmental conditions within a DGR. However, these studies indicate a dependence of the corrosion rate on $(P_{CO2})^q$, where q is typically of the order of 0.66 (de Waard and Milliams, 1976; de Waard and Lotz, 1993; de Waard et al., 1991, 1995). The empirical model used to derive a value for q was fitted to data for CO_2 partial pressures up to 1 MPa.

In GGM, the corrosion rate of carbon and galvanized steel is taken to be a function of the CO_2 partial pressure, with the overall corrosion reaction given by Equation (3.34). Although the pH of the environment is not specifically calculated within the model, the use of an enhanced corrosion rate in the presence of CO_2 implicitly takes into account the acidification resulting from the dissolution of CO_2 in the aqueous phase. In terms of the model, the rate of reaction given by Equation (3.34) is treated as a multiplier of the anaerobic corrosion rate (see Equation (3.38)). (Under aerobic conditions, the degree of enhancement is minimal as O_2, rather than H^+, is the dominant oxidant). Therefore, depending upon the partial pressure of CO_2, the anaerobic corrosion rate is enhanced by an appropriate factor. If there is no CO_2 present, the factor is 1. The relative amounts of Fe_3O_4 and $FeCO_3$ formed are determined by the values of the respective rate constants and, in the case of $FeCO_3$, by the P_{CO2}.

3.3.1.2 Passivated Carbon Steel

Passivated carbon steel comprises waste forms grouted in cementitious materials and structural steel (rebar, rails, etc.) in contact with concrete. These materials are treated separately from

the plain carbon and galvanized steel inventories because of the effect of the cementitious material on the corrosion rate. The high pH environment in the cement results in passivation of the carbon steel and, consequently, a lower corrosion rate.

Although the rate of corrosion of passivated carbon steel is lower, the mechanism is treated in exactly the same fashion as for the plain carbon and galvanized steel. Thus, the aerobic and anaerobic corrosion of passivated carbon steel are given by Equations (3.28) and (3.32), respectively, and the reduction of FeOOH is given by Equation (3.33). In alkaline environments, Fe_3O_4 is more stable than $Fe(OH)_2$ (Pourbaix 1974) and is likely to be the stable long-term corrosion product.

At the elevated pH expected to persist for some time in cementitious materials, Fe_3O_4 is thermodynamically more stable than $FeCO_3$. Therefore, enhanced corrosion of passivated carbon steel due to the presence of elevated CO_2 partial pressures is not included in GGM.

3.3.1.3 Stainless Steels and Nickel Alloys

Stainless steels and nickel alloys are present as container materials and as used reactor components such as from steam generators or pressure tube end fittings. These materials contain Fe, Ni, Cr, Mo, and other minor alloying elements, in amounts dependent on the composition of the particular alloy.

Corrosion of these alloys proceeds with the formation of a protective, or passive, film typically comprising Cr(III) or Ni(II), and possibly small amounts of other alloying elements (ASM 1987, 2003, 2005; Clayton and Olefjord 1995). Over long periods of time, however, other elements within the alloy, notably Fe, must also be oxidized since the amount of Cr in the alloys is limited. There is currently an incomplete understanding of how passive materials corrode over long periods of time, both from the viewpoint of the stability of the Cr-rich passive film that forms initially and from the viewpoint of how the corrosion behaviour evolves as the elements responsible for passivity become consumed.

In the absence of a complete understanding of their long-term corrosion behaviour, the corrosion of the passive materials is treated in GGM in the same manner as carbon steel, and they are assumed to fully oxidize although at a slower rate.

Thus, the aerobic and anaerobic corrosion of stainless steel are assumed to be given by Equations (3.28) and (3.32), respectively, and it is further assumed that oxidized corrosion products formed during the aerobic phase are subsequently reduced by a reaction analogous to Equation (3.33). This is an acceptable assumption for the corrosion of stainless steels, since these materials contain a high percentage of Fe (typically 60-80%, Sedriks 1996). For the Ni-based alloys, the assumption is considered reasonable, even though the aerobic corrosion products formed for these materials, Cr(III) and Ni(II), are not reduced during the aerobic-anaerobic transition in the same manner as Fe(III). However, the degree of aerobic corrosion of the passive materials is minimal, since not only is the inventory of O_2 relatively small compared with the inventory of organic and metallic materials, but the O_2 that is present also tends to be consumed by degradation of cellulose and/or the corrosion of carbon and galvanized steel rather than by the corrosion of the passive materials. Under anaerobic conditions, the Ni-based alloys are assumed to corrode to corrosion products with an average metal to oxygen ratio of 1.33, as with Fe. The predominant valence for Ni corrosion products is +2, compared with a value of 2.67 for Fe in the form of Fe_3O_4. Therefore, this overstates by

~33% the amount of H_2 generated during the anaerobic phase from Ni. This is a sufficient approximation, since these alloys are also not dominant in the waste.

The corrosion rates of passive materials are higher under sour-service conditions, i.e., in the presence of CO_2 and H_2S gases (ASM 1987, 2003, 2005). The pressure of CO_2 developed in a deep repository could approach that typically found in down hole applications in the oil and gas industry. Therefore, the passive alloys undergo accelerated corrosion and the formation of carbonate-containing corrosion products, as for carbon and galvanized steels (Equation (3.34)).

3.3.1.4 Zirconium Alloys

Zirconium alloy waste may comprise fuel sheaths/hulls, pressure tubes and/or other components of the decommissioned reactors. Typically these alloys contain small amounts of Nb, which is approximated as oxidizing similar to Zr.

Under aerobic conditions the corrosion of Zr is given by

$$Zr + O_2 \rightarrow ZrO_2 \tag{3.35}$$

and under anaerobic conditions by

$$Zr + 2H_2O \rightarrow ZrO_2 + 2H_2 \tag{3.36}$$

The oxide film on zirconium alloys is a stable, effective barrier to corrosion. There are few reports of the use of Zr alloys exposed to aqueous environments with high pressures of CO_2. Neither the corrosion rate nor the nature of the corrosion products is affected by the presence of high CO_2 partial pressure.

3.3.2 Reaction Kinetics

The general expression for the consumption of the metallic wastes and container materials is given by

$$-\frac{dQ_\ell}{dt} = h \sum_{m=1,2} \frac{A_{\ell,1}\rho_\ell}{M_\ell} R_{\ell,m,1} + \varepsilon \sum_{m=1,2} \frac{A_{\ell,2}\rho_\ell}{M_\ell} R_{\ell,m,2} \tag{3.37}$$

where Q_ℓ [mol] is the quantity of metallic material ℓ (where ℓ = 1, 2, 3, 4 for carbon and galvanized steel, passivated carbon steel, passive alloys, and Zr alloys, respectively), ρ_ℓ [kg·m^{-3}] and M_ℓ [kg·mol^{-1}] are the density and equivalent atomic mass of metallic material ℓ, respectively, $A_{\ell,n}$ [m^2] is the surface area of material ℓ exposed to the vapour phase (n = 1) and submerged (n = 2), and $R_{\ell,m,n}$ [m·s^{-1}] is the corrosion rate of material ℓ under redox conditions m (m = 1, 2 for aerobic and anaerobic conditions, respectively) and degree of saturation n (n = 1, 2 for unsaturated and saturated conditions, respectively). The fraction of the surface area submerged is taken to be equal to the degree of saturation S, with the fraction exposed to the vapour phase equal to (1 – S). $R_{\ell,m,n}$ is zero if conditions are not in the appropriate redox regime; i.e., $R_{\ell,1,n}$ = 0 under anaerobic conditions, and $R_{\ell,2,n}$ = 0 under aerobic conditions. h and ε are scaling factors used to model the effects of relative humidity and water-limited conditions, respectively. They are defined in Table 3-1.

Corrosion of carbon and galvanized steels, and the stainless steel and Ni-based passive alloys, is also enhanced by the presence of CO_2. In the repository, CO_2-enhanced corrosion will occur primarily under anaerobic conditions (m = 2) but could be possible under both saturated and unsaturated conditions (n = 1, 2 respectively).

In GGM, the effect of CO_2 on the rate of corrosion (expressed as a rate of consumption in $mol \cdot s^{-1}$) is given by

$$-\frac{dQ_\ell}{dt} = \frac{\rho_\ell}{M_\ell}\left(hA_{\ell,1}R_{\ell,1,1} + h\left(1 + \left(\frac{P_{CO2}}{P_{CO2}^{ref}}\right)^q\right)A_{\ell,1}R_{\ell,2,1} + \varepsilon A_{\ell,2}R_{\ell,1,2} + \varepsilon\left(1 + \left(\frac{P_{CO2}}{P_{CO2}^{ref}}\right)^q\right)A_{\ell,2}R_{\ell,2,2}\right) \quad (3.38)$$

where ℓ = 1, 3 (carbon and galvanized steel, and stainless steel and Ni-based alloys, respectively), and P_{CO2}^{ref} [Pa] is a reference CO_2 partial pressure at which the corrosion rate is twice the value in the absence of CO_2.

The consumption and generation of various gases (O_2, CO_2, and H_2), corrosion products (FeOOH, $FeCO_3$, and Fe_3O_4), and of H_2O are estimated from the respective corrosion rates using appropriate stoichiometric coefficients from Equations (3.28) and (3.32)-(3.36).

As noted in Section 3.3.1.3, the long-term corrosion behaviour of stainless steels and Ni-based alloys is described by the same stoichiometric equations used for carbon and galvanized steel.

The same corrosion rates are used for stainless steel and nickel alloys. Based on evidence from the literature, any differences in the corrosion rates for these alloys is within the reproducibility of the reported corrosion rate of approximately half an order of magnitude. Under anaerobic conditions, the amount of H_2 produced by corrosion depends on the metal/oxygen ratio in the respective oxide formed for each metal. As noted above (Section 3.3.1.3), this can result in an approximately 33% variation in the rate of H_2 generation between stainless steels and Ni-based alloys. This variation, however, is again within the reproducibility of the measured corrosion rates and the use of the same corrosion rates for stainless steels and passive Ni alloys is, therefore, justified. A detailed list of input parameters for GGM is given in Table 3-1.

3.3.3 Summary of Corrosion Modelling for Application to a Repository for L&ILW

The basic corrosion model includes:

1. Aerobic and anaerobic corrosion of carbon and galvanized steel, passivated carbon steel, stainless steel and nickel alloys, and zirconium alloys;
2. Corrosion under saturated and unsaturated conditions;
3. Consumption of O_2 and CO_2 and, under anaerobic conditions, the generation of H_2;
4. The reductive dissolution of Fe(III) formed during the aerobic period;
5. Treatment of the corrosion of carbon and galvanized steel and passive alloys in the presence of CO_2, leading to enhanced corrosion rates and the formation of $FeCO_3$, and in the absence of CO_2 leading to the formation of Fe_3O_4; and
6. Rationalization for the formation of Fe_3O_4 as a long-term, stable corrosion product.

3.4 CORROSION GAS GENERATION PROCESSES FOR APPLICATION TO USED FUEL

The corrosion model in this section has been developed for NWMO's Fifth Case Study (5CS), which is investigating a repository within a hypothetical sedimentary formation. It is designed for application to a steel used fuel container (UFC) in the presence of a bentonite buffer at room-scale, so that the near-field response of the geosphere and engineered sealing materials to its corrosion and consequent gas generation can be assessed.

3.4.1 Background

Corrosion of carbon steel (C-steel) used fuel containers has a number of impacts on the performance of the repository system. First, corrosion in its various forms is the major contributing factor to container failure (King 2007), following which the release of radionuclides to the near field becomes possible. Second, dissolved ferrous species can interact with bentonite and convert swelling smectite clays to non-swelling illitic forms, resulting in a partial loss of swelling capacity (Wersin et al., 2007). Third, anaerobic corrosion will result in the generation of hydrogen that may form a gaseous H_2 phase in the repository, the presence of which could impact the migration of radionuclides. This section is focussed primarily on the estimation of the rate of H_2 generation due to corrosion of the container.

The corrosion behaviour of the container will change with time as the environment in the repository evolves. From a corrosion perspective, the most important environmental factors are the UFC temperature, the redox conditions, the degree of saturation of the buffer material, and the composition of the bentonite pore water in contact with the UFC. For a DGR in low-permeability sedimentary host rock, saturation of the DGR may take tens of thousands of years. This slow saturation has led to the definition of four phases in the evolution of the environment, namely:

- An early aerobic period prior to the onset of aqueous corrosion;
- An unsaturated aerobic phase following the condensation of liquid water on the container surface;
- An unsaturated anaerobic phase once all of the initially trapped O_2 has been consumed; and
- A long-term saturated anaerobic phase once the buffer material has become completely saturated by groundwater.

Hydrogen is produced by the cathodic reduction of H_2O or H^+. The vast majority of H_2 that will be produced in the repository will result from the uniform corrosion of C-steel during the (unsaturated and saturated) anaerobic phase. Hydrogen can be produced under aerobic conditions due to the reduction of H^+ in acidic environments in pits, crevices, or porous corrosion products formed as a result of the hydrolysis of Fe(III) species (Akiyama et al., 2010; Tsuru et al., 2005). Local reduction of H^+ may lead to enhanced hydrogen absorption and environmentally assisted cracking (King, 2009) but will not lead to the generation of significant H_2 and is not considered further here.

Hydrogen generated by corrosion can undergo a number of subsequent processes. The H_2 that is evolved could be consumed by microbes (Pedersen, 2000) in those parts of the near- and far-fields in which the environment is conducive to microbial activity (that is, a water activity greater

than 0.96: Stroes-Gascoyne et al., 2006, 2007, 2008). Another fraction of the hydrogen will be absorbed by the C-steel as atomic H, either from adsorbed H atoms prior to their evolution as H_2 or via the dissociative absorption of gaseous H_2. Absorbed H will diffuse through the container wall and desorb on the inner surface as H_2 gas. This process will continue until the H_2 partial pressure inside the container is the same as that outside. Thus, the container acts as a sink for a fraction of the H produced through anaerobic corrosion.

The remainder of this section deals with the rate of generation of H_2, rather than its fate in the repository. The environmental conditions in the repository are first considered, with emphasis on those conditions that affect the rate of corrosion (H_2 generation). Next, the uniform corrosion behaviour of C-steel for each the four main phases in the evolution of the repository environment is summarised, with discussion of the transition between the various phases.

3.4.2   Environmental Conditions

The environment in the repository will evolve with time as (i) the initially trapped O_2 is consumed, (ii) the heat output from the container decays, and (iii) the repository saturates with incoming groundwater. The latter effect may be particularly important for a repository in sedimentary rock of low hydraulic conductivity as it may take tens of thousands of years for the DGR to saturate.

The corrosion behaviour of the container will also change with time in response to this environmental evolution. A series of four phases of corrosion behaviour can be defined, namely:

Phase 1   A period during the initial thermal transient when the relative humidity in the repository is below that necessary for the formation of liquid H_2O on the container surface. Corrosion during this phase will be limited to slow air oxidation.

Phase 2:   An early phase of unsaturated aerobic conditions prior to saturation of the repository and during which corrosion is supported by the reduction of the O_2 trapped initially in the pores of the buffer and backfill materials.

Phase 3:   An intermediate unsaturated anaerobic phase following the consumption of the O_2 but prior to the saturation of the repository. Corrosion during this period is supported by the cathodic reduction of H_2O accompanied by the evolution of H_2.

Phase 4:   A long-term saturated anaerobic period following saturation of the repository. As for Phase 3, corrosion during Phase 4 is supported by the cathodic reduction of H_2O accompanied by the evolution of H_2.

In addition to the evolution of the redox conditions and the degree of saturation, the temperature will also change during these different phases. The precise time dependence of the container temperature will depend on the rate of saturation, which is not known *ab initio*. However, in general, it is clear that Phases 1 and 2 will be warmer than Phase 3, with Phase 4 encompassing the period of long-term ambient conditions.

The onset of aqueous corrosion (i.e., the transition from Phase 1 to Phase 2) is dependent on the relative humidity (RH) at the container surface. Aqueous corrosion is possible above a critical or threshold RH that is determined by the nature of the surface and the presence of

surface contaminants. Water condenses on porous surfaces or corrosion products by capillary condensation. Salts absorb moisture from the atmosphere in a process known as deliquescence at a critical deliquescence RH (DRH) that is a function of temperature and the type of salt. Salts that are highly soluble deliquesce at lower RH than sparingly soluble salts.

A number of other environmental parameters, in addition to the temperature, RH, and redox conditions, also affect the uniform corrosion behaviour of the container, including:

Pore-water chemistry: Under saturated conditions, the container surface will be in contact with bentonite pore water. At least initially, the composition of the pore water may differ from that of the ground water. Eventually, however, the pore water will equilibrate with the ground water.

pH Calcite minerals in the bentonite will effectively buffer the pH in the range pH 7-8.

Mass transport: The low hydraulic conductivity of compacted sodium bentonite will limit mass transport to diffusion only. During the aerobic phase, the rate of corrosion may be limited by the rate of transport of O_2 to the container surface, although the diffusivity of O_2 in unsaturated bentonite is high (King et al., 1996).

Radiation: Gamma radiolysis of water will produce oxidizing and reducing radiolysis products. However, the maximum surface absorbed dose rate for a 10-cm-thick C-steel UFC will be <1 $Gy \cdot h^{-1}$ and there will be no significant effect on the corrosion rate (Shoesmith and King 1999).

Operational phase: It is implicitly assumed that there is no significant corrosion prior to the sealing of the repository. An extended operational phase could allow O_2 ingress and additional corrosion of the container.

Microbial activity: Microbial activity is suppressed by the presence of highly compacted bentonite and saline solutions (Stroes-Gascoyne et al., 2006, 2007, 2008). Therefore, microbial activity is unlikely close to the container and there will be no effect on the uniform corrosion behaviour.

Stress: Applied and residual stresses affect the environmentally assisted cracking behaviour of the container but have no effect on uniform corrosion.

Mineral impurities: Mineral impurities in the host rock (e.g., pyrite) will have an insignificant effect on the uniform corrosion behaviour of the container.

3.4.3 Summary of Reaction Stoichiometries and Rate Expressions

The corrosion is described through the identification of four phases designed to capture the slow breakthrough of water to the containers through the bentonite buffer with decreasing temperatures:

- Phase 1: Dry Air Oxidation;
- Phase 2: Aerobic Unsaturated Conditions;
- Phase 3: Anaerobic Unsaturated Conditions; and
- Phase 4: Anaerobic Saturated Conditions.

It is important to note that these four phases do not necessarily occur sequentially. Phases 1 and 2 both occur under aerobic conditions and the degree to which the Phase 1 and Phase 2 corrosion processes are active depends on the relative humidity. The Phase 3 and 4 corrosion

processes proceed under anaerobic conditions after Phase 1 and Phase 2. The degree to which the Phase 3 and Phase 4 corrosion processes are active depends on whether or not liquid water has moved through to the container walls or not. The Phase 3 process also depends on relative humidity. The conceptual model used to switch the corrosion processes on and off depending on the relative humidity and saturation is described in Section 3.4.5.

3.4.4 Basic Rates

This section summarizes the corrosion process and basic rates for each phase, following Appendix A, and converts to SI units for consistency with the rest of the GGM theory.

3.4.4.1 Phase 1: Dry Air Oxidation

Prior to the formation of liquid water on the container surface, corrosion will take the form of slow oxidation in "dry" air. (Dry air may contain some water vapour but insufficient to form a liquid phase). Oxidation of the UFC will result in the formation of a duplex Fe_3O_4/Fe_2O_3 surface film (Desgranges et al., 2003). Oxide growth can be modelled in terms of the reaction:

$$4Fe + 3O_2 \rightarrow 2Fe_2O_3 \tag{3.39}$$

Oxidation kinetics for Fe and a low-alloy steel have been found to follow both parabolic and logarithmic rate laws, although parabolic kinetics have generally been assumed for modelling purposes (Desgranges et al., 2003; Larose and Rapp, 1997; Terlain et al., 2001). The weight gain W (kg m^{-2}), as a function of time t (s), is given by:

$$W^2 = K_p \cdot t \tag{3.40}$$

where K_p (kg^2 m^{-4} s^{-1}) is the temperature-dependent parabolic rate constant given by the Arrhenius form:

$$K_p = K_0 \exp(-E_a/RT) \tag{3.41}$$

where K_0 (kg^2 m^{-4} s^{-1}) is a pre-exponential factor and E_a (J mol^{-1}) the activation energy. Therefore the penetration rate of the corrosion front into the container, R_1 (m s^{-1}) is written as

$$R_1(t, T; t_1, D_1, E_1) = \frac{D_1}{\sqrt{t - t_1}} \exp\left(-\frac{E_1}{2RT}\right) \tag{3.42}$$

for times $t > t_1$ where D_1 (m s$^{-1/2}$) is a basic corrosion rate constant; E_1 (J mol^{-1}) is the molar activation energy; R (J K^{-1} mol^{-1}) is the molar gas constant; T (K) is the temperature; t_1 (s) is the time at which the corrosion starts (emplacement time); and t (s) is the time. The rate is evaluated as zero for times $t <= t_1$.

3.4.4.2 Phase 2: Aerobic Unsaturated Conditions

Once the container surface is wetted by liquid water, a period of aerobic corrosion under unsaturated conditions is expected to occur (assuming that all of the initially trapped O_2 has not been consumed by oxidation of the container). Corrosion will result in the consumption of O_2

and H_2O, but not the generation of H_2. The nature of the corrosion reaction depends, in part, on the presence of anions such Cl^-, SO_4^{2-}, and CO_3^{2-}, which will lead to the formation of various forms of green rust. Since the nature of the surface deposits is not precisely known, the overall corrosion reaction will be described here by the formation of a hydrated Fe(III) species:

$$4Fe + 3O_2 + 2H_2O \rightarrow 4\alpha/\gamma\text{-FeOOH} \qquad (3.43)$$

with the α- and γ- forms representing goethite and lepidocrocite, respectively. Depending on the RH and the distribution of surface salt contaminants, the corrosion reaction may be more or less localized. Localized corrosion will be favoured by low RH and a sparse distribution of surface salts.

Based on a review of aerobic corrosion rates, with an emphasis on data from studies with backfill, Foct and Gras (2003) proposed an Arrhenius expression for the aerobic corrosion rate. Therefore Phase 2 corrosion (aerobic unsaturated conditions) is represented by the process:

$$4Fe + 3O_2 + 2H_2O \rightarrow 4FeOOH \qquad (3.44)$$

for which the penetration rate of the corrosion front into the container, R_2 (m s^{-1}) is written as

$$R_2(T; D_2, E_2) = D_2 \exp\left(-\frac{E_2}{RT}\right) \qquad (3.45)$$

where D_2 (m s^{-1}) is a basic penetration rate constant; E_2 (J mol^{-1}) is the molar activation energy; R (J K^{-1} mol^{-1}) is the molar gas constant; and T (K) is the temperature.

3.4.4.3 Phase 3: Anaerobic Unsaturated Conditions

In the absence of O_2, C-steel corrodes with the evolution of H_2:

$$Fe + 2H_2O \rightarrow Fe(OH)_2 + H_2 \qquad (3.46)$$

Ferrous hydroxide can convert to magnetite via the Schikkor reaction:

$$3Fe(OH)_2 \rightarrow Fe_3O_4 + 2H_2O + H_2 \qquad (3.47)$$

The overall stoichiometry for the formation of Fe_3O_4, therefore, and the most conservative from the viewpoint of H_2 production, as follows::

$$3Fe + 4H_2O \rightarrow Fe_3O_4 + 4H_2 \qquad (3.48)$$

This is used to represent Phase 3 corrosion (anaerobic unsaturated conditions). Based on studies of anaerobic corrosion of C-Steel from the literature by Newman et al. (2010) and Debruyn (1990), the penetration rate of the corrosion front into the container, R_3 (m s^{-1}) under conditions of high relative humidity, is written as

$$R_3(T; D_3, E_3) = D_3 \exp\left(-\frac{E_3}{RT}\right) \qquad (3.49)$$

where D_3 (m s^{-1}) is a basic penetration rate constant; E_3 (J mol^{-1}) is the molar activation energy; R (J K^{-1} mol^{-1}) is the molar gas constant; and T (K) is the temperature.

3.4.4.4 Phase 4: Anaerobic Saturated Conditions

In the presence of compacted bentonite, C-steel corrodes with the formation of a carbonate-containing corrosion product (Papillon et al., 2003; King, 2007, 2008). The source of carbonate is calcite and other carbonate minerals in the bentonite (or in the host rock). The overall stoichiometry of the reaction for Phase 4 corrosion (anaerobic saturated conditions) can be written as:

$$Fe + CO_3^{2-} + 2H_2O \rightarrow FeCO_3 + H_2 + 2OH^- \tag{3.50}$$

Following Gras (1996), the penetration rate of the corrosion front into the container, R_4 (m s^{-1}) can be written in Arrhenius format as:

$$R_4(T; D_4, E_4) = D_4 \exp\left(-\frac{E_4}{RT}\right) \tag{3.51}$$

where D_4 (m s^{-1}) is a basic penetration rate constant; E_4 (J mol^{-1}) is the molar activation energy; R (J K^{-1} mol^{-1}) is the molar gas constant; and T (K) is the temperature.

3.4.5 Corrosion Process Activation

Section 3.4.4 gives the basic rate expressions for the processes associated with each of the four corrosion phases. The activation of each of these processes and the actual rate at which they proceed is dependent on the temperature, saturation and relative humidity within the volume of interest. The volume of interest in the current context is a portion of the grid used by TOUGH2 to discretize the space surrounding the used fuel container and extending into the bentonite; a 'compartment'. In this section, we define the mathematics controlling the actual rate at which carbon steel inventory in a given compartment is consumed.

In the following, the symbol Ω is given the value 1 under aerobic conditions and 0 under anaerobic conditions.

3.4.5.1 Phase 1 and Phase 2: Aerobic, High Temperature

It is assumed that during these two phases the temperature is sufficiently high and that it is sufficiently early that liquid water is prevented from coming into contact with the container surface. Therefore, the corrosion rate is independent of the saturation. The Phase 1 process occurs under low RH conditions and switches off as RH increases, while the Phase 2 process switches on as RH increases. Therefore the Phase 1 and Phase 2 processes may potentially overlap.

As with the L&ILW corrosion model (Section 3.3), corrosion processes are configured to become activated over a range of relative humidity values. To characterize the effect of relative humidity on the corrosion rates, the code uses a relative humidity modulation factor, h (-), which is defined as zero below the lower limit, one above the upper limit, and as increasing monotonically between the two. The exact form depends on the parameterization of the GGM. See Section 3.8.

Defining ρ_1 (kg m^{-3}) and M_1 (kg mol^{-1}) as the density and molar mass of carbon steel and A_1 (m^2) as the total surface area of carbon steel within the compartment, the overall rate of consumption of Fe in mol s^{-1} can then be expressed as

$$\Phi_1 = \Omega \frac{\rho_1 A_1 (1-h)}{M_1} R_1(t, T; t_1, D_1, E_1) \tag{3.52}$$

for Phase 1 (dry air oxidation), and

$$\Phi_2 = \Omega \frac{\rho_1 A_1 h}{M_1} R_2(T; D_2, E_2) \tag{3.53}$$

for Phase 2 (aerobic unsaturated conditions). The Ω terms ensure that these processes are only active under aerobic conditions.

3.4.5.2 Phase 3 and Phase 4: Anaerobic, Temperature Descending

It is assumed each compartment extends deep enough into the bentonite so it may contain drier and wetter zones. At the start of the anaerobic phase the container will still be hot. There will be a 'dry' zone close to the container that will remain free from liquid water. Further away from the container there may be a 'wet' zone with free liquid water. Overall, the water saturation for the compartment may be non-zero - but the corrosion rate will initially remain saturation independent. The Phase 3 process will switch on as the RH increases.

Eventually the liquid water will break through and contact the container surface, but the water may not be filling the entire pore space of the compartment (due to the resaturation transient and because gas is being produced) so the contact with water might be localized. The liquid water will transport with it the carbonate required for the Phase 4 process. Therefore, the Phase 4 process switches on as this happens.

The break-through of the water to the container surface is modelled as follows. A parameter (d) that can be interpreted as the bulk water saturation above which breakthrough of water to the container surface occurs for each compartment. Then, while the saturation is below d it is assumed that the free water is located in a wet-zone of the compartment, away from the container and so corrosion follows Phase 3. As the saturation increases from d to 1 it is assumed that the water breaks through to the container surface and corrosion follows Phase 4.

Then, defining δ as a variable that increases linearly from 0 to 1 as the saturation (S) increases from d to 1;

$$\delta(S; d) = \begin{cases} 0 & \text{when } S < d, \\ \dfrac{S-d}{1-d} & \text{when } S \geq d, \end{cases} \tag{3.54}$$

the overall rate of consumption of Fe in mol s^{-1} can be expressed as:

$$\Phi_3 = (1-\Omega)(1-\delta) \frac{\rho_1 A_1 h}{M_1} R_3(T; D_3, E_3) \tag{3.55}$$

for Phase 3 (anaerobic unsaturated conditions), and

$$\Phi_4 = (1 - \Omega)\delta\frac{\rho_1 A_1}{M_1}R_4(T; D_4, E_4)$$

<div align="right">(3.56)</div>

for Phase 4 (anaerobic saturated conditions) provided O_2 is not present, or is zero otherwise. The $(1 - \Omega)$ terms ensure that these processes are only active under anaerobic conditions.

Implicit in the above model is the assumption that no CO_3^{2-} is transported to the container surface via the water vapour during Phase 3, even when the RH is high. The expressions above are configured to switch off the Phase 3 process under wet container conditions (as the saturation increases from d to 1).

Sometimes the TOUGH2 discretization of the GGM compartment is sufficiently detailed to cause heterogeneity in the saturation and relative humidity within the elements of the GGM compartment. In that case, it is necessary to provide the corrosion model with upscaled saturation and relative humidity properties accounting for the heterogeneity within the compartment, and thus allowing for a more detailed pattern of water breakthrough to the container surface to be captured. This upscaling is described in Section 4.3 of QUINTESSA and GEOFIRMA (2011a).

3.4.5.3 Summary of the Carbon Steel Consumption Rate

The rate expressions for the four corrosion phases given in Section 3.4.5.1 and Section 3.4.5.2 can be combined to give the following expression for the total rate of consumption (mol s^{-1}) of carbon steel due to corrosion:

$$\Phi_{COMBINED} = \frac{\rho_1 A_1}{M_1}\left[\begin{array}{c}\Omega\{(1 - h)R_1(t, T; t_1, D_1, E_1) + hR_2(T; D_2, E_2)\}\\ +(1 - \Omega)\{(1 - \delta)hR_3(T; D_3, E_3) + \delta R_4(T; D_4, E_4)\}\end{array}\right]$$

<div align="right">(3.57)</div>

where:

- ρ_1 (kg m^{-3}) and M_1 (kg mol^{-1}) are the density and molar mass of carbon steel;
- A_1 (m^2) as the total surface area of carbon steel within the compartment;
- Ω (-) is 1 under aerobic conditions and 0 under anaerobic conditions;
- h (-) varies from 0 to 1 as the relative humidity changes from the lower to upper thresholds;
- δ (-) changes from 0 to 1 as liquid water breaks through to the container surface; and
- R_1 to R_4 (m s^{-1}) are the basic temperature and time dependent corrosion rates given in Section 3.4.4.

3.5   ADDITIONAL PROCESSES

3.5.1   Gas Mitigation Processes

There are a number of processes by which the impact of gas production in the repository could be mitigated, either by design or because of inherent reactions within the repository.

Two natural processes that will result in the consumption of gas are included. First, the conversion of H_2 and CO_2 to CH_4 is modelled as part of the microbial reaction scheme (Equation (3.19), Section 3.2.1.2). Methanogenesis is an important cause of gas consumption,

since five moles of gas (four moles of H_2 and one mole of CO_2) are consumed for every mole of CH_4 produced.

Second, reaction between H_2S and dissolved metal ions, primarily Fe(II), will result in the formation (and rapid precipitation due to low solubility) of metal sulphides. Since Fe(II) will be the principal dissolved metal ion in the repository, the precipitation of metal sulphides is represented by

$$Fe(II) + H_2S \rightarrow FeS + 2H^+ \tag{3.58}$$

where the stoichiometry of iron sulphide is uncertain, but is here represented by the species "FeS". The kinetics of the precipitation of iron sulphide are taken to be first order with respect to the concentration of H_2S, on the basis that Fe(II) is likely to be present in excess in the system, and is given by

$$-\frac{dQ_{H2S}}{dt} = V_{FeS}C_{H2S}SV_v \tag{3.59}$$

where dQ_{H2S}/dt [mol s^{-1}] is the rate of change of the amount of H_2S in the repository, C_{H2S} [mol m^{-3}] is the concentration of H_2S, SV_V [m^3] is the saturated volume, and V_{FeS} [s^{-1}] is the first-order rate constant for the formation and precipitation of FeS, respectively.

"Gas scavengers" can also be deliberately added to the repository. For example, magnesium oxide is added to the WIPP facility to consume CO_2 via the precipitation of magnesium carbonate (Krumhansl et al., 2000). In GGM, this reaction is included to enable the effect of this gas mitigation strategy to be estimated:

$$5MgO + 5H_2O + 4CO_2 \rightarrow Mg_5(CO_3)_4(OH)_2{\cdot}4H_2O \tag{3.60}$$
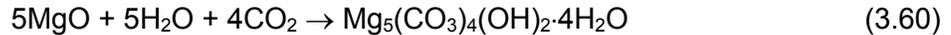
The rate of CO_2 removal by precipitation of magnesium carbonate is represented by

$$-\frac{dQ_{CO2}}{dt} = \frac{4}{5}Q_{MgO}V_{MgO} \tag{3.61}$$

where dQ_{CO2}/dt [mol s^{-1}] is the rate of change of the amount of CO_2 in the repository, respectively, Q_{MgO} [mol] is the quantity of MgO, and V_{MgO} [s^{-1}] is the first-order rate constant for the loss of MgO.

3.5.2   Carbonation of Concrete

Another potential sink for CO_2 in the repository is the carbonation of the cementitious material. The carbonation of concrete is represented by

$$Ca(OH)_2 + CO_2 \rightarrow CaCO_3 + H_2O \tag{3.62}$$

This process could consume significant quantities of CO_2, especially if the repository is grouted. However, this reaction is not currently included in GGM.

3.5.3   Water Availability

Once saturation in the repository reaches zero, the water consuming saturated phase reactions become limited by the rate of ingress of water from the geosphere. Rate constants for water-

limited processes occurring in the vapour phase, including microbial processes, biomass generation and corrosion, are relative humidity dependent as described in Section 3.2.1.3, Section 3.3.1 and Section 3.4.5. Other processes in the vapour phase are always active.

3.5.4   Gas Leakage and Influx

Gas can leak from the repository and be transported through the geosphere or, depending on the conditions, can move into the repository from the geosphere. The flow of gas through the geosphere is modelled by TOUGH2 independently of GGM using information about gas and water generation rates within the repository provided by GGM. The gas flow modelling enables the gas pressure at the repository to be calculated and fed back to GGM, which in turn uses this information to reassess the total number of moles of gas in the repository, to calculate the number of moles of gas which have leaked from or flowed into the repository and to repartition the gas in the repository between the vapour and saturated phases. When gas flows from the geosphere into the repository, its composition is assumed to match the composition of the existing gas within the repository. The validity of this assumption needs to be evaluated on a case by case basis depending on the assumed geosphere bulk gas and whether gas flowing into the repository is returning gas previously generated within the repository or 'fresh' bulk gas from the geosphere.

3.6   IMPLEMENTATION OF GGM

The definitions of all model parameters appearing in GGM model equations, including reactants, products and rate constants are given in Table 3-1.

Table 3-1: List of Model Parameters for the Gas Generation Model and their Internal Units.

Symbol	Definition	L&ILW	UF	Units
A_l	The total surface area of metal l.	✓	✓	m^2
$A_{l,n}$	Surface area of metal l under saturation conditions n	✓		m^2
$A_{1,1}$	Surface area of carbon and galvanized steel exposed to vapour phase	✓		m^2
$A_{1,2}$	Surface area of carbon and galvanized steel exposed to solution phase	✓		m^2
$A_{2,1}$	Surface area of passivated carbon steel exposed to vapour phase	✓		m^2
$A_{2,2}$	Surface area of passivated carbon steel exposed to solution phase	✓		m^2
$A_{3,1}$	Surface area of stainless steel and Ni-based alloy exposed to vapour phase	✓		m^2
$A_{3,2}$	Surface area of stainless steel and Ni-based alloy exposed to solution phase	✓		m^2

Symbol	Definition	L&ILW	UF	Units
$A_{4,1}$	Surface area of Zr alloy exposed to vapour phase	✓		m^2
$A_{4,2}$	Surface area of Zr alloy exposed to solution phase	✓		m^2
C_k	Concentration of product k in the water	✓		$mol \cdot m^{-3}$
C_{CO2}	Concentration of dissolved carbon dioxide in the water	✓		$mol \cdot m^{-3}$
C_{H2}	Concentration of dissolved hydrogen in the water	✓	✓	$mol \cdot m^{-3}$
C_{H2S}	Concentration of dissolved hydrogen sulphide in the water	✓		$mol \cdot m^{-3}$
C_{CH4}	Concentration of dissolved methane in the water	✓		$mol \cdot m^{-3}$
C_{O2}	Concentration of dissolved oxygen in the water	✓	✓	$mol \cdot m^{-3}$
C_{N2}	Concentration of dissolved nitrogen in the water	✓		$mol \cdot m^{-3}$
C_{NO3}	Concentration of dissolved nitrate in the water	✓		$mol \cdot m^{-3}$
C_{SO4}	Concentration of dissolved sulphate	✓		$mol \cdot m^{-3}$
D	Biomass decay rate	✓		s^{-1}
D_p	The basic rate constant for the phase p corrosion of carbon steel under non-isothermal conditions.		✓	Mixed
D_1	The basic rate constant for the phase 1 (dry-air oxidation) corrosion of carbon steel under non-isothermal conditions.		✓	$m\ s^{-1/2}$
D_2	The basic rate constant for the phase 2 (aerobic unsaturated) corrosion of carbon steel under non-isothermal conditions.		✓	$m\ s^{-1}$
D_3	The basic rate constant for the phase 3 (anaerobic unsaturated) corrosion of carbon steel under non-isothermal conditions.		✓	$m\ s^{-1}$
D_4	The basic rate constant for the phase 4 (anaerobic saturated) corrosion of carbon steel under non-isothermal conditions.		✓	$m\ s^{-1}$

Symbol	Definition	L&ILW	UF	Units
d	The ratio of the expected bentonite wet-zone thickness to the ratio of the thickness of the compartment as measured away from the container wall. Alternatively, this can be thought of as the saturation above which water breaks through to the container wall.		✓	Unitless
δ	max(0,(S-d)/(1-d)). This increases linearly from 0 to 1 as the saturation increases from d to 1 and is used to model the breakthrough of water to the container wall within a compartment.		✓	Unitless
ε	A constant with value between 0 and 1 chosen to balance the rate of consumption of water due to saturated phase reactions with the rate of ingress of water when at zero saturation. Has the value 1 under partially or fully saturated conditions.	✓		Unitless
E_p	The molar activation energy for the phase p corrosion of carbon steel under non-isothermal conditions.		✓	$J\ mol^{-1}$
E_1	The molar activation energy for the phase 1 (dry-air oxidation) corrosion of carbon steel under non-isothermal conditions.		✓	$J\ mol^{-1}$
E_2	The molar activation energy for the phase 2 (aerobic unsaturated) corrosion of carbon steel under non-isothermal conditions.		✓	$J\ mol^{-1}$
E_3	The molar activation energy for the phase 3 (anaerobic unsaturated) corrosion of carbon steel under non-isothermal conditions.		✓	$J\ mol^{-1}$
E_4	The molar activation energy for the phase 4 (anaerobic saturated) corrosion of carbon steel under non-isothermal conditions.		✓	$J\ mol^{-1}$
γ	The number of seconds per year		✓	$s\ y^{-1}$
g	S+h(1-S). This factor is used to scale processes that are RH dependent in the vapour phase.		✓	Unitless
h	A RH modulation function, varying from 0 to 1 in the range RH_{min} to RH_{max}	✓	✓	Unitless
J_{ki}	Stoichiometric coefficient for product k formed from organic substrate i	✓		Unitless

Symbol	Definition	L&ILW	UF	Units
J_{H2O}	Flux of water into the volume	✓	✓	$mol \cdot s^{-1}$
K_i	Solubility constant for species i	✓		$mol \cdot m^{-3} \cdot Pa^{-1}$
K_{CO2}	Solubility constant for carbon dioxide	✓		$mol \cdot m^{-3} \cdot Pa^{-1}$
K_{H2}	Solubility constant for hydrogen	✓	✓	$mol \cdot m^{-3} \cdot Pa^{-1}$
K_{H2S}	Solubility constant for hydrogen sulphide	✓		$mol \cdot m^{-3} \cdot Pa^{-1}$
K_{CH4}	Solubility constant for methane	✓		$mol \cdot m^{-3} \cdot Pa^{-1}$
K_{O2}	Solubility constant for oxygen	✓	✓	$mol \cdot m^{-3} \cdot Pa^{-1}$
K_{N2}	Solubility constant for nitrogen	✓		$mol \cdot m^{-3} \cdot Pa^{-1}$
K_R	Fraction of dead biomass recycled into cellulose	✓		Unitless
m	The number of moles of bound water per mole of styrene monomer	✓		-
M_ℓ	Effective molecular mass of metal ℓ	✓		$kg \cdot mol^{-1}$
M_1	Effective molecular mass of carbon and galvanized steel	✓	✓	$kg \cdot mol^{-1}$
M_2	Effective molecular mass of passivated carbon steel	✓		$kg \cdot mol^{-1}$
M_3	Effective molecular mass of stainless steel and Ni-based alloys	✓		$kg \cdot mol^{-1}$
M_4	Effective molecular mass of Zr alloys	✓		$kg \cdot mol^{-1}$
Ω	1 under aerobic conditions and 0 under anaerobic conditions		✓	Unitless
P_i	Partial pressure of gaseous species i	✓		Pa
P_{CO2}	Partial pressure of carbon dioxide	✓		Pa
P_{CO2}^{ref}	Reference partial pressure of CO_2 for enhancement of corrosion	✓		Pa
P_{H2}	Partial pressure of hydrogen	✓	✓	Pa
P_{H2S}	Partial pressure of hydrogen sulphide	✓		Pa
P_{CH4}	Partial pressure of methane	✓		Pa
P_{O2}	Partial pressure of oxygen	✓	✓	Pa
P_{N2}	Partial pressure of nitrogen	✓		Pa
q	Exponent for enhancement of corrosion rate by CO_2	✓		Unitless

Symbol	Definition	L&ILW	UF	Units
q_{CO2}	Amount of gaseous carbon dioxide in the volume	✓		mol
q_{H2}	Amount of gaseous hydrogen in the volume	✓	✓	mol
q_{H2S}	Amount of gaseous hydrogen sulphide in the volume	✓		mol
q_{CH4}	Amount of gaseous methane in the volume	✓		mol
q_{O2}	Amount of gaseous oxygen in the volume	✓	✓	mol
q_{N2}	Amount of gaseous nitrogen in the volume	✓		mol
Q_{ℓ}	Quantity of metallic material ℓ	✓	✓	mol
Q_1	Quantity of carbon and galvanized steel	✓	✓	mol
Q_2	Quantity of passivated carbon steel	✓		mol
Q_3	Quantity of stainless steel and Ni-based alloys	✓		mol
Q_4	Quantity of Zr alloys	✓		mol
Q_{FeOOH}	Quantity of iron oxyhydroxide	✓	✓	mol
Q_{FeCO3}	Quantity of iron carbonate	✓	✓	mol
Q_{Fe3O4}	Quantity of magnetite	✓	✓	mol
Q_{FeS}	Quantity of iron sulphide	✓		mol
Q_{Fe2O3}	Quantity of iron (III) oxide		✓	mol
Q_{H2O}	Quantity of water	✓	✓	mol
Q_{MgO}	Quantity of magnesium oxide	✓		mol
Q_C	Quantity of (dry) cellulose monomer	✓		mol
Q_R	Quantity of styrene monomer from (dry) IX resin waste	✓		mol
Q_P	Quantity of styrene monomer from (dry) plastics and rubbers	✓		mol
Q_{CO2}	Quantity of carbon dioxide in the volume	✓		mol
Q_{H2}	Quantity of hydrogen in the volume	✓	✓	mol
Q_{H2S}	Quantity of hydrogen sulphide in the volume	✓		mol
Q_{CH4}	Quantity of methane in the volume	✓		mol
Q_{O2}	Quantity of oxygen in the volume	✓	✓	mol
Q_{N2}	Quantity of nitrogen in the volume	✓		mol
Q_{AIR}	Rate of generation of bulk gas component in the volume. This quantity represents both gas and dissolved phases of the bulk gas.	✓	✓	kg/s

Symbol	Definition	L&ILW	UF	Units
$Q_{CO_3^{2-}}$	Quantity of carbonate ions in the volume		✓	mol
$R_{\ell,m,n}$	Corrosion rate of metal ℓ under redox conditions m and degree of saturation n within a L&ILW repository	✓		m·s^{-1}
$R_{1,1,1}$	Corrosion rate of carbon and galvanized steel under aerobic unsaturated conditions within a L&ILW repository	✓		m·s^{-1}
$R_{1,2,1}$	Corrosion rate of carbon and galvanized steel under anaerobic unsaturated conditions within a L&ILW repository	✓		m·s^{-1}
$R_{1,1,2}$	Corrosion rate of carbon and galvanized steel under aerobic saturated conditions within a L&ILW repository	✓		m·s^{-1}
$R_{1,2,2}$	Corrosion rate of carbon and galvanized steel under anaerobic saturated conditions within a L&ILW repository	✓		m·s^{-1}
$R_{2,1,1}$	Corrosion rate of passivated carbon steel under aerobic unsaturated conditions within a L&ILW repository	✓		m·s^{-1}
$R_{2,2,1}$	Corrosion rate of passivated carbon steel under anaerobic unsaturated conditions within a L&ILW repository	✓		m·s^{-1}
$R_{2,1,2}$	Corrosion rate of passivated carbon steel under aerobic saturated conditions within a L&ILW repository	✓		m·s^{-1}
$R_{2,2,2}$	Corrosion rate of passivated carbon steel under anaerobic saturated conditions within a L&ILW repository	✓		m·s^{-1}
$R_{3,1,1}$	Corrosion rate of stainless steel and Ni-based alloys under aerobic unsaturated conditions within a L&ILW repository	✓		m·s^{-1}
$R_{3,2,1}$	Corrosion rate of stainless steel and Ni-based alloys under anaerobic unsaturated conditions within a L&ILW repository	✓		m·s^{-1}
$R_{3,1,2}$	Corrosion rate of stainless steel and Ni-based alloys under aerobic saturated conditions within a L&ILW repository	✓		m·s^{-1}
$R_{3,2,2}$	Corrosion rate of stainless steel and Ni-based alloys under anaerobic saturated conditions within a L&ILW repository	✓		m·s^{-1}

Symbol	Definition	L&ILW	UF	Units
$R_{4,1,1}$	Corrosion rate of Zr alloys under aerobic unsaturated conditions within a L&ILW repository	✓		$m \cdot s^{-1}$
$R_{4,2,1}$	Corrosion rate of Zr alloys under anaerobic unsaturated conditions within a L&ILW repository	✓		$m \cdot s^{-1}$
$R_{4,1,2}$	Corrosion rate of Zr alloys under aerobic saturated conditions within a L&ILW repository	✓		$m \cdot s^{-1}$
$R_{4,2,2}$	Corrosion rate of Zr alloys under anaerobic saturated conditions within a L&ILW repository	✓		$m \cdot s^{-1}$
RH_{min}	A Relative Humidity value (fractional) below which all vapour phase corrosion and microbial reactions are modelled to have ceased.	✓	✓	Unitless
RH_{max}	A Relative Humidity value (fractional) above which all vapour phase corrosion and microbial reactions are modelled as fully active.	✓	✓	Unitless
ρ_ℓ	Density of metal ℓ	✓		$kg \cdot m^{-3}$
ρ_1	Density of carbon and galvanized steel	✓	✓	$kg \cdot m^{-3}$
ρ_2	Density of passivated carbon steel	✓		$kg \cdot m^{-3}$
ρ_3	Density of stainless steel and Ni-based alloys	✓		$kg \cdot m^{-3}$
ρ_4	Density of Zr alloys	✓		$kg \cdot m^{-3}$
S	Degree of saturation. Ratio of volume of free water within volume (excludes bound water) and void volume.	✓	✓	Unitless
t	Time		✓	S
t_1	The time at which Phase 1 corrosion starts under non-isothermal conditions. This is equivalent to the emplacement time.		✓	S
T	Temperature		✓	K
$V_{i,j}$	Rate constant for the degradation or organic substrate i under microbial condition j	✓		s^{-1}
$V_{C,a}$	Rate constant for the aerobic degradation of cellulose	✓		s^{-1}
$V_{C,b}$	Rate constant for the oxidation of cellulose by nitrate reduction	✓		s^{-1}

Symbol	Definition	L&ILW	UF	Units
$V_{C,c}$	Rate constant for the oxidation of cellulose by ferric ion reduction	✓		s^{-1}
$V_{C,d}$	Rate constant for the oxidation of cellulose by sulphate reduction	✓		s^{-1}
$V_{C,e}$	Rate constant for the generation of methane from cellulose	✓		s^{-1}
$V_{R,a}$	Rate constant for the aerobic degradation of IX resins	✓		s^{-1}
$V_{R,b}$	Rate constant for the oxidation of IX resins by nitrate reduction	✓		s^{-1}
$V_{R,c}$	Rate constant for the oxidation of IX resins by ferric ion reduction	✓		s^{-1}
$V_{R,d}$	Rate constant for the oxidation of IX resins by sulphate reduction	✓		s^{-1}
$V_{R,e}$	Rate constant for the generation of methane from IX resins	✓		s^{-1}
$V_{P,a}$	Rate constant for the aerobic degradation of plastics and rubbers	✓		s^{-1}
$V_{P,b}$	Rate constant for the oxidation of plastics and rubbers by nitrate reduction	✓		s^{-1}
$V_{P,c}$	Rate constant for the oxidation of plastics and rubbers by ferric ion reduction	✓		s^{-1}
$V_{P,d}$	Rate constant for the oxidation of plastics and rubbers by sulphate reduction	✓		s^{-1}
$V_{P,e}$	Rate constant for the generation of methane from plastics and rubbers	✓		s^{-1}
V_{FeS}	Rate constant for the precipitation of FeS	✓		s^{-1}
V_{FeOOH}	Rate constant for the reductive dissolution of FeOOH	✓		s^{-1}
V_{MgO}	Rate constant for the conversion of magnesium oxide to magnesium carbonate	✓		s^{-1}
V_{H1}	Rate constant for the microbial oxidation of H_2 via iron reduction	✓		s^{-1}
V_{H2}	Rate constant for the microbial oxidation of H_2 via sulphate reduction	✓		s^{-1}
V_{H3}	Rate constant for the microbial generation of methane from H_2 oxidation	✓		s^{-1}
V_v	Void volume	✓	✓	m^3

Symbol	Definition	L&ILW	UF	Units
X	Biomass	✓		mol
X_a	Biomass of aerobes	✓		mol
X_b	Biomass of denitrifiers	✓		mol
X_c	Biomass of iron reducers	✓		mol
X_d	Biomass of sulphate reducers	✓		mol
X_e	Biomass of methanogens	✓		mol
X_{dead}	Dead and non-recyclable biomass	✓		mol
X_{tot}	Live (hydrated) biomass	✓		mol
Y_j	Biomass yield coefficient for microbial condition j	✓		Unitless
Y_a	Biomass yield coefficient for aerobes	✓		Unitless
Y_b	Biomass yield coefficient for denitrifiers	✓		Unitless
Y_c	Biomass yield coefficient for iron reducers	✓		Unitless
Y_d	Biomass yield coefficient for sulphate reducers	✓		Unitless
Y_e	Biomass yield coefficient for methanogens	✓		Unitless

Note: A tick indicates that this parameter is used by the associated repository model.

3.6.1   Mass-Balance Equations

The equations provided in this section combine terms from all processes – including those applicable to both the L&ILW and Used Fuel repository models. In practice the user is responsible for selecting a relevant subset of processes via the choice of appropriate rate constants. Rate constants and inventories for processes that are not relevant to the given application should be set to zero. See Table 3-1 for an indication of the parameters that are relevant to each application.

3.6.1.1 Organics

The three types of organic material considered are cellulose, IX resins, and plastics and rubbers. The mass-balance equations for each of these species are:

$$-\frac{dQ_C}{dt} = \varepsilon g \left(V_{C,a} + V_{C,b} + V_{C,c} + V_{C,d} + V_{C,e} \right) Q_C - \frac{5}{6} K_R (X_a + X_b + X_c + X_d + X_e) D \qquad (3.63)$$

for cellulose,

$$-\frac{dQ_R}{dt} = \varepsilon g \left(V_{R,a} + V_{R,b} + V_{R,c} + V_{R,d} + V_{R,e} \right) Q_R \qquad (3.64)$$

for IX resins, and

$$-\frac{dQ_P}{dt} = \varepsilon g\left(V_{P,a} + V_{P,b} + V_{P,c} + V_{P,d} + V_{P,e}\right)Q_P \tag{3.65}$$

for plastics and rubbers, where $V_{i,j}$ [s^{-1}] is the degradation rate constant for substrate i (i = C, R, P for cellulose, IX resins, and plastics and rubbers, respectively) under conditions j (j = a, b, c, d, e for aerobic respiration, denitrification, iron reduction, sulphate reduction, and methanogenesis, respectively). $V_{i,j} = V_i$ if j is the currently active TEA, and $V_{i,j} = 0$ otherwise, where V_i is the input degradation rate of organic substrate i. The constant ε in the above equations always has a value between 0 and 1. When the saturation is positive, it is equal to 1, but when the saturation is zero, it is reduced (if necessary) so as to balance the rate of consumption of water due to saturated phase reactions with the rate of ingress of water into the repository.

3.6.1.2 Metallic Materials

The rates of metal corrosion (in mol·s^{-1}) are given by

$$-\frac{dQ_1}{dt} = \frac{\rho_1}{M_1}\left(hA_{1,1}R_{1,1,1} + h\left(1+\left(\frac{P_{CO2}}{P_{CO2}^{ref}}\right)^q\right)A_{1,1}R_{1,2,1} + \varepsilon A_{1,2}R_{1,1,2} + \varepsilon\left(1+\left(\frac{P_{CO2}}{P_{CO2}^{ref}}\right)^q\right)A_{1,2}R_{1,2,2}\right)$$
$$+\frac{1}{2}V_{FeOOH}Q_{FeOOH} + \Phi_1 + \Phi_2 + \Phi_3 + \Phi_4 \tag{3.66}$$

for carbon and galvanized steel,

$$-\frac{dQ_2}{dt} = \frac{\rho_2}{M_2}\left(hA_{2,1}R_{2,1,1} + hA_{2,1}R_{2,2,1} + \varepsilon A_{2,2}R_{2,1,2} + \varepsilon A_{2,2}R_{2,2,2}\right) \tag{3.67}$$

for passivated carbon steel,

$$-\frac{dQ_3}{dt} = \frac{\rho_3}{M_3}\left(hA_{3,1}R_{3,1,1} + h\left(1+\left(\frac{P_{CO2}}{P_{CO2}^{ref}}\right)^q\right)A_{3,1}R_{3,2,1} + \varepsilon A_{3,2}R_{3,1,2} + \varepsilon\left(1+\left(\frac{P_{CO2}}{P_{CO2}^{ref}}\right)^q\right)A_{3,2}R_{3,2,2}\right) \tag{3.68}$$

for stainless steel and Ni-based alloys, and

$$-\frac{dQ_4}{dt} = \frac{\rho_4}{M_4}\left(hA_{4,1}R_{4,1,1} + hA_{4,1}R_{4,2,1} + \varepsilon A_{4,2}R_{4,1,2} + \varepsilon A_{4,2}R_{4,2,2}\right) \tag{3.69}$$

for Zr alloys, where V_{FeOOH} is the first-order rate constant for the reduction of FeOOH via Equation (3.33) and the other terms are defined in Equation (3.37), Equation (3.38) and Table 3-1.

3.6.1.3 Gases

Six gaseous species are considered O_2, N_2, CO_2, H_2, H_2S, and CH_4. The total number of moles of gas is constantly being adjusted to take into account the flux of gas into or out of the repository (see Section 3.5.4). All gases partition between the gaseous and aqueous phases according to Equation (3.97), Equation (3.98) and Equation (3.99).

The contributions to the rate of change of the total number of moles of gas molecules within the repository due to reactions for the gaseous species are given below.

$$-\frac{dQ_{O2}}{dt} = \varepsilon g(1-Y_a)[6V_{C,a}Q_C + 10V_{R,a}Q_R + 10V_{P,a}Q_P]$$

$$+\left[\frac{3\rho_1}{4M_1}\left(hA_{1,1}R_{1,1,1} + \varepsilon A_{1,2}R_{1,1,2}\right) + \frac{3\rho_2}{4M_2}\left(hA_{2,1}R_{2,1,1} + \varepsilon A_{2,2}R_{2,1,2}\right)\right]$$

$$+\left[\frac{3\rho_3}{4M_3}\left(hA_{3,1}R_{3,1,1} + \varepsilon A_{3,2}R_{3,1,2}\right) + \frac{\rho_4}{M_4}\left(hA_{4,1}R_{4,1,1} + \varepsilon A_{4,2}R_{4,1,2}\right)\right]$$

$$+\frac{3}{4}\Phi_1 + \frac{3}{4}\Phi_2$$

(3.70)

for O_2,

$$\frac{dQ_{N2}}{dt} = \varepsilon g(1-Y_b)[2.4V_{C,b}Q_C + 4V_{R,b}Q_R + 4V_{P,b}Q_P]$$

(3.71)

for N_2,

$$\frac{dQ_{CO2}}{dt} = \varepsilon g(1-Y_a)[6V_{C,a}Q_C + 8V_{R,a}Q_R + 8V_{P,a}Q_P] + \varepsilon g(1-Y_b)[6V_{C,b}Q_C + 8V_{R,b}Q_R + 8V_{P,b}Q_P]$$

$$+ \varepsilon g(1-Y_c)[6V_{C,c}Q_C + 8V_{R,c}Q_R + 8V_{P,c}Q_P] + \varepsilon g(1-Y_d)[6V_{C,d}Q_C + 8V_{R,d}Q_R + 8V_{P,d}Q_P]$$

$$+ \varepsilon g(1-Y_e)[3V_{C,e}Q_C + 3V_{R,e}Q_R + 3V_{P,e}Q_P] - \varepsilon g\frac{(1-Y_e)}{4}V_{H3}(C_{CO2}SV_v + hq_{CO2})$$

$$- 2\varepsilon g(Y_aV_{R,a} + Y_bV_{R,b} + Y_cV_{R,c} + Y_dV_{R,d} + Y_eV_{R,e})Q_R$$

$$- 2\varepsilon g(Y_aV_{P,a} + Y_bV_{P,b} + Y_cV_{P,c} + Y_dV_{P,d} + Y_eV_{P,e})Q_P$$

$$- \frac{1}{2}\varepsilon g(Y_cV_{H1}Q_{FeOOH} + Y_dV_{H2}C_{SO4}SV_v + Y_eV_{H3}(C_{CO2}SV_v + hq_{CO2}))$$

$$- \frac{\rho_1}{M_1}\left[\left(\frac{P_{CO2}}{P_{CO2}^{ref}}\right)^q (hA_{1,1}R_{1,2,1} + \varepsilon A_{1,2}R_{1,2,2})\right] - \frac{\rho_3}{M_3}\left[\left(\frac{P_{CO2}}{P_{CO2}^{ref}}\right)^q (hA_{3,1}R_{3,2,1} + \varepsilon A_{3,2}R_{3,2,2})\right]$$

$$- \frac{4}{5}\varepsilon V_{MgO}Q_{MgO}$$

(3.72)

for CO_2,

$$\frac{dQ_{H2}}{dt} = -\varepsilon g(1-Y_c)V_{H1}Q_{FeOOH} - \varepsilon g(1-Y_d)V_{H2}C_{SO4}SV_v - \varepsilon g(1-Y_e)V_{H3}(C_{CO2}SV_v + hq_{CO2})$$
$$- \varepsilon g Y_c V_{H1}C_{FeOOH}SV_v - \varepsilon g Y_d V_{H2}C_{SO4}SV_v - \varepsilon g Y_e V_{H3}(C_{CO2}SV_v + hq_{CO2})$$
$$+ \frac{4}{3}\frac{\rho_1}{M_1}\left[\left(1+\frac{3}{4}\left(\frac{P_{CO2}}{P_{CO2}^{ref}}\right)^q\right)(hA_{1,1}R_{1,2,1} + \varepsilon A_{1,2}R_{1,2,2})\right] \tag{3.73}$$
$$+ \frac{4}{3}\frac{\rho_2}{M_2}(hA_{2,1}R_{2,2,1} + \varepsilon A_{2,2}R_{2,2,2}) + \frac{4}{3}\frac{\rho_3}{M_3}\left[\left(1+\frac{3}{4}\left(\frac{P_{CO2}}{P_{CO2}^{ref}}\right)^q\right)(hA_{3,1}R_{3,2,1} + \varepsilon A_{3,2}R_{3,2,2})\right]$$
$$+ \frac{2\rho_4}{M_4}(hA_{4,1}R_{4,2,1} + \varepsilon A_{4,2}R_{4,2,2}) + \frac{1}{2}V_{FeOOH}Q_{FeOOH} + \frac{4}{3}\Phi_3 + \Phi_4$$

for H_2,

$$\frac{dQ_{H2S}}{dt} = \varepsilon g(1-Y_d)\left[3V_{C,d}Q_C + 5V_{R,d}Q_R + 5V_{P,d}Q_P\right]$$
$$+ \varepsilon g \frac{(1-Y_d)}{4}V_{H2}C_{SO4}SV_v - V_{FeS}C_{H2S}SV_v \tag{3.74}$$

for H_2S, and

$$\frac{dQ_{CH4}}{dt} = \varepsilon g(1-Y_e)\left[3V_{C,e}Q_C + 5V_{R,e}Q_R + 5V_{P,e}Q_P\right] + \varepsilon g\frac{(1-Y_e)}{4}V_{H3}(C_{CO2}SV_v + hq_{CO2}) \tag{3.75}$$

for CH_4.

3.6.1.4 Terminal Electron Acceptors

In addition to O_2, Fe(III), and CO_2, GGM also includes two other terminal electron acceptors, namely: nitrate and sulphate ions. The mass-balance equations for these latter two species are given by:

$$-\frac{dC_{NO3}}{dt} = \varepsilon g \frac{(1-Y_b)}{SV_v}\left[4.8V_{C,b}Q_C + 8V_{R,b}Q_R + 8V_{P,b}Q_P\right] \tag{3.76}$$

for NO_3^-, and

$$-\frac{dC_{SO4}}{dt} = \varepsilon g \frac{(1-Y_d)}{SV_v}\left[3V_{C,d}Q_C + 5V_{R,d}Q_R + 5V_{P,d}Q_P\right] + \varepsilon g\frac{(1-Y_d)}{4}V_{H2}C_{SO4} \tag{3.77}$$

for SO_4^{2-}.

3.6.1.5 Biomass

Biomass is generated as a result of microbial metabolism, growth and decay of which consumes and produces water and needs to be tracked for an accurate water mass balance.

The biomass mass balances are given by

$$\frac{dX_a}{dt} = \varepsilon g Y_a \left(\frac{6}{5} V_{C,a} Q_C + 2V_{R,a} Q_R + 2V_{P,a} Q_P \right) - X_a D \qquad (3.78)$$

for aerobes,

$$\frac{dX_b}{dt} = \varepsilon g Y_b \left(\frac{6}{5} V_{C,b} Q_C + 2V_{R,b} Q_R + 2V_{P,b} Q_P \right) - X_b D \qquad (3.79)$$

for denitrifiers,

$$\frac{dX_c}{dt} = \varepsilon g Y_c \left(\frac{6}{5} V_{C,c} Q_C + 2V_{R,c} Q_R + 2V_{P,c} Q_P + \frac{1}{10} V_{Hl} Q_{FeOOH} \right) - X_c D \qquad (3.80)$$

for iron reducers,

$$\frac{dX_d}{dt} = \varepsilon g Y_d \left(\frac{6}{5} V_{C,d} Q_C + 2V_{R,d} Q_R + 2V_{P,d} Q_P + \frac{1}{10} SV_v V_{H2} C_{SO4} \right) - X_d D \qquad (3.81)$$

for sulphate reducers, and

$$\frac{dX_e}{dt} = \varepsilon g Y_e \left(\frac{6}{5} V_{C,e} Q_C + 2V_{R,e} Q_R + 2V_{P,e} Q_P + \frac{1}{10} V_{H3} \left(C_{CO2} SV_v + hq_{CO2} \right) \right) - X_e D \qquad (3.82)$$

for methanogens.

The total quantity of live (hydrated) biomass is given by $X_{tot} = X_a + X_b + X_c + X_d + X_e$. The total quantity of dead (dehydrated) biomass that cannot be recycled (X_{dead}) is also tracked in the code, and is given by:

$$\frac{dX_{dead}}{dt} = (1 - K_R)(X_a + X_b + X_c + X_d + X_e)D . \qquad (3.83)$$

3.6.1.6 Corrosion Products

A number of different corrosion products are tracked in the code, including $FeOOH$, $FeCO_3$, Fe_3O_4, Fe_2O_3 and FeS. The mass-balance equations for these species are given by:

$$\frac{dQ_{FeOOH}}{dt} = -\varepsilon g (1 - Y_c)[24V_{C,c} Q_C + 40V_{R,c} Q_R + 40V_{P,c} Q_P] - 2\varepsilon g (1 - Y_C)V_{Hl} Q_{FeOOH}$$
$$+ \left[\frac{\rho_1}{M_1} \left(hA_{1,1} R_{1,1,1} + \varepsilon A_{1,2} R_{1,1,2} \right) + \frac{\rho_2}{M_2} \left(hA_{2,1} R_{2,1,1} + \varepsilon A_{2,2} R_{2,1,2} \right) + \frac{\rho_3}{M_3} \left(hA_{3,1} R_{3,1,1} + \varepsilon A_{3,2} R_{3,1,2} \right) \right] \qquad (3.84)$$
$$- Q_{FeOOH} V_{FeOOH} + \Phi_2$$

for FeOOH,

$$\frac{dQ_{FeCO3}}{dt} = \frac{\rho_1}{M_1} \left(\frac{P_{CO2}}{P_{CO2}^{ref}} \right)^q \left(hA_{1,1} R_{1,2,1} + \varepsilon A_{1,2} R_{1,2,2} \right) + \frac{\rho_3}{M_3} \left(\frac{P_{CO2}}{P_{CO2}^{ref}} \right)^q \left(hA_{3,1} R_{3,2,1} + \varepsilon A_{3,2} R_{3,2,2} \right) \qquad (3.85)$$

for FeCO₃,

$$\frac{dQ_{Fe3O4}}{dt} = \frac{\rho_1}{3M_1}\left(hA_{1,1}R_{1,2,1} + \varepsilon A_{1,2}R_{1,2,2}\right) + \frac{\rho_2}{3M_2}\left(hA_{2,1}R_{2,2,1} + \varepsilon A_{2,2}R_{2,2,2}\right)$$
$$+ \frac{\rho_3}{3M_3}\left(hA_{3,1}R_{3,2,1} + \varepsilon A_{3,2}R_{3,2,2}\right) + \frac{1}{2}V_{FeOOH}Q_{FeOOH} + \frac{1}{3}\Phi_3 + \Phi_4 \tag{3.86}$$

for Fe₃O₄,

$$\frac{dQ_{Fe2O3}}{dt} = \frac{1}{2}\Phi_1 \tag{3.87}$$

for Fe₂O₃ and

$$\frac{dQ_{FeS}}{dt} = SV_v V_{FeS} C_{H2S} \tag{3.88}$$

for FeS.

3.6.1.7 Water

Water is consumed and produced by both microbial and corrosion reactions. The rate of generation of water is given by:

$$\frac{dQ_{H2O}}{dt} = -\varepsilon\frac{dC}{dt} + \frac{dD}{dt} \tag{3.89}$$

where

$$\frac{dC}{dt} = -S \left\{ \begin{array}{l} (1-Y_a)[5V_{C,a}Q_C + 4V_{R,a}Q_R + 4V_{P,a}Q_P] + (1-Y_b)[7.4V_{C,b}Q_C + 8V_{R,b}Q_R + 8V_{P,b}Q_P] \\[4pt] \quad - (1-Y_c)[7V_{C,c}Q_C + 16V_{R,c}Q_R + 16V_{P,c}Q_P] + (1-Y_d)[5V_{C,d}Q_C + 4V_{R,d}Q_R + 4V_{P,d}Q_P] \\[4pt] \quad - (1-Y_e)[V_{C,e}Q_C + 6V_{R,e}Q_R + 6V_{P,e}Q_P] + (1-Y_d)SV_v V_{H2}C_{SO4} \\[4pt] \quad + \frac{1}{2}(1-Y_e)V_{H3}(C_{CO2}SV_v + hq_{CO2}) \\[4pt] \quad - 27.4(Y_a V_{C,a} + Y_b V_{C,b} + Y_c V_{C,c} + Y_d V_{C,d} + Y_e V_{C,e})Q_C \\[4pt] \quad - 50(Y_a V_{R,a} + Y_b V_{R,b} + Y_c V_{R,c} + Y_d V_{R,d} + Y_e V_{R,e})Q_R \\[4pt] \quad - 50(Y_a V_{P,a} + Y_b V_{P,b} + Y_c V_{P,c} + Y_d V_{P,d} + Y_e V_{P,e})Q_P \\[4pt] \quad - \frac{17}{10}\left(Y_c V_{H1}Q_{FeOOH} + Y_d V_{H2}C_{SO4}SV_v + Y_e V_{H3}(C_{CO2}SV_v + hq_{CO2})\right) \\[4pt] \quad - V_{MgO}Q_{MgO} \end{array} \right\}$$

$$+ \frac{\rho_1}{2M_1}(A_{1,2}R_{1,1,2}) + \frac{\rho_2}{2M_2}(A_{2,2}R_{2,1,2}) + \frac{\rho_3}{2M_3}(A_{3,2}R_{3,1,2})$$

$$+ \frac{4}{3}\frac{\rho_1}{M_1}\left[\left(1 + \frac{3}{4}\left(\frac{P_{CO2}}{P_{CO2}^{ref}}\right)^q\right)(A_{1,2}R_{1,2,2})\right] + \frac{4}{3}\frac{\rho_2}{M_2}[A_{2,2}R_{2,2,2}] \qquad\qquad (3.90)$$

$$+ \frac{4}{3}\frac{\rho_3}{M_3}\left[\left(1 + \frac{3}{4}\left(\frac{P_{CO2}}{P_{CO2}^{ref}}\right)^q\right)(A_{3,2}R_{3,2,2})\right] + \frac{2\rho_4}{M_4}[A_{4,2}R_{4,2,2}]$$

$$+ 2\Phi_4$$

is the rate of consumption of water due to processes that operate under saturated conditions only, and

$$\frac{dD}{dt} = (1-S)h \left\{ \begin{array}{l} (1-Y_a)[5V_{C,a}Q_C + 4V_{R,a}Q_R + 4V_{P,a}Q_P] + (1-Y_b)[7.4V_{C,b}Q_C + 8V_{R,b}Q_R + 8V_{P,b}Q_P] \\ \quad - (1-Y_c)[7V_{C,c}Q_C + 16V_{R,c}Q_R + 16V_{P,c}Q_P] + (1-Y_d)[5V_{C,d}Q_C + 4V_{R,d}Q_R + 4V_{P,d}Q_P] \\ \quad - (1-Y_e)[V_{C,e}Q_C + 6V_{R,e}Q_R + 6V_{P,e}Q_P] + (1-Y_d)SV_v V_{H2}C_{SO4} \\ \quad + \frac{1}{2}(1-Y_e)V_{H3}(C_{CO2}SV_v + hq_{CO2}) \\ \quad - 27.4(Y_a V_{C,a} + Y_b V_{C,b} + Y_c V_{C,c} + Y_d V_{C,d} + Y_e V_{C,e})Q_C \\ \quad - 50(Y_a V_{R,a} + Y_b V_{R,b} + Y_c V_{R,c} + Y_d V_{R,d} + Y_e V_{R,e})Q_R \\ \quad - 50(Y_a V_{P,a} + Y_b V_{P,b} + Y_c V_{P,c} + Y_d V_{P,d} + Y_e V_{P,e})Q_P \\ \quad - \frac{17}{10}(Y_c V_{H1}Q_{FeOOH} + Y_d V_{H2}C_{SO4}SV_v + Y_e V_{H3}(C_{CO2}SV_v + hq_{CO2})) \\ \quad - V_{MgO}Q_{MgO} \end{array} \right\}$$

$$+ 25(1-K_R)(X_a + X_b + X_c + X_d + X_e)D + \frac{137}{6}K_R(X_a + X_b + X_c + X_d + X_e)D$$

$$- \frac{\rho_1}{2M_1}(A_{1,1}hR_{1,1,1}) - \frac{\rho_2}{2M_2}(A_{2,1}hR_{2,1,1}) - \frac{\rho_3}{2M_3}(A_{3,1}hR_{3,1,1})$$

$$- \frac{4}{3}\frac{\rho_1}{M_1}\left[\left(1 + \frac{3}{4}\left(\frac{P_{CO2}}{P_{CO2}^{ref}}\right)^q\right)(A_{1,1}hR_{1,2,1})\right] - \frac{4}{3}\frac{\rho_2}{M_2}[A_{2,1}hR_{2,2,1}]$$

$$- \frac{4}{3}\frac{\rho_3}{M_3}\left[\left(1 + \frac{3}{4}\left(\frac{P_{CO2}}{P_{CO2}^{ref}}\right)^q\right)(A_{3,1}hR_{3,2,1})\right] - \frac{2\rho_4}{M_4}[A_{4,1}hR_{4,2,1}] \qquad (3.91)$$

$$- \frac{1}{2}\Phi_2 - \frac{4}{3}\Phi_3$$

is the rate of generation of water due to the remaining terms, including the death of biomass and vapour phase processes.

3.6.1.8 Other Species

If MgO is added to the repository to mitigate the effect of CO_2, it is necessary to track the amount of remaining MgO. The amount of the product ($Mg_5(CO_3)_4(OH)_2 \cdot 4H_2O$) is not specifically calculated in the code, but can be obtained from the loss of MgO and the stoichiometry of the reaction in Equation (3.60).

The mass-balance equation for MgO is given by:

$$-\frac{dQ_{MgO}}{dt} = V_{MgO}Q_{MgO} \qquad (3.92)$$

The depletion of carbonate ions due to Phase 4 corrosion of used fuel containers from an initial specified inventory is modelled as follows:

$$\frac{dQ_{CO_3^{2-}}}{dt} = -\Phi_4 \qquad (3.93)$$

3.6.2 Assumptions

A number of assumptions have been made in the development of GGM. Table 3-2, Table 3-3 and Table 3-4 list the assumptions for a L&ILW repository and their basis for the conceptual microbial model, the conceptual corrosion model, and the overall gas generation model, respectively. The assumptions implicit in the model for the corrosion of used fuel containers are given in Table 3-5.

Table 3-2: Assumptions Included in Conceptual Microbial Model for a L&ILW Repository

Assumption	Basis
Conversion of organic polymer to its soluble intermediates is the rate-limiting step in the degradation of organics.	Mechanistically justifiable and simplifies modelling of microbial processes.
Degradation of IX resins is possible.	Degradation of IX resins is allowed, but they can be treated as recalcitrant by setting the appropriate rate constants to zero.
Degradation of plastics and rubbers is possible and can be treated in the same manner as the degradation of IX resins.	Degradation of plastics and rubbers is allowed, but they can be treated as recalcitrant by setting the appropriate rate constants to zero. The treatment of plastics and rubbers in the same manner as IX resins is a simplification, but preserves the basic conversion process from organic carbon to CH_4 and CO_2.
Kinetics of degradation of organic material are first order.	Reasonable assumption provided that value for rate constant is derived from experimental data on the same basis. Supported by the modelling of hydrolysis of polymers such as cellulose in other environments.
Microbial activity slows as the A_w falls below 0.8, and ceases at a water activity (A_w) below 0.6..	Consistent with data (Shreir 1976) and mechanistically justifiable.
Microbial kinetics are independent of the amount of biomass.	Simplifies the modelling of microbial kinetic processes. Essentially assumes that there is enough biomass that the rate has saturated (e.g., surfaces are fully covered by microbes).
Nitrogen is not limiting for microbial growth.	Simplifies the modelling of microbial processes by limiting the number of species in the model. It is also conservative with respect to gas generation, since it ensures microbial reactions proceed to completion.
There is sufficient pH-buffering capacity in the environment to permit consumption of acidic fermentation products.	Simplifies modelling of microbial processes. It is also conservative with respect to gas generation since it ensures microbial reactions proceed to completion.

Assumption	Basis
Decay of one "mole" of biomass generates 25 moles of water.	Reasonable assumption based on mean water content of biomass of 80% (by weight).
9 moles of bound water are freed per mole of styrene monomer as it degrades.	Calculation based on 40% bound water by weight for the resins and 8 moles of styrene monomer per 10 moles of dry resin (which include functional groups).
Carbon from a fraction of the dead biomass is recycled.	Consistent with mechanistic understanding.
Availability of phosphorus and sulphur do not limit microbial growth.	Simplifying assumption for modelling purposes. It is also conservative with respect to gas generation since it ensures microbial reactions proceed to completion.
All microbes required to catalyze the reactions modelled are present within the repository.	This is also conservative with respect to gas generation since it ensures microbial reactions proceed to completion. Also mechanistically supportable since microbes will enter the repository via a range of routes.

Table 3-3: Assumptions Included in Conceptual Corrosion Model for a L&ILW Repository

Assumption	Basis
Vapour phase corrosion becomes active in the range 60-80% RH.	Mechanistically justifiable and commonly observed threshold from atmospheric corrosion studies.
Magnetite is the stable long-term anaerobic corrosion product of the corrosion of steel.	Reasonable assumption based on information available in the literature. Conservative in terms of the maximum amount of H_2 produced.
Corrosion of stainless steel and Ni-based alloys can be represented by the formation of $FeOOH$ and Fe_3O_4 under aerobic and anaerobic conditions, respectively.	Simplifying assumption for modelling purposes. Reasonable assumption for stainless steels, which typically contain 60-80% Fe. Reasonable for Ni-based alloys as corrosion rate is low and amount of "Fe(III)" predicted to be formed from these materials is small compared with that formed from carbon and galvanized steels. Differences in amounts of H_2 formed because of difference in valences of corrosion products can be adjusted through value of initial inventory of these materials.
CO_2-enhanced corrosion occurs for carbon and galvanized steel and stainless steel and Ni-based alloys only.	Reasonable assumption based on evidence in the literature. Passive carbon steels are less likely to be affected due to pH-buffering capacity of cementitious materials (the assumed passivating agent). No evidence for enhanced effect of CO_2 on Zr alloys.

Table 3-4: Assumptions Included in the Overall Gas Generation Model for a L&ILW Repository

Assumption	Basis
Transport of species in the repository is rapid on the timescale of interest and no concentration gradients develop.	Simplifies modelling by removing the need to predict the spatial dependence of the concentrations of various species. Reasonable assumption for long time scale (years or more) of interest for a repository.
All Fe(III) formed is present as FeOOH and is available for microbial consumption and/or reductive dissolution.	Ferric corrosion products will likely be present as a mixture of Cl^-, SO_4^{2-}, and CO_3^{2-} -containing forms of Green Rust. However, provided the water mass balance is accurately predicted, the actual form of corrosion product is relatively unimportant since the concentrations of Cl^- and SO_4^{2-} are not tracked in the model. The solubility of Fe(III) is likely to be limited at the near-neutral to moderately alkaline pH values expected in the repository, so the assumption that the Fe(III) is available for microbial metabolism may result in an over-estimate of the extent of microbial iron reduction in the model.
Assumes first-order kinetics for the formation of magnesium carbonates from MgO.	Consistent with mechanistic understanding.
Kinetics of FeS precipitation are first order with respect to the concentration of H_2S.	Reasonable assumption based on known kinetics of reaction.
Excess Fe(II) available for precipitation of FeS.	Reasonable assumption based on large surface area and quantity of ferrous materials in repository and fact that sulphide will only be formed under anaerobic conditions.
Gas generation reactions and water transport are assumed to take place under isothermal conditions (based on a typical temperature of around 20 °C at the repository horizon).	Temperatures in an L&ILW DGR are expected to be around geosphere conditions due to the low heat sources. Long-term thermal changes in the geosphere will be driven by glacial cycling. At OPG's DGR, repository temperatures are expected to reach a minimum of 17 °C under glacial conditions compared with 22 °C at the present date.

Table 3-5: Assumptions Included in Conceptual Corrosion Model for a Used Fuel Repository

Assumption	Basis
Vapour phase corrosion becomes active in the range 60-80% RH.	Mechanistically justifiable and commonly observed threshold from atmospheric corrosion studies. See Newman et al. (2010) and on evidence from the atmospheric corrosion literature (Leygraf and Graedel 2000, Rozenfeld 1972).
Local reduction of H+, which may lead to enhanced hydrogen absorption and environmentally assisted cracking (King 2009), is not considered.	It will not lead to the generation of significant quantities of H_2.
There is no significant corrosion prior to the sealing of the repository.	An extended operational phase could allow O_2 ingress and additional corrosion of the container.
There will likely be a transformation of corrosion products as the environmental conditions evolve, but this is not considered. For example, the reductive dissolution of Fe(III) solids formed during Phases 1 and 2 could support additional Fe dissolution but this is not explicitly considered.	These are considered to be second order effects.

3.6.3   Problem Solution Method

The GGM model described here is implemented using FORTRAN 77 subroutines, thus enabling it to be driven by TOUGH2, which is also written in FORTRAN 77 (J3 2008).

GGM consists of first-order coupled differential equations given by the mass balance equations and non-differential equations, such as Henry's law. The mass balance equations are evolved forward in time using a modified Euler time stepping scheme, and the non-differential equations are solved for the remaining variables at each time step. Reactions are generally ceased once any of the reactants have been exhausted. One special case that is treated differently is water, for which there may be resupply to the repository at a slow rate and for which rates of affected processes may be reduced so that the total rate of consumption of water balances the rate of ingress.

In this model, gas is generated via degradation reactions in the saturated part of the repository and under unsaturated conditions if the relative humidity exceeds RH_{min} (typically set to 60%). The gas repartitions between the saturated and unsaturated parts of the repository according to Henry's Law effectively instantaneously. Gas partitioning has been treated mathematically to ensure that its numerical discretization can be implemented in a manner consistent with all the other processes and can be treated by evolving differential equations for the total number of moles in the repository. Details of this treatment of gas repartitioning are given in Section 3.7.

The GGM code has a large number of variables that are highly coupled. GGM uses an adaptive time stepping algorithm that chooses a time resolution sufficient to capture the changes that can occur on the disparate timescales of the various physical processes. There is also coupling with TOUGH2 via gas and water generation, pressure, saturation, relative humidity and void volume. For efficiency, GGM does not require TOUGH2 and GGM to take the same time steps. GGM provides TOUGH2 with a suggested maximum time step based on the current rate of change of the GGM inputs and outputs.

3.7   GAS REPARTITIONING

3.7.1   Mathematical Encapsulation

Consider an enclosed volume V (m³), with saturation S (-), at temperature T (K). Several ideal gas species exist in the volume. The total number of moles of gas i in the volume is known to be N_i. The gas partitions itself between the unsaturated and the saturated phases according to Henry's law. The equilibrium partial pressure, p_i (Pa), and number of moles of gas i, n_i (mol), in the unsaturated phase and the concentration of gas in solution in the saturated phase, c_i (mol m⁻³), are the unknown variables.

Writing expressions for the total number of moles of gas in the system, the ideal gas law modified to accept a compressibility factor Z (-), and Henry's law gives three equations for the three unknowns:

$$N_i = n_i + c_i SV \tag{3.94}$$

$$p_i(1 - S)V = n_i ZRT \tag{3.95}$$

$$c_i = p_i K_i \tag{3.96}$$

where R (m³ Pa K⁻¹ mol⁻¹) is the molar gas constant and K_i (mol m⁻³ Pa⁻¹) is the solubility constant for gas i. These can be solved readily to give:

$$c_i = \frac{N_i}{V} \frac{ZRTK_i}{1+S(ZRTK_i-1)} \tag{3.97}$$

$$p_i = \frac{1}{K_i} c_i \tag{3.98}$$

$$n_i = N_i - c_i SV \tag{3.99}$$

3.7.2   Implications for GGM

The total gas generation rate, Q_{air} (mol s⁻¹), can be calculated as:

$$
\begin{aligned}
Q_{air} &= \sum_i \frac{\partial n_i}{\partial t} \\
&= \sum_i \left(\frac{\partial N_i}{\partial t} - \frac{\partial c_i}{\partial t} SV - c_i \frac{\partial S}{\partial t} V \right) \\
&= \sum_i \left[f_i V \frac{S(1-S)}{1+S(RTK_i-1)} - RTK_i N_i \frac{\partial S}{\partial t} \left(\frac{1}{1+S(RTK_i-1)} \right)^2 \right]
\end{aligned}
\tag{3.100}
$$

using Equations (3.97) and (3.99).

N_i is the total number of moles of gas i in the volume, in both gas and dissolved phases.

The initial partial pressure of each gas in the repository is specified rather than the initial total number of moles. However, it is the initial total number of moles that is required as an initial condition for the mass balance equations. To determine the initial total number of moles of each gas in the repository, $N_i^{(0)}$, from the initial partial pressure, $p_i^{(0)}$, Equation (3.97) and Equation (3.98) are rearranged to give:

$$N_i^{(0)} = p_i^{(0)} V \frac{(1+S(ZRTK_i-1))}{ZRT}$$

(3.101)

3.8   RELATIVE HUMIDITY MODULATION

There are two options available for the relative humidity modulation function, h: a linear ramp and a smoothed linear ramp. These are described in the following sections.

For the L&ILW repository model, the modulation is applied directly to all vapour phase corrosion rate constants: R_{111}, R_{121}, R_{211}, R_{221}, R_{311}, R_{321}, R_{411}, R_{421}. For the corrosion of used fuel containers, the model for relative humidity dependence is given in Section 3.4.5. It is applied to the vapour phase fraction of all microbial processes (apart from the death of biomass, which is assumed to continue at its normal rate), g, via the expression:

$$g = S + (1-S)h.$$

(3.102)

The affected microbial rate constants are: V_{H1}, V_{H2}, V_{H3}, $V_{C,a}$, $V_{C,b}$, $V_{C,c}$, $V_{C,d}$, $V_{C,e}$, $V_{R,a}$, $V_{R,b}$, $V_{R,c}$, $V_{R,d}$, V_{Re}, $V_{P,a}$, $V_{P,b}$, $V_{P,c}$, $V_{P,d}$, $V_{P,e}$.

3.8.1   Type 1: Linear Ramp

The relative humidity modulation function is taken as varying linearly between $RH_{min}=0.6$ and $RH_{max}=0.8$:

$$h(RH) = \begin{cases} 1 & 1 < X \\ X & 0 < X < 1, \\ 0 & X < 0 \end{cases} \quad \text{where} \quad X = \left(\frac{RH - RH_{min}}{RH_{max} - RH_{min}} \right)$$

(3.103)

3.8.2   Type 2: Smoothed Linear Ramp

This is a variation on the linear ramp that has a continuous first derivative due to the introduction of curvature at end of the ramp. The following values are hard-wired: $\beta=0.1$, $\varepsilon=0.05$.

$$h(RH) = \begin{cases} 1 - \dfrac{(1-X)^2}{B + A(1-X)} & 1 - \beta < X \\[3mm] \varepsilon + C(X - \beta) & \beta < X < 1 - \beta \\[3mm] \dfrac{X^2}{B + AX} & X < \beta \end{cases} \tag{3.104}$$

Where:

$$X = \left(\frac{RH - RH_{min}}{RH_{max} - RH_{min}} \right), \quad A = \frac{\beta(2 - \alpha\gamma)}{\varepsilon}, \quad B = \frac{\beta^2}{\varepsilon}\left(\frac{\alpha\beta}{\varepsilon} - 1 \right), \quad C = \frac{1 - 2\varepsilon}{1 - 2\beta}$$

3.9   WATER-LIMITING CONDITIONS

Considering the water balance for the repository:

$$\frac{dA_{H2O}}{dt} = \frac{dQ_{H2O}}{dt} + J_{H2O} = -\varepsilon \frac{dC}{dt} + \frac{dD}{dt} + J_{H2O} \tag{3.105}$$

where dA_{H2O}/dt (mol s^{-1}) is the rate of change of the amount of water in the repository, dQ_{H2O}/dt (mol s^{-1}) is the rate of production of water via the gas generation reactions, which splits into components dC/dt and dD/dt given by Equations (3.90) and (3.91) and J_{H2O} (mol s^{-1}) is the rate of ingress of water into the repository.

Under normal circumstances, the water consuming saturated phase reactions will proceed at their normal rate and $\varepsilon = 1$ will be set. Once zero saturation has been reached, if water consuming reactions continue to proceed at a sufficient rate, the saturation will remain zero and $dA_{H2O}/dt = 0$. Under such circumstances, the saturated phase water-consuming reactions to consume water that naturally will be allowed to enter the repository, but not to draw water into the repository. This is achieved by choosing ε so that the rate of saturated phase water consumption is balanced by the natural rate of water ingress. Then:

$$\varepsilon = \frac{\dfrac{dD}{dt} + J_{H2O}}{\dfrac{dC}{dt}} \tag{3.106}$$

holds, provided that the rate of water consumption due to saturated phase processes, dC/dt, is positive and the rate of increase of water due to other gas generation reactions and water ingress is less than the rate of water consumption. This ensures that $0 \le \varepsilon \le 1$.

3.9.1 The Molar Mass of Gas

GGM keeps track of the number of moles of each gas species within the repository. As part of its gas calculations, GGM uses the molar masses of the gas species, which are supplied as input parameters. One output of the GGM is the gas generation rate. Note that the required quantity is the equivalent rate of generation of TOUGH2 bulk gas in kg s^{-1} (Q_{T2}), rather than the internal rate of change of mass of gas as would be calculated directly by GGM (Q_{GGM}).

The latter would be calculated as the sum over gas components of the products of the individual gas-component generation rates in mol s^{-1} and the molar masses of those components:

$$Q_{GGM} = \sum_g R_g \mu_g \qquad (3.107)$$

where Q_{GGM} (kg s^{-1}) is the total internal gas generation rate, and R_g (mol s^{-1}) and μ_g (kg mol^{-1}) are the rate of generation and molar mass of GGM gas component g, respectively.

The actual rate of generation required by TOUGH2 is obtained by taking the total rate of change of number of moles and multiplying by the molar mass of bulk gas as supplied by TOUGH2 (via the PEMMA subroutine argument) as follows:

$$Q_{T2} = P_{EMMA} \sum_g R_g \qquad (3.108)$$

where Q_{T2} (kg s^{-1}) is the total rate of change of mass of TOUGH2 bulk gas due to gas generation, P_{EMMA} (kg mol^{-1}) is the molar mass of TOUGH2 bulk gas and R_g (mol s^{-1}) is the rate of generation of GGM gas component g.

4.   THEORY – TOUGH2

TOUGH2 is a general-purpose numerical simulation program for multi-phase fluid and heat flow in porous and fractured media developed by the Lawrence Berkeley National Laboratory (Pruess et al., 1999). TOUGH2 is modular, setting up equations and solving them in a general form, with specific definitions for the fluid mixture, such as phase components and primary variables, provided in a single fluid property or Equation-of-State (EOS) module. Only one EOS module can be linked to TOUGH2 at a time, and T2GGM uses the EOS3 module, which simulates the transport of air and water.

TOUGH2 describes advective fluid flow using a multi-phase extension of Darcy's law and diffusive flow using a multi-phase extension of Fick's law. For numerical simulation, equations are solved at each node within a discretized space. Space discretization uses the Integral Finite Difference (IFD) method. In contrast to most field modeling approaches, the IFD method does not assume any spatial configuration or connectivity of nodes. Elements (or blocks) define the volumetric properties of nodes. Connections define the flows between nodes. There is no *a priori* assumption about how nodes are connected.

The EOS3 module defines two-phase flow of water and air, or single-phase flow of water or air. For T2GGM Version 3.1 and onwards, an option is provided to represent the gas phase by an alternative gas, either CH_4, CO_2 or H_2. Thermophysical properties of water are represented by steam-table equations, while the air is treated as ideal gas. In T2GGM Version 3.2, an option is provided to include the compressibility factor of non-ideal gases in all ideal-gas equations. Dissolution of air in water is modeled with Henry's law.

The phase relationship between gas and liquid is based on a capillary pressure function and a relative permeability function. T2GGM includes the standard functions available within TOUGH2/EOS3. Additionally, a modified Van Genuchten formulation was ported from iTOUGH2 (Finsterle 1999). This modified formulation addresses a shortcoming with the standard van Genuchten model where capillary pressure goes to infinity as liquid saturation approaches the residual liquid saturation value. In the modified formulation, the capillary pressure function is extended as a linear function at low saturations. Section 4.2 provides the equations for the modified van Genuchten formulation.

Several additional subroutine calls were added to TOUGH2 which are responsible for managing the interface with GGM in order to perform tasks such as initialization, time stepping and updating of sources and sinks based on GGM output data.

TOUGH2 modifications in T2GGM Version 3.1 and onwards also include options to provide time-variable permeability, time-variable Dirichlet boundary conditions and a simple 1D hydromechanical model to assess the effects of an applied glacial stress. Time-variable permeability and boundary conditions are straightforward modifications that are extensions of existing TOUGH2 or TOUGH2-MP features, whereby existing values of permeability or boundary conditions are updated from input functions at the beginning of each time step. The theory behind the 1D hydromechanical model is described in detail in Section 4.1.

TOUGH2 modifications in T2GGM Version 3.2 include options to

* Simultaneously solve of two different models linked together at identified boundary junction points. This approach prevents incongruent boundary conditions in nested models.

- Improve convergence failure handling by detecting incipient failure and automatically restarting simulations with modified convergence parameters.
- Use GPU matrix solvers to improved computational performance.
- Integrate with FLAC3D to calculate stress fields for poro-elastic coupling or damage-permeability coupling, as described in detail within Section 4.4.
- Provide pressure-dependent permeability and capillary pressure to represent dilatant flow, described in detail in Section 4.5.
- Provide saturation-dependent intrinsic permeability and capillary pressure for bentonite materials, as described in Section 4.6.

T2GGM Version 3.1 include a parallel version, based on TOUGH2-MP. The TOUGH2-MP version uses the same GGM code as T2GGM, but requires a slightly different interface on the TOUGH2 side of the code. The different interface is required to address the parallelization of the code: TOUGH2-MP partitions the grid and assigns each processor a portion of the grid. Consequently, the TOUGH2–GGM interface must collect the appropriate parameters required by GGM from the appropriate processors (namely the processors conducting calculation on the repository nodes), and similarly, must distribute GGM outputs to these same processors. T2GGM v3.2 is not currently available in a parallel version.

4.1   SIMPLE 1D HYDROMECHANICAL MODEL

The effect of future glaciation on groundwater and gas transport in the formations surrounding a deep geologic repository for radioactive waste is an important issue. In a sedimentary setting, the units providing geological confinement can have small but significant gas saturations. The presence of gas in formations is expected to greatly reduce the magnitude of hydromechanical coupling. Modelling systems such as TOUGH-FLAC (Rutqvist and Tsang 2003) combine the two-phase flow capability of TOUGH2 with mechanical simulators, but these simulators are demanding to use, in terms of computational and human effort, and may require some approximation in accounting for the markedly increased fluid compressibility in a gas-water system.

To avoid these limitations, a simple one-dimensional (1D) hydromechanical coupling algorithm was implemented directly in TOUGH2. The algorithm relies on the simplifying assumptions of horizontally bedded formations and uni-axial strain. These limitations do not preclude modelling the effects of relatively uniform changes in mechanical loading over a large area, such as occurs during continental glaciations or laterally extensive erosion/deposition events. The approach used was inspired by the methods described for pure vertical strain and single phase flow in Wang (2000) and Neuzil (2003), and is similar to that implemented in FRAC3DVS-OPG (Therrien et al., 2010), but has been extended to two-phase flow systems.

In TOUGH2, the mass balance equation can be written as follows (Pruess et al., 1999):

$$\frac{d}{dt}\int_{V_n} M^\kappa dV_n = \int_{\Gamma_n} F^\kappa \cdot n d\Gamma_n + \int_{V_n} q^\kappa dV_n \tag{4-1}$$

This expression integrates over the subdomain V_n, which is bounded by the surface Γ_n, with n being an inward pointing vector, normal to the surface element $d\Gamma_n$. The symbol κ represents the mass component (i.e., water, air). Hydromechanical coupling under a homogeneous and laterally extensive load is implemented within the mass accumulation term, which has the following general form (Pruess et al., 1999):

$$M^{\kappa} = \phi \sum_{\psi} S_{\psi} \rho_{\psi} X_{\psi}^{\kappa} \tag{4-2}$$

where

ϕ =   porosity (-);

S_{ψ} =   saturation of phase ψ (-);

ρ_{ψ} =   density of phase ψ (kg/m^3), a function of pressure and phase compressibility;

X_{ψ}^{κ} =   mass fraction of component kappa in phase ψ (-).

Unlike single-phase codes, porosity (ϕ) in TOUGH2 is not constant, but is updated at the end of each iteration to account for changes in pressure. The change in porosity as a function of the pressure is analogous to the addition or subtraction of water from storage in single-phase codes. The expression for the updated porosity for the current timestep (ϕ_t), including hydromechanical effects, is:

$$\phi_t = \phi_{t-1} + \phi_{t-1} C_{pore} dp + S_{S-1D} \zeta d\sigma_{zz} \tag{4-3}$$

where

ϕ_{t-1} = porosity of previous timestep(-);

C_{pore} = pore compressibility (Pa^{-1}), COM in the ROCKS record;

dp =   change in pressure during timestep $t-1$ (Pa);

S_{S-1D} = specific storage (Pa^{-1});

ζ =   1-dimensional loading efficiency (-);

$d\sigma_{zz}$ = change in vertical load during timestep $t-1$ (Pa).

The third term in Equation (4.3), namely $\phi_{t-1} C_{pore} dp$, represents the change in porosity due to the change in pore pressure during timestep $t-1$. This expression has always been in TOUGH2, and is analogous to the storage term in single-phase flow mass balance equations. The fourth term in Equation (4.3), ($\phi_{t-1} S_{S-1D} \zeta d\sigma_{zz}$) is the new hydromechanical term, and represents the change in porosity due to the change in vertical load during timestep $t-1$. The terms of Equation (4.3) which are unique to the hydromechanical formulation are the one-dimensional loading efficiency (ζ), the change in vertical load ($d\sigma_{zz}$), and the one-dimensional (uniaxial) specific storage (S_{S-1D}).

The hydromechanical capability requires the one-dimensional loading efficiency to be defined for each material type. This parameter is used to determine what percentage of the applied vertical stress is borne by the pore-fluids. The equation used to calculate one-dimensional loading efficiency (ζ) is (Neuzil 2003):

$$\zeta = \frac{\beta(1+v)}{3(1-v) - 2\alpha\beta(1-2v)} \tag{4-4}$$

where

β =   Skempton's coefficient (-)

$\alpha =$ Biot-Willis coefficient (-)

$v =$ Poisson's Ratio (-)

Strictly speaking S_{S-1D} should be calculated according to Equations (4.5) through (4.9) (Wang 2000; Neuzil 2003):

$$S_{S-1D} = \left(\frac{1}{K} - \frac{1}{K_S}\right)(1 - \lambda) + \phi\left(\frac{1}{K_f} - \frac{1}{K_\phi}\right) \tag{4-5}$$

$$\frac{1}{K_S} = \frac{1-\alpha}{K} \tag{4-6}$$

$$\lambda = \frac{2\alpha(1-2v)}{3(1-v)} \tag{4-7}$$

$$\frac{1}{K_f} = \frac{S_w}{K_w} + \frac{S_g}{K_g} \tag{4-8}$$

$$\frac{1}{K_\phi} = -\frac{1}{\phi}\left[\left(\frac{1}{K} - \frac{1}{K_S}\right)\left(\frac{1}{\beta} - 1\right) - \frac{\phi}{K_f}\right] \tag{4-9}$$

where

K = Drained bulk modulus (Pa), $(1/K = \phi C_{pore})$;

$K_S =$ Unjacketed bulk modulus, often denoted solid phase bulk modulus (Pa);

$K_f =$ Effective fluid bulk modulus (Pa);

$S_w =$ Water saturation (-);

$S_g =$ Gas saturation (-);

$K_w =$ Water bulk modulus, calculated by TOUGH2 (Pa);

$K_g =$ Gas bulk modulus, calculated by TOUGH2 (Pa);

$K_\phi =$ Unjacketed pore compressibility (Pa).

Although the storage coefficient is not used directly in TOUGH2, the implementation of pore compressibility in TOUGH2 is equivalent to a storage coefficient defined as follows:

$$S_S = \frac{1}{K} + \frac{\phi}{K_f} \tag{4-10}$$

This equation is a simplified version of Equation (4.5), which implicitly assumes incompressible grains ($\alpha = 1$). In order for the pressure effects of externally applied loads and changes in pore pressure to be expressed in a consistent fashion, it is necessary to use this simplified form of the storage coefficient equation.

At first glance, it appears that the 1D hydromechanical term is a function of fluid compressibility, and thereby gas saturation; however, the term $S_{S-1D}\ \zeta$ (see Equation (4.3)) reduces to:

$$S_{S-1D}\,\zeta = \frac{\left(\frac{1}{K}-\frac{1}{K_S}\right)(1+v)}{3(1-v)} \qquad (4\text{-}11)$$

Thus, this formulation is a function of material parameters which we assume (in a linear poroelastic model), do not change significantly (i.e. $S_{S-1D}\,\zeta$ is a constant).

A judicious choice of the input parameters ζ and C_{pore} allows us to use a simplified expression to calculate $S_{S-1D}\,\zeta$, which is also consistent with the definition of the storage coefficient in TOUGH2:

$$S_{S-1D}\,\zeta = \phi\left(C_{pore} + \frac{1}{K_{water}}\right)\zeta \qquad (4\text{-}12)$$

The input value C_{pore} should be corrected to account for uniaxial rather than triaxial mechanical constraints.

This simple approach is a good estimate of the effect of hydromechanical coupling on in-situ pore pressures.

In T2GGM version 3.2, the option to spatially vary the applied loading was provided to simulate the advance and retreat of a glaciation event. In this case, the loading rate at any one point on the surface is applied to the full column of rock below that point. 1D assumptions of uni-axial strain still apply. When modelling a process such as glacial advance that is two- or three-dimensional, this will introduce some errors in the physical representation of stress propagation and induced pore pressures, particularly where applied stress varies rapidly (e.g. at a glacial terminus). These errors are expected to have only a small influence on predictions of the effect hydromechanical coupling on the overall flow system, but should be considered in analysing modelling results which use this 1D hydromechanical model.

4.2 MODIFIED VAN GENUCHTEN RELATIVE PERMEABILITY AND CAPILLARY PRESSURE FUNCTIONS

The modified van Genuchten functions (Luckner et al., 1989) in T2GGM are based on those within iTOUGH2 (Finsterle 1999).

The van Genuchten functions use an effective degree of liquid saturation, defined as follows:

$$S_{ec} = \frac{S_l - S_{lrc}}{1 - S_{lrc}} \qquad (4\text{-}13)$$

$$S_{ek} = \frac{S_l - S_{lrk}}{1 - S_{lrk} - S_{gr}} \qquad (4\text{-}14)$$

where S_{ec} is the effective liquid saturation for capillary pressure;

S_{ek} is the effective liquid saturation for relative permeability;

S_l is the liquid saturation;

S_{lrk} is the residual liquid saturation for relative permeability;

S_{lrc} is the residual liquid saturation for capillary pressure; and

S_{gr} is the residual gas saturation.

The modified van Genuchten functions are defined by the following equations:

For capillary pressure:

$$P_c = -\frac{1}{\alpha}\left[S_{ec}^{-1/m} - 1\right]^{1/n} \tag{4-15}$$

where P_c is the capillary pressure;

     α is a van Genuchten fitting parameter, where the inverse is analogous to the air entry pressure (Pa^{-1});

     m is a van Genuchten fitting parameter (unitless); and

     n is a van Genuchten fitting parameter (unitless), analogous to the pore size distribution index. If not otherwise specified, $n = 1/(1-m)$.

For relative permeability:

$$k_{rl} = S_{ek}^{1/2}(1 - (1 - S_{ek}^{1/m})^m)^2 \tag{4-16}$$

$$k_{rg} = (1 - S_{ek})^{1/3}(1 - S_{ek}^{1/m})^{2m} \tag{4-17}$$

where k_{rl} is the relative permeability of the liquid phase; and

     k_{rg} is the relative permeability of the gas phase.

The Mualem implementation of the van Genuchten relative gas permeability is similar to the Luckner model, with the exponent changed from 1/3 to 1/2:

$$k_{rg} = (1 - S_{ek})^{1/2}(1 - S_{ek}^{1/m})^{2m} \tag{4-18}$$

4.3   RELATIVE HUMIDITY CALCULATION

Relative humidity (RH) is used to control onset of vapour phase (predominantly Phase 3) corrosion. T2GGM Version 3.2 calculates relative humidity in one of two ways: (1) the Kelvin equation, or (2) the average vapour pressure of the repository elements divided by the maximum water vapour pressure. Using the second approach may overstate RH as it does not account for vapour pressure lowering due to suction potential or capillary pressure effects. These effects are considered in the Kelvin equation.

The Kelvin equation can be expressed as:

$$RH = \exp\left(\frac{P_c M_w}{\rho_l RT}\right) \tag{4-19}$$

Where:

RH   is the relative humidity;

P_c is the capillary pressure (Pa);

M_w is the molecular weight of water (kg mol-1);

ρ_l is the liquid density (kg m-3);

T   is the temperature (K); and

R   is the ideal gas constant (J K-1 mol-1).

For T2GGM Version 3.0 and later, the temperature dependent value for the maximum water vapour pressure is given by Antoine's equation (Reid et at. 1987):

$$P_{v,max} = 10^{\left(A-\frac{B}{C+T}\right)} \tag{4-20}$$

Where $P_{v,max}$ is the maximum water vapour pressure, T is the temperature , and A, B and C are constants. For water between a temperature range of 1 and 100°C, $P_{v,max}$ in mmHg and T in °C, A = 8.07131, B = 1730.63 and C = 233.426 (Dortmund Data Bank, www.ddbst.com).

4.4   FLAC INTEGRATION (T2GGM-FLAC3D)

The effect of coupled hydromechanical processes on groundwater, gas transport and mechanical response (deformation) in the formations surrounding a deep geologic repository for radioactive waste is an important issue. To allow us to consider these processes, we investigated the TOUGH-FLAC algorithm originally developed at LBNL by Rutqvist and Tsang (2003), which couples TOUGH2 and FLAC3D. This algorithm leverages the strengths of each code; two-phase flow is simulated in TOUGH2, while mechanical processes are handled by FLAC3D. Major changes to the original TOUGH-FLAC algorithm were made to be compatible with T2GGM, to model hydromechanical coupling due to poroelasticity and to model the elasto-plastic development of damaged zones around tunnels caused by stress redistribution and pore pressure changes.

4.4.1   Poroelastic Hydromechanical Model

This poroelastic implementation of FLAC3D extends the 1D hydromechanical model described in Section 4.1. By simulating elastic processes using a full mechanical simulator (FLAC3D) we no longer require the simplifying assumption of uniaxial loading.

In this poroelastic model, pore pressure is determined using T2GGM and deformation is determined using FLAC3D. The codes are coupled through a set of subroutines in T2GGM (Fortran code) and FLAC3D scripts (in the "Fish" language, a FLAC3D scripting language). The algorithm functions as follows:

I- The pore pressure distribution is evaluated in T2GGM. At each time step these pore pressures are passed to FLAC3D, which uses the pore pressures and determines the mean effective stress distribution and deformation at each time step.

II- At the beginning of the next timestep, the total stresses evaluated by FLAC3D are returned to T2GGM. The poroelastic response to the change in stress is evaluated in T2GGM by calculating the change in porosity ($\Delta\phi_\sigma$) resulting from a change in total stress at each time step.

$$\phi_t = \phi_{t-1} + \phi_{t-1} C_{por} dp + \Delta\phi_\sigma \qquad (4\text{-}21)$$

$$\Delta\phi_\sigma = \left(\frac{1}{K} + \frac{\phi_t}{K_f}\right) B \, d\sigma \qquad (4\text{-}22)$$

Where: ϕ_t is the porosity for the current timestep;

u is the pore pressure;

ϕ_{t-1} is the porosity of previous timestep;

C_{por} is the pore compressibility (Pa^{-1});

dp is the change in pressure during timestep t-1 (Pa);

$\Delta\phi_\sigma$ is the change in porosity due to change in total stress dσ;

K, K_f are the bulk modulus and fluid modulus, respectively;

B is the Skempton parameter; and

$d\sigma$ is the change in total stress;

The theoretical basis of these equations is very similar to the description for 1D hydromechanical coupling described in Section 4.1. The primary difference being that now the stress field is not assumed to be uniaxial, and the coupling parameter is now Skempton's B rather than the one-dimensional loading efficiency (ζ)

4.4.2 Elasto-Plastic Hydromechanical Model (T2GGM-FLAC3D)

The purpose of the poroelastic coupling algorithm described in the previous section is to link changes in mechanical loading to changes in pore pressure. The purpose of the coupled elasto-plastic hydromechanical model is to link changes in mechanical stress and pore pressure to damage in the rock fabric. This damage is then empirically linked to changes in the permeability of the rock. This was originally developed for the HG-A project (Walsh et al., 2014) to model the

EDZ development and EDZ permeability in an underground tunnel. Clearly, such processes are important for groundwater and gas transport in the formations surrounding a deep geologic repository for radioactive waste. To allow us to consider elasto-plastic mechanical processes, we developed a hydromechanical model which includes damage induced permeability changes, time dependent permeability reduction through swelling, and problem specific calculation of permeability using a function in the FLAC3D scripting language Fish. Poroelastic responses are not modelled using this algorithm, as one of the primary assumptions of poroelasticity (elastic deformation) is violated.

4.4.2.1 EDZ Damage, Stress and Permeability

As described in Section 4.4.1, the pore pressure distribution is evaluated in T2GGM. At each time step these pore pressures are passed to FLAC3D, which uses the pore pressures and determines the mean effective stress distribution, deformation, and irreversible damage at each time step. At the beginning of the next time step, the stress distribution and damage state evaluated by FLAC3D are returned to T2GGM. T2GGM then evaluates the resulting changes in permeability using the following damage-stress-permeability relationship:

$$log\, k_d = A + Be^{C\sigma_{avg}} \tag{4-23}$$

$$\sigma_{avg} = \frac{\sigma_1 + \sigma_2 + \sigma_3}{3} \tag{4-24}$$

Where: σ_{avg} is the average *effective* stress (Pa), and

   A, B, C are fitting parameters.

Currently, laboratory-scale data connecting degree of damage or failure mode to changes in permeability is not available, so it is necessary to propose a function for the damage-stress-permeability relationship (shown above) and then calibrate the coefficients of the function by comparing model predictions which are sensitive to permeability to experimentally determined values.

The coefficients A, B, and C are fitting parameters, calibrated using experimental results. Parameter A represents a residual or irreducible permeability present at high stresses. Parameter *B* is a function of the failure mode. This parameter controls the degree of post-damage permeability increase when confining stress declines to zero. This increase over the residual permeability exponent (A) is equal to B when the applied stress is zero (exponent is zero, and $log\, k_d = A + B$). Parameter C controls the slope of the permeability-stress relationship. As parameter C increases, the permeability drops more rapidly with rising confining stress. More details on this relationship can be found in Walsh et al. (2014).

4.4.2.2 EDZ Swelling and Permeability

In some geological materials, there is evidence that fracture permeability may be reduced through self-sealing, primarily due to swelling of the fracture wall material. The permeability change as a result of swelling (self-healing of a damage zone) is modeled as an exponential decay function of time as follows:

$$k = k_d e^{D(t-t_0)} \tag{4-25}$$

Where: D is a fitting parameter controlling the rate of permeability decay with time;

k_d is the damaged permeability (m²);

t_0 is the time of swelling initiation; and

t is the current time in seconds.

The fitting parameter D must be obtained by the calibration of the model results to experimental data.

4.4.2.3 Problem Specific Permeability Modification

The coupling subroutine in T2GGM contains a final option for T2GGM-FLAC coupling. If this option is activated T2GGM will read a permeability value calculated using a function written in the FLAC3D scripting language "Fish."   This allows for flexible implementation of problem-specific stress-permeability relationships. For HG-A modelling in Walsh et al. (2014) it was used to calculate leakage (i.e. permeability) around a packer system as a function of effective stress on the packer-rock interface.

4.5   PRESSURE-DEPENDENT PERMEABILITY AND CAPILLARY PRESSURE

Pressure-dependent permeability and capillary pressure functions were implemented in T2GGM Version 3.2 to simulate dilatant flow mechanisms.   A simple linear function for pressure-dependent permeability was implemented, assuming a linear relationship between pressure and permeability. In this case, an initial pressure (P1) is defined representing the onset of pathway dilation, and an upper pressure (P2) is defined corresponding to the maximum increase in permeability. The intrinsic permeability (k) is calculated as defined below:

$$k = k_0 \qquad\qquad\qquad\qquad\qquad\qquad\qquad\qquad\qquad P < P1 \qquad\qquad (4\text{-}26)$$
$$k = k_0\left(1 + \left(k_{factor} - 1\right)((P - P1)/(P2 - P1))\right) \qquad P1 < P < P2$$
$$k = k_{factor}k_0 \qquad\qquad\qquad\qquad\qquad\qquad\qquad\qquad P > P2$$

where k is the modified permeability;

k_0 is the initial permeability;

k_{factor} is the scaling factor;

P is the current pressure;

$P1$ is the initial pressure at the onset of dilation; and

$P2$ is the pressure corresponding to the maximum increase in permeability.

$P1$ can be conceptualized as the minimum total stress, assuming that (a) gas pathways develop once the gas pressure exceeds the total stress in the system, where the total stress is equal to the pore pressure plus the swelling pressure (Graham et al., 2012), and (b) the total stress in the bentonite remains constant over the course of the simulation. $P2$ and k_{factor} are calibration parameters. k_0 is the measured permeability for the bentonite, and P is calculated by T2GGM.

T2GGM uses an upstream weighting scheme, which causes the permeability at the gas front to be defined by the permeability on the gas side. Note that this pressure-dependent function modifies the intrinsic rock permeability for gas. Relative permeabilities are applied as factors to the intrinsic permeability in the mass balance equations.

Several additional features to the linear pressure-dependent permeability function are provided to improve T2GGM's description of dilatant flow:

- $P1$ and $P2$ can be provided as constants, or can be specified as spatial scalars (i.e., each bentonite element has a different $P1$ and $P2$). Specifying $P1$ and $P2$ as spatial scalars allows definition of dilatant flowpaths, specifically allowing for narrow, non-planar pathways.
- Fracture directionality – If the expected direction of dilatant flow paths is inferred from pressure measurements, the directionality of pressure-dependent permeability can be limited to horizontal connections, simulating horizontal fractures, or vertical connections, simulating vertical fractures. The determination of a horizontal or vertical connection is determined through the ISOT parameter in the CONNE record, which defines the directionality of each connection. The default assumes both horizontal and vertical connections are modified.
- An additional scaling factor is provided to directly scale gas permeability independently of pressure. This scale factor is applied to the intrinsic gas permeability of nodes which are identified as having pressure-dependent permeabilities, regardless of the pressure at that node.

Capillary pressure (P_c) describes the pressure difference between fluid and gas phases at the phase interface. A high capillary pressure inhibits the movement of the gas phase by providing an additional threshold by which gas phase pressure must exceed liquid phase pressure to move the interface. To simulate dilation, pressure increases that would dilate a pathway result in a reduction in the capillary pressure as well as increasing the permeability. In fractures, both the permeability and the capillary pressure are a function of the fracture aperture. In low-permeability porous media, empirical relationships have been developed relating P_c to the intrinsic permeability (Davies 1991, Horseman 2000). In T2GGM, the capillary pressure is scaled by element permeability, which is, as described above, pressure-dependent. Capillary pressure is modified according to one of three permeability-dependent functions:

Leverett function:

$$P_c = P_{c0}\sqrt{\frac{k}{k_0}} \tag{4-27}$$

Direct function:

$$P_c = P_{c0} \frac{k_0}{k}$$

(4-28)

Cubic law function:

$$P_c = P_{c0} \frac{\sqrt[3]{k_0}}{\sqrt[3]{k}}$$

(4-29)

where P_c is the modified capillary pressure; and

P_{c0} is the initial capillary pressure calculated by the capillary pressure function.

4.6   BENTONITE STATES

From experimental results, it is apparent that bentonite properties are not constant and are in fact highly non-linear with dependencies on variables such as saturation. For example, when bentonite pellets absorb water and swell can cause the material permeability to change between something akin to fine gravel and a very fine-grained, virtually impermeable homogeneous material. This section provides the basis for defining the permeability and capillary pressure of bentonite based on saturation. The first sub-section describes the swelling of bentonite, and the changes to permeability wrought by saturation. The second sub-section describes swelling pressure, which is a function of saturation, as a criterion at which dilatant flow will occur and its use with pressure-dependent permeability and capillary pressure as described in Section 4.5.

4.6.1   Swelling Stages

Swelling is the change in volume as a result of change in water content. Under mechanically unconstrained conditions, the maximum swelling volume is called the free swelling volume, measured as a percentage of the original volume.   If the increase in volume is restricted (mechanically constrained conditions) swelling processes will lead to an increase in the confinement pressure until a maximum pressure is reached, called the swelling pressure (ASTM, 1996). Both free swelling and confined swelling are a function of clay content, clay mineralogy, and as-placed conditions.

The evolution of swelling processes, either free or confined, can be defined in three stages:

1. **Stage I – Preliminary swelling**: Swelling processes start with inflowing water binding chemically to the clay particles. Change in volume is minimal, and the porosity of the clay will remain unsaturated.

2. **Stage II – Advanced swelling**: Water inflow starts filling the porosity of the clay, and the bulk of the clay swelling occurs.

3. **Stage III – Fully swollen:** Swelling processes are complete, material is fully water saturated and material properties remain constant.

A more complete description of processes and equations that will be used to describe swelling and its effects on porosity, permeability and capillary pressures are presented in the following

subsections. The final sub-section provides a graphical representation of the change in permeability and capillary pressure during bentonite saturation.

4.6.1.1   Placement conditions

Within this document, two porosities are defined for this clay fabric:

- **Micro-porosity**: The intra-element porosity, or the porosity within each clay grain.
- **Macro-porosity**: The void space between clay aggregates, and other materials present (such as sand).

Figure 4-1 illustrates the arrangement of micro- and macro-porosity.
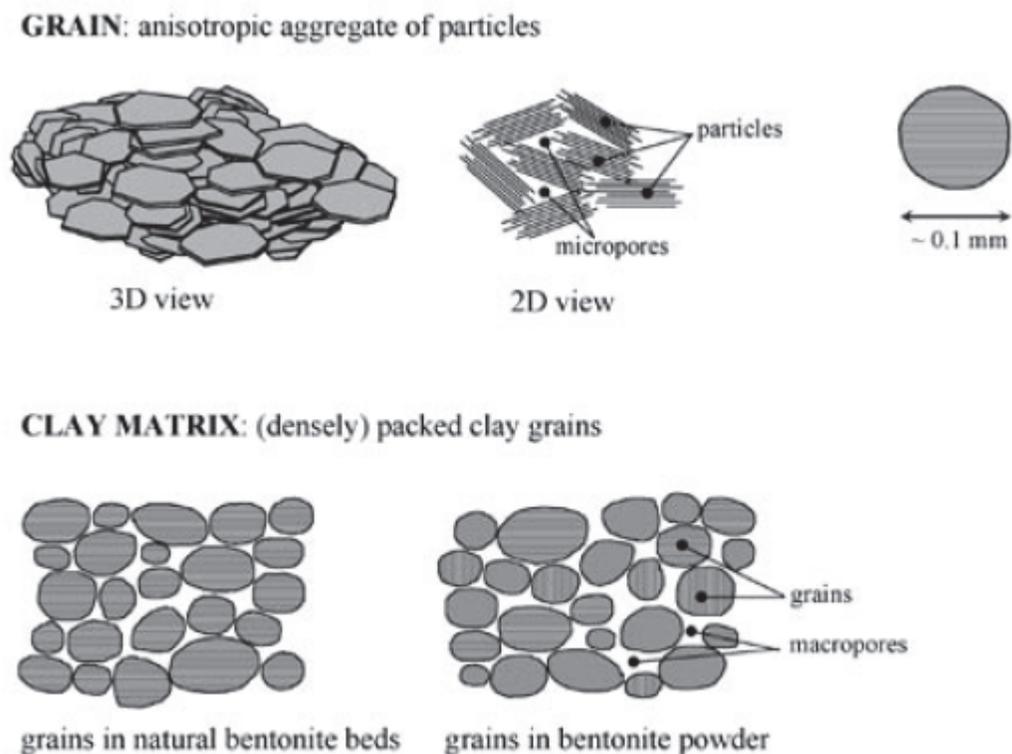
Figure 4-1: Microfabric of compacted clay (Kröhn, 2003)

In the context of a DGR, two additional porosities may be defined depending on the type of bentonite:

- **Mega-porosity**: For granular gap fill only, the void volume between bentonite pellets.
- **Gap**: The space between emplaced bentonite and the rock wall or other confining structures.

Free-swelling will occur as long as there is large enough mega-porosity and/or a gap-volume. In a confined space such as a deep geologic repository, once any gaps are filled, confined

swelling will occur. The processes in the stages described below are the same whether the swelling is free or confined. The difference between free and confined swelling is accounted for by the changes in the different porosities.

Bentonite or bentonite mixtures will have different swelling capacities depending on their mineralogy. Not all components of bentonite have an expansive or swelling capacity. Expansive minerals of bentonite include montmorillonite and saponite.

4.6.1.2 Stage I - Preliminary Swelling

Once water begins to saturate the material, swelling will begin. Initially, the negatively charged clay surface will attract the positively charged end of the polar water molecule, forming a strongly attracted layer of water with a higher density (up to 1.41 g/cm^3, Martin (1960)). The amount of water attracted to the clay surface is a function of specific internal surface area, initial compaction water content, compaction dry density, and clay mineralogy. Physically, this water is bound and not readily available for flow.

From a modelling perspective, this bound water is handled by a liquid saturation threshold: the relative permeability to water will be zero until water saturation exceeds the threshold, where the threshold is representative of the maximum amount of bound water. Preliminary swelling will be complete once the threshold is reached. The threshold will be less than the residual liquid saturation defined for the relative water permeability, and consequently preliminary swelling will be complete at a low liquid saturation.

Swelling during this stage is expected to be relatively low, and it is consequently assumed that permeability and capillary pressure are constant over this stage. This assumption is supported by descriptions of water-bentonite interactions (Ravina and Low, 1971), which describes water to conform to the structure of the bentonite while the water layer is thin, but as the thickness of the water layer increases, the bentonite conforms to the structure of the water, resulting in swelling. Preliminary swelling is considered to occur while the water layer is thin. It is also supported based on calculations of the estimated thickness of the water layer around each particle, which show that the bound water thickness is small compared to the total thickness of water around each pore (see Figure 4-2). The thickness (t) of the bound water layer is calculated with the following equation:

$$t = w/\rho_w/A_s \tag{4-30}$$

where: w is the water content of bentonite (mass of water divided by total mass),

   ρ_w is the water density (mass of water divided by volume of water), and

   A_s is specific surface area for montmorillonite (area of particle/mass of particle).

In Figure 4-2, w and ρ_w were obtained from Martin (1960) and A_s was assumed to be 840 m^2/g (Mitchell and Soga, 2005).

If the density of the bentonite is very high (such as bentonite blocks), preliminary swelling may be significant, as the small thickness of the bound water layer will have a greater proportional impact on the smaller porosity. However, in the context of the DGR, bentonite blocks are typically installed at a relatively high initial saturation (5CS used initial saturations of 65%, NWMO 2013), when preliminary swelling will be complete.
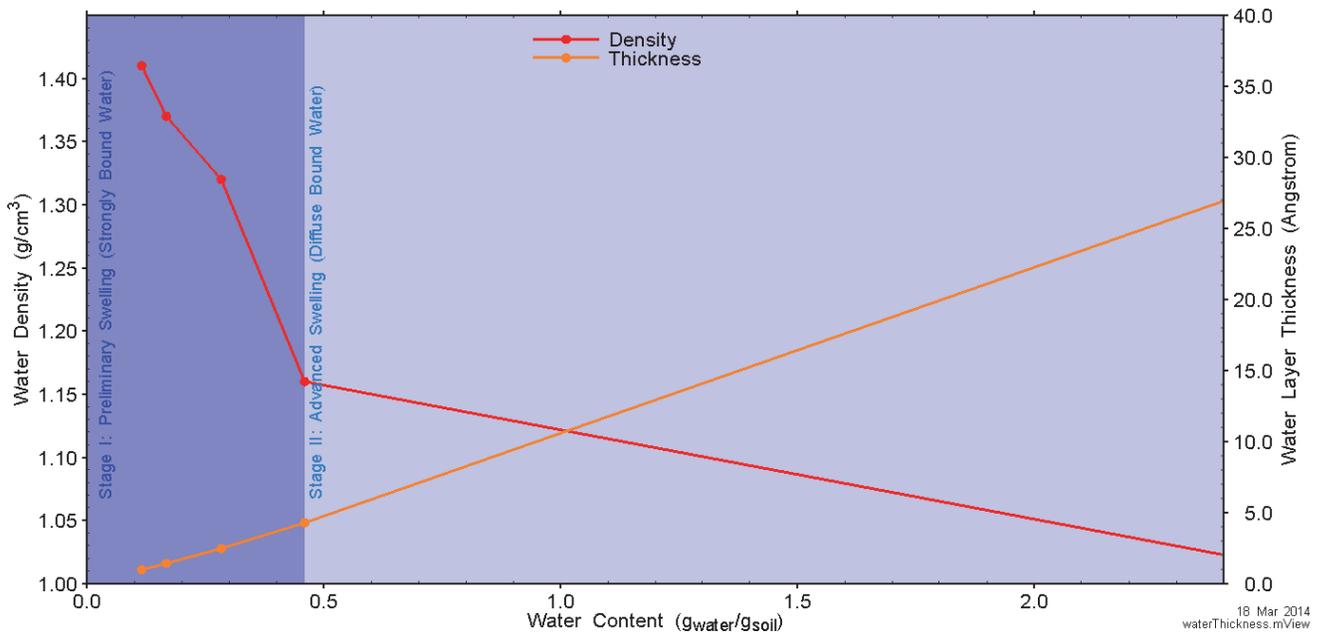
Figure 4-2: Water density and thickness versus water content in montmorillonite.

4.6.1.3 Stage II - Advanced Swelling

This stage will start once the clay surface is fully saturated with strongly bound water. At this stage the bulk volume is still unsaturated. Clay particles within the aggregate cluster are expected to keep attracting water to form a layer of loosely bound water (or diffuse layer). At the beginning of advanced swelling, the bound water layers of adjacent particles overlap with each other. As water moves to surround the clay minerals, the attracted water will push the particles away from each other leading to an increase in the micro-porosity and a new pore size distribution (see Figure 4-3). If free swelling, the material will swell. If confined, the material will be unable to swell and a swelling pressure will develop. Consequently, there will be a transition in pore size distribution from macro pore dominated to micro pore dominated, as shown in Figure 4-3.
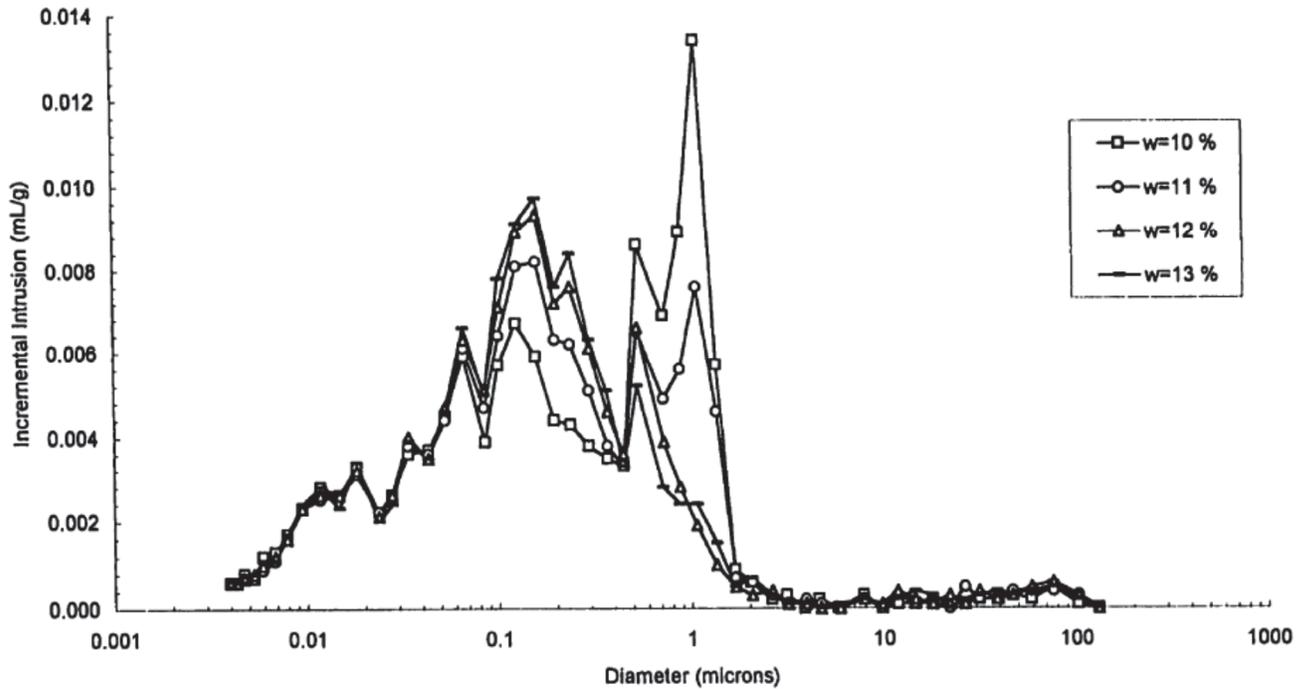
Figure 4-3: Pore size distribution in a clay compacted at different water contents (w) (from Halayko, 1998).

Advanced swelling under constrained conditions is expected to lead to a lower permeability, much lower for materials with high bentonite content. Figure 4-4 shows an example of hydraulic conductivity for a bentonite sand mixture decreasing from 1.2E-13 to 3E-14 m/s when suction decreases from 50 to 25 MPa (Cui et al., 2008). Suction decreases as water saturation increases. Figure 4-5 shows the decrease in bentonite gas permeability, as saturation decreases (Villar, 2002).
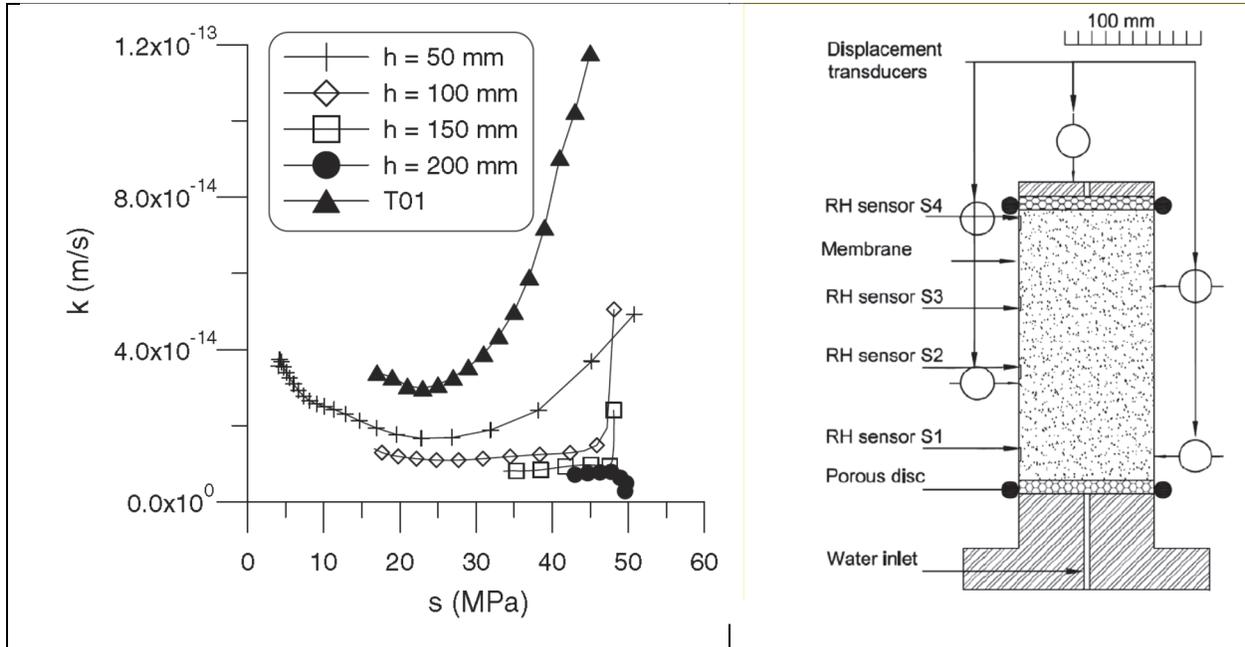
Figure 4-4: Hydraulic conductivity (K) as a function of suction (S) for bentonite sand mixture (Cui et al., 2008) at different locations (e.g. h=50mm at Sensor Location S1). TO1 is a relationship for the entire sample.
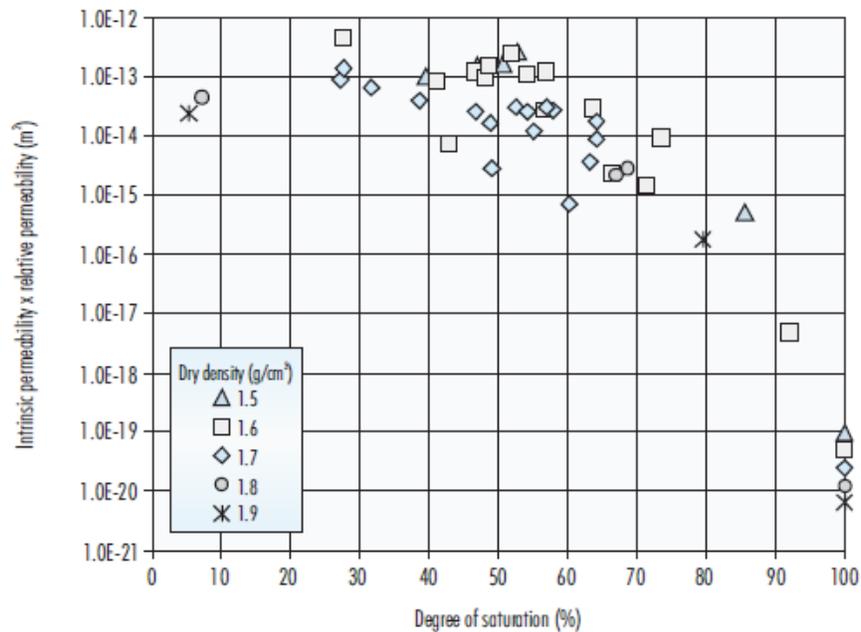
Figure 4-5: Gas permeability of bentonite as a function of saturation (Villar, 2002)

The decrease in permeability can be considered based on changes to the porosity distribution of the bentonite. Changes in porosity during swelling are fundamental to the method described here for numerical simulation of the swelling processes and prediction of material property changes as a result of swelling. The fundamental assumption underpinning this model is that as advanced swelling progresses, micro-porosity increases at the expense of the other types of porosity defined above. During free-swelling, gap porosity is still present and all increases in micro-porosity are subtracted from the gap porosity while macro-porosity and mega-porosity (if present) are held constant. Once all gaps are closed, further swelling continues to increase the micro-porosity, now at the expense of mega-porosity (if present) and then macro-porosity.

Porosity changes are based on changes in saturation. Micro-porosity (n_{micro}) increases can be modelled base on the following equation from Xie et al. (2004):

$$n_{micro} = S_l^a \beta n_{micro,max}$$ (4-31)

Where S_l is the liquid saturation,

a is a fitting exponent,

β is the fraction of expansive minerals, and

$n_{micro,max}$ is the maximum micro-porosity assuming all particles are expansive and free swelling.

If swelling is confined, increases in micro-porosity will result in equivalent reductions in macro-porosity. If swelling is free, it is assumed that the macro-porosity will remain constant, while the gap volume and mega-porosity will decrease. Gap volume will decrease first, and once the gap is extinguished, mega-porosity will then be decreased. It is assumed that advanced swelling is complete once the system has reached full saturation.

These changes in porosity can be translated to permeability (k) using the Kozeny-Carman equation (Kozeny, 1927, Carman, 1941), which is typically presented in terms of void ratio (e, $e = n/(1 - n)$, where n is porosity):

$$k = \frac{1}{bT^2 S_0^2} \left(\frac{e^3}{1 + e} \right)$$ (4-32)

where b is the pore shape factor,

T is the tortuosity factor,

S_o^2 is the effective particle diameter.

While the Kozeny-Carman equation was initially developed for cohesionless soil, corrections to this equation have been developed to extend this equation to fine grained soils with unequal pore size distributions (Olsen, 1962), such as clay and bentonite. Using a known initial permeability and void ratio (k_o and e_o), and assuming that porosity changes due to swelling have a greater impact on permeability than changes due to pore shape factor or tortuosity factor, the calculation of permeability can be simplified to the following equation:

$$k_i = k_0 \left(\frac{1 + e_0}{e_0{}^3} \right) \left(\frac{e_i{}^3}{1 + e_i} \right) \qquad\qquad (4\text{-}33)$$

The permeability of each scale (micro, macro,mega and gap) can be calculated from the porosity of that scale. The total permeability (k_t) of the bentonite can then be calculated using a weighted arithmetic mean:

$$k_t = k_{micro} \frac{n_{micro}}{n_t} + k_{macro} \frac{n_{macro}}{n_t} + k_{mega} \frac{n_{mega}}{n_t} + k_{gap} \frac{n_{gap}}{n_t} \qquad\qquad (4\text{-}34)$$

Note that an arithmetic mean is equivalent to assuming each scale (micro, macro, mega and gap) are in parallel. This assumes that the porosity and permeability of each scale are connected across a model element, which is not unreasonable given that measured values of permeability and porosity, which will provide the basis for input parameters, typically measure connected permeability and porosity.

In addition to permeability, as the pore distribution changes, the capillary pressure also changes. Capillary pressure (P_c) will simply be modelled using van Genuchten equations (or similar). The van Genuchten capillary pressure distributions are typically measured in intact, compacted bentonite. In other words, they do not necessarily apply over the full range of saturations to gap fill material. To correct for this, the effective saturation of the micro- and macro-porosity, rather than the total saturation of the element will be used to calculate the capillary pressure. This assumes that all water entering the bentonite preferentially resides within the micro-porosity, with the saturations of the macro- porosity only increasing once the micro-porosity is fully saturated, and the mega- porosity only increasing once the macro-porosity is fully saturated. This is illustrated in Figure 4-6; note that the mega-porosity remains gas saturated at all saturations where it is present, while the micro porosity remains water saturated over almost the entire range of saturations. Due to swelling, mega porosity disappears as water saturations increase. Effective micro- plus macro- porosity saturation will be greater than the total saturation of the bentonite, as long as a mega-porosity is available. Using a higher saturation in the capillary pressure calculation will lower the capillary pressure. Mega-porosity only exists for pelletized backfill, and consequently, capillary pressures are only modified for these materials.
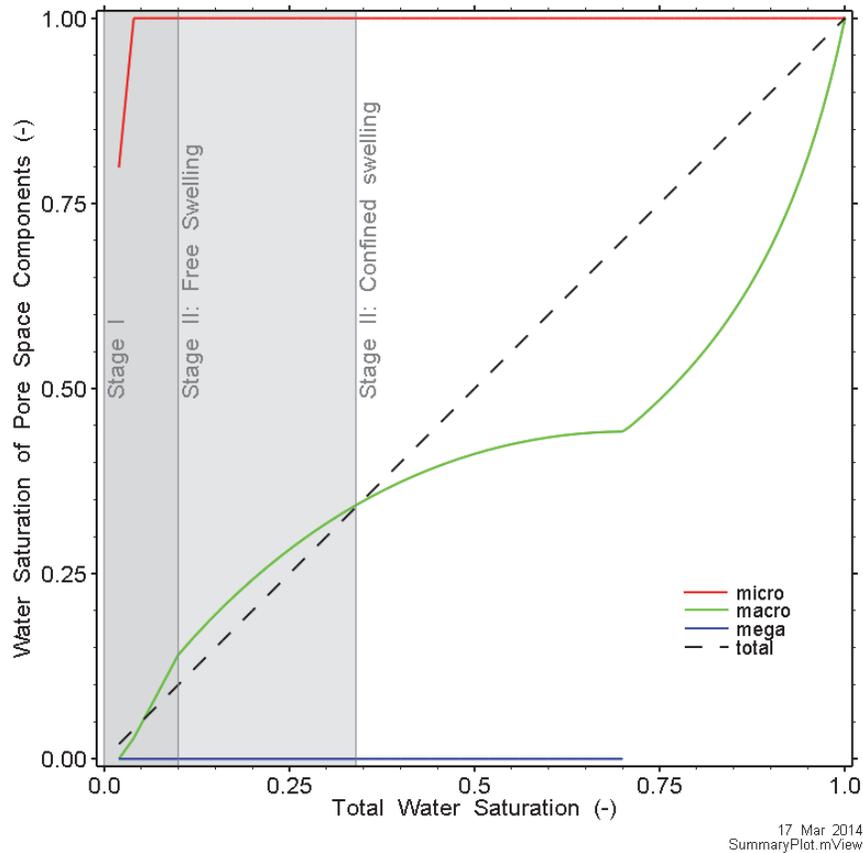
Figure 4-6: Saturation of micro-, macro- and mega- porosities. Effective saturation of micro- and macro- porosities is also shown.

4.6.1.4 Stage III - Fully Swollen

At this stage, micro and macro-pores are filled with water and swelling has reached its maximum capacity for confined swelling. It is assumed that free swelling is not a possibility at this stage, as the bentonite seals within a DGR would be designed with sufficient dry density (of swelling materials) to seal any gaps once fully saturated. Permeability at this stage is constant, and can be set to the existing reference parameters for saturated bentonite.

4.6.1.5 Evolution of Bentonite Properties during the Swelling Process

Figure 4 7 shows the permeability and capillary pressure as it changes with saturation. The change in micro-, macro-, mega- and gap porosities are also shown, with micro-porosity increasing as advanced swelling progresses, at the sequential expense of gap, mega- and macro- porosities. As a result of this redistribution of porosities, the permeability of the gap, mega-, macro-, and micro-porosities changes. Although the permeability of the micro-porosity increases with saturation, the total permeability drops as the large and more permeable pores close (see the second panel in Figure 4-7). Capillary pressure is reduced until mega-porosity is eliminated.
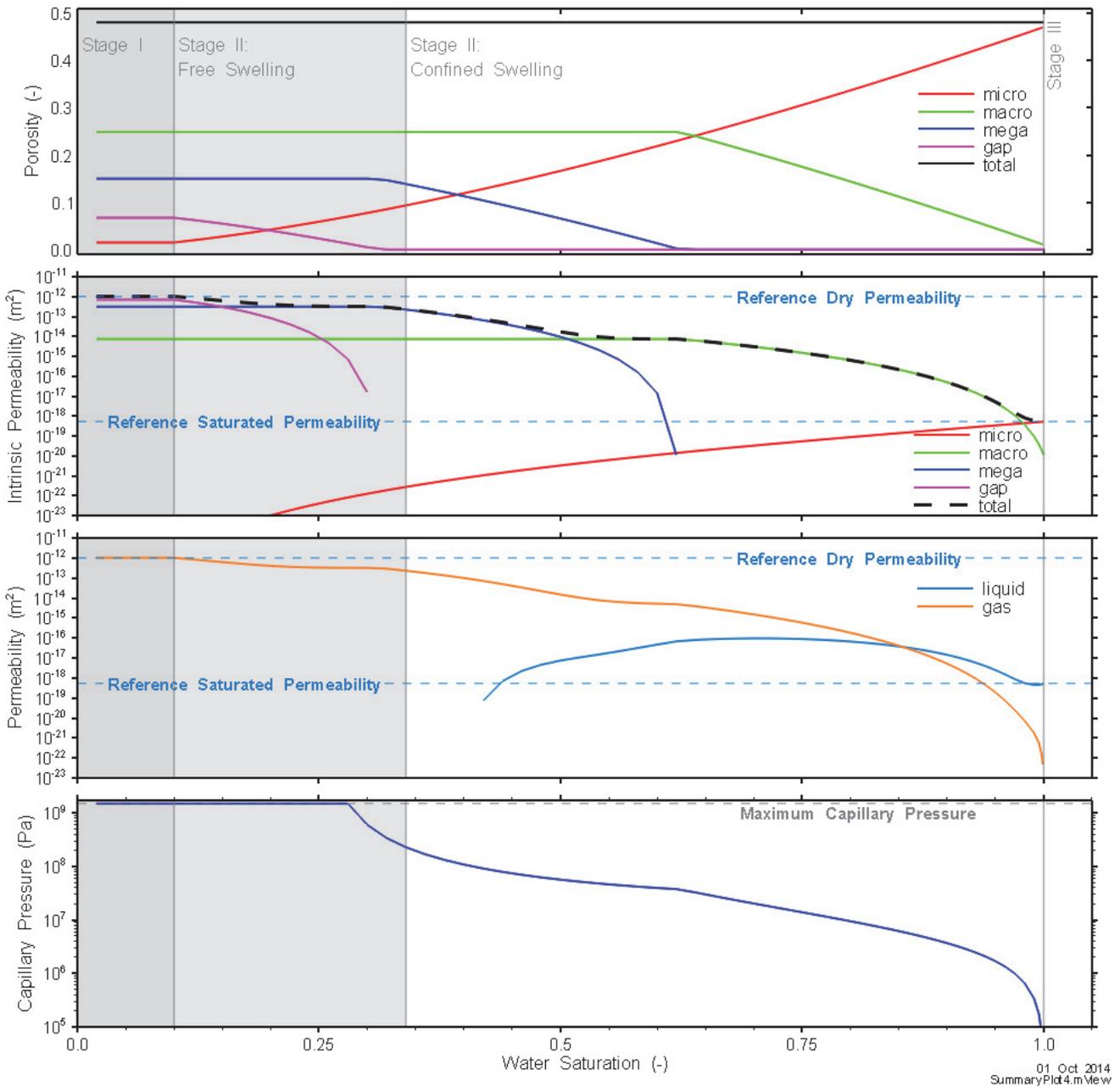
Figure 4-7: Schematic Approximation of the Volume Changes due to Free and Constrained Swelling of Compacted Sand-Bentonite with an Initial Technological Void

4.6.2   Swelling Pressure and Dilatant Flow

Swelling pressure develops during confined swelling as described in the previous section. The pressure developed is assumed inconsequential for two-phase flow. However, as previously

discussed, the value of swelling pressure, along with the liquid pressure, defines the criterion at which dilatant flow will occur.

Existing methodology for dilatant flow paths in T2GGM is described in Section 4.5. This methodology assumes that dilatant flow will occur when gas pressures exceed the total stress, or dilatant flow criterion, which is provided as an input. In a partially saturated bentonite, this criterion may vary considerably based on the saturation and swelling pressure at the time gas pressure rises sufficiently to cause dilatant flow. As shown in Figure 4-8, the swelling pressure can be assumed to relate linearly to the change in water saturation.
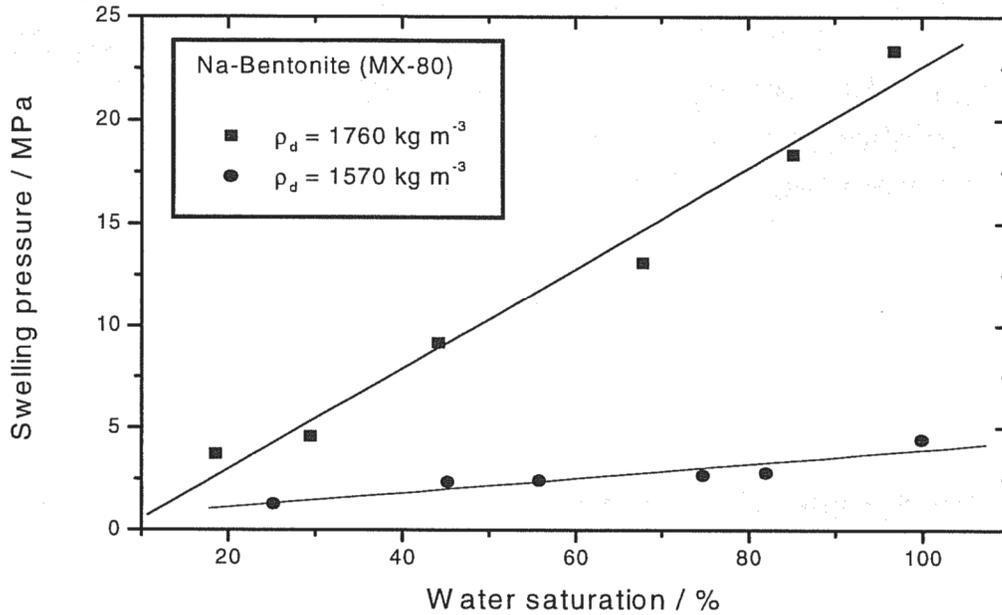
Figure 4-8: Swelling pressure as a function of water saturation and dry density. Figure from Jobmann (1988) using data from Studer et al. (1984) and Börgesson (1984).

Assuming the swelling pressure is zero at the saturation at which free swelling is complete and confined swelling begins, the swelling pressure can be calculated at any saturation provided the maximum swelling pressure (MSP) at saturation is known.

The magnitude of MSP for backfill materials depends mainly on the fraction of clay within the backfill the fraction of montmorillonite within the clay, and the salinity of the porewater (represented by the total dissolved solid TDS). MSP can be estimated as a function of the effective montmorillonite dry density (EMDD) (Baumgartner, 2006):

$$P_S = Ae^{B \times EMDD} \tag{4-35}$$

$$EMDD = \frac{f_m \cdot f_c \cdot \rho_d}{\left[1 - \left(\frac{(1-f_c) \cdot \rho_d}{G_a \cdot \rho_w}\right) - \left(\frac{(1-f_m) \cdot f_c \cdot \rho_d}{G_n \cdot \rho_w}\right)\right]} \tag{4-36}$$

Where: A and B are fitting parameters depending on the groundwater salinity (example
A=1×10^{-2} , B= 4.58 for TDS = 0);
f_m is the mass fraction of montmorillonite in clay f_c;
f_c is the mass fraction of clay in dry soil;
ρ_d and ρ_w are the dry density and water density, respectively;
G_a is the relative density of aggregate component; and
G_n is the relative density of non-montmorillonite component in clay (2.64 to 2.7).

If the gas pressure is greater than swelling pressure plus liquid pressure, dilatant flow will occur. In partially liquid saturated bentonite, the water pressure may be negative. In this case the appropriate dilatant flow criterion is simply the gas pressure exceeding the swelling pressure (Birgersson et al., 2008). Dilatant flow is only expected to occur in mostly saturated bentonite, with mostly saturated considered to be a liquid saturation greater than 80-90% (Hume, 1999, Halayko, 1998, and Harrington and Horseman 2003). The actual liquid saturation at which dilatant flow occurs does not need to be known, but a minimum is input to ensure dilatant flow only occurs in saturated bentonite.   Dilatant flow can then be implemented using a pressure dependent permeability modification as developed in Section 4.5.

5. VERIFICATION

5.1 INTRODUCTION

Verification for T2GGM Version 3.0, 3.1 and 3.2 is summarised here and is built upon the verification undertaken for previous versions (QUINTESSA and GEOFIRMA 2011a).

Verification involves the checking of the software against its specifications. The types of verification undertaken are:

1. Performing unit tests for new code features;
2. Running a test suite to ensure plausible and accurate output that is consistent with the Theory Manual (Section 3); and
3. Review of the code for accuracy and maintainability.

Validation of the model, the determination of the accuracy and applicability of the software results with respect to their intended application, is discussed separately in Section 6.

GGM is developed and tested independently using a driver program to approximate geosphere behaviour, before being integrated with TOUGH2 for further testing. Historic and current GGM and T2GGM testing is summarised in Sections 5.2 and 5.6, respectively. Results of GGM Testing for Versions 3.0, 3.1 and 3.2 are described in Sections 5.3, 5.4 and 5.5. Results of T2GGM testing for Versions 3.0, 3.1 and 3.2 are described in Sections 5.7, 5.8 and 5.9.

5.2 GGM VERIFICATION SUMMARY

The GGM code was reviewed by a member of staff that was not otherwise involved in coding for GGM to check for accuracy of code modifications at Versions 1.0, 1.3 and 3.0. A review of the code to check for maintainability was also undertaken at Versions 1.0, 2.0 and 3.0. Tests designed to select solver parameters that provide suitable numerical convergence and stability of results were undertaken at Version 1.0 and 2.0. Unit tests have been undertaken for all major code modifications, including:

- Relative humidity, zero-saturation behaviour, subroutine reorganisation, time-step control, conservation of mass, and Version 2.0;
- Water mass balance and relative humidity at Version 2.1; and
- Multi-compartment functionality, file format changes, non-isothermal functionality, temperature dependent corrosion rates and restart capability at Version 3.0.

At Version 1.3, a test suite was set-up to ensure that GGM produces plausible output in a number of alternative calculation cases. For each test, mass balance and stability of results are checked. This test suite has since been run at Versions 1.3 and 2.0. This testing has been performed by a third party that is not involved in the development of the code. The test suite includes four sets of tests. Set 1 includes general tests for different combinations of processes under water- saturated conditions: corrosion, microbial degradation, biomass (with and without recycling). The tests in Set 2 include different initial inventories designed to check mass balance of key species (carbon and iron). Tests in Set 3 have been chosen to test the effect of different relative humidity behaviour. Tests in Set 4 are designed to test behaviour under conditions of low water saturation.

A more detailed summary of the testing of GGM undertaken for Versions 3.0 and 3.1 are given in the following sections.

5.3   GGM VERSION 3.0 VERIFICATION RESULTS

The following changes were made to GGM between Version 2.1 and 3.0:

1. The multiple compartment functionality and associated changes to the file format.

2. Changes to allow for time varying temperatures.

3. Changes to allow for temperature dependent corrosion rates.

4. Changes to allow for a restart capability.

The tests that were undertaken at each stage are summarised in Table 5-1 to Table 5-4. In addition to the tests outlined below, further tests were undertaken in the context of T2GGM to check that the updated code provides results that are compatible with previous versions. This testing is described in Section 5.7.2. Any issues identified during testing were corrected.

Table 5-1: Stage 1 Tests: Multi-Compartment and File Format Changes

Test Number	Description
1.1	Check that it is possible to reproduce an existing GGM Version 2.1 standalone case using a single compartment isothermal setup.
1.2	Check that it is possible to reproduce two different GGM Version 2.1 variant standalone cases using a two-compartment isothermal setup.
1.3	A combined compartment output file produced by the GGM was sent to Geofirma to ensure that it complies with the format required by their mView scripts.

Table 5-2: Stage 2 Tests: Non-Isothermal Functionality

Test Number	Description
2.1	Check that by specifying a constant temperature, the existing isothermal results using the L&ILW corrosion processes can be reproduced.
2.2	A standalone case is run with a constant saturation (and gas volume) and a prescribed time varying temperature (using the driver program). Gas pressures are checked to be varying in accordance with the changes in temperature.

Table 5-3: Stage 3 Tests: Temperature-Dependent Corrosion Rates

Test Number	Description
3.1	The modulation functions are calculated for a range of input values to ensure that they have been correctly implemented
3.2	An existing case with a prescribed temperature profile is run and the resulting output is checked for plausibility.

.

Table 5-4: Stage 4 Tests: Restart Capability

Test Number	Description
4.1	Compartment based input files are copied and given restart file names. The GGM is started in restart mode. The results are checked to ensure that the code produces identical results to a normal start.
4.2	A restart file is requested part way through a standalone run. The GGM is restarted from that point. The two sets of results are checked to ensure that they are the same after the restart.

5.4   GGM VERSION 3.1 VERIFICATION RESULTS

No changes were made to the GGM code between Versions 3.0 and 3.1 – the incrementation in the version number was made solely to maintain consistency with the T2GGM versioning. Since no changes were made to GGM, verification of GGM Version 3.1 was not required.

5.5   GGM VERSION 3.2 VERIFICATION RESULTS

Updates to allow for a non-ideal gas law were verified with coupling to T2GGM. Checks to ensure that previous behaviour was reproduced, and that the introduced compressibility factor was having the desired effect were undertaken. See Section 5.9.2.

Updates to allow for upscaling of the used-fuel corrosion model were verified with coupling to T2GGM. Checks to ensure that previous behaviour was reproduced, and that upscaling with more than one element per compartment was having the desired effect were undertaken. See Section 5.9.4.

Updates to facilitate the saving and restoring of the state of GGM required some code reorganisation that involved many files. These changes were checked by ensuring that when run in standalone mode, GGM produced identical results before and after the code reorganisation. The full functionality was tested with coupling to T2GGM, as described in Section 5.9.6.

5.6   T2GGM VERIFICATION SUMMARY

Testing for T2GGM has focussed on unit tests for code modifications and updates to the GGM. These unit tests have included the following:

- relative humidity behaviour at Versions 1.0, 2.0, 2.1 and 3.0;
- zero-saturation behaviour at Version 1.0 and 2.0;
- verification of repository void volume changes at Version 1.3;
- verification of timestep control and alternative gases at Version 2.0;
- multiple compartment, time-varying permeability, time-varying boundary conditions, optimised time-step adjustment, alternative neon as and revised file formats at Version 3.0;
- the 1D hydromechanical model and restart capability at Version 3.1;
- real gas properties at Version 3.2;
- model linking at Version 3.2;

- upscaled used fuel corrosion at Version 3.2;
- convergence failure handling at Version 3.2;
- GPU matrix solver at Version 3.2;
- FLAC integration at Version 3.2;
- Pressure-dependent permeability at Version 3.2; and
- Bentonite states at Version 3.2.

Tests against analytical results have been employed where possible. For example:

- the maximum vapour pressure for the relative humidity calculation has been compared against Antoine's equation at Version 3.0;
- the 1D Hydromechanical Model model and FLAC integration results have been compared with an analytical solution for one-dimensional consolidation (Terzaghi 1943).

the 1D Hydromechanical Model model results have also been compared with an analytical solution for coupling in a semi-infinite column with gradual loading (Lemieux et al., 2008).In addition, tests have been undertaken to ensure that results produced with newer versions are consistent with those from earlier versions and to check numerical convergence and stability. The code has also been reviewed for maintainability.

A more detailed summary of the testing undertaken at Version 3.0, 3.1, and 3.2 is given in the following sections.

5.7 T2GGM VERSION 3.0 VERIFICATION RESULTS

The T2GGM Version 3.0 verification considers modifications made to the TOUGH2 components of T2GGM for Version 3.0. The first test, described in Section 5.7.2, also considers the full code, assuring that code modifications for Version 3.0 had no impact on previous Version 2.1 functionality.

5.7.1 T2GGM Version 3.0 Verification Models

This section provides the specifications for previously undocumented models used in the verification of T2GGM Version 3.0.

5.7.1.1 5CS Multiple Container Model

This is a 3D model representing a single tunnel extending from the access tunnel to just beyond two containers. Only half of a room is modelled, plus 10 m out into the host rock. The model extends from 20 mBGS to 1500 mBGS.

5.7.1.2 A simple 2D test case with 1D flow for testing time-variable permeability

A simple 2D model, 10 m in the X direction and 5 m in the Y direction. A total of 60 nodes, 10 in the X direction and 6 in the Y direction. Dirichlet boundary conditions were defined at X = 0 and X = 10 m, with pressures at 2E5 Pa at X = 0 m, and 1.001E5 Pa at X = 10 m. The simulation is fully water saturated (no gas) and isothermal. All nodes have the following rock properties: a permeability of 1E-12 m^2, a porosity of 0.25 and a compressibility of 1E-8 Pa^{-1}. Time-variable permeability is defined for nodes with an X value greater than 5 m: the initial permeability of 1E-12 m^2 decreases by one order of magnitude between 4.32E6 and 6.048E6 seconds, and the permeability remains at 1E-13 m^2 for the remainder of the simulation.

5.7.1.3 A simple 1D test case for testing time-variable boundary conditions

A simple 1D model extends 10 m in the X direction with 10 nodes. All nodes have the following rock properties: a permeability of 1E-19 m^2, a porosity of 0.1 and a compressibility of 1e-9 Pa^{-1}. The simulation is isothermal and has a total run time of 1000 seconds. Dirichlet boundary conditions were defined at X = 0 and X = 10 m, with pressures at 1.9 MPa at X = 0 m, and 1 MPa at X = 10 m and gas saturations at 0.75 at X = 0 m, and 0.1 at X = 10 m. Time-variable boundary conditions were defined at X = 10 m, with changes in pressure from 1 MPa to 1.5 MPa and in saturation from 0.1 to 0.5 occurring between 1 and 10 seconds.

5.7.2 Previous Functionality

Modifications to T2GGM for Version 3.0 should not affect existing functions within T2GGM. 3DSRS GG1 (GEOFIRMA and QUINTESSA 2011) was used as the test case, and was run with both Version 2.1 and 3.0. For the non-water limited case the results were found to be the same. For the water-limited case, the general character of the results was the same, with some small differences in the timing at which the simulation ceases to be water-limited. This timing is very sensitive to convergence criteria, and due to changes in GGM time-stepping with Version 3.0, exactly the same results have not been obtained (see Figure 5-1). Reduction in either the GGM or the TOUGH2 convergence criteria improves results, however too low convergence criteria cause severe numeric instability. Optimal convergence criteria have not yet been determined.
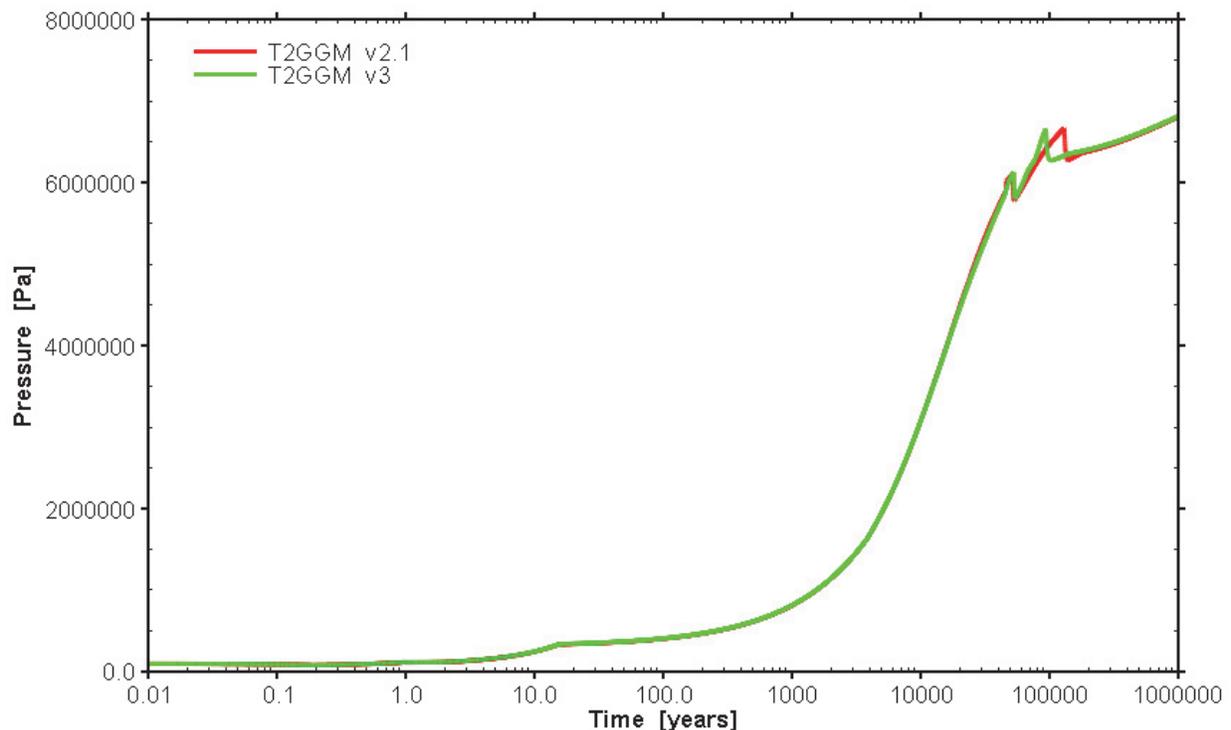
Figure 5-1: Pressure in the GGM Container for 3DRS GG1 Water Limited Case, for both Version 2.1 and Version 3.0.

Note that very small differences are also attributed to the value used for maximum vapour pressure. Version 2.1 uses a hard-coded maximum vapour pressure at 20°C (2340.05 Pa),

whereas the simulation is isothermal at 22°C, which has a maximum vapour pressure of 2634.8 Pa using the Antoine equation. While this is only a 300 Pa difference, it can have a minor impact on resulting pressures in the form of a small offset. The maximum vapour pressure effects the calculation of RH and air pressure (gas pressure minus vapour pressure), both of which are inputs to GGM.

5.7.3 Relative Humidity Calculation

The relative humidity calculation is identical to previous versions of T2GGM, with the exception that the maximum vapour pressure is now temperature dependent using Antoine's equation. No specific output is available for the maximum vapour pressure calculated by the Antoine equation. Consequently, a debug file, containing temperature and resulting maximum vapour pressure, was written for the test case only. Using the 5CS Multiple Container model as the test case, the maximum vapour pressures output in the debug file were compared to hand calculations using the Antoine equation, as well as maximum water table values published in the CRC Handbook (1995). As shown in Figure 5-2, maximum vapour pressures were identical to hand calculations using Antoine's equation.
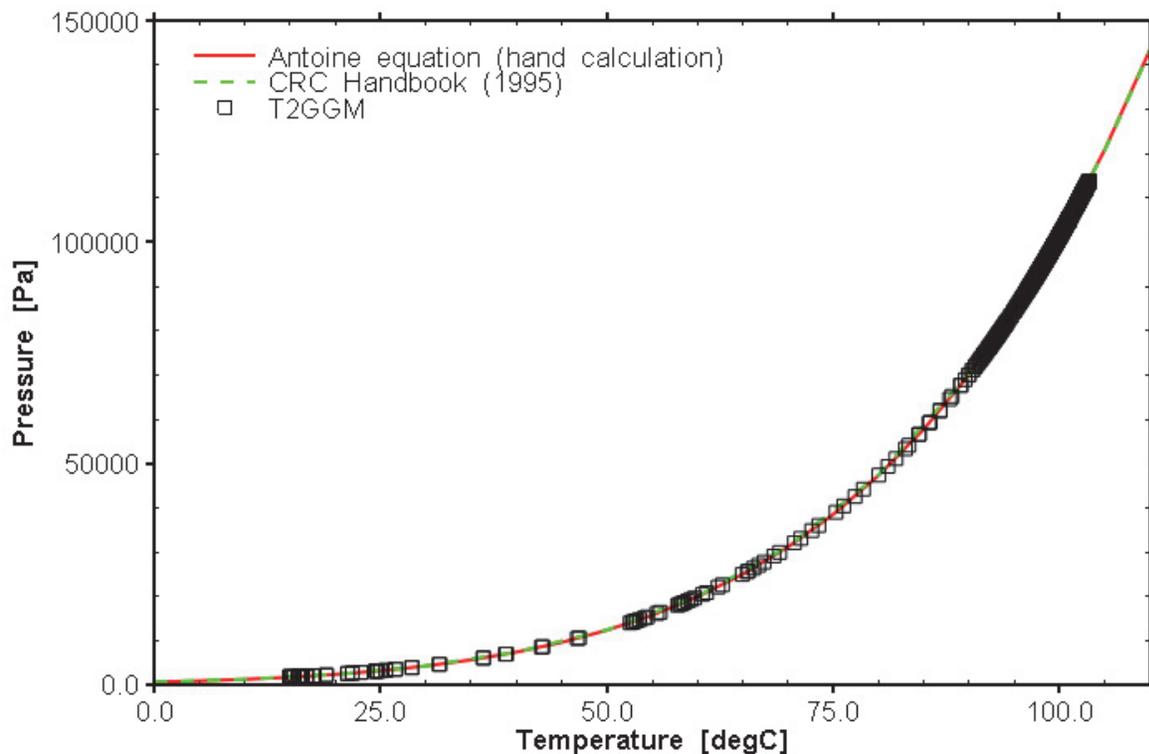
Figure 5-2: Temperature-dependent Maximum Water Vapour Pressures as Calculated by T2GGM, Compared to Hand Calculations and Published Values

5.7.4 Multiple Compartments

Resulting pressures, saturations and temperatures for each compartment provided in the GGM output files are compared to average pressures, saturations and temperatures for the compartment elements as calculated in mView from TOUGH2 output. The 5CS Multiple

Container model, which contains two compartments, was used as the test case. Pressures, saturations and temperatures matched between T2GGM and GGM, for both compartments, although it should be noted that pressures calculated from T2GGM output were slightly higher than GGM (~0.5%), attributed to precision errors in the check calculations.

5.7.5   Time-varying Permeability

Time-varying permeability was tested using a simple 2D test case, with 1D flow. Permeabilities in the half of the grid were reduced by a factor of 0.1 part way through the simulation. Figure 5-3 shows the pressure results for the time-varying permeability test case. Note that the slight deviation in pressure at 5 m between the analytical hand-calculation and simulation results is due to differences in discretization. The test was considered successful as (1) early time pressure results (before permeability changes) compared exactly to a simulation with constant permeability, (2) late time pressure results were the same as a hand calculation of expected pressures due to the reduction in permeability, and (3) the change in pressure results occurred at the expected time based on the time-varying permeability definition.
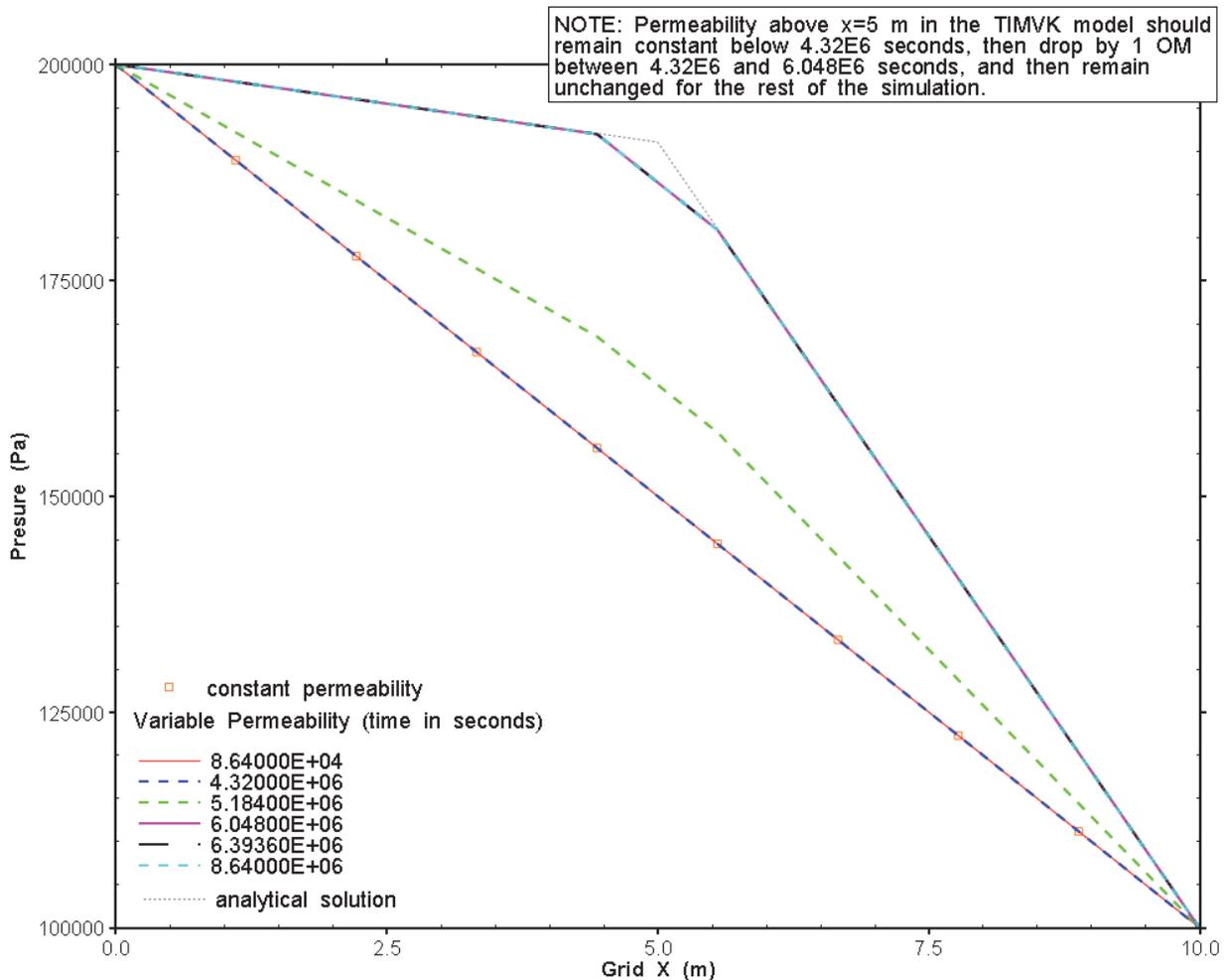
Figure 5-3: Results for Time-varying Permeability Test Case

5.7.6   Time-varying Boundary Conditions

A simple 1D test case verifies the correct implementation of time-variable boundary conditions. The test case modifies pressure, saturation and temperature in a single step change at a single boundary condition node. Inspection of the output file shows pressure, saturation and temperature at the boundary condition node to change according to the specification in the TIMBC input record.

5.7.7   Optimized Time-Step Adjustment

The implementation of the optimized time-step adjustment is verified by inspection of the output file for the 5CS Multiple Container test case. Time step increases are by a factor of 1.8, as specified in the input record. Also, as specified in the input record, time step decreases are by a factor of 1.5, and a time step increase is not applied until at least 2 time steps have been completed.

5.7.8   Alternative Ne Gas

The 1D test case for the time-variable boundary conditions was recalculated with neon as the gas, instead of air. The output file generated showed the correct values for neon (where the output file provides values for input read), and a hand calculation confirmed correct values of dissolved neon in liquid.

5.7.9   Revised File formats

Revised file formats are verified by inspection of output files and post-processing of results from the 3DRS GG1 test case (GEOFIRMA and QUINTESSA 2011), which has output times up to one million years. High precision times and format modifications were implemented to address output issues at longer times; these long output times are provided in this test case. High-precision times have been correctly implemented, as evidenced by the output times in the mView processed NOUT file (a binary file containing TOUGH2 nodal output for each output time). By examination of the output files, all output is correctly formatted (i.e. no overflow *** output). The new FOFT/COFT format, implemented in the GGMCALC.COMP output, is correctly read and processed within mView. Data in the GGMCALC.COMP output file (new FOFT/COFT format) matches the data in the GGMCALC table file (since there is only one compartment in this case, these two files should have identical data).

5.8   T2GGM VERSION 3.1 VERIFICATION RESULTS

Modifications for Version 3.1 include the 1D hydromechanical model, as well as the restart capability.

5.8.1   1D Hydromechanical Model

Three test cases are presented for the 1D hydromechanical model verification: the first two are fully water-saturated models compared to analytic solutions, and the third tests the model in a two-phase system. This third test verifies appropriate model execution rather than comparing to an analytic solution, as analytical solutions for partially gas saturated systems do not exist.

5.8.1.1   1D Consolidation after Terzaghi (1943)

For this full water-saturated case, model results are compared with the analytical solution for one-dimensional consolidation by Terzaghi (1943). In this problem, a layer of water-saturated rock is subjected to an instantaneously applied vertical load at the upper surface. The rock layer has a specified thickness (h), and water is allowed to drain at the surface, where pressure is maintained constant. Hydraulic boundaries on all other sides are set as zero-flow. Mechanical boundary conditions on the vertical sides are roller boundaries, allowing only vertical movement. The analytical solution for pore pressure (P_p) is as follows (Jaeger et al., 2007):

$$P_p(z,t) \ = \frac{\alpha M \sigma_{zz}}{(\lambda + 2G + \alpha^2 M)} * \sum_{i=1,3,\dots}^{\infty} \frac{4}{i\pi} \sin\left(\frac{i\pi z}{2h}\right) \exp\left(\frac{-i^2 \pi^2 kt}{4\mu S h^2}\right) \tag{5.1}$$

where:
$\alpha =$ Biot-Willlis coefficient (-);
$t =$ time (s);
$z =$ depth (m);
$M =$ Biot modulus (Pa);
$\sigma_{zz} =$ instantaneous vertical load (Pa);
$\lambda =$ drained Lame's modulus (Pa);
$G =$ Shear modulus (Pa);
$h =$ maximum depth (or thickness) of rock layer (m);
$k =$ permeability (m^2);
$\mu =$ dynamic viscosity (kg m^{-1}s^{-1});
$S =$ uniaxial storage coefficient (Pa^{-1}).

A T2GGM model of a similar system was developed. As T2GGM applies load as a rate, it was not possible to obtain an instantaneous application of load. Instead, load was applied at such a rate that maximum loading was achieved within 0.1 years, which was short (i.e., nearly instantaneous) when compared to the total runtime of approximately 100 years. A second minor divergence between the numerical model and the analytical model is that TOUGH2 does not assume constant water density and compressibility, but calculates these as a function of temperature and pressure. However, over the pressure range examined here, the impact of this second divergence on results was minor.

Model properties are shown in Table 5-5. For comparison's sake, the mechanical parameters used are equivalent to those used for a similar verification exercise by Nasir et al. (2011), namely Young's modulus (E) of 4x10^7 and Poisson's ratio (ν) of 0.3. The T2GGM model used a porosity of 0.1.

A comparison of analytical and numerical model results is shown in Figure 5-4. For this run the applied load (σ_{zz}) was 3.0 MPa. The time axis is plotted as dimensionless time, defined as $kt/\mu S h^2$. The agreement between numerical and analytical solutions is good, although the T2GGM model does seem to drain slightly faster at greater depths and times.

Table 5-5: Model Properties for the Terzaghi (1943) Verification Case

Analytical		TOUGH2	
Property	Value	Property	Value
k (m^2)	2.04 x 10^{-15}	k (m^2)	2.04 x 10^{-15}
S (Pa^{-1})*	1.86 x 10^{-8}	C_{pore} (Pa^{-1})*	1.86 x 10^{-7}
α	1.0	ζ	1.0
h (m)	1000	h (m)	1000

*S and C_{pore} are different parameters describing the compressibility of the rock. These parameters are equivalent, based on a rock compressibility of 3.33 x 10^7 Pa.
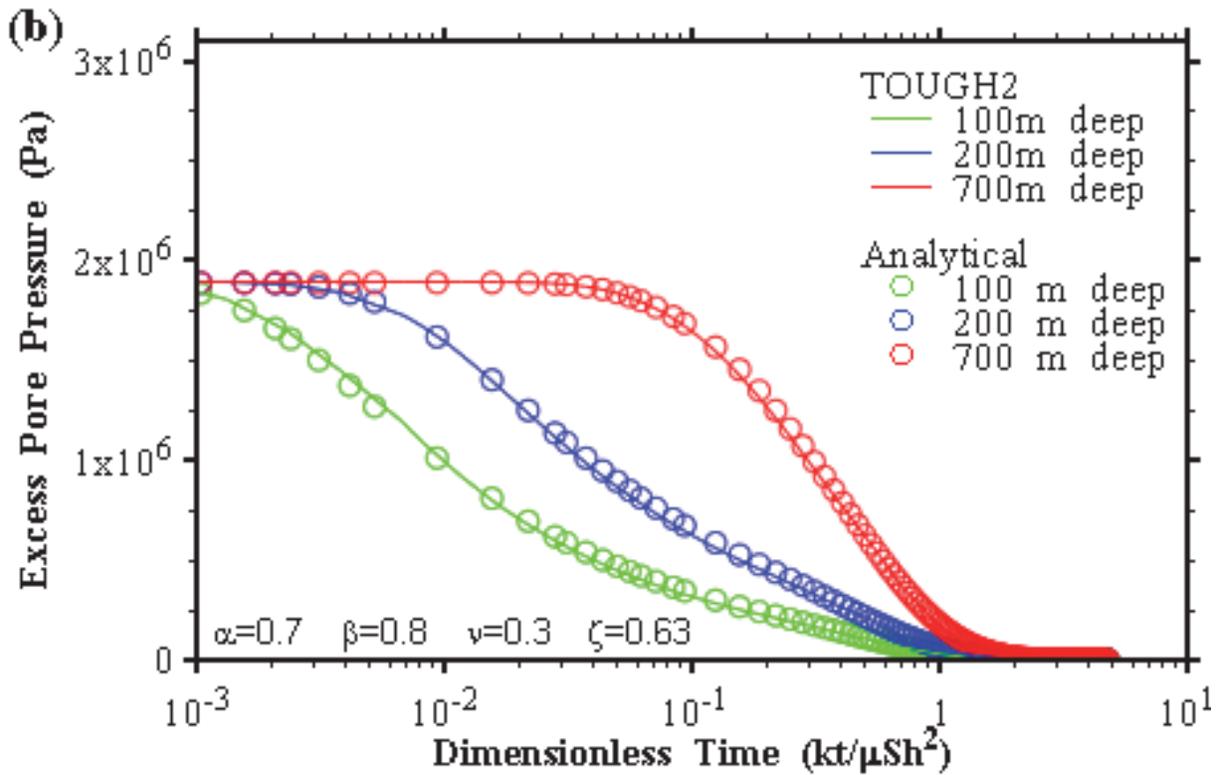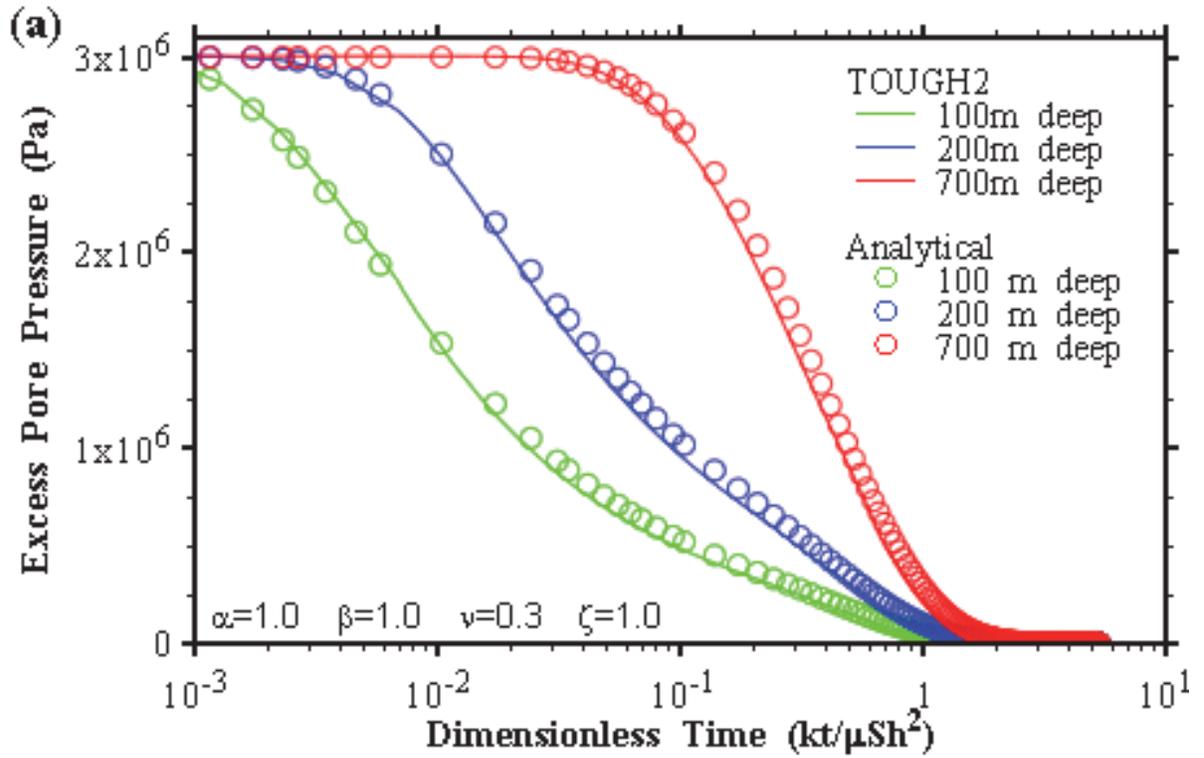
Figure 5-4: Analytical and T2GGM Pressure Time-Series, Various Depths, (a) $\zeta = 1$, (b) $\zeta = 0.63$

5.8.1.2 1D Hydromechanical Coupling in a Semi-infinite Column with Gradual Loading

For this fully-water saturated verification case, the analytical solution described in Lemieux et al. (2008) was used. This is an analytical solution for one-dimensional hydromechanical coupling in a semi-infinite column. In this model, the applied stress is continually increased as a linear function of time. The top of the column is drained (hydraulic head is held constant at zero) and the base of the column is at an infinite distance. The analytical solution to this problem is as follows:

$$h(z,t) = \frac{\zeta}{\rho g} \frac{d\sigma_{zz}}{dt} \left[t - \left(t + \frac{z}{2D} \right) erfc \left(\frac{z}{2\sqrt{Dt}} \right) + z \sqrt{\frac{t}{\pi D}} exp \left(-\frac{z^2}{4Dt} \right) \right]$$ (5.2)

where:
ζ =   one dimensional loading efficiency (-);
ρ =   fluid density (kg/m^3);
g =   gravity (m/s^2);
$d\sigma_{zz}/dt$ = stress application rate (Pa/s), a constant as discussed above;
t =   time (s);
z =   depth (m);
D =   hydraulic diffusivity (m^2/s), hydraulic conductivity divided by specific storage.

Note that there is a slight difference between Equation (5.2) and the solution shown in Lemieux et al. (2008), which has a typographical error.

A similar system was modelled using T2GGM. Model properties are shown in Table 5-6. The primary difference between the numerical model and the analytical model was the total vertical depth of 7000 m for the numerical model. The analytical model is semi-infinite, but a greater depth in the numerical model would have led to pore pressures in excess of 100 MPa, which is a hard-coded cut-off beyond which the TOUGH2 EOS3 module does not function. The T2GGM model had a constant specified pressure of 100 kPa (~1 atm) at the top, a no-flow boundary at the base, and was water saturated throughout. As with the previous verification case, the analytical model assumes constant water density and compressibility unlike TOUGH2, which has a minor impact on results over the pressure range examined here.

Table 5-6: Model Properties for the Second Verification Case*

Analytical		TOUGH2	
Property	Value	Property	Value
K_{zz} (m/a)	1.0×10^{-3}	k_{zz} (m^2)	3.23×10^{-18}
S_s (m^{-1})	1.0×10^{-6}	C_{pore} (Pa^{-1})	5.70×10^{-10}
ζ	Varies	ζ	varies

*Values provided in this table are the input requirements for each model. The input requirements for each model are different (i.e., the analytical model requires hydraulic conductivity (K_{zz}) and specific storage (S_s) and the TOUGH2 model requires permeability (k_{zz}) and pore compressibility (C_{pore})), and the parameters provided for each model are equivalent once standard unit conversions and equations are applied.

The TOUGH2 pressure results were converted to hydraulic head, and compared against the analytical solution, as shown in Figure 5-5. Despite the slightly different assumptions between the two models, the TOUGH2 results are a good match with the analytical solution.

The impact of changing the loading efficiency was also assessed, in both the analytical and the T2GGM models (see Figure 5-6). Once again, the numerical and analytical models correspond very well. As expected, reducing the loading efficiency reduces the mechanically-induced pressure rise in the 1D column.
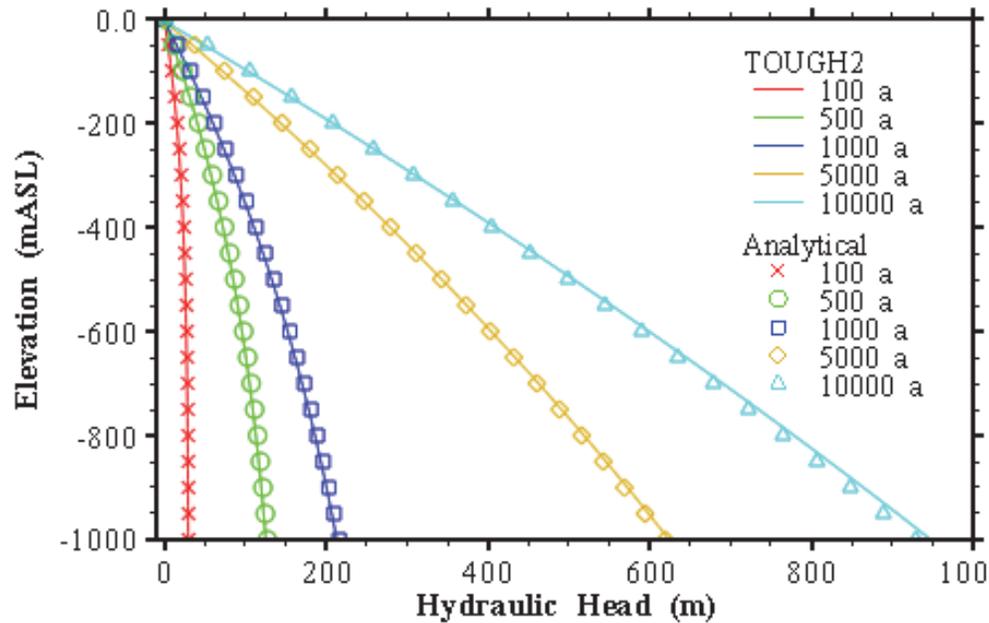
Figure 5-5: Analytical and T2GGM Calculated Hydraulic Head versus Depth at Different Times
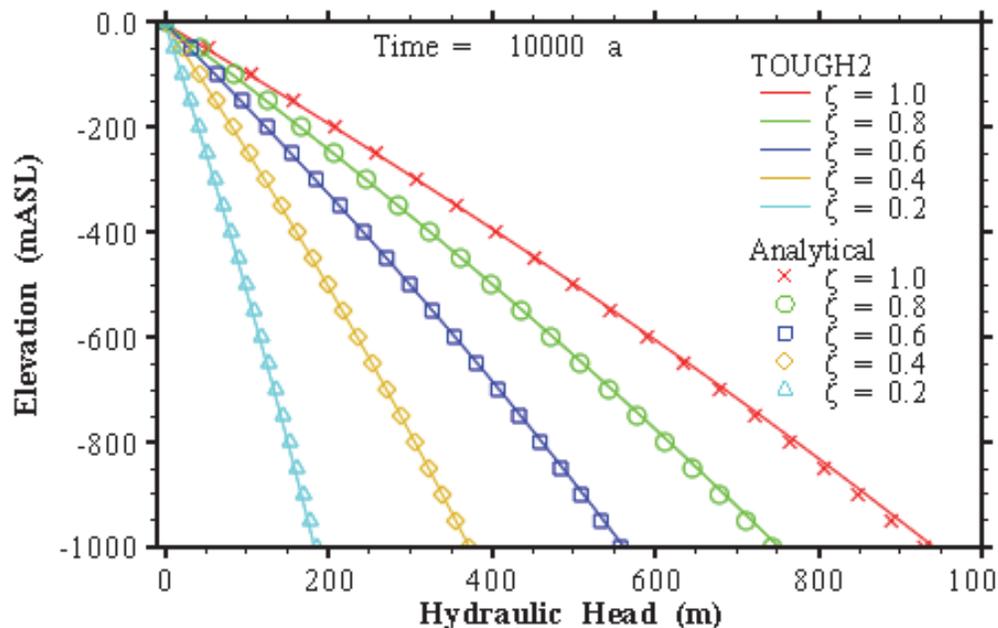
Figure 5-6: Analytical and T2GGM Calculated Hydraulic Head versus Depth at 10 000 years, for Different Loading Efficiencies (ζ)

5.8.1.3 A Simple Two-phase Test Case

In this section, a homogeneous, one-dimensional model is used to examine the effects of gas in a hydromechanical system. It should be emphasized that this verification is by inspection only; analytical data does not exist to verify the two-phase component of the 1D hydromechanical model.

The example is simplified and artificial, but nevertheless allows us to focus on the effects of gas without the complexity inherent in most natural systems. This homogeneous system is loaded (as shown in Figure 5-7), and the change in water pressure (expressed in m H_2O) under various conditions is assessed. The permeability is rather low to remove drainage effects, and a generic capillary pressure curve, typical of such low permeability rock, was used. Water pressure was initialized at hydrostatic, gas pressure was initialized in equilibrium with the water pressure as a function of the capillary pressure curve. Loading efficiency (ζ) was set to 0.7.

Figure 5-7 shows how the initial gas saturation affects the hydromechanical (HM) process: as gas saturation (S_G) increases, the degree of HM coupling drops as gas is able to compress and minimize the pressure impact of a mechanical load. Porosity changes due to pressure-dependent compressibility (term 2 of Equation 4.3) compensate for any porosity changes due to mechanical loading, which are constant regardless of gas saturation (term 3 of Equation 4.3). Low gas saturations can still have a profound effect on the HM response. Also interesting to note, for the models with very low gas saturations, the changing shape of the curve indicates a transition from two-phase to fully saturated behavior as the increased pressure causes the gas in the system to dissolve.

The impact of alternate parameters, such as compressibility and depth, are described in detail within Walsh et al. (2012).
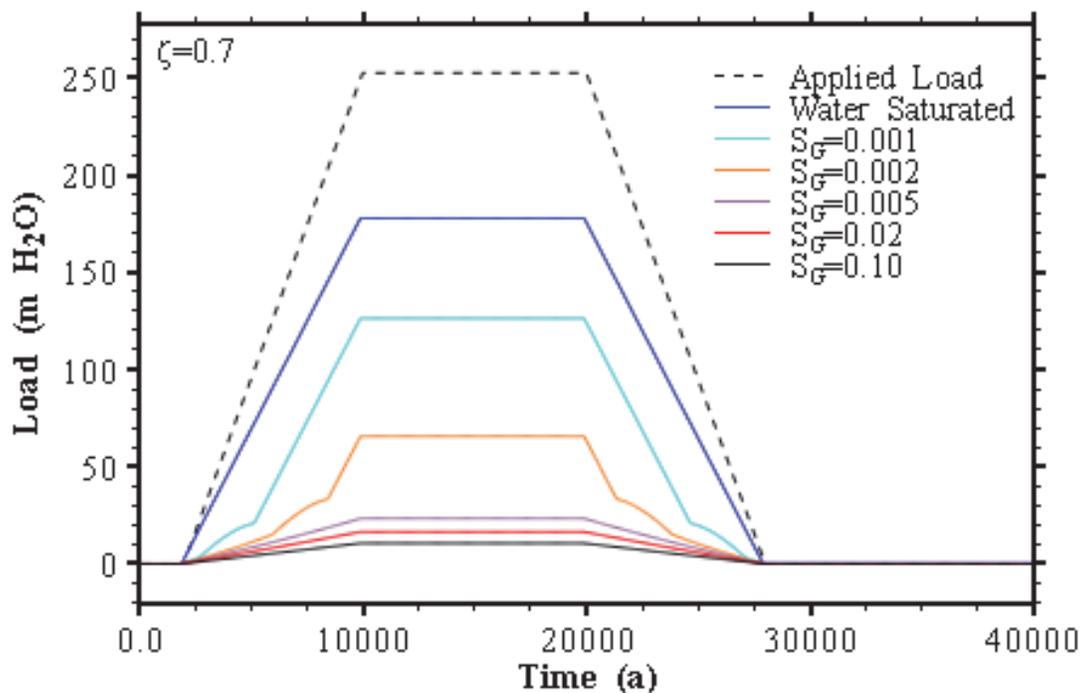
Figure 5-7: Effect of Gas Saturation

5.8.2   Restart Capability

3DRS GG1 NWL (GEOFIRMA and QUINTESSA 2011) was used as the test case, and the original simulation run with Version 3.1 was restarted at 200 years. Figure 5-8 compares the pressure in the repository for the original simulation and the restarted simulation, showing results to be identical.
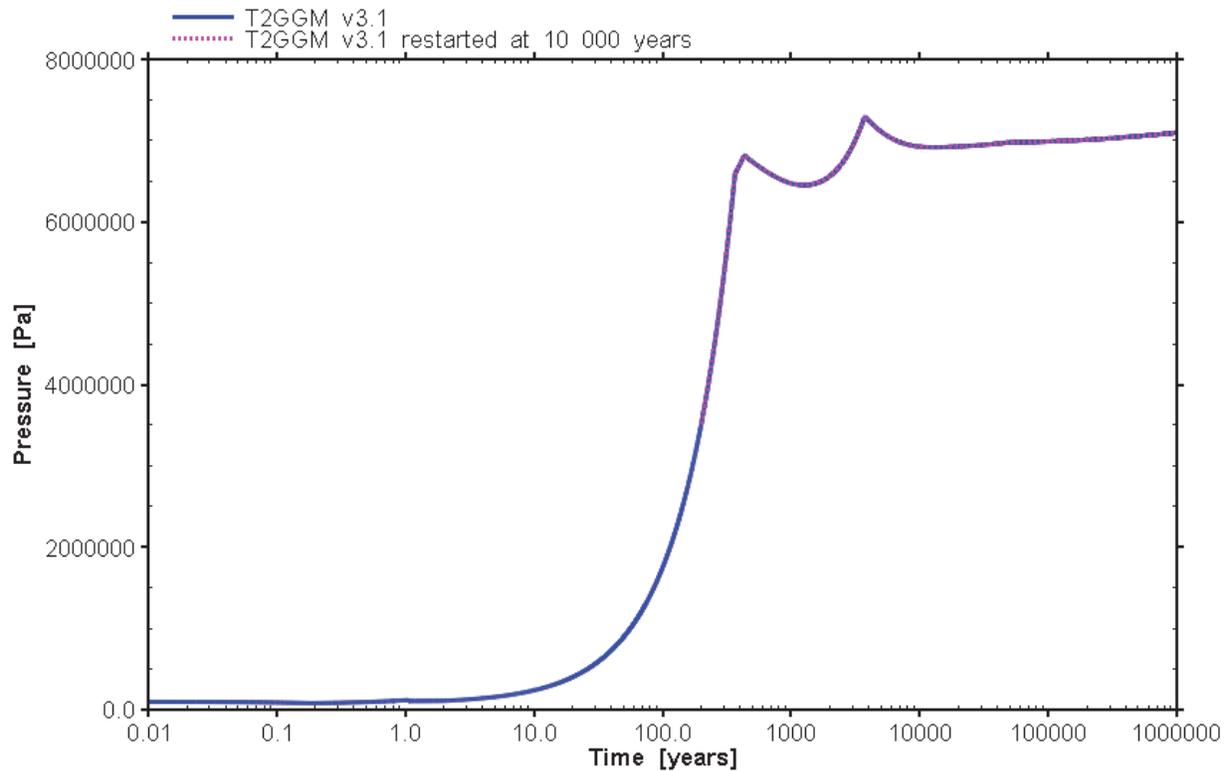
Figure 5-8: Pressure in the GGM Container for 3DRS GG1 NWL Case, Comparing Version 3.1 and a Restart at 200 Years

5.9   T2GGM VERSION 3.2 VERIFICATION RESULTS

5.9.1   Previous Functionality

3DSRS GG1 (GEOFIRMA and QUINTESSA 2011) was simulated with version 3.1 and 3.2 to ensure previous functionality is unaffected by version 3.2 modifications. Results for both the non water limited (NWL) and water limited (WL cases matched, as shown in Figure 5-9.
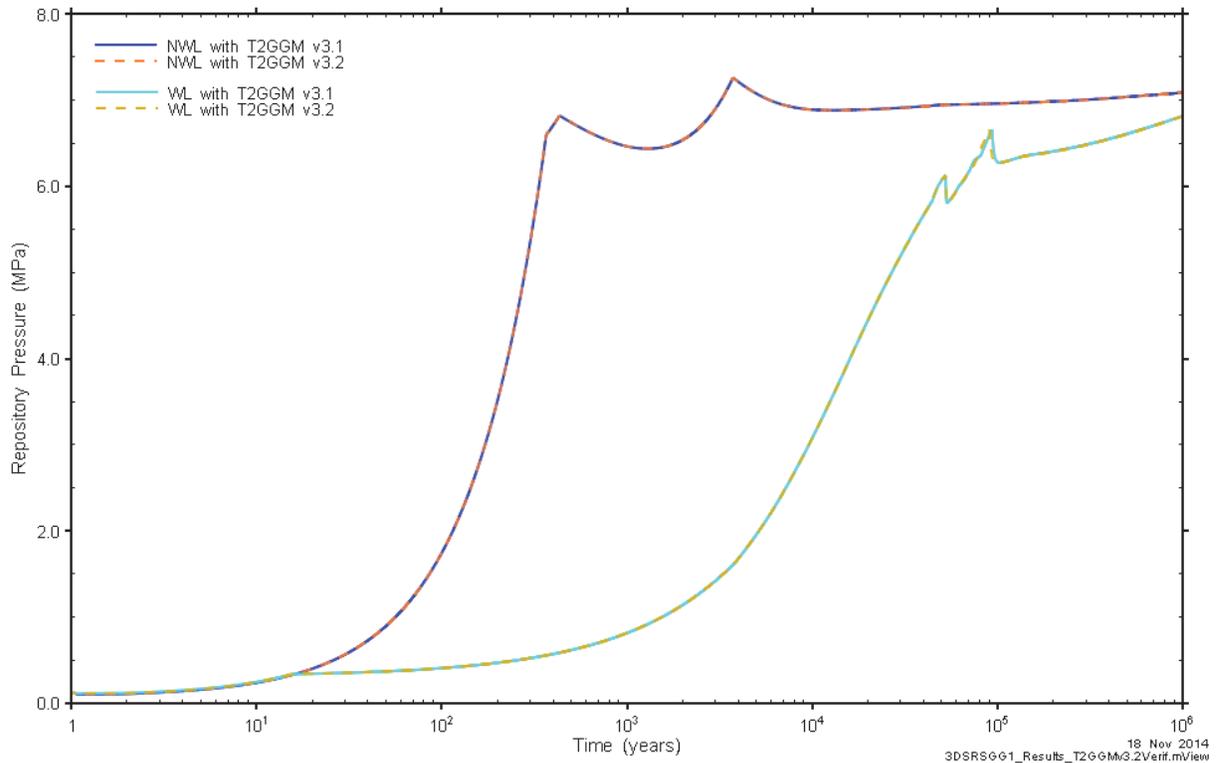
Figure 5-9: Previous Functionality Comparison Between Version 3.1 and Version 3.2

5.9.2   Real Gas Properties

A simple 3D test case was developed to test the real gas properties in the TOUGH2 portion of the code: a cube 50 m in dimension, where initial gas pressures are 1 MPa, and top and bottom boundaries are set to 20 MPa. The simulations allow pressures to equilibrate over a single simulation day. Pressures in the middle of the model are used to calculate z factors, and these values are compared to the values independently calculated from the WebGasEOS webpage (Reagan et al., 2005). The calculations from this webpage are based on the TOUGH++ code.

Comparisons were made for pure gas at 15°C, as shown in Figure 5-10 and for two-phase gas and vapour mixtures at 80°C as shown in Figure 5-11. Model results compared well to the website calculations. Note that website results were not available for helium. Simulation results for pure gas compare well to compressibility charts published by Reid et al. (1987), although the comparison is approximate based on the resolution of available charts. No data was available for comparison of helium and water vapour mixtures.
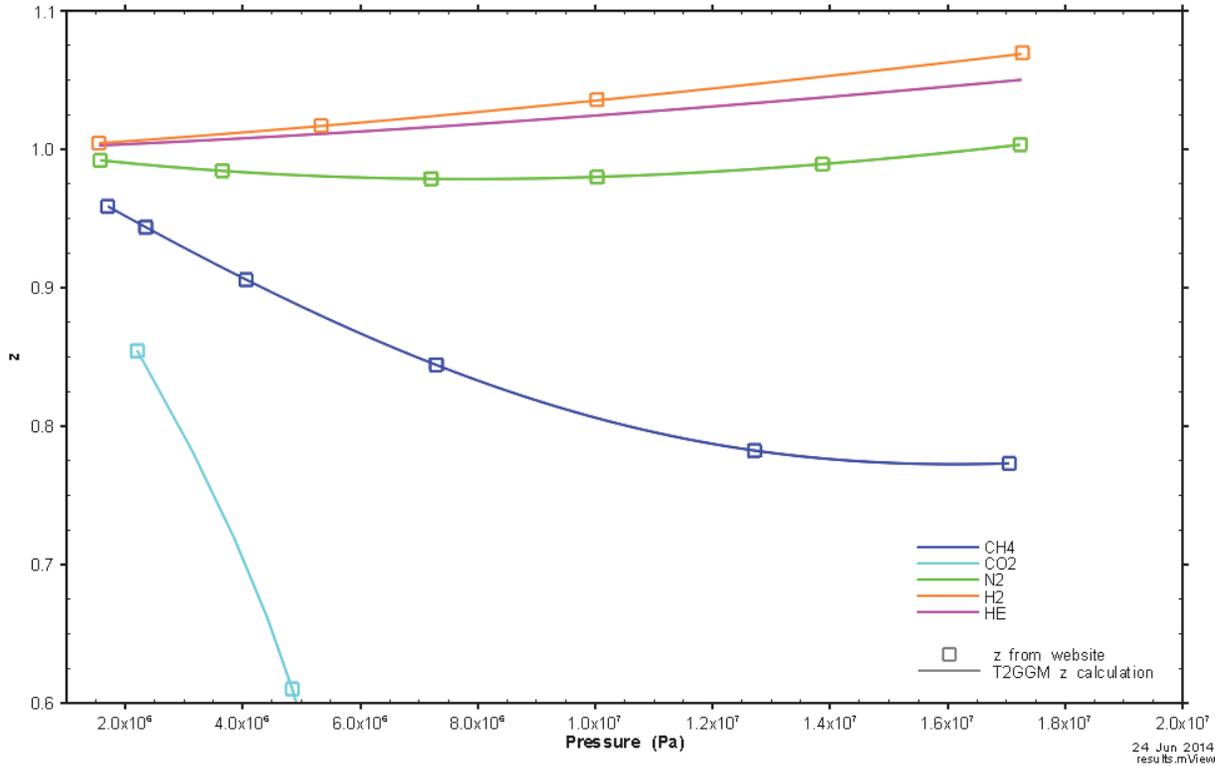
Figure 5-10: Z Compressibility Factor for Pure Gas
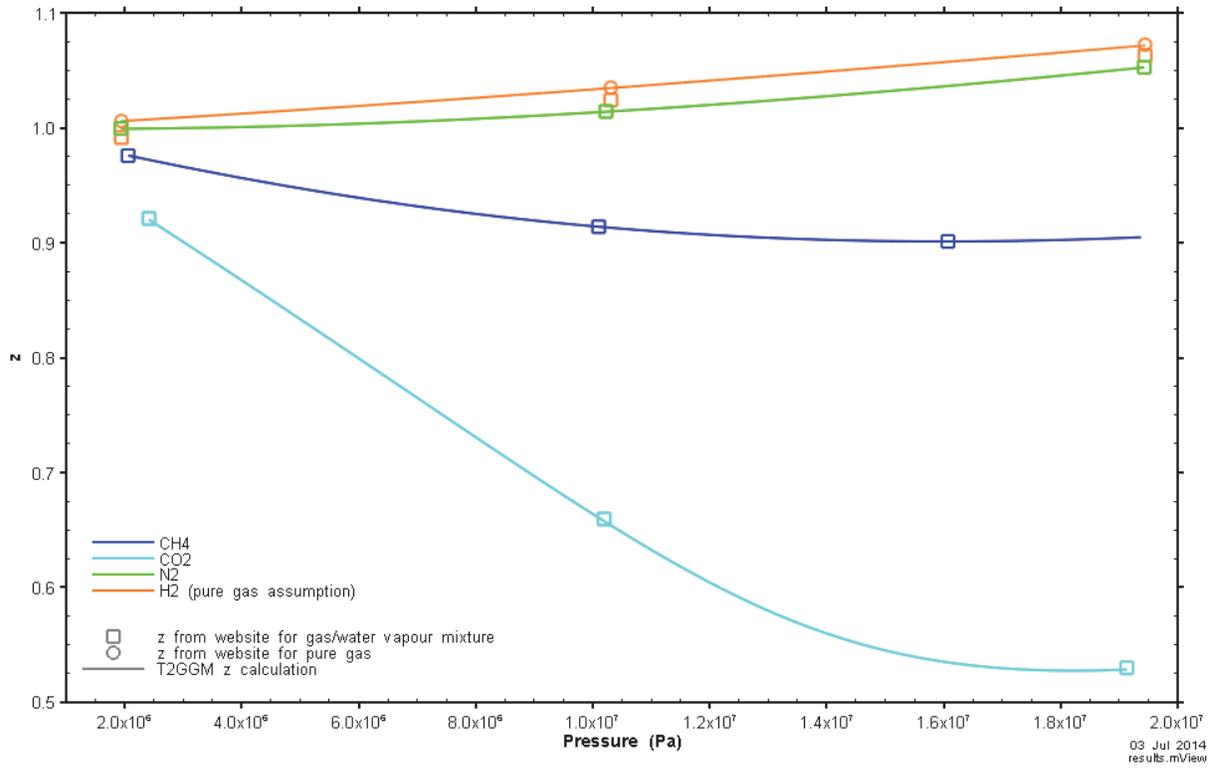
Figure 5-11: Z Compressibility Factor for Gas and Water Vapour Mixtures

Real gas properties within GGM were tested with a modified version of the test case, where a GGM compartment was created in the middle of the repository. GGM input parameters from the 5CS were used. The amount of gas for the ideal gas and non-ideal gas case are compared in Figure 5-12. It is expected that the amount of gas (n), multiplied by the compressibility factor Z, will match the amount of gas in the ideal gas case (nZ =PV/RT), and this is indeed the case. There are minor differences at later times due to the slightly different timing of the disappearance of oxygen.
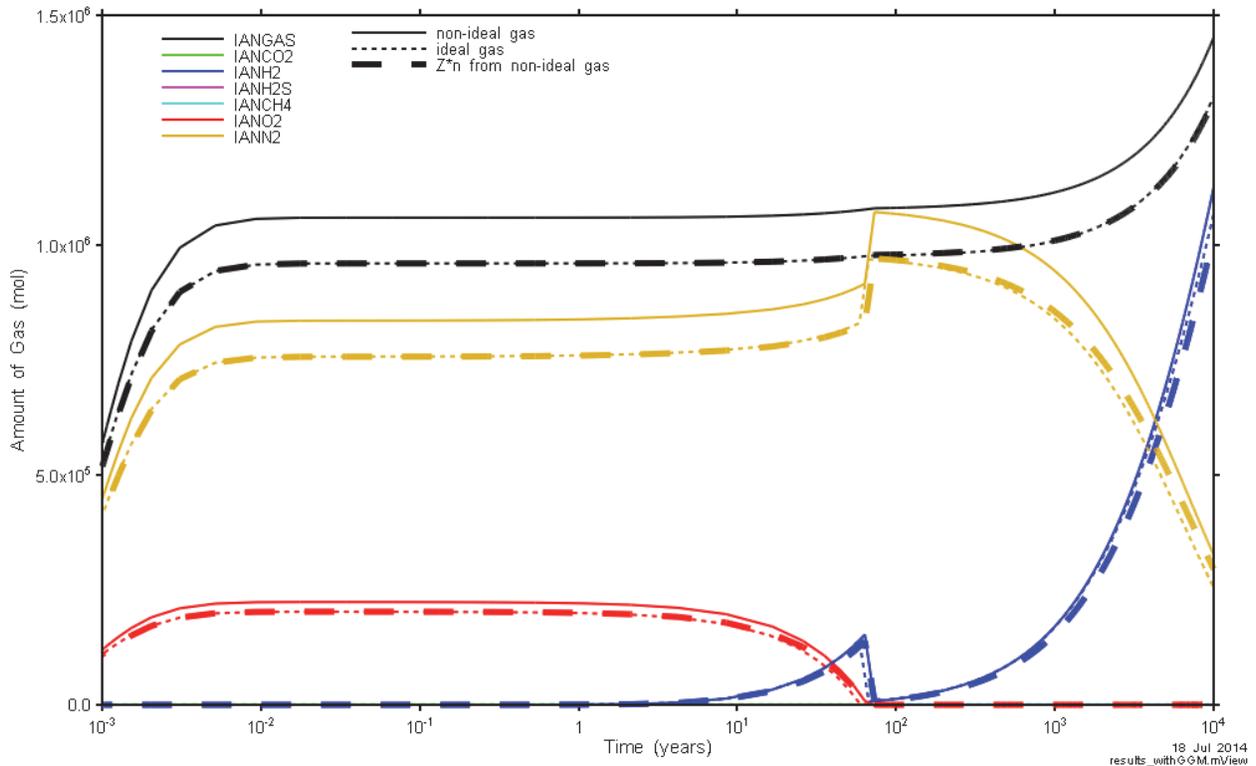
Figure 5-12: Comparison of Amount of Gas between Ideal and Non-Ideal Gas Properties

5.9.3   Model Linking

A simple verification case based on the 5CS room-scale and shaft-scale models (NWMO, 2013) was developed to test the model linking features. Although analogous to the combined room and repository model, the verification case used a much simpler discretization and a specified source term rather than a gas generation rate calculated using the GMM capabilities. The basic geometry is as shown in Figure 5-13. The room and repository models each have a high permeability channel embedded in a low permeability rock mass. Gas is injected at a constant rate (0.1 kg/s) at one end of the room (yellow node in Figure 5-13). The Flow Node at the other end of the room model corresponds to the room exit – flows calculated there are injected into the repository model at each of 7 Pressure nodes (red symbols in Figure 5-13). The test model has fixed pressure boundary conditions at each end (magenta symbols in Figure 5-13) set at atmospheric pressure. Gas injected into the repository model tunnel feature leaves the models at both ends. The test case is verified by comparing the flow rates at the boundaries to those that would occur if 0.1 kg/s gas rate was injected directly into each pressure node. Results

shown in Figure 5-14 indicate that total flows correspond to expectations (0.7 kg/s) and that the flow out of the room model is consistent with the 0.1 kg/s injection.
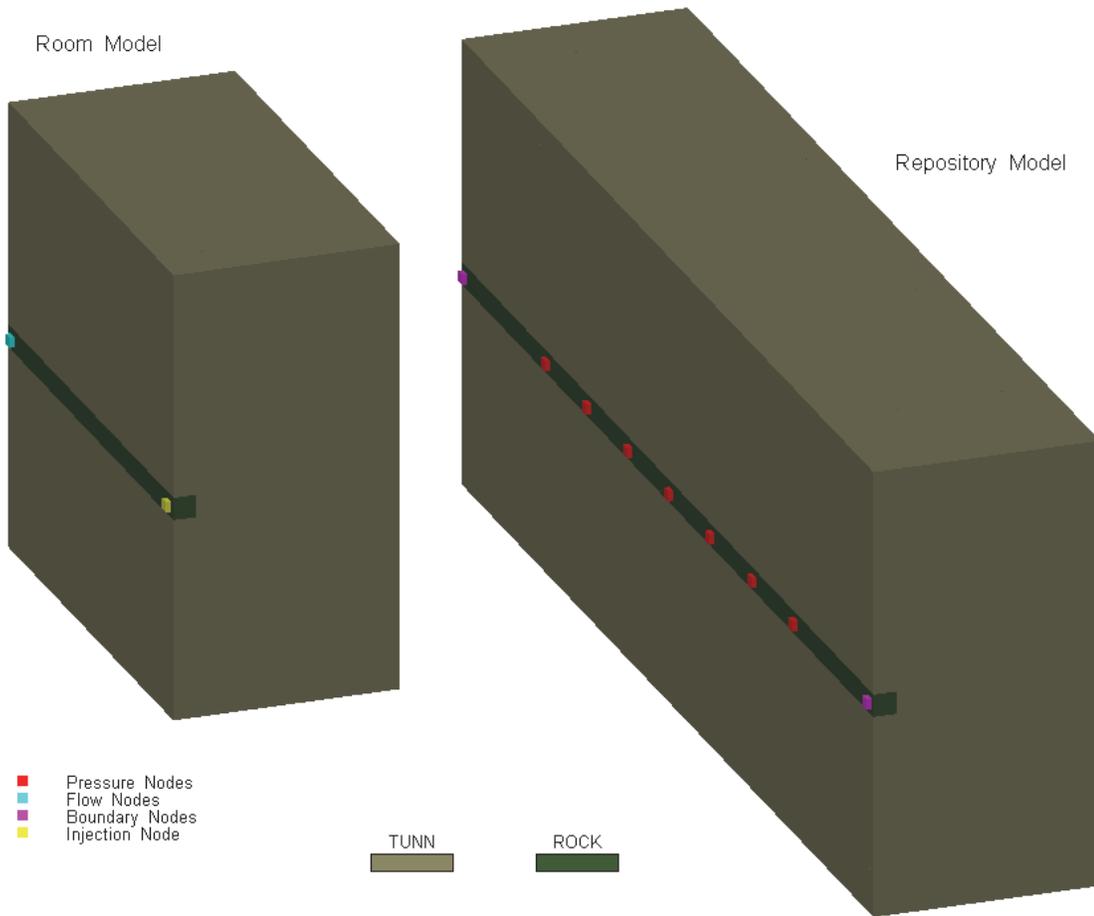
Figure 5-13: Model Linking Basic Verification Model
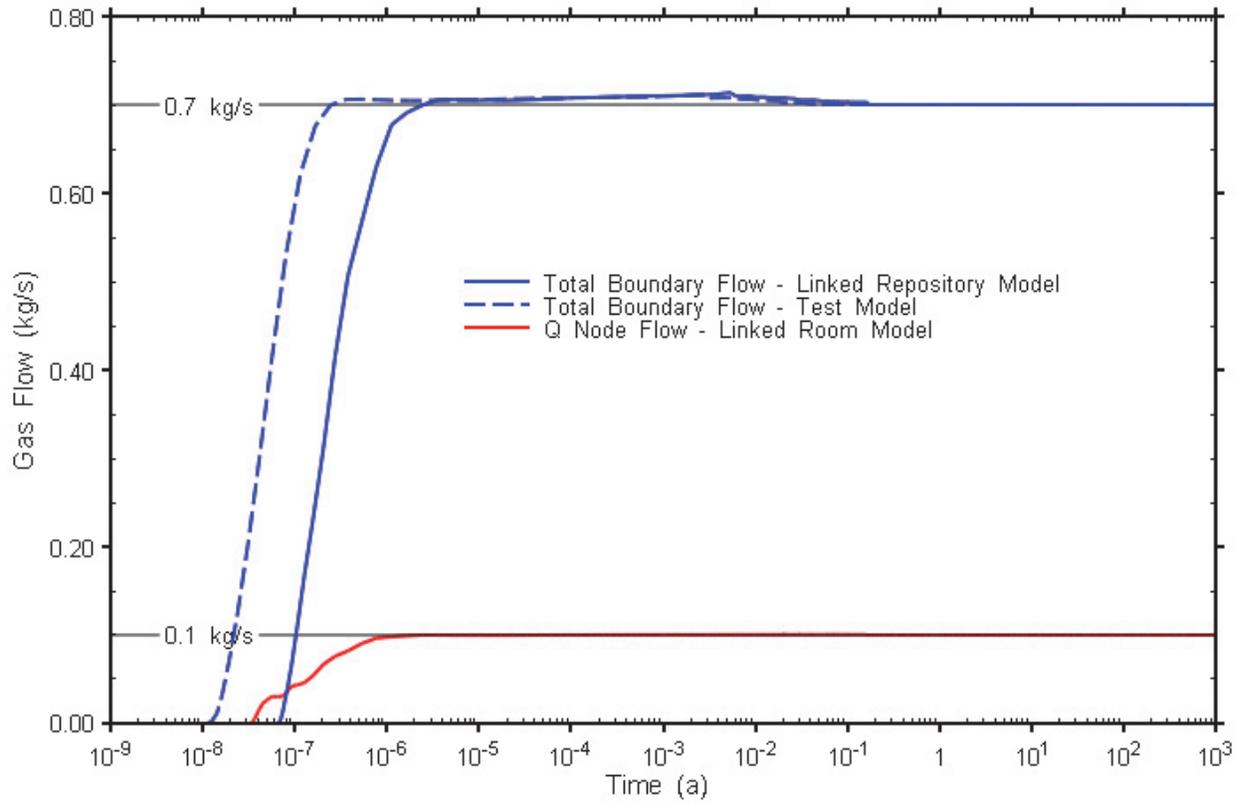
Figure 5-14: Model Linking Flow Verification

Figure 5-15 illustrates the steady-state pressure distribution.
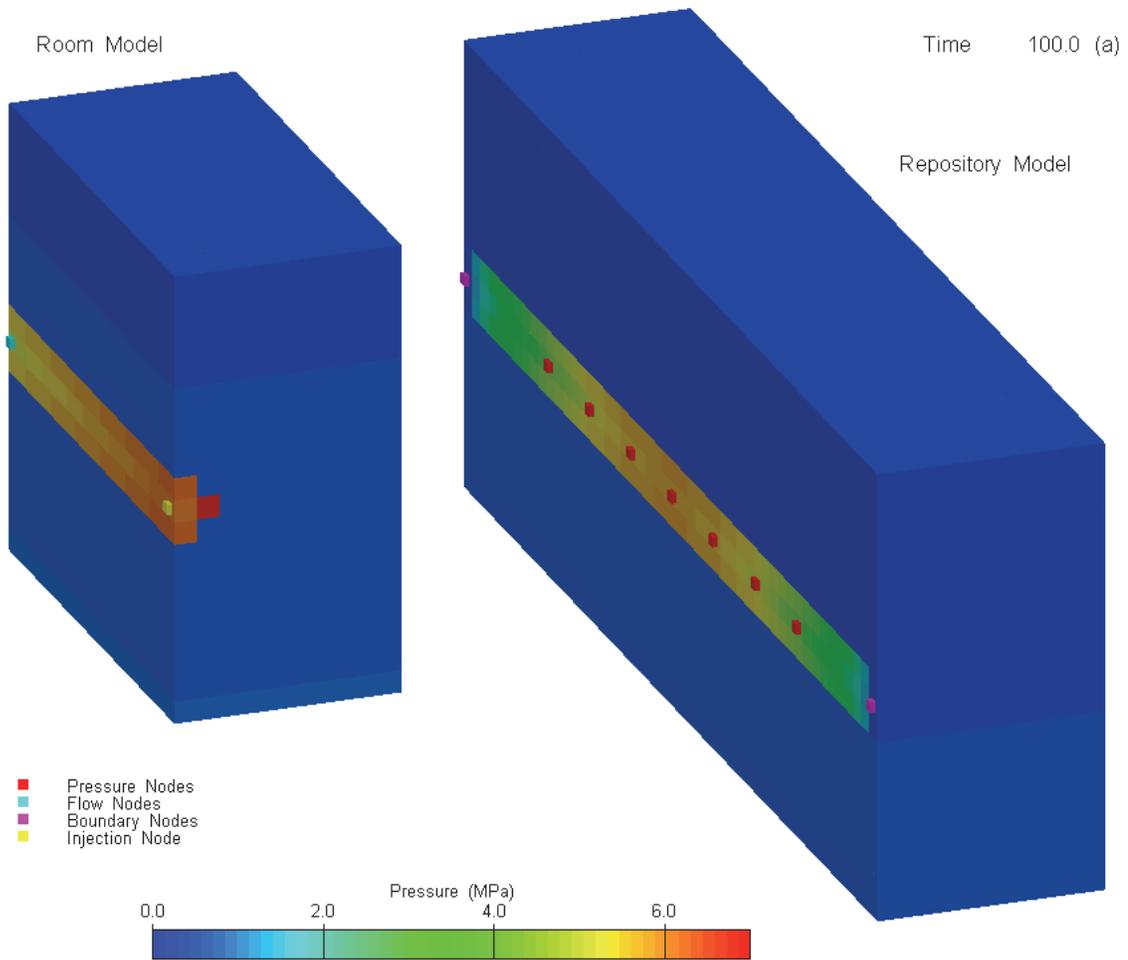
Figure 5-15: Model Linking Example Pressure Distribution

5.9.4   Upscaled Used Fuel Corrosion

Upscaled used fuel corrosion was checked using two test cases: the 5CS Room-Scale model documented in NWMO (2013) and a 5CS Quarter-Container model (see Section 5.9.10.1). The 5CS Room-Scale model is used to test the saturation upscaling, but does not provide a good test of the relative humidity corrosion upscaling. Consequently, the 5CS Quarter-Container model, with container failure at time zero and PBTS at 0.3, was simulated in order to obtain low humidity values and consequently test relative humidity corrosion upscaling.

5.9.4.1 Phase 3 and Phase 4 Corrosion Upscaling: 5CS Room-Scale Model

Figure 5-16 provides the liquid saturation values for all repository elements, as well as the saturation modulation factor D. The saturation modulation factor D is applied to phase 4 corrosion. The upscaled saturation modulation factor output by T2GGM (IAD4, dark blue line in Figure 5-16) matches the value calculated from nodal output (orange dashed line in Figure 5-16). The effects of upscaling are shown by plotting the saturation modulation factor calculated

based on the average repository liquid saturation, the approach taken when upscaling is not activated (and the approach taken prior to upscaling modifications).
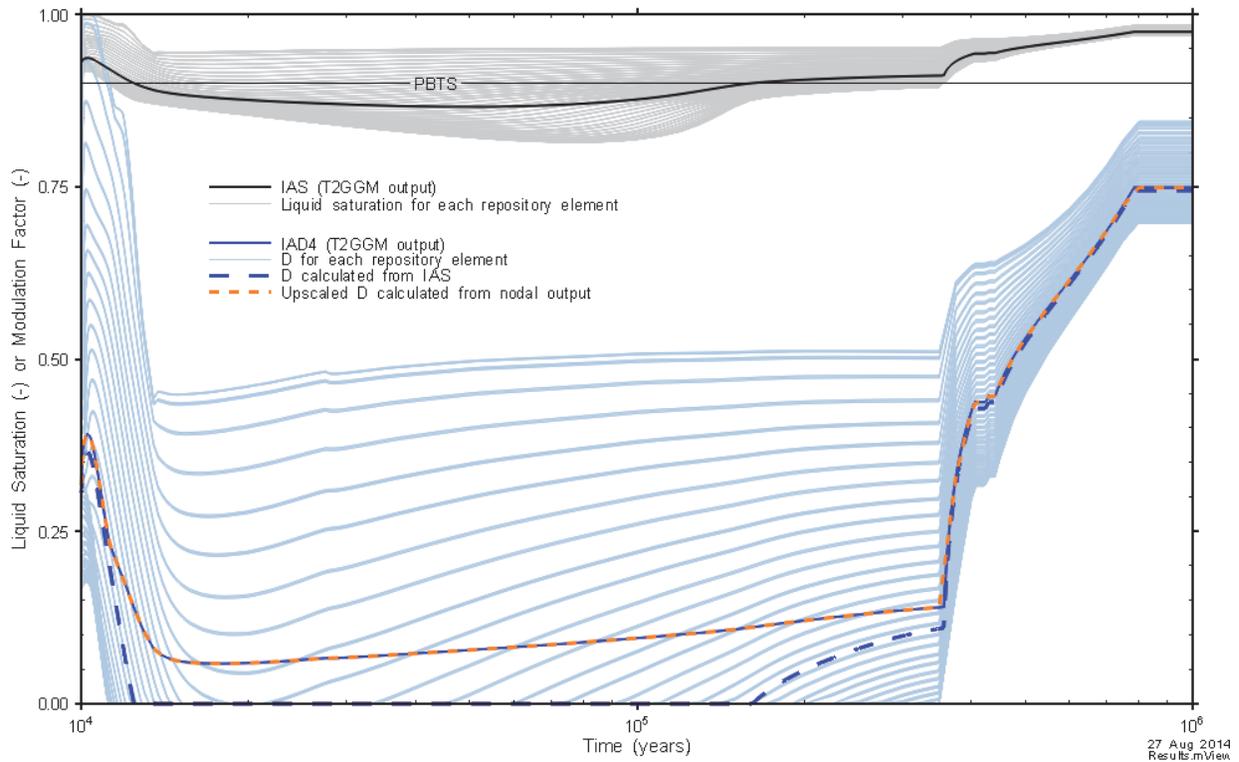
Figure 5-16: Verification of Phase 4 Corrosion Modulation Factors

Phase 3 corrosion is multiplied by the saturation modulation factor (1-D) and the relative humidity (H) modulation factor. Figure 5-17 provides the (1-D) and H modulation factors, as well as the resulting (1-D)*H modulation factors, compared to the factors calculated from nodal output.
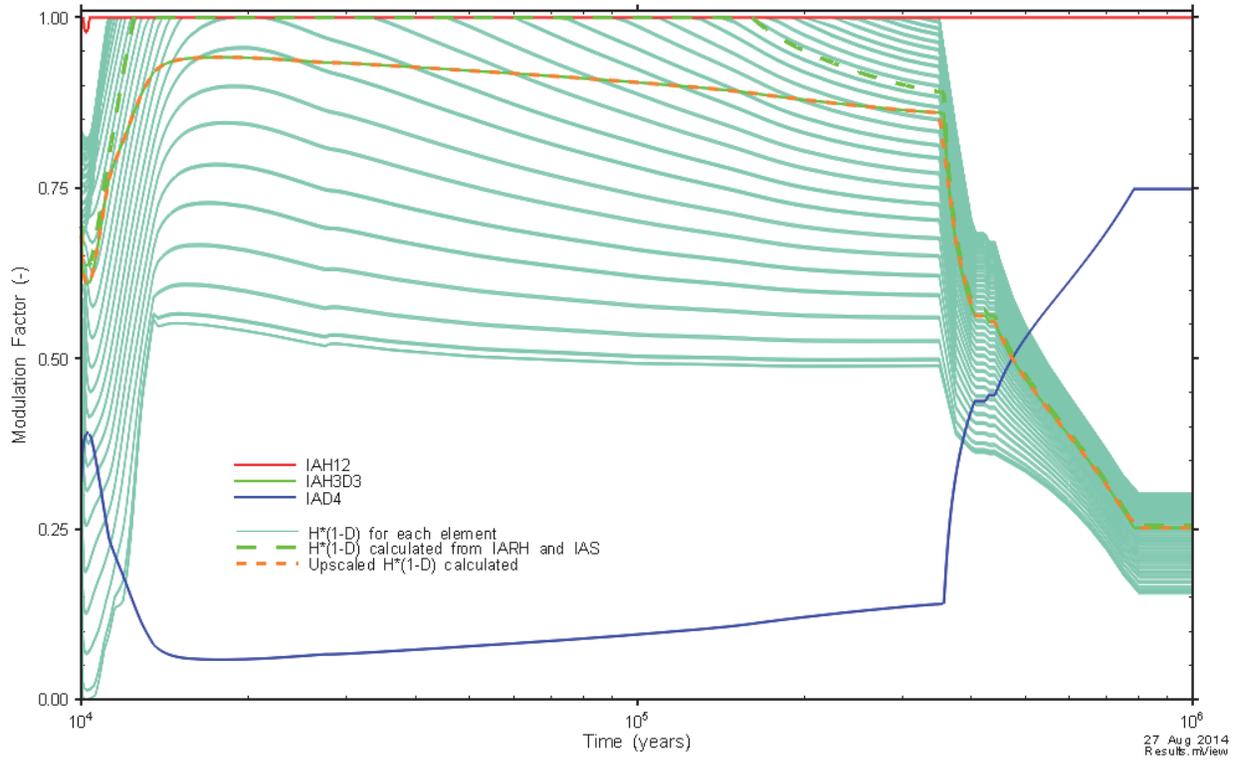
Figure 5-17: Verification of Phase 3 Corrosion Modulation Factors

Figure 5-18 shows the Phase 3 and Phase 4 corrosion rates for the 5CS Room-Scale model for the upscaled modulation factors, compared to modulation factors calculated based on repository averages.
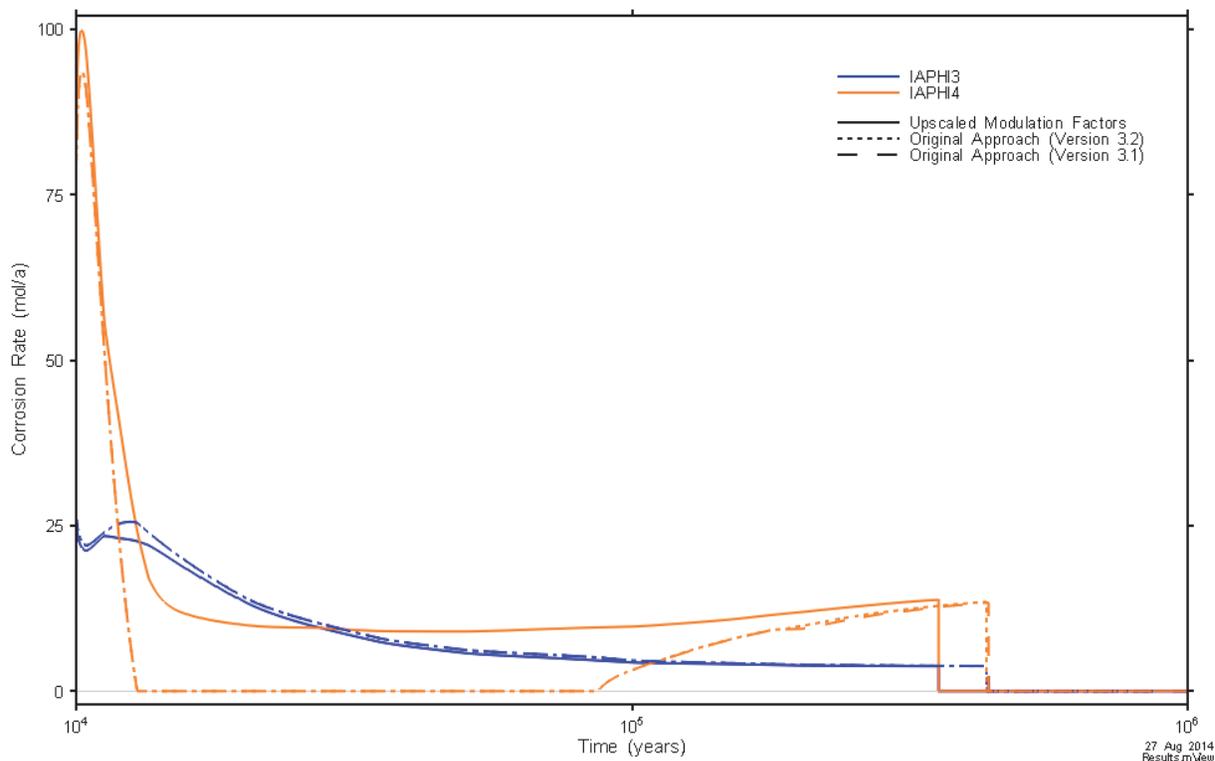
Figure 5-18: Phase 3 and Phase 4 Upscaled Corrosion Rates for 5CS Room-Scale Model

5.9.4.2 Relative Humidity Corrosion Upscaling: 5CS Quarter-Container Model

Figure 5-19 provides the relative humidity at each repository element, as well as the relative humidity modulation factor H. The relative humidity modulation factor H is applied to Phase 2 and 3 corrosion, and (1-H) is applied to Phase 1 corrosion. The upscaled relative humidity modulation factor output by T2GGM (IAH12, solid red line in Figure 5-19) matches the value calculated from nodal output (dashed green line in Figure 5-19).
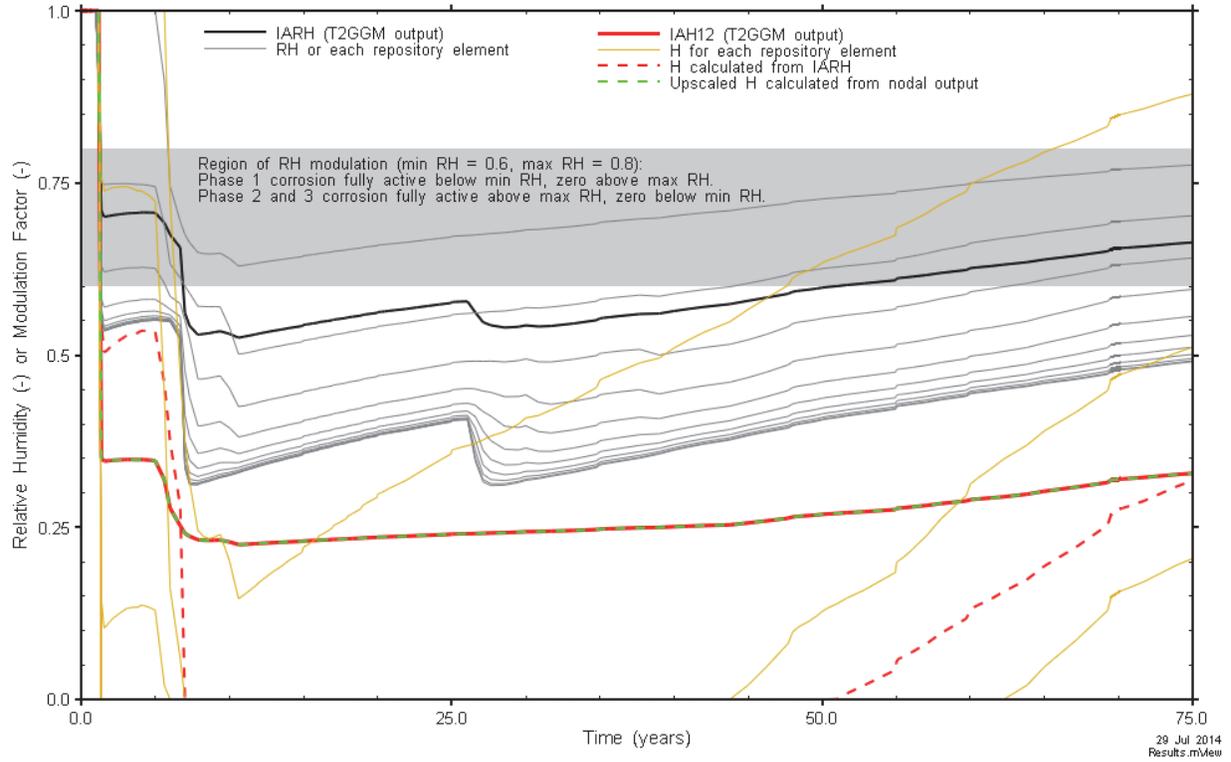
Figure 5-19: Verification of Relative Humidity Modulation Factors

Figure 5-20 shows the effect of the relative humidity modulation factor on Phase 3 corrosion. The H*(1-D) modulation factor output by T2GGM (IAH3DA, green line in Figure 5-20) matches the factor calculated from nodal output (orange dashed line in Figure 5-20).
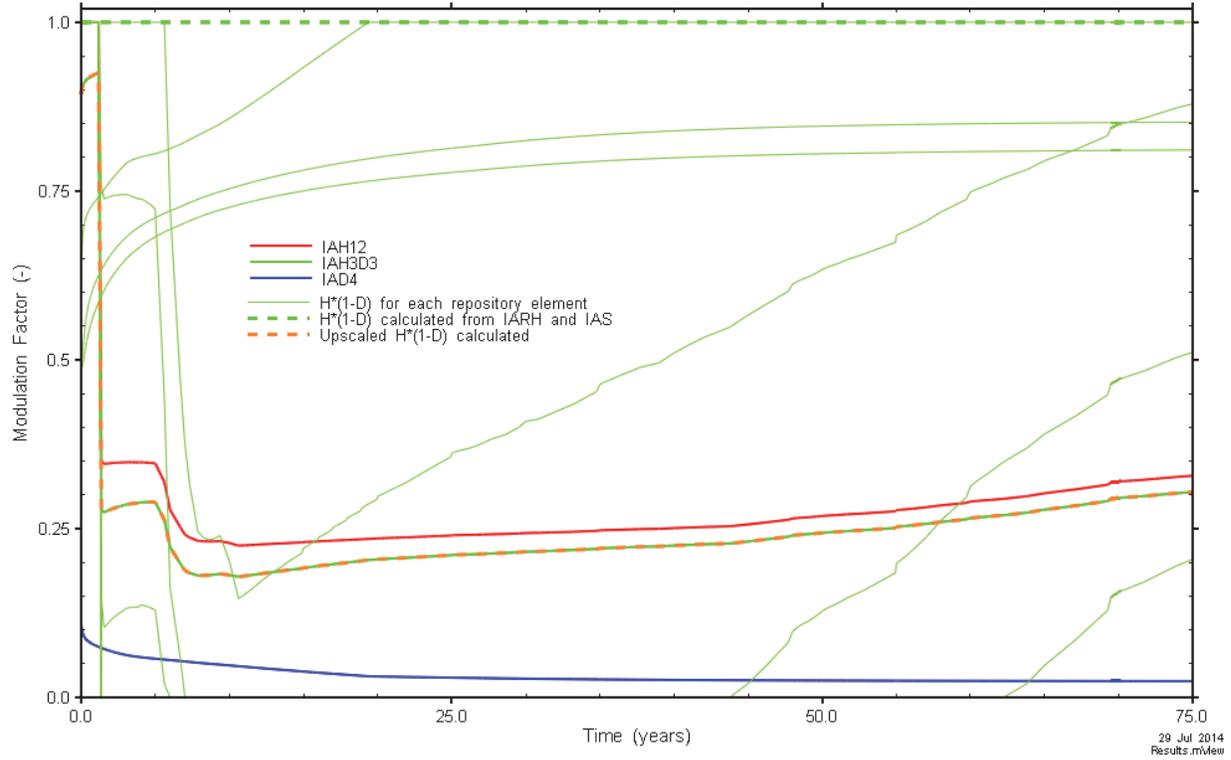
Figure 5-20: Verification of Phase 3 Corrosion Modulation Factors

5.9.5   Kelvin Equation for Relative Humidity

The verification test for the Kelvin equation relative humidity calculation uses the 5CS Room-Scale model (NWMO, 2013), with the GGM PBTS parameter (threshold at which corrosion begins to switch from Phase 3 to Phase 4 corrosion) reduced to 0.5. Figure 5-21 shows the relative humidity as calculated by T2GGM matches the relative humidity calculate externally using nodal output.
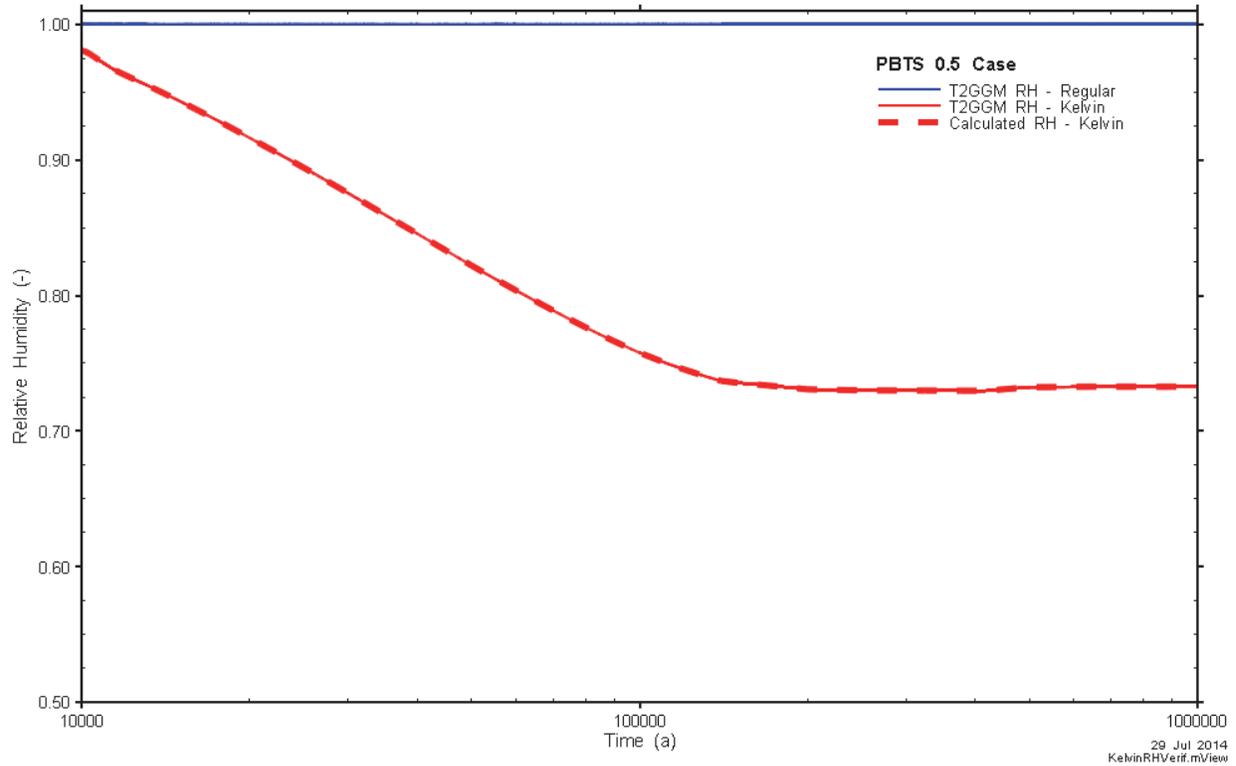
Figure 5-21: Verify Kelvin Equation Calculation

Figure 5-22 and Figure 5-23 show that for this case, using the Kelvin equation has minimal impact on repository saturation and gas generation results. Note that for both RH methods, the inventory is consumed at approximately 400 000 years.
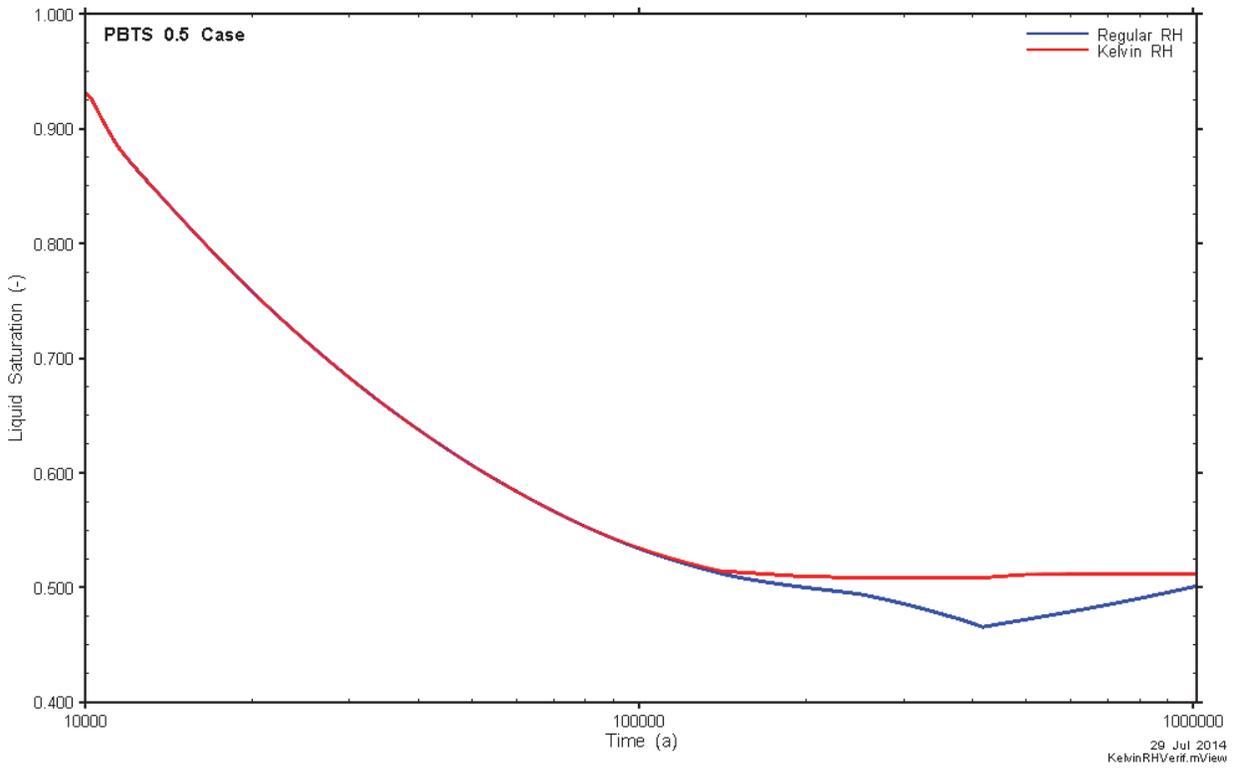
Figure 5-22: Repository Saturation for 5CS Room-Scale Model with 0.5 PBTS and Kelvin Equation for RH
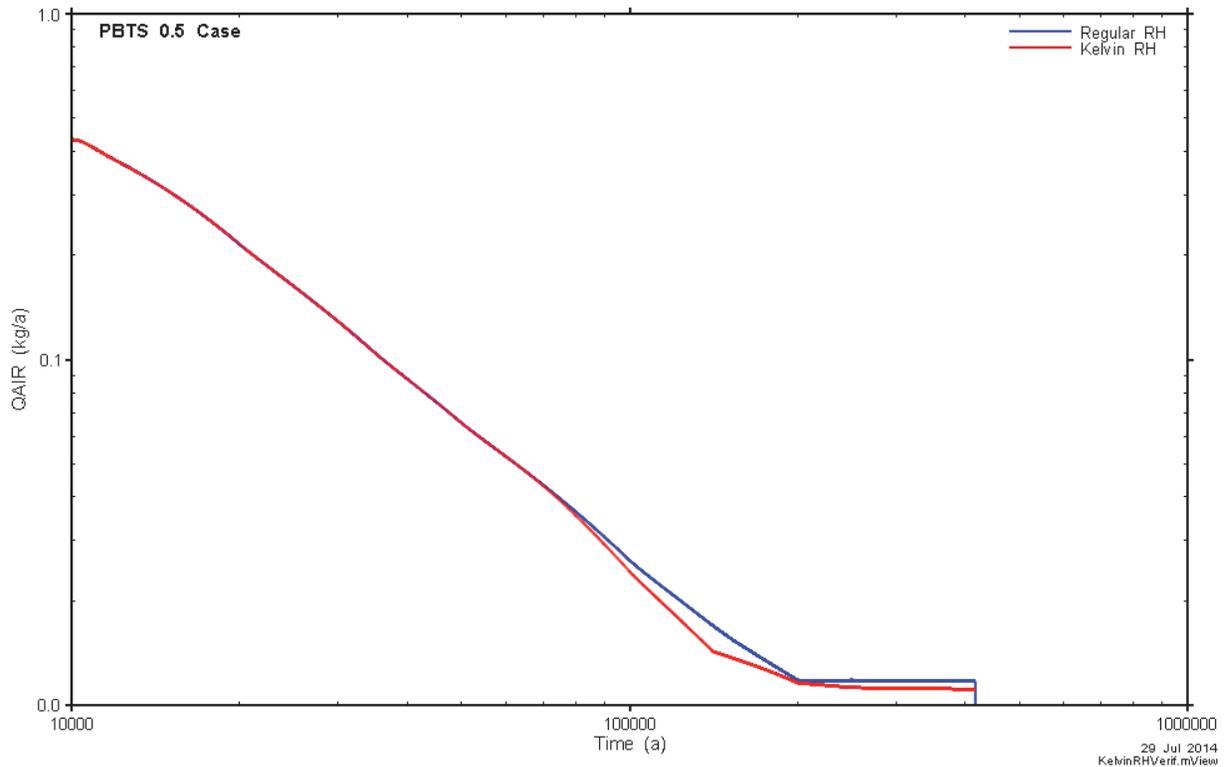
Figure 5-23: Repository Gas Generation Rate for 5CS Room-Scale Model with 0.5 PBTS and Kelvin Equation for RH

5.9.6 Convergence Failure Handling

Convergence failure handling was verified by running the 3DSRS GG1 simulation with the GFRES input block, and four defined strategies. Both the sequential and revert options were tested: the sequential option with the NWL simulation and the revert option with the WL simulation. Output files were inspected to ensure strategies were correctly implemented. Results matched the 3DSRS GG1 simulation without convergence handling, as shown in Figure 5-24. Note that the peak pressures in the WL simulation are very sensitive to the convergence criterion, resulting in the very small differences in peak pressure. Very low initial convergence criterion was required to initiate simulation failure and test the GFRES option, but once the simulation stabilized at a higher convergence criterion (the same criterion as used in the no GFRES case), the simulation reverts to the low convergence criterion until failure occurs once again. The sensitivity to convergence criterion was confirmed by running the simulation with different convergence criterion, and is apparent in the small oscillations in the curve near the peak (not discernible in Figure 5-24).
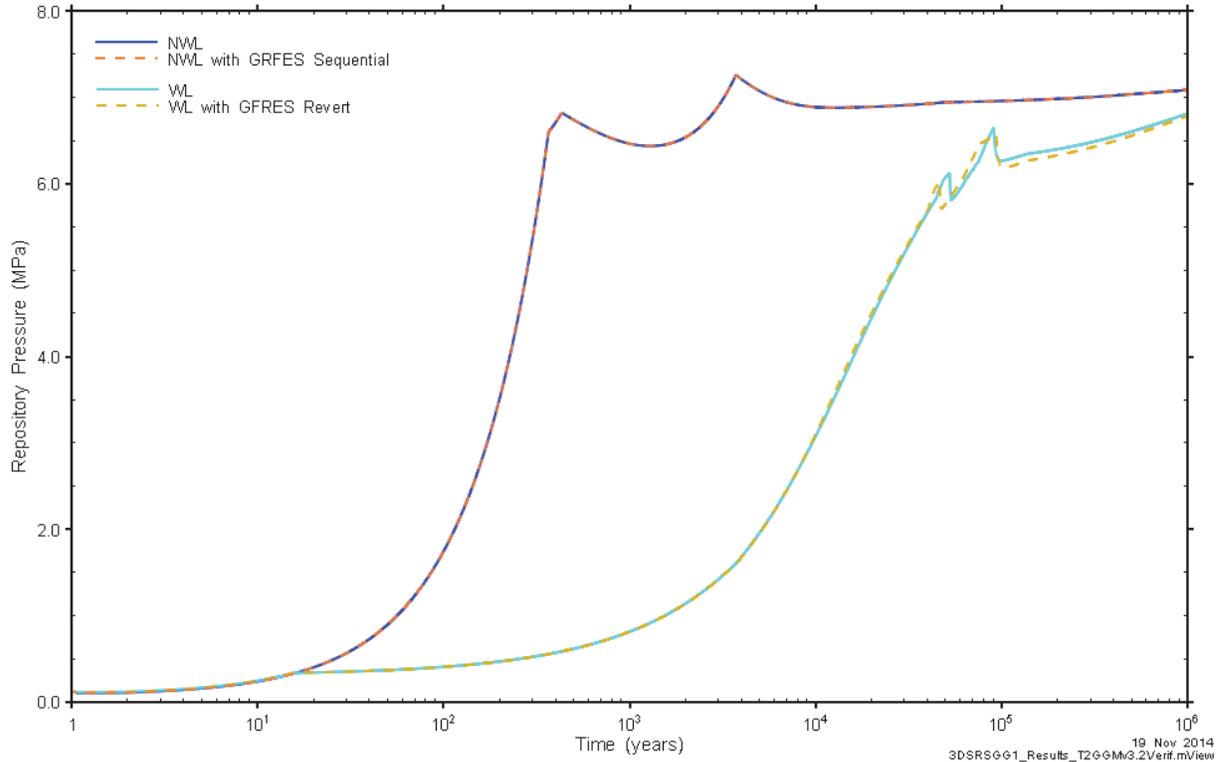
Figure 5-24: Repository Pressure comparison for verification of GFRES implementation.

5.9.7   GPU Matrix Solver

The GPU matrix solver was tested by running the 3DSRS GG1 and the FORGE Module Scale (Calder, 2014) simulations with the GPU solver, and comparing results to the code using standard solvers. The 3DSRS model has 10,089 nodes and the FORGE Module Scale model has 121,847 nodes. Results for the matrix solver matched results from the standard solvers.

Run times are outlined in Table 5-7. All simulations were completed on the same CPU (Intel Xeon 2.83 GHz and 32 GB RAM with a GEFORCE GTX 560 Ti GPU). The BiCGSTAB solver was selected, with no preconditioning by the GPU solvers.

Two issues are identified as possible contributions to the longer run times obtained by the GPU solver for the 3DSRS GG1 simulation: (1) As described in the GPU solver documentation (Paralution, 2014), small problems have improved performance on a CPU due to improved caching. A modern GPU would be expected to further improve run times and minimize overhead. (2) TOUGH2 uses a slightly different BiCGSTAB solver than the Paralution GPU library: the BiCGSTAB(m) algorithm, which according to the TOUGH2 manual, "provides improved convergence behavior when iterations are started close to the solution, i.e., near steady state." (Pruess et al., 1999). This slightly different solver likely contributes to the slower run times for the 3DSRS GG1 model, as many time steps with the GPU solver had approximately two times as many iterations. This was not observed for the FORGE module scale simulations. The slightly different solver implementation complicates the transition from standard to GPU solvers, as a model that solves well under the TOUGH2 solver may be less stable under the GPU solver.

Table 5-7: GPU Matrix Solver Run Times

Model	Solver	Run Time (hours)
3DSRS GG1	GPU solver	34.5
	Standard solvers	16
FORGE Module Scale	GPU solver	50.4
	Standard solver	114.3

5.9.8   FLAC Integration

Two test cases are presented for the T2GGM-FLAC hydromechanical model verification. The first case is the analytical solution for one-dimensional water-saturated consolidation by Terzaghi (1943). This is the same as the first test case for the 1D hydromechanical model described in Section 5.8.1.1 and is used to test the poroelastic T2GGM-FLAC model. The second case is the HG-A experiment model (Walsh et al., 2014) used as a verification test case to ensure that the elasto-plastic damage permeability model is performing correctly and producing reasonable results. For the elasto-plastic model, an analytical solution is not available.

5.9.8.1   1D Consolidation after Terzaghi (1943)

For this full water-saturated case, model results are compared with the analytical solution for one-dimensional consolidation by Terzaghi (1943). In this problem, a layer of water-saturated rock is subjected to an instantaneously applied vertical load at the upper surface. The rock layer has a specified thickness (h), and water is allowed to drain at the surface, where pressure is maintained constant. Hydraulic boundaries on all other sides are set as zero-flow.

A T2GGM-FLAC model of a similar system was developed. As T2GGM applies load as a rate, it was not possible to obtain an instantaneous application of load. Instead, load was applied at such a rate that maximum loading was achieved within 0.1 years, which was short (i.e., nearly instantaneous) when compared to the total runtime of approximately 100 years. A second minor divergence between the numerical model and the analytical model is that TOUGH2 does not assume constant water density and compressibility, but calculates these as a function of temperature and pressure. However, over the pressure range examined here, the impact of this second divergence on results was minor.

Model properties are shown in Table 5-8. For comparison's sake, the mechanical parameters used are equivalent to those used for a similar verification exercise by Nasir et al. (2011), namely Young's modulus (E) of 4×10^7 and Poisson's ratio (ν) of 0.3. The T2GGM model used a porosity of 0.1.

A comparison of analytical and numerical model results is shown in Figure 5-25. For this run the applied load (σ_{zz}) was 3.0 MPa. The time axis is plotted as dimensionless time, defined as $kt/\mu Sh^2$. The agreement between numerical and analytical solutions is good, although the T2GGM model does seem to drain slightly faster at greater depths and times.

Table 5-8: Model Properties for the Terzaghi (1943) Verification Case

Analytical		T2GGM-FLAC	
Property	Value	Property	Value
k (m^2)	2.0 x 10^{-15}	k (m^2)	2.0 x 10^{-15}
S (Pa^{-1})	1.86 x 10^{-8}	C_{bulk} (Pa^{-1})	1.86 x 10^{-8}
α	1.0	B	1.0
h (m)	1000	h (m)	1000

Figure 5-25: Analytical and T2GGM Pressure Time-Series at 100, 200, and 700m Depths.

5.9.8.2 Modelling the HG-A Experiment

The elasto-plastic hydromechanical model is not amenable to an analytical solution, and cannot be tested in the same fashion as the poroelastic hydromechanical model, for which analytical solutions are available for simplified systems. However, this model can be assessed to confirm that functioning of the model conforms to the theory and equations outlined in Section 4.4.2. As the HG-A model includes all available components of the model, including damage dependent permeability, effective stress dependent permeability, and time-dependent fracture healing, this was chosen as an appropriate test case. FLAC3D requires the selection of an elasto-plastic model from the group of FLAC3D plastic models (examples include Drucker-Prager, Mohr-

Coulomb, Ubiquitous-Joint, etc.). The Ubiquitous-Joint Model (UJM) was selected for the purpose of model verification. The UJM model accounts for the elasto-plastic behaviour of the anisotropic (bedded) Opalinus clay by modelling it as a Mohr-Coulomb solid with weak planes at a specific orientation (see Itasca, 2012 for details).

To test the functioning of the model, two nodes within the modelled damage zone were chosen, and all parameters related to the permeability calculation at this location were extracted. The permeability of these nodes was calculated manually and compared to the modelled permeability at the nodes (see Figure 5-26).

This verification exercise also showed that the model is behaving in a physically reasonable manner. There is a general reduction in permeability with time caused by self-healing. At approximately 50 days, pore pressure increased suddenly, while the confining stress (packer pressure) remained relatively stable. In the model, this reduces the effective stress and causes a corresponding permeability increase. When the pore pressure drops at approximately 85 days, the opposite occurs.
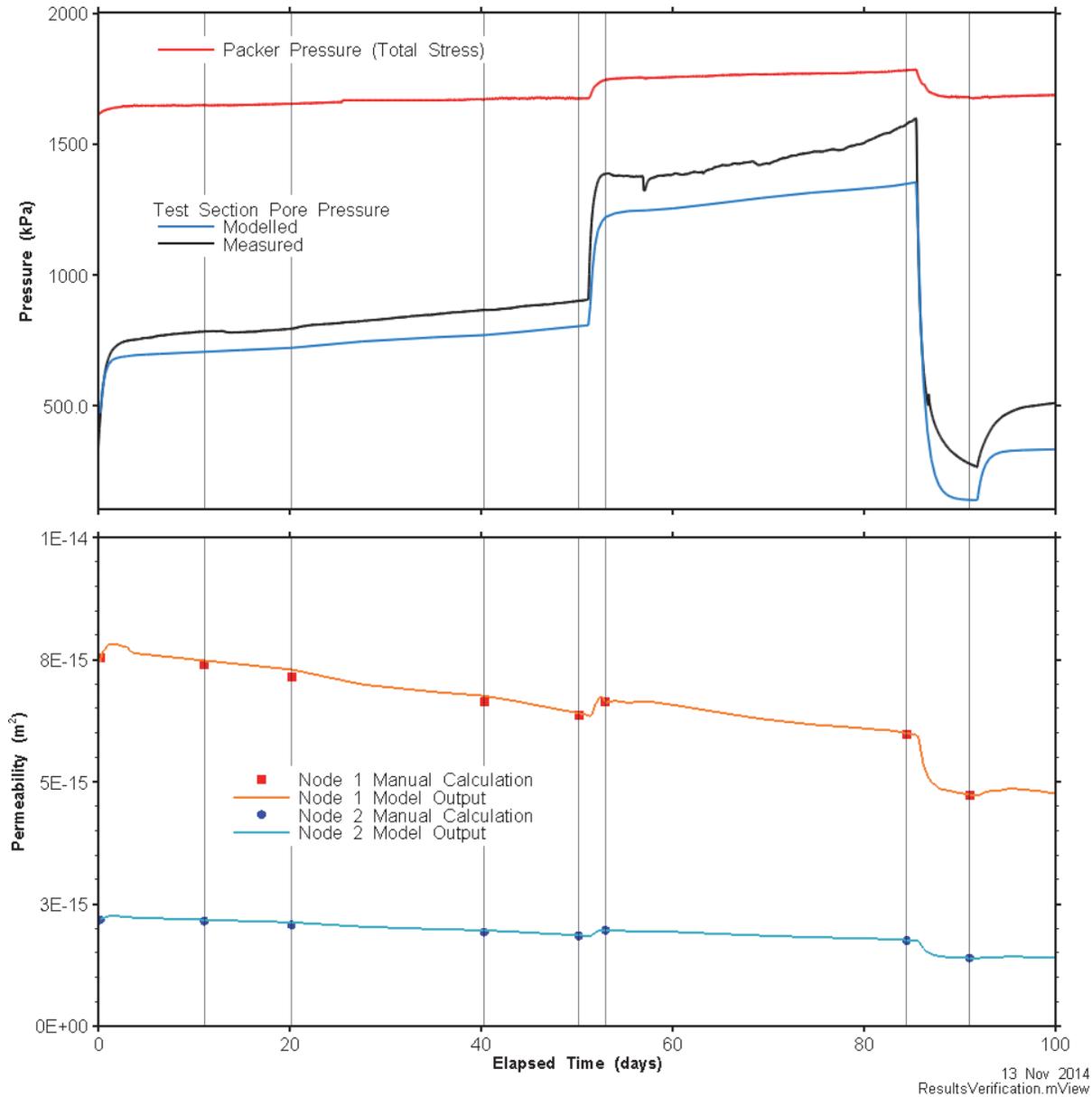
Figure 5-26: Permeability calculation verification.

A second confirmation that the model is producing reasonable results can be found by comparing model results to experimental observations. Figure 5-27 shows the damaged zone predicted by the model, and compares it to laser scans of the tunnel wall following excavation. There is qualitative agreement between the modelled damage distribution and the measurements. In particular, the locations where multiple failure modes overlap correspond well to locations where breakouts in the tunnel wall were observed.
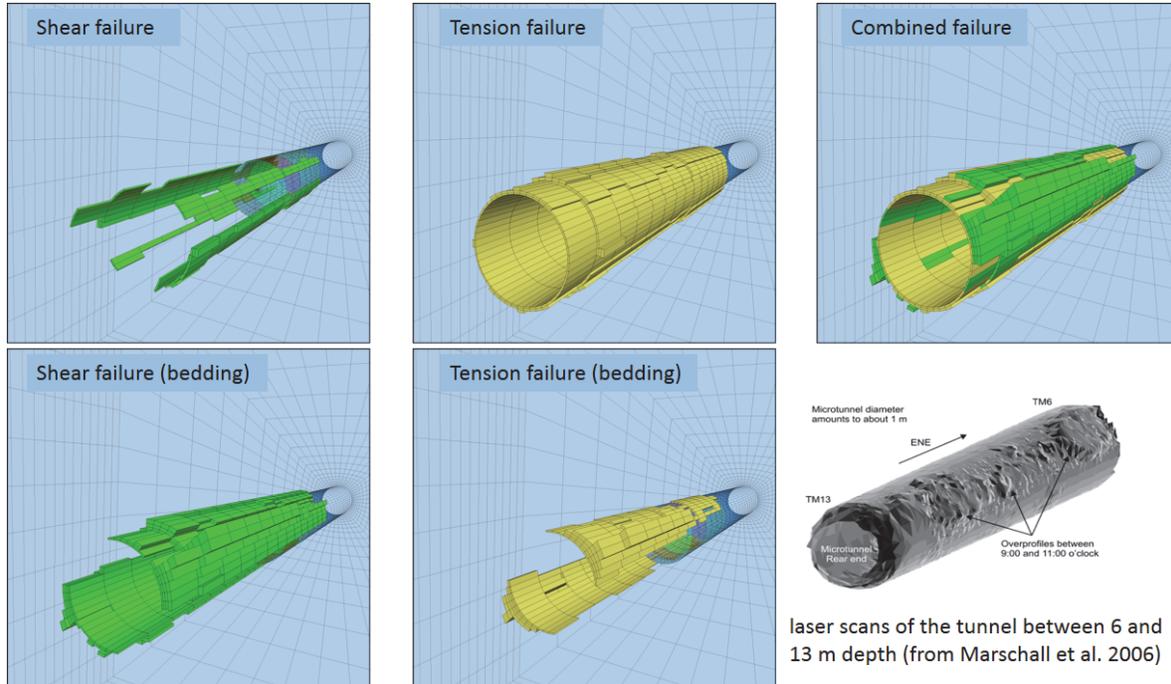
Figure 5-27: Four Failure Modes Delineating the EDZ Extents Compared with a Laser Scan of the Tunnel Wall Following Excavation (Walsh et al., 2014).

5.9.9   Pressure-dependent Permeability and Capillary Pressure (LASGIT)

The correct implementation of the new pressure-dependent permeability and capillary pressure function was verified with a simple 1D test case. The test case implemented the pressure-dependent permeability and capillary pressure function at all nodes, and as the pressure increased as the result of gas injection, the permeability and capillary pressure of the nodes were modified. Inspection of the output file showed the correct modified permeability and capillary pressure deviations from the input permeability and calculated capillary pressure for the given saturation.

5.9.10   Bentonite States

Two cases are presented to verify the implementation of the modelling approach: the 5CS Quarter-Container model and an infiltration test (Cui et al., 2008 and Wang, 2013). Verification of the 5CS Quarter-Container model is used to check that the code performs as designed and is compared to spreadsheet models. The infiltration test is used to compare the model to published experimental results.

5.9.10.1 5CS Quarter-Container Model

The 5CS Quarter-Container model plan-section domain of 4 m × 10 m represents the area of influence of a single container located in the middle of a placement room in the middle of the repository. The vertical domain extends a total of 1480 m, from the top of bedrock to 1000 m below the repository – this was required to match long-term temperature response, which

proved sensitive to boundary conditions. The repository is located at a nominal depth of 500 mBGS.

When verifying new code, test models should start simple, and add complexity to ensure the code works for a range of conditions. For most test cases, the EBS was simplified to a single bentonite material, with the bentonite properties outlined in Table 5-9:

Table 5-9: Bentonite Input Parameters for 5CS Quarter-Container Model

Parameter	Units	Value
bound water saturation(S_{bw})	-	0.1
micro-porosity exponent (a)	-	1.5
expansive mineral fraction (β)	-	1
maximum micro-porosity ($n_{micro,max}$)	-	0.386
initial mega-porosity	-	0.15
initial mega-porosity permeability	m^2	3.30E-12
total porosity (POR)	-	0.486
maximum saturated permeability (PER)	m^2	5.30E-19

The gap volume is assumed to be 4% of the room (0.35 m^3).

Bentonite evolution within T2GGM is verified by evaluating the changes in porosities and permeabilities of the micro, macro, mega and gap components of the bentonite-based EBS for three cases, as follows

- No gas generation.

- No gas generation with EBS consisting of two bentonite-based materials as in the original quarter-container model (HCB pedestal and gap fill).

- No gas generation with dilatant flow.

5.9.10.1.1   No Gas Generation

Figure 5-28 and Figure 5-29 shows the changes in micro, macro, mega, and gap porosities and permeabilities with both saturation and time, respectively. This case is verified by comparing results to spreadsheet calculations, shown in Figure 5-28 as symbols. Note that the spreadsheet calculations are based on a single node, while the T2GGM results are an average of 155 nodes, resulting in small differences between code and spreadsheet at low saturations. Figure 5-29 shows the variation in results at each node, highlighting the range of porosity and

permeability at low saturation contributing to the small differences between the model and spreadsheet calculations shown in Figure 5-28.
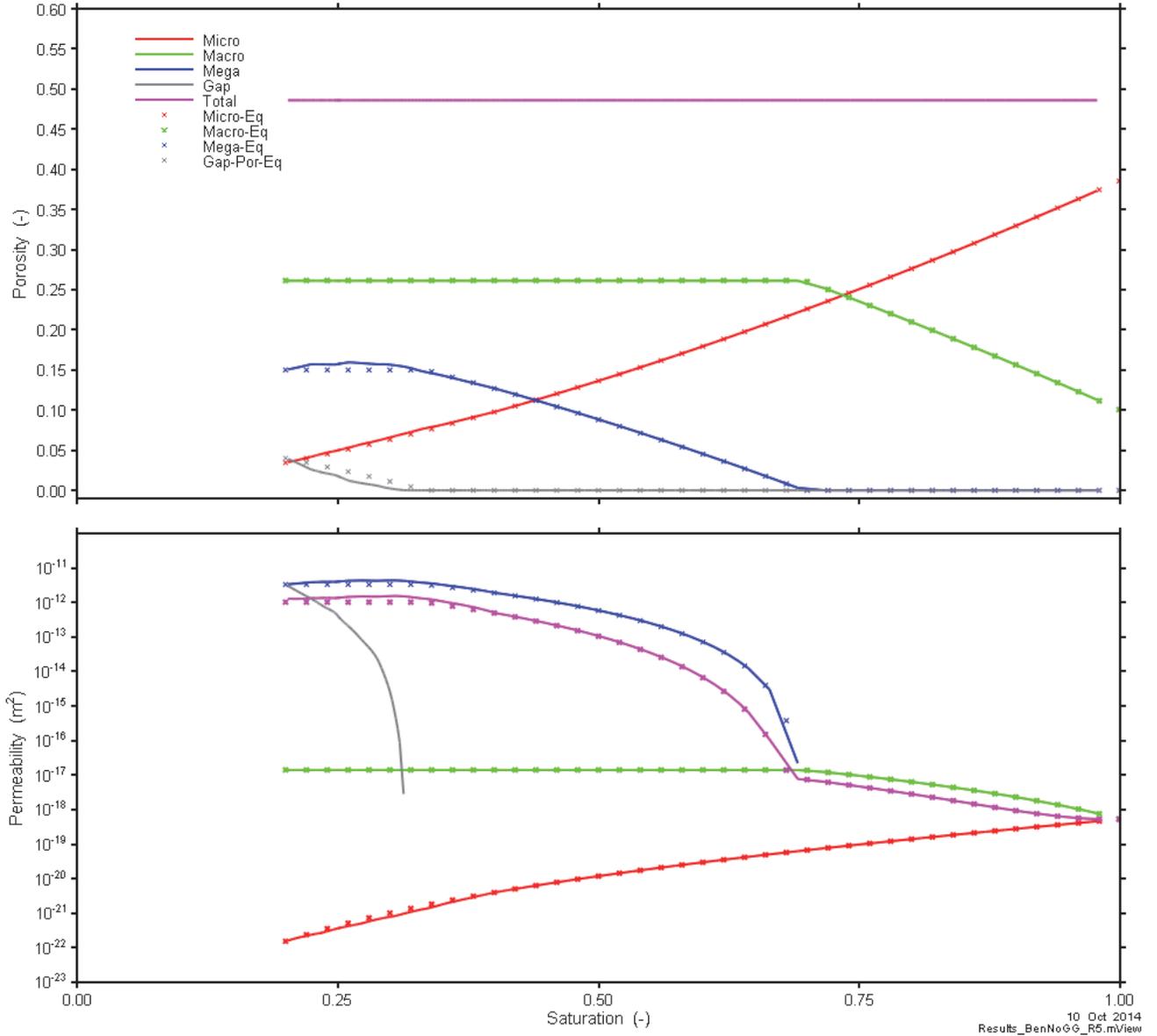
Figure 5-28: Room Average Porosities and Permeablities as a Function of Saturation (lines) Compared with Spreadsheet Results (symbols) for 5CS Quarter-Container Model with No Gas Generation
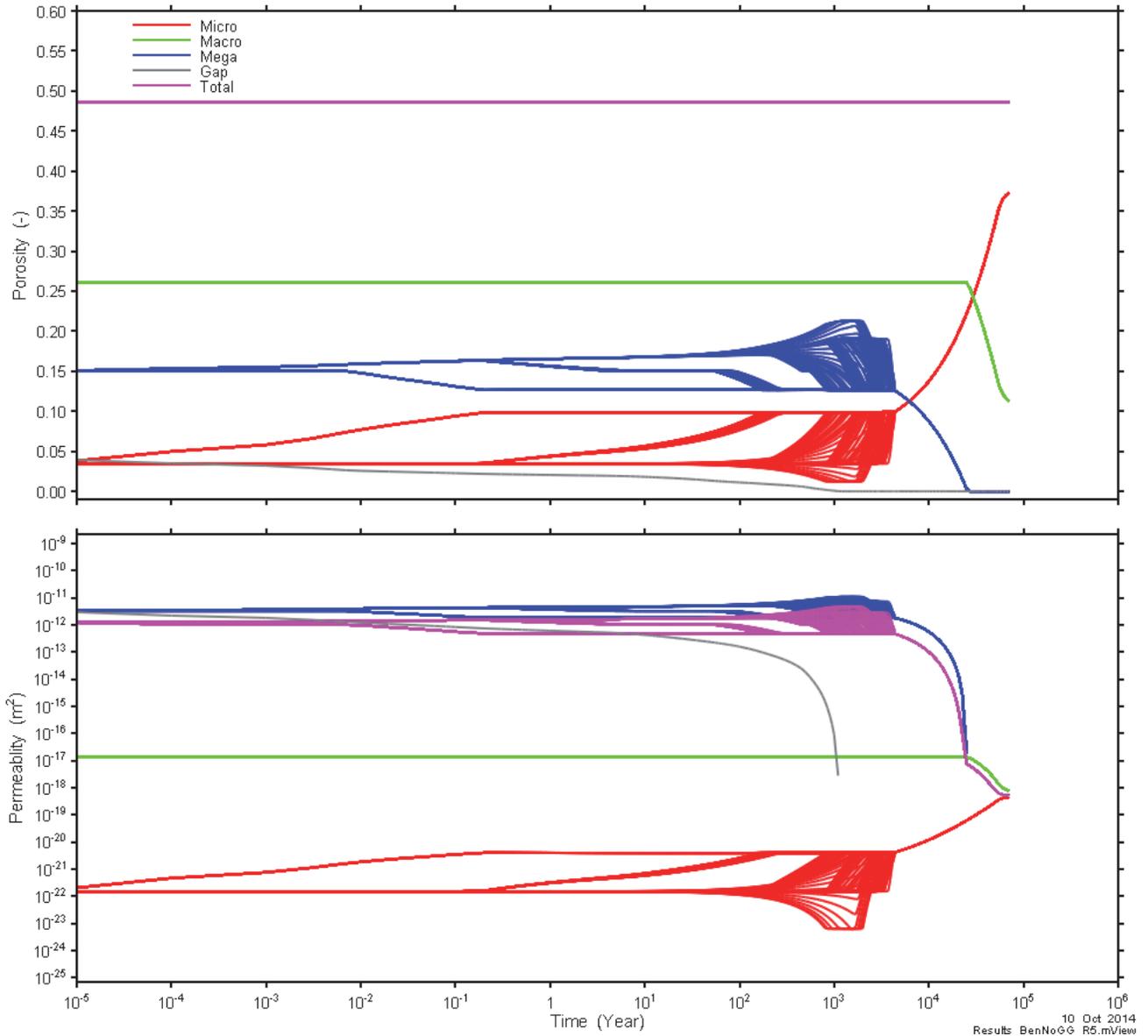
Figure 5-29: Porosities and Permeabilities as a Function of Time for 5CS Quarter-Container Model with No Gas Generation

Figure 5-30 and Figure 5-31 shows the saturation and total permeability at different times, showing the heterogeneity in saturation and permeability at low saturations (1000 years), the homogeneity in saturation and permeability by 10,000 years, and the full liquid saturation and saturated permeability at 70,000 years.
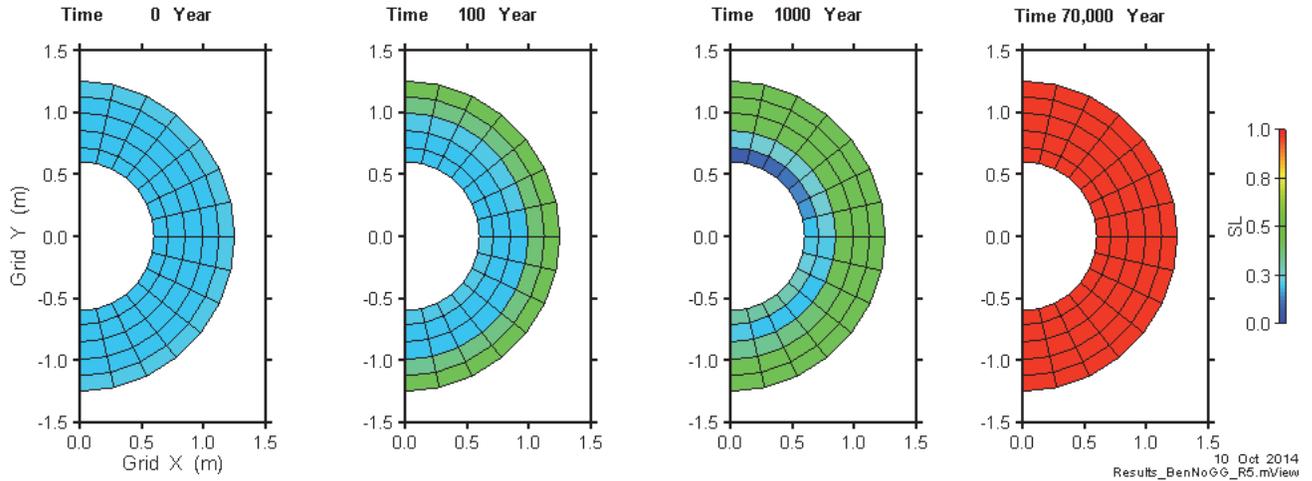
Figure 5-30: EBS Saturation for 5CS Quarter-Container Model with No Gas Generation
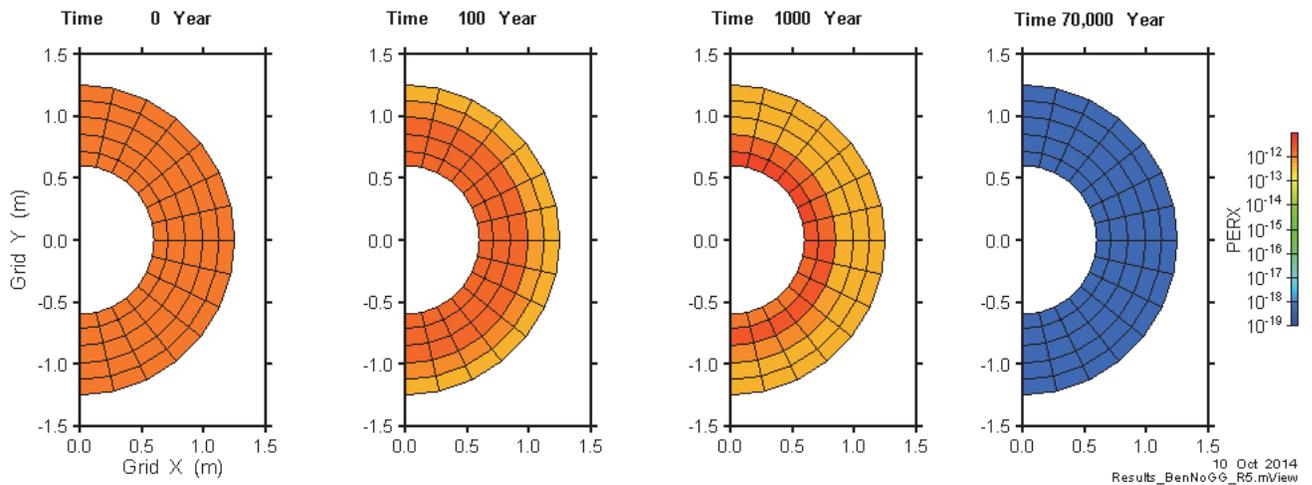
Figure 5-31: EBS Permeability for 5CS Quarter-Container Model with No Gas Generation

5.9.10.1.2   No Gas Generation and Two Bentonite Materials

In this case, the HCB pedestal and gap fill are modelled separately. They have the same properties as the single bentonite material outlined in Table 5-9, except for the mega porosity properties outlined in Table 5-10.

Table 5-10: Bentonite Mega-Porosity Parameters

Parameter	Units	Single Bentonite Material	Gap Fill	HCB Pedestal
initial mega-porosity	-	0.15	0.15	0.01
initial mega-porosity permeability	m^2	3.30E-12	3.30E-11	3.30E-13

The intent of this test case was to ensure that multiple bentonite material types may be considered in a single bentonite evolution zone. Figure 5-32 shows the evolution of porosities and permeabilities with time, and Figure 5-33 and Figure 5-34 shows the saturation and total permeability at different times.
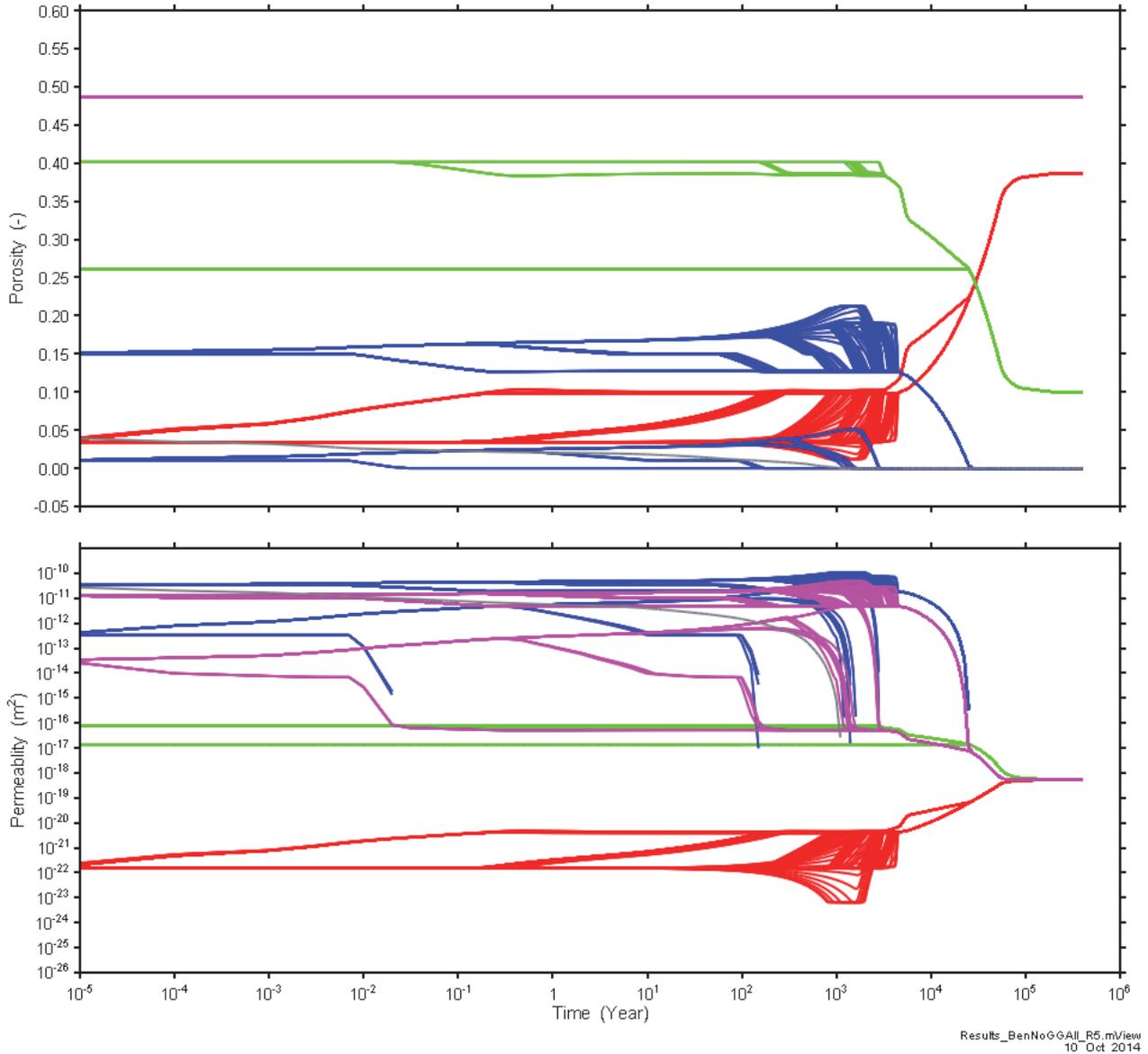
Figure 5-32: Porosities and Permeabilities as a Function of Time for 5CS Quarter-Container Model with No Gas Generation and Two Bentonite Materials
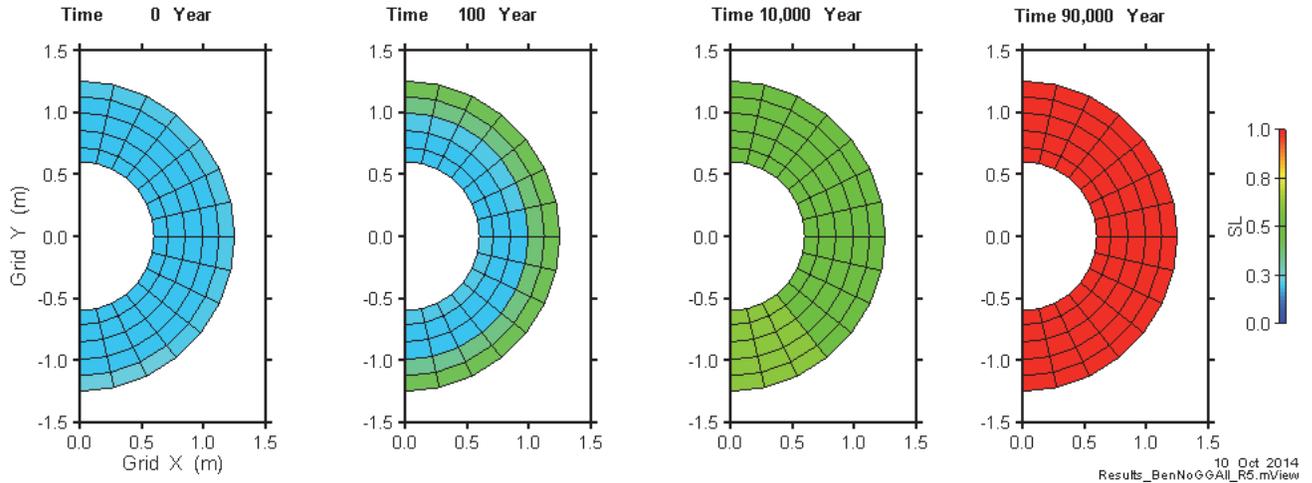
Figure 5-33: EBS Saturation for 5CS Quarter-Container Model with No Gas Generation and Two Bentonite Materials
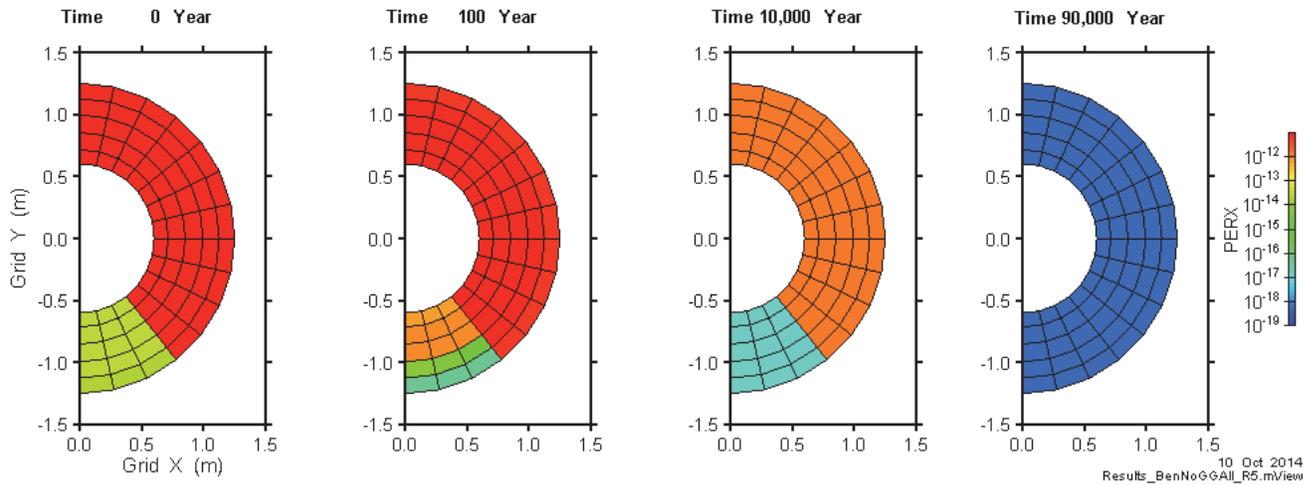
Figure 5-34: EBS Permeability for 5CS Quarter-Container Model with No Gas Generation and Two Bentonite Materials

5.9.10.1.3   With Dilatant Flow

This case is identical to the no gas generation case with bentonite evolution, with the addition of pressure-dependent permeability and capillary pressure to simulate dilatant flow. Two additional parameters are required for bentonite evolution when dilatant flow is considered: the maximum swelling pressure set to 0.6 MPa, and the dilatant flow minimum liquid saturation, set to 80%. Additional input parameters for pressure-dependent permeability and capillary pressure include the scaling factor, set to 1000, and the pressure range over which the permeability is modified, set to 1 MPa. Only a small set of bentonite elements are selected for pressure-dependent permeability, shown in Figure 5-35, to improve simulation of a pathway of high permeability similar to dilatant flow.
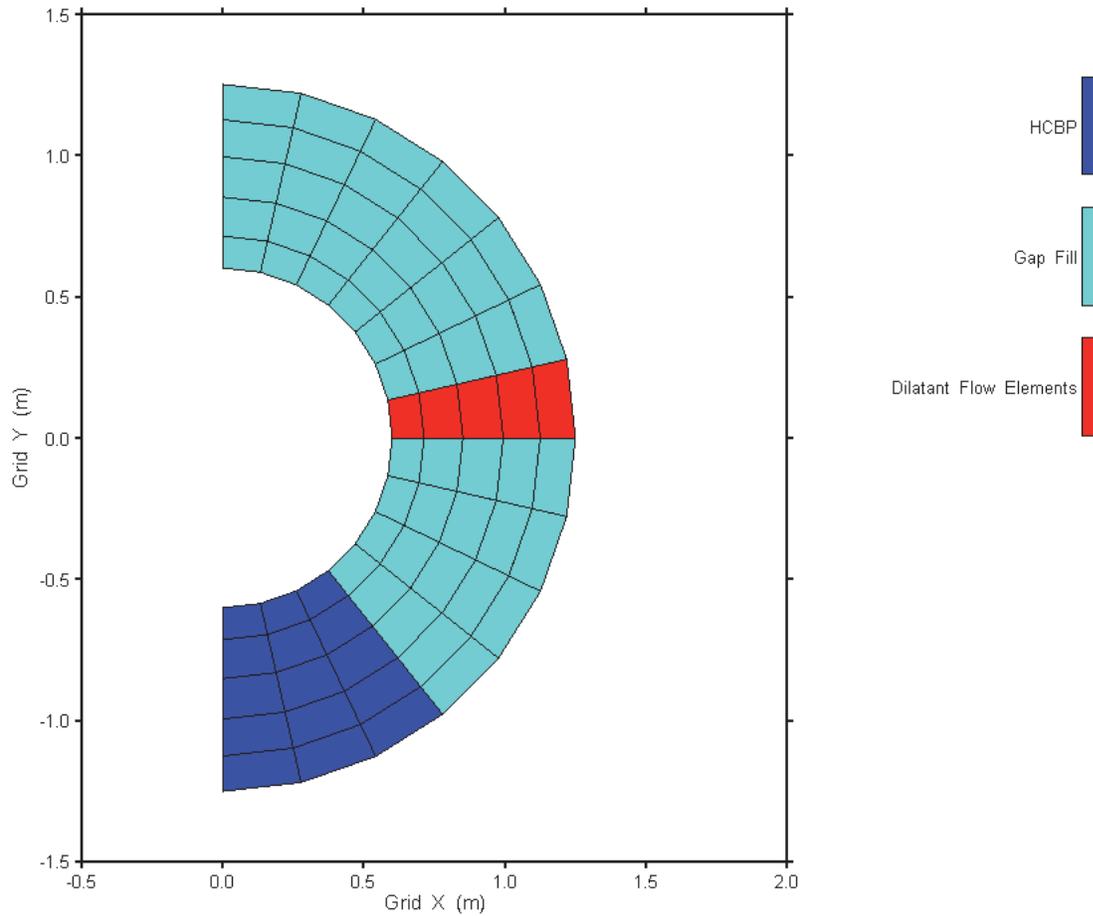
Figure 5-35: EBS Dilatant Flow Elements for 5CS Quarter-Container Model

Once dilatant flow was initiated, simulation times slowed dramatically. However, sufficient time had elapsed to evaluate the code, and consequently, results presented here do not represent complete simulations.

Figure 5-36 shows the evolution of both gas pressure and swelling pressure. The gas pressure exceeds the swelling pressure at 67,440 years, triggering dilatant flow at a liquid saturation greater than 80%, the minimum input value, as shown in Figure 5-37. Note that liquid pressure is negative at the time of dilatant flow, and therefore the threshold for dilatant flow is the swelling pressure.
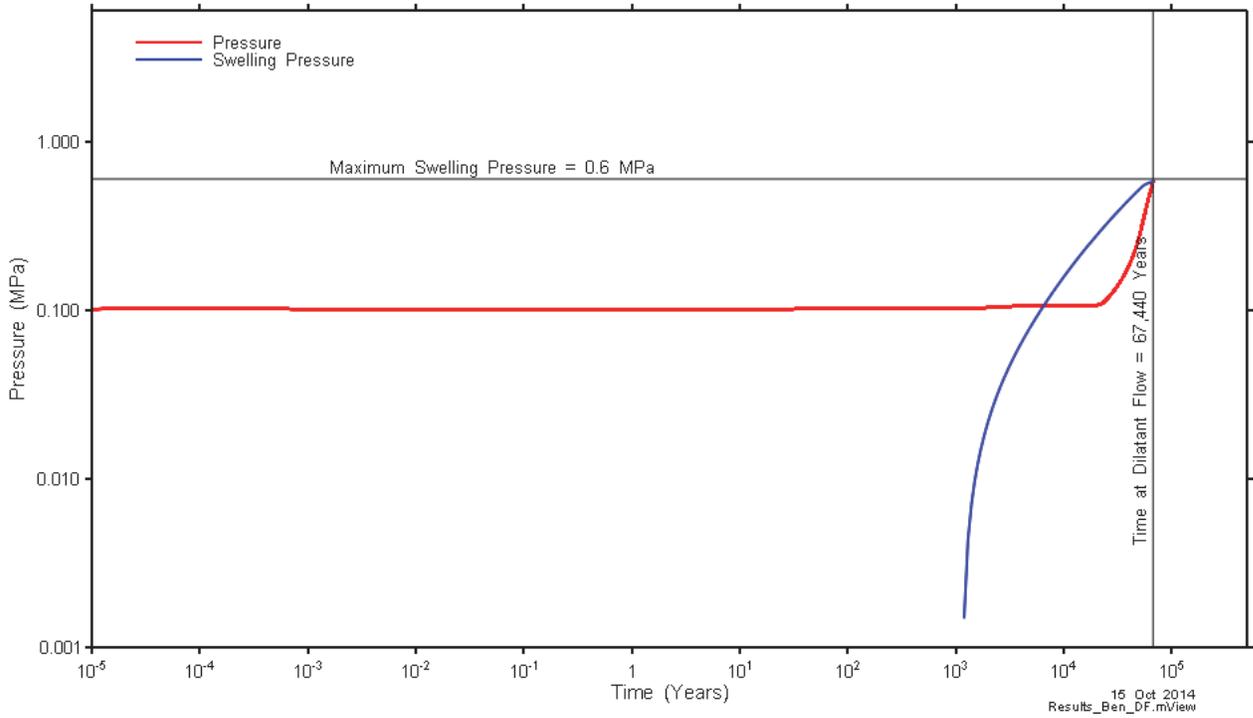
Figure 5-36: EBS Gas Pressure and Swelling Pressure Evolution for 5CS Quarter-Container Model with Bentonite Evolution and Dilatant Flow
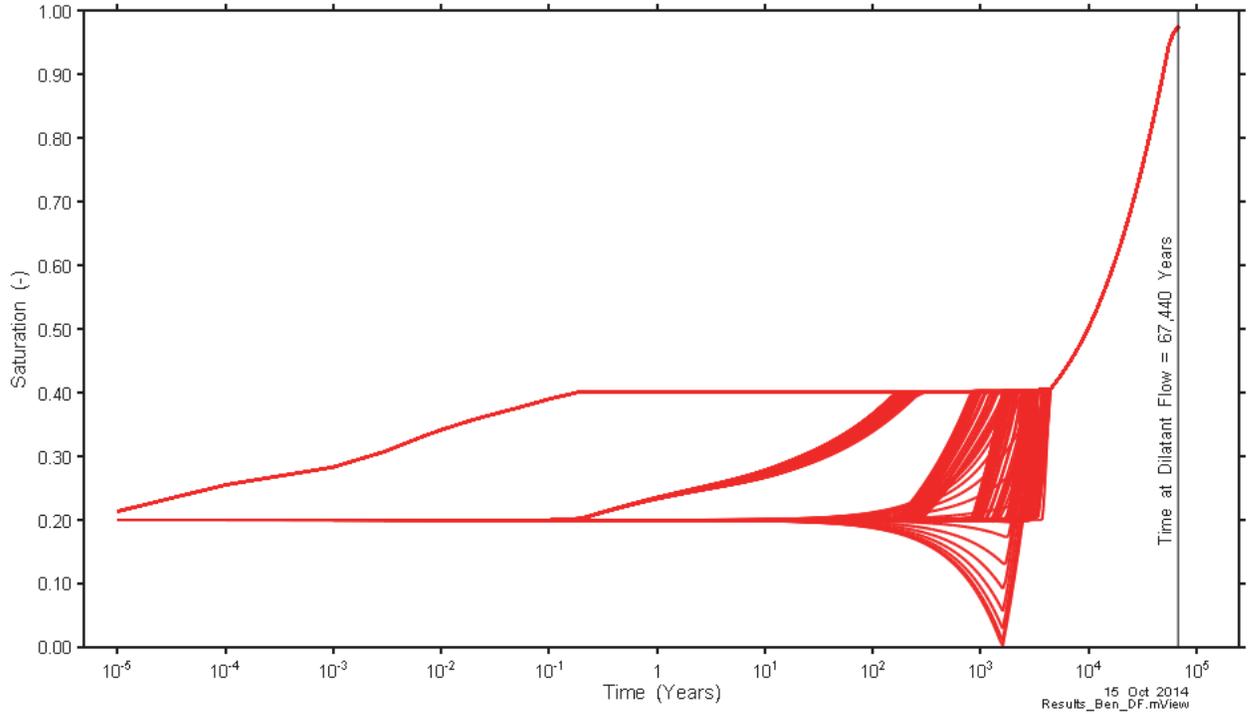
Figure 5-37: EBS Saturation Evolution for 5CS Quarter-Container Model with Bentonite Evolution and Dilatant Flow

Figure 5-38 and Figure 5-39 show the evolution of saturation and permeabilities at different times before dilatant flow.
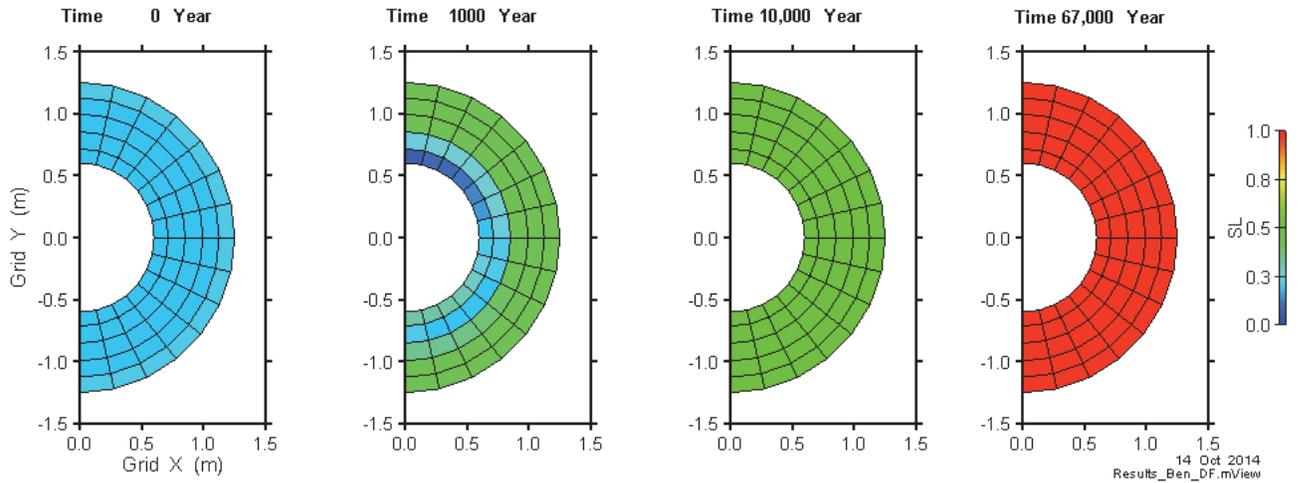
Figure 5-38: EBS Saturation for 5CS Quarter-Container Model with Bentonite Evolution and Dilatant Flow and with No Gas Generation
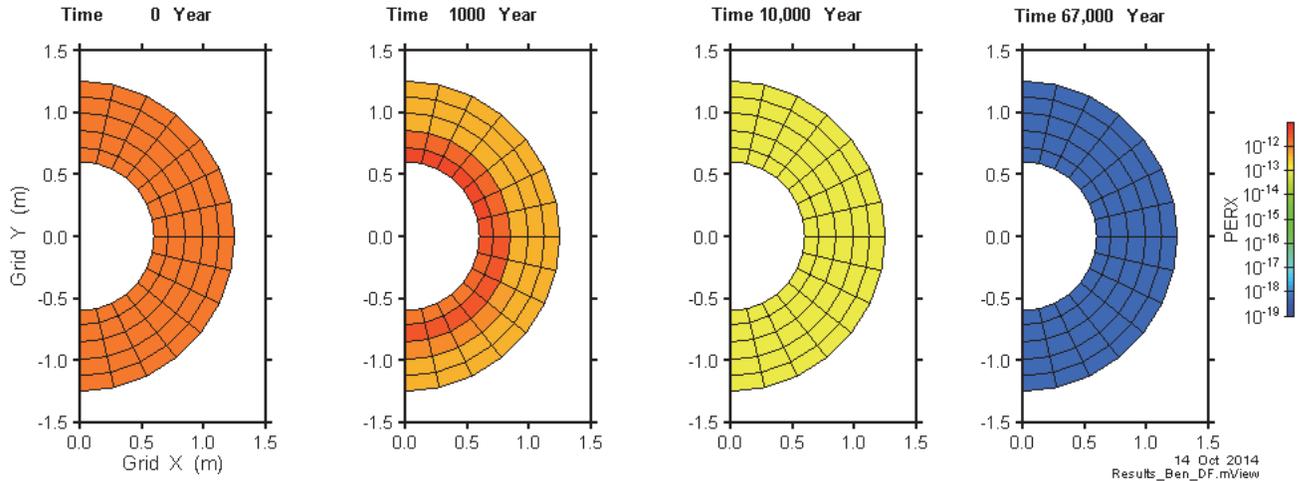
Figure 5-39: EBS Permeability for 5CS Quarter-Container Model with Bentonite Evolution and Dilatant Flow and with No Gas Generation

Once dilatant flow is initiated, the permeability of the dilatant flow elements are increased gradually as expected, see Figure 5-40. The final permeability is approximately 6.0E-19 m², which is the expected permeability given the gas pressure is only 0.001 MPa greater than the swelling pressure threshold. If gas pressures increases to values greater than 1 MPa above the dilatant flow threshold, the full scaling factor of 1000 is applied to the permeability. The gradual increase in permeability is by design, to prevent sudden large changes in permeability resulting in numeric instability.
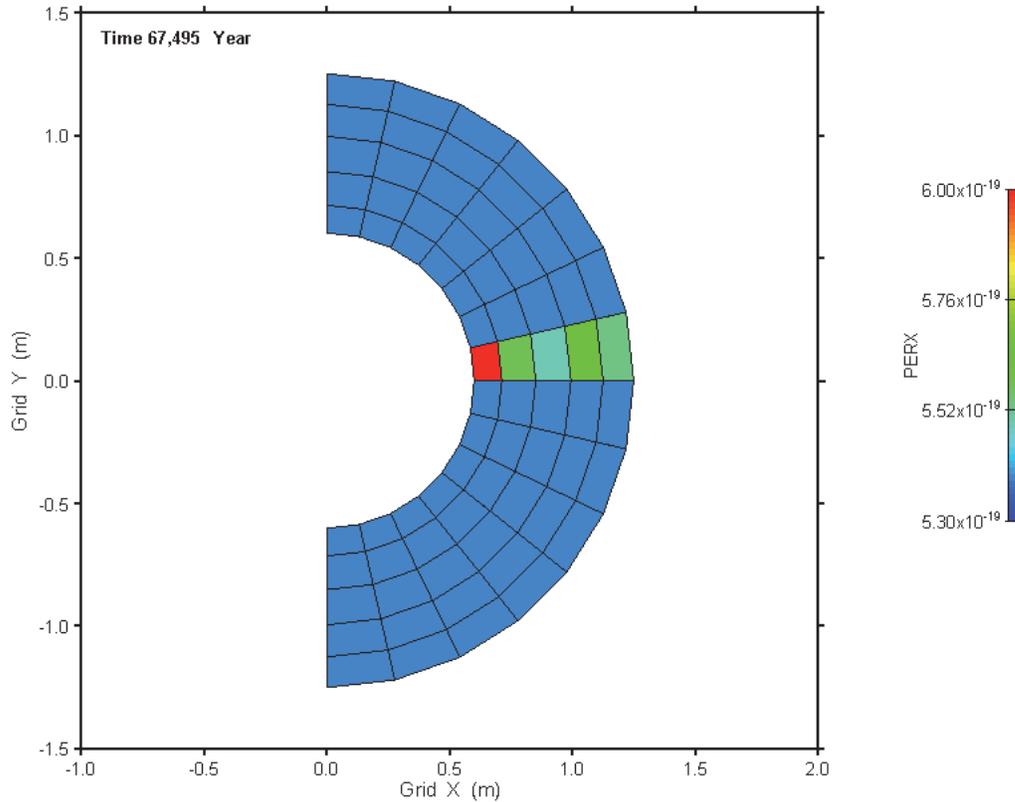
Figure 5-40: EBS Permeabilities at 67495 Years, after dilatant flow has been initiated, for the 5CS Quarter-Container Model with Bentonite Evolution and Dilatant Flow

5.9.10.2 Infiltration Test

The test case is an infiltration laboratory test performed on compacted sand/bentonite mixture specimens, published in two papers (Cui et al, 2008; Wang, 2013). The main output of the experimental test that can be predicted by the bentonite state T2GGM model is the time history of the suction pressure (or capillary pressure), calculated by relative humidity measurements.

The infiltration test was performed on a bentonite-sand specimen, 50mm in diameter and 250mm in height as shown in Figure 5-41. During the test, water was allowed to infiltrate from the bottom of the sample, while the top of the sample was kept open to the atmosphere. As water infiltrated upwards, the relative humidity (RH) of the sample was measured at four different locations along the length of the sample (RH1 to RH4 as shown in Figure 5-41). Resulting RH data are shown in Figure 5-42. Table 5-11 provides the properties of the sand bentonite mixture.

Table 5-11: Properties of the sand/bentonite mixture

Parameter	Units	Value
Initial water content	%	7.7
Initial relative humidity	%	70
Montmorillonite content in bentonite	%	48
Sand\bentonite ratio	-	30/70
Dry density (ρ_d)	Mg/m^3	2.0
Total porosity (POR) (Calculated)	-	0.267
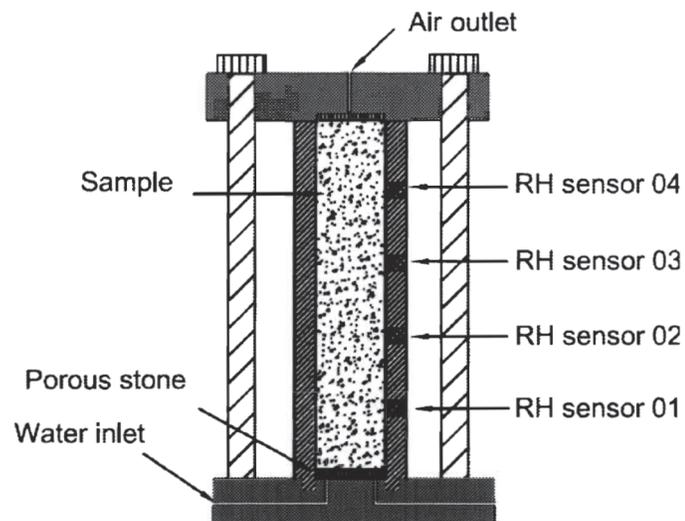
Figure 5-41: Illustration of the Infiltration Test (Cui et al, 2008)
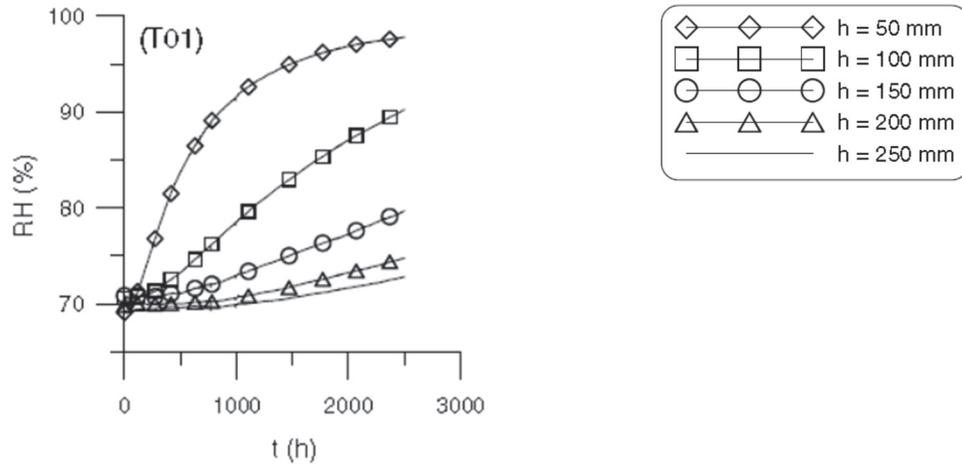
Figure 5-42: Infiltration Test Relative Humidity Results at Different Locations for Test Set T01 (Cui et al, 2008)

The infiltration test is simulated with a 3D model for three cases. The first case includes bentonite evolution using the input parameters shown in Table 5-12. Second and third cases are without bentonite evolution, using two different constant permeabilities. Model results are compared to capillary pressures calculated from the relative humidity results presented in Figure 5-42.

Table 5-12: Bentonite Input Parameters for the Infiltration Test Model

Parameter	Units	Value
bound water saturation(S_{bw})	-	0.1
micro-porosity exponent (a)	-	1.5
expansive mineral fraction (β)	-	1
maximum micro-porosity ($n_{micro,max}$)	-	0.234
initial mega-porosity	-	0.001
initial mega-porosity permeability	m^2	3.30E-16
total porosity (POR)	-	0.267
maximum saturated permeability (PER)	m^2	2.00E-20

Figure 5-43 shows capillary pressure evolution due to infiltration at four locations for the case including bentonite evolution. The results were fitted to the measured data by modifying the following bentonite and capillary pressure input parameters:

- Maximum micro-porosity ($n_{micro,max}$) (0.234);

- Initial mega-porosity (0.001);

- Initial mega-porosity permeability (3.3E-16 m²);

- S_{lrk} – residual liquid saturation for relative permeability functions (1.000E-03);

- $1/\alpha$ – analogous to gas entry pressure (0.715E+07 Pa);

- van Genuchten n parameter– analogous to pore size distribution index (2.35); and

- van Genuchten m parameter (2.900E-01).

The cases without bentonite evolution used the same set of parameters as the fitted case including bentonite evolution.
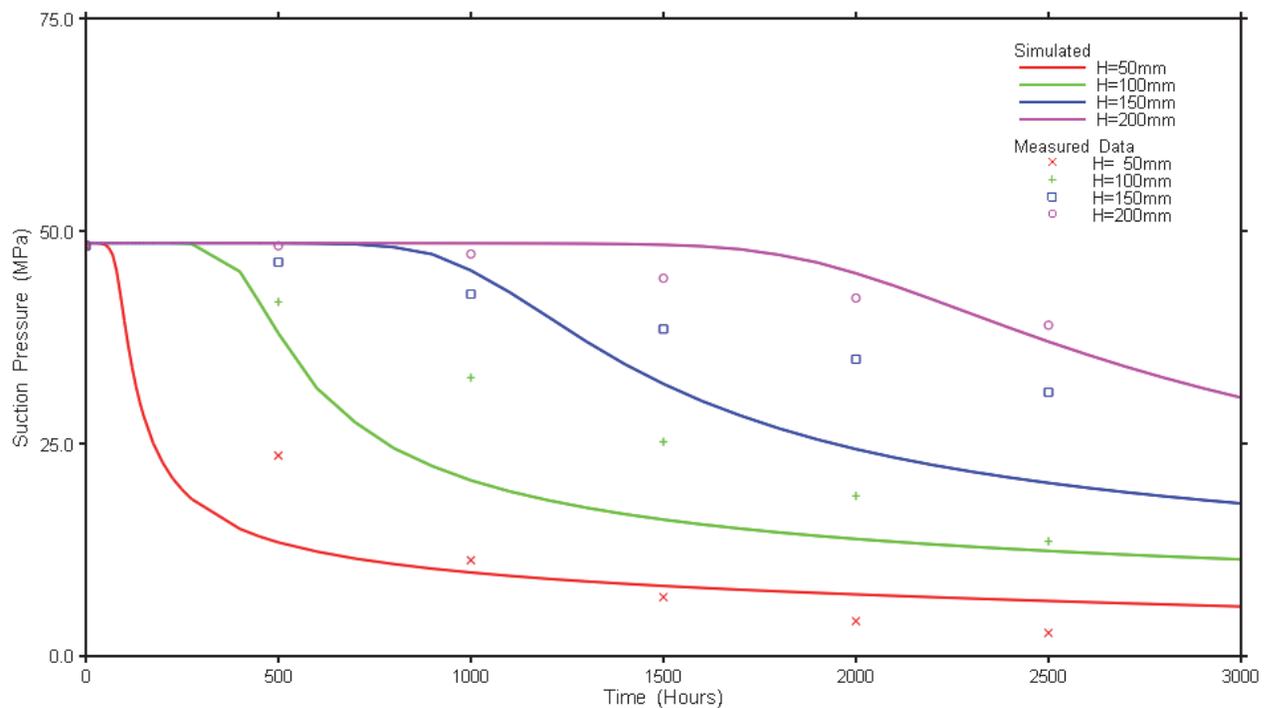
Figure 5-43: Capillary Pressures for Infiltration Test Model with Bentonite Evolution Compared to Experimental Capillary Pressures at Different Locations

Figure 5-44 shows the capillary pressure evolution due to infiltration for the model without bentonite evolution, which had a constant bentonite permeability of 2.0E-20 m², equal to the saturated permeability for the model with bentonite evolution. The results demonstrate that a constant permeability cannot simulate the range of pressures observed across the sample in the infiltration test. Using a higher permeability of 2.0E-19 m², as shown in Figure 5-45, is equally incapable of simulating the infiltration test.
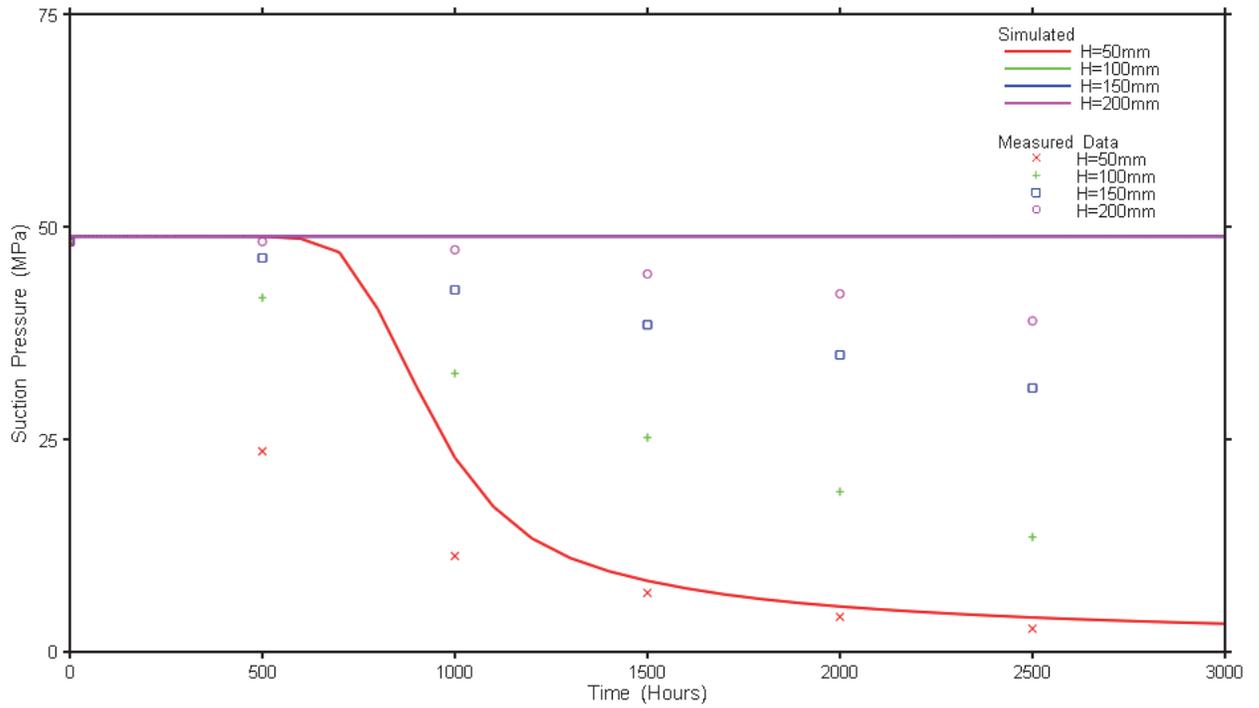
Figure 5-44: Capillary Pressures for Infiltration Test Model without Bentonite Evolution (Using a Constant Permeability of 2.0E-20 m^2) Compared to Experimental Capillary Pressures at Different Locations
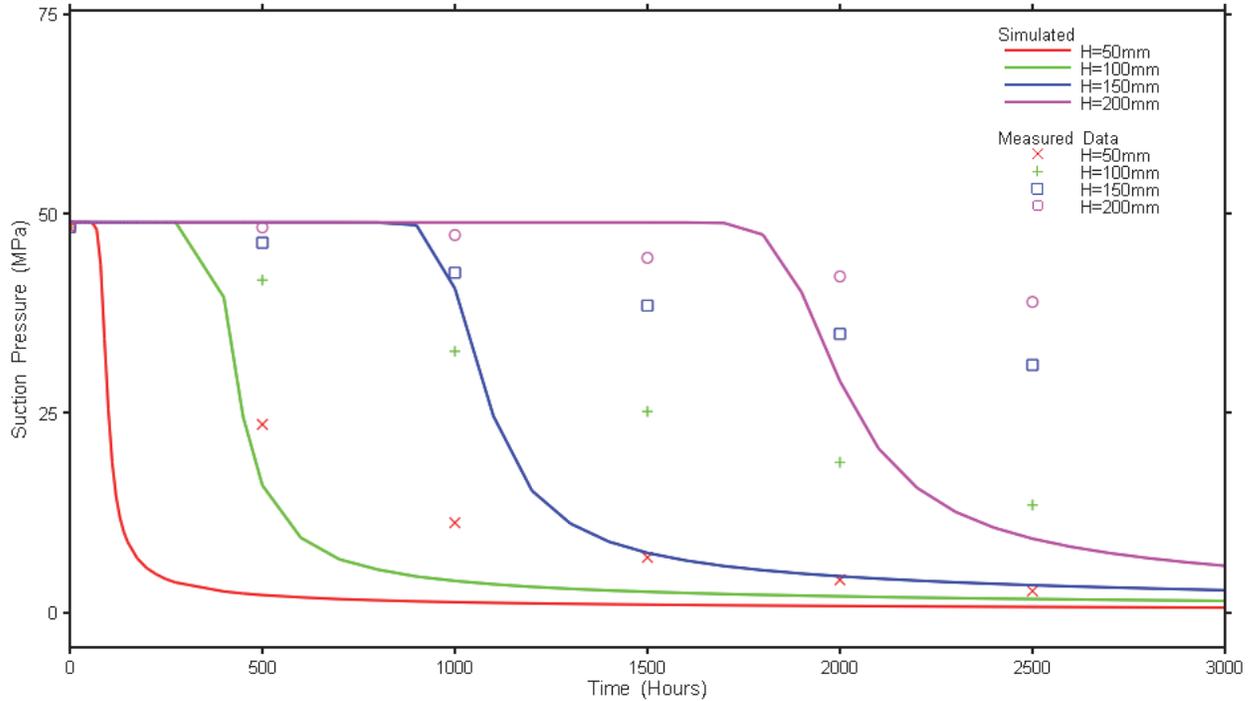
Figure 5-45: Capillary Pressures for Infiltration Test Model without Bentonite Evolution (Using a Constant Permeability of 2.0E-19 m^2) Compared to Experimental Capillary Pressures at Different Locations

5.9.11 Extension of 1D Hydromechanical Model to Allow Spatially-Variable Loading

In order to simulate the advance and retreat of a glaciations event, the applied loading rate is varied spatially. Hydromechanical effects are still one-dimensional, and the loading rate at any one point on the surface is applied to the full column of rock below that point.

To test spatially-variable loading, the single phase Lemieux test described in Section 5.8.1.2 was repeated. The one-dimensional model was expanded to a two-dimensional model with 5 horizontal nodes. The model was run with three different loading configurations:

(1) v3.1 approach – a single loading rate was applied at all nodes in the model, which is equivalent to the approach that was verified for Version 3.1;

(2) v3.2 spatially-constant approach – the same loading rate was applied at each node column using the spatially-variable method developed for Version 3.2; and

(3) v3.2 spatially-variable approach – different loading rates were applied at each node column. The loading rate at each of the five horizontal node columns were 0.9, 0.95, 1.0, 1.05 and 1.1 times the loading rate applied at a single column in the v3.2 spatially-constant model, and the sum of these different loading rates is equal to the total loading rate applied to both the v3.2 spatially-constant and v3.1 models.

Figure 5-46 presents the results, and as expected, results for the Version 3.1 and 3.2 approaches match exactly, and compare well to analytical results.
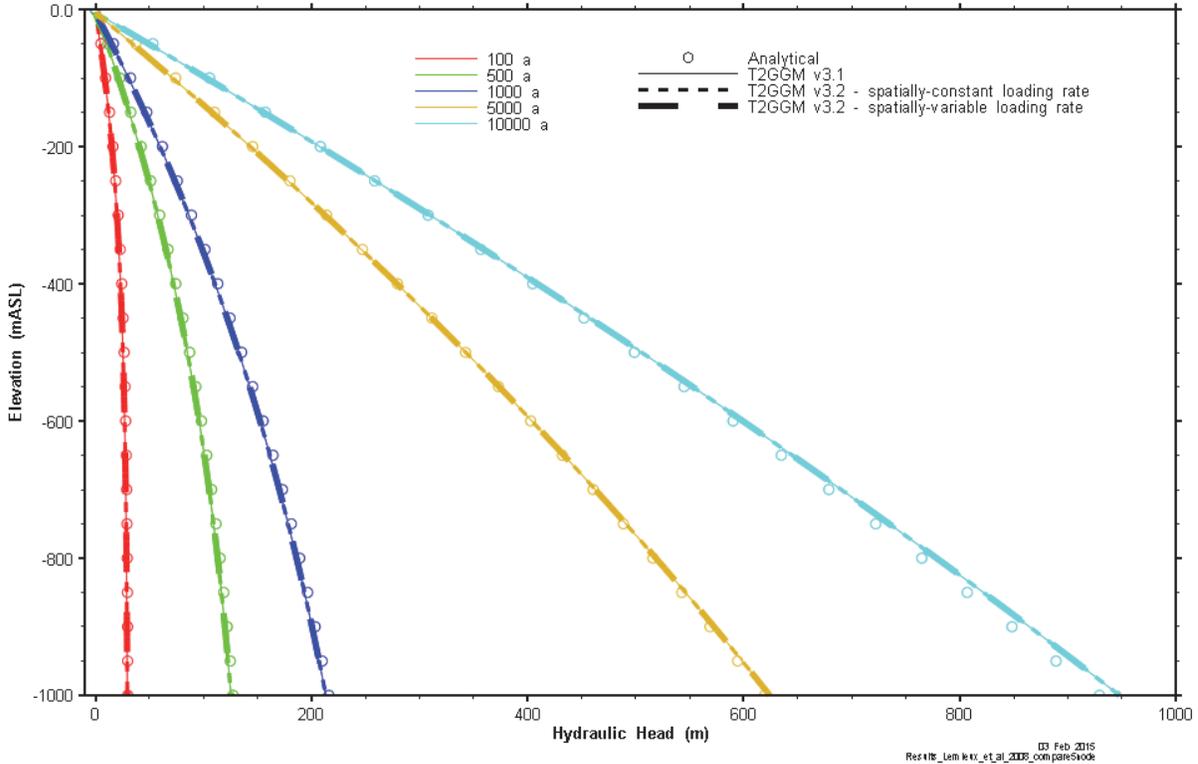
Figure 5-46: Analytical and T2GGM Calculated Hydraulic Head versus Depth at Different Times: Verfication of Extension to 1D Hydromechanical Model

5.9.12 High Water Saturation Check

A case with high water saturation is conducted to test the interface of GGM and T2. The test case is based on the 3DSRS GG1 model, as used for the previous functionality tests in Section 5.9.1, with permeability increased by three orders of magnitude and initial quantities of organic and metallic materials (inventory) decreased by one order of magnitude. These changes to permeability and inventory are required to obtain a high water saturation case. Water saturation for the test case is presented in Figure 5-47. Simulation results are only shown up to 800 000 years, as the repository becomes fully saturated with water at that time. The GGM model is no longer applicable when the repository attains a liquid saturation of one.

A mass balance around the repository is illustrated in Figure 5-48. This mass balance considers the amount of methane, the predominant gas in the 3DSRS test case, within and leaving the repository, as calculated by GGM and T2. The total amount within and leaving the repository equals the amount of methane generated by GGM and the initial amount of methane in the repository.

There is good correspondence between the GGM and T2 models. The amount within the repository in the gas phase is exactly the same, as would be expected since GGM calculates the amount of gas within the repository from T2 inputs. The amount of dissolved methane within the repository in T2 begins to decrease by approximately 250 000 years, as compared to GGM, attributed to differences in discretization. GGM considers the repository as a single block, and the equilibrium assumption of Henry's law is applied to the total volume of water in the repository. The T2 repository is divided into 360 nodes, all except two of which are fully

saturated with water by 800 000 years. The equilibrium assumption of Henry's law is applied on a block by block basis, and consequently, the amount of liquid calculated as being in equilibrium with gas is much smaller by the end of the simulation (2 nodes instead of 360 nodes).

The amount of methane gas leaving the repository also differs between the two models, attributed to the different ways in which this amount is calculated for each model.

- For GGM, the amount leaving the repository in gas phase is calculated by summing the amount for each gas component that has left the volume estimated by the change in pressure provided by T2 (an output from GGM).
- For T2, the amount leaving the repository is inferred from the total T2 mass balance. The amount of methane, in gas and liquid phase, outside of the repository is summed, removing any initial gas found outside the repository and adding the amount of advective flow out the top of the model. The amount of methane diffusing out the top of the model has not been included. The diffusive amount likely accounts for the small differences in total mass balance after 600 000 years.

Despite these differences in the calculated amounts of methane within and leaving the repository, there is good correspondence in the mass balance around the repository for GGM and T2. GGM mass within and leaving the repository is 99.4% of the mass generated plus initial mass, whereas T2 mass within and leaving the repository is 96.5%. The difference between GGM and T2 mass within and leaving the repository starts to emerge between 600 000 and 800 000 years, which is the time that T2 dissolved mass starts leaving the top of the model, the diffusive part of which has not been included in Figure 5-48.
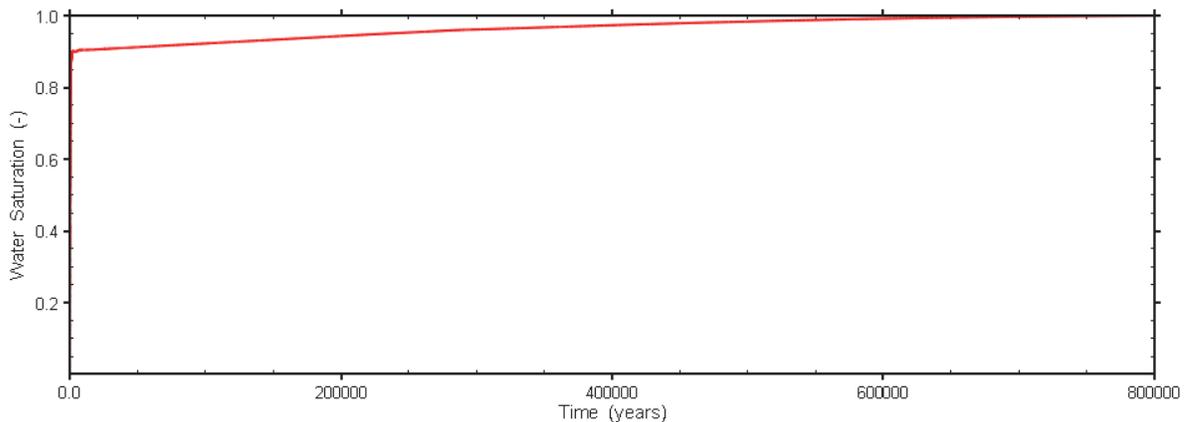
Figure 5-47: Water Saturation of the Test Case
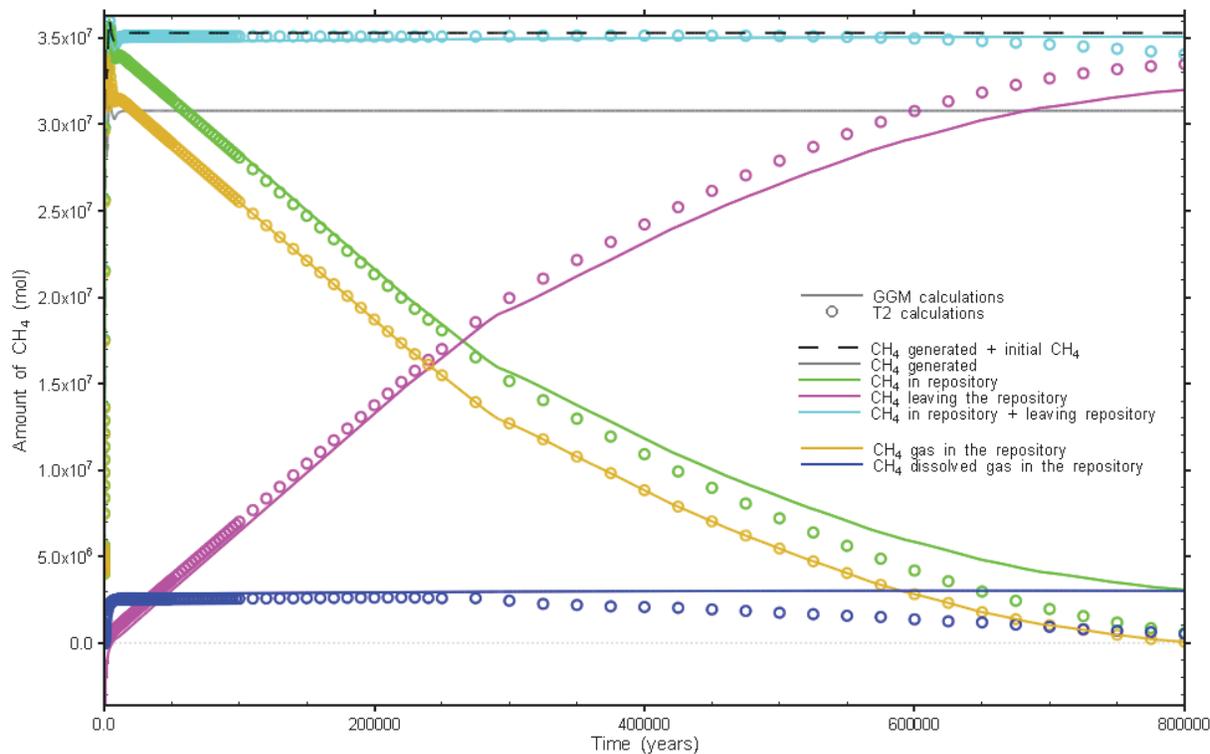
Figure 5-48: Mass Balance of T2GGM interface check

5.10 ANALYSIS SUMMARY

GGM Version 3.2 has been demonstrated to be able to solve the equations described in the Theory Manual (Section 3) accurately. It has been shown that GGM is suitable for use as a module that can be interfaced with the TOUGH2 gas transport code, the combined code being T2GGM Version 3.2. The standalone GGM typically takes several minutes to run and the integrated T2GGM code takes between several hours or several days to run depending on the case.

6.   VALIDATION

Validation, as defined in the NWMO Software Procedures (NWMO 2010) involves determining the accuracy of the software results with respect to its intended application. The results of T2GGM are intended to calculate:

- The magnitude and timing of the peak gas pressure;
- The evolution of the repository saturation;
- The rates of gas and water generation within the repository; and
- The flux of gas and water through the geosphere.

Validation of T2GGM has been undertaken as a process of continuously testing the code and increasing confidence in the results. The approach taken to validation combines expert review, comparisons with independent calculations, and comparisons against experiments.

The main validations to date are below.

- The TOUGH2 gas transport model is a widely used model for two-phase flow and gas transport in geological media, including for deep geologic repositories (e.g., Talandier et al 2006, Nagra 2008, FORGE 2010, Bate et al. 2012, Calder and Avis 2015).
- T2GGM has been used by NWMO in international projects:
  - Swiss HG-A gas permeation experiment at Mont Terri (Walsh et al. 2014, Alcolea et al. 2015);
  - Swedish LASGIT gas experiment at Aspo; and
  - European code comparison on gas transport in repositories (Calder 2014).
- T2GGM has been compared with FRAC3DVS for saturated system, obtaining consistent results (Section 7.3.3, QUINTESSA et al 2011).
- The GGM gas generation model is consistent with general literature and with approaches adopted in other waste management organizations for similar models. All results have undergone internal review by the experts responsible for developing GGM Theory. Results for T2GGM Version 1.2 also underwent external peer review.
- T2GGM Version 1.3 transport results were compared with an oil & gas industry-standard gas modelling code GEM for one reference case (ARC 2010). Due to inherent differences in the code purposes, only a limited comparison was possible, but the results were consistent.
- T2GGM Version 2.1 demonstrates mass balance for the key modelled species.
- At Version 2.0, GGM was compared against data from the Finnish large scale Gas Generation Experiment (GGE) (Appendix B, QUINTESSA and GEOFIRMA, 2011a).

7. USER MANUAL

7.1 TOUGH2

For general usage of TOUGH2, please see the TOUGH2 User's Guide (Pruess et al., 1999).
Specific details relating to the implementation of GGM and other TOUGH2 modifications are
detailed in the following sections.

7.1.1 GGM Input

GGM is invoked by the GGMIN keyword. GGMIN input following the keyword is specified in
Table 7-1.

Table 7-1: GGMIN Input

Line	Variables	Format
1	Version number. The current version number for the inputs described below is 2.	I2
2	NORMG– If not equal to zero, gas injection flow is distributed to all gas source elements with a gas saturation greater than zero. NORML – If not equal to zero, liquid injection flow is distributed to all liquid sink elements with a liquid saturation greater than zero. SCALEFACTORG – If not equal to zero, scale factors distribute GGM flows to the gas source elements are calculated at each time step based on the amount of gas available in each source element. These scale factors replace values read into the XGASSRC array described below. May increase run times, but increase model stability. SCALEFACTORL – If not equal to zero, scale factors distribute GGM flows to the liquid sink elements are calculated at each time step based on the amount of water available in each sink element. These scale factors replace values read into the XLIQSNK array described below. May increase run times, but increase model stability.	4I2
3	VOLFAC – repository volume factor	E15.5
4	GASRSAT – Residual gas saturation, below which no gas can be removed from the repository (if QAIR is less than zero).	*
5	USELIQCTRL - flag (0, 1) to control whether liquid saturation limits are enforced. NORML is only applied if USELIQCRTL is set to 1.	*
6	LSATOFFVAL - used only if USELIQCTRL = 1. The liquid saturation below which no water is extracted from a liquid sink element. Water extraction is also eliminated for an element if the element RH is below RHMINLIM (see below). If one or more elements have saturations greater than LSATOFFVAL and NORML is true, then liquid injection flow is distributed. If all liquid sink elements are below LSATOFFVAL, then no liquid is extracted. If this condition is true, then RH is set to RHLIMMIN (see below) on subsequent time steps, until at least saturation in at least one liquid extraction element exceeds LSATONVAL.	*
7	LSATONVAL - the minimum saturation threshold required for one or more liquid extraction elements for liquid extraction to resume, after it has been previously terminated due to saturation at all liquid extraction nodes being less than LSATOFFVAL.	*
8	USERHCTRL - flag (0, 1) which determines whether RH input to GGM is scaled based on residual liquid saturations. This is the most effective	*

	way to balance GGM water consumption with geosphere inflow as it slows down vapour phase reactions gradually as a saturation limit is reached.	
9	RHLSATMIN - minimum liquid saturation for RH control	*
10	RHLSATMAX - maximum liquid saturation for RH control	*

11	RHLIMMIN - RH value for minimum saturation and lower limit of element RH for liquid extraction from an element. This value should be equivalent to PRHMIN in order to maintain correspondence to GGM, however, it is included as a separate parameter for stability reasons: it may be practical to have a value greater than PRHMIN to minimize stability issues at single liquid sink elements if the repository does not become fully de-saturated with liquid (i.e., repository liquid saturation remains above LSATONVAL) over the course of the simulation.
	
	The code fragment below describes the scaling approach
	
	   IF ((RH.GT.RHLIMMIN).AND.(USERHCTRL.EQ.1))THEN
	    RHMULT = TANH((STOT-RHLSATMIN)/(0.5*(RHLSATMAX-RHLSATMIN)))
	    IF (RHMULT.GT.1.0) RHMULT = 1.0;
	    IF (RHMULT.LT.0.0) RHMULT = 0.0;
	    RH = RHLIMMIN + (RH - RHLIMMIN) * RHMULT;
	   END IF
		*

12	GGM_RESTART_READ – If true, causes the GGM restart input to be read (instead of the normal input file). GGM_RESTART_WRITE – If true, causes GGM restart information to be written at each output time step.	2L4
13	USE_KELVIN_RH – if true, GGM will use the Kelvin equation to calculate RH. If false, RH is calculated as the average vapour pressure divided by the maximum vapour pressure.	L4
14	USE_UPMOD – if true, GGM calculates upscaled factors for Phase 1, 2, 3 and 4 corrosion to account for heterogeneity in saturation and RH within each compartment. If false, these factors are calculated using compartment-average saturation and RH.	L4
15	NREPO – number of repository elements NCOMP – number of compartments	2I5
16	EREP(NREPO) – names of repository elements ICOMP(NREPO) – compartment ID of repository element	(A5, E) for NREPO lines
17	NGASSRC – number of gas source elements	I5
18	EGASSRC(NREP) – names of gas source elements XGASSRC(NGASSRC) – scaling factor for each source element	(A5, E) for NGASSRC lines
19	NLIQSNK – number of liquid sink elements	I5
20	ELIQSNK(NREP) – names of liquid sink elements XLIQSNK (NLIQSNK) – scaling factor for each sink element	(A5, E) for NLIQSNK lines
21	NREPCONN – number of connections contributing water to the repository	I5
22	EREPCONN(NREPCONN) – names of connections contributing water to the repository EREPSIDE (NREPCONN) – names of element on repository side of the connection	(A10,1X,A5) for NREPCONN lines

Note that gas source and liquid sink elements may be the same. Also note that although gas source and liquid sink elements are expected to be in the repository this is not checked. Nodes should be specified using standard TOUGH2 node naming conventions.

7.1.2   Alternative Gas Input (ALTGAS record)

The EOS3 module used by T2GGM assumes that air is the gas, however, an alternative gas may be specified by changing the Henry's constant, molar mass, specific heat capacity (not used in isothermal T2GGM calculations), and viscosity. Viscosity is calculated as a temperature dependent variable within TOUGH2.

To specify a gas other than air, provide the ALTGAS input record, which specifies the alternative gas to be used, as well as alternative parameter values. Alternative gases that can be specified include CH_4, CO_2, H_2, He and Ne. Default values for each gas are hard-coded into TOUGH2 subroutine EOS in a manner similar to the existing air parameters; however, the input record for ALTGAS provides the ability to override any of the default parameter values. Details of the inputs are specified in Table 7-2.

Table 7-2: ALTGAS Input Record

Parameters	Format	Description
ALTGA	A5	First line of record. Once these characters have been read, the following line is read, containing the parameters detailed below.
ALTGA.1 (first line)		
ALTGAS	A5	Characters specifying the gas to use: AIR, CO2, CH4, H2, HE or NE.
VISC_METHOD	I5	Integer flag specifying the viscosity calculation to use. A value less than or equal to zero uses the EOS3 default viscosity calculation for air. Greater than zero uses the TMVOC based viscosity calculation specific to the gas specified by ALTGAS.
ALT_H	E10.4	Alternative value of Henry's constant to be used. Units are: (mole fraction) Pa^{-1}.
ALT_AMA	E10.4	Alternative value of molar mass to be used. Units are: g mol^{-1}.
ALT_CVGAS	E10.4	Alternative value of specific heat capacity to be used. Units are: J kg^{-1} K^{-1}.
ALT_VISCG	E10.4	Alternative value of isothermal viscosity to be used. Units are: Pa s.
CALC_Z	I5	Integer flag to turn on non-ideal gas calculations. Value greater than zero will result in the calculation of the z compressibility factor for non-ideal gases. Default value is zero.

The ALTGAS input record also includes the flag CALC_Z, which if greater than 0, calculates the z compressibility factor. Note that for H2 and He, non-ideal gas behaviour is only strictly applicable for pure gas (i.e. no water vapour). At low temperatures, neglecting water vapour is typically negligible; at high temperatures, hydrogen and helium non-ideal gas calculations should be used with caution.

As previously mentioned, viscosity is calculated as a temperature dependent parameter specifically for air. New temperature dependent viscosity routines were included, based on routines found in TMVOC that consider the multiple gases, including CH_4, CO_2, H_2 and He. A temperature dependent function for neon was not readily available. Since neon is currently only used in the LASGIT project, which is isothermal, a constant value of 32.1 μPa s at 300 K (CRC 1995) was coded for neon viscosity.

The parameters defined for the gas are echoed in the standard output. Hard-coded values specified in the EOS subroutine are given in Table 7-3.

Table 7-3: ALTGAS Constant Values

ALTGAS ID	Henry's Law Constant (H) (mole fraction Pa^{-1})	Molecular Weight (AMA) (g mol^{-1})	Specific Heat Capacity (CVGAS) (J kg^{-1} K^{-1})
AIR	1.0E-10	28.96	733
H2	2.82E-11	2.016	0.0143
CO2	1.23E-09	44.00	839
CH4	4.93E-11	16.043	2191
HE	6.72E-11	4.003	5193.1
NE	8.045E-11	20.1797	1030

7.1.3   1D Hydromechanical Model (TIMHM record)

The 1D hydromechanical model allows specification of a time-varying, one-dimensional mechanical load, such as might be expected from glaciation effects, as described in Section 4.1. This model is invoked by using the TIMHM record, as detailed in Table 7-4. The input record must appear after the ROCKS record.

Table 7-4: TIMHM Input Record

Parameter	Format	Description
TIMHM	A5	First line of record. Once these characters have been read, the following lines are read, containing the parameters detailed below.
TIMHM.1 (first line)		
VER	I5	Current version is 2.
twoPhase	I5	Integer flag specifying the equation used to calculate S_{S-1D} ζ: if greater than zero, Equation (4.11) is used, otherwise Equation (4.12) is used.
calcKsKphi	I5	Integer flag: if greater than zero, 1/Ks is calculated according to Equation (4.6), otherwise1/ Ks is equal to zero. It is recommended that this flag be set to zero to maintain consistency with internal TOUGH2 assumptions.
oneDCOM	I5	Integer flag: if greater than zero, the pore compressibility specified in the ROCKS parameters (COM) is assumed to be three-dimensional, otherwise it is assumed to be one-dimensional. It is recommended that this flag be set to zero to maintain consistency with internal

Parameter	Format	Description
		TOUGH2 assumptions (and that the COM specified in ROCKS is a 1D compressibility).
compSAT	I5	Integer flag: if greater than zero, capillary pressure is corrected for changes in porosity (i.e. capillary pressure is at a saturation equal to the current saturation + the change in porosity). It is recommended that this flag be set to zero.
TIMHM.2 (second line)		
WATERCOM	E14.7	Compressibility of water, only used if twoPhase equals zero (i.e. used in Equation (4.12)).
TIMHM.3 (third line)		
nZeta	I5	The number of material groups (i.e. specifies the number of TIMHM.4 rows to read)
TIMHM.4 (repeated nZeta times)		
matName	*	Material name, must match a name in the ROCKS record.
Zeta	*	1D loading efficiency (ζ), only used if twoPhase equals zero (i.e. used in Equation (4.12)).
Nu	*	Poisson's ratio (ν), only used if twoPhase greater than zero (used in Equation (4.11)). *
Alpha	*	Biot-Willis coefficient (α), used if twoPhase greater than zero (calculates 3D 1/K used in Equation (4.11) from 1D COM).*
TIMHM.5		
npoint_HM	I5	Number of points on the HM loading curve.
nStress	I5	Number of stress time-series.
maxNnodes	I5	Maximum number of nodes associated with a stress time-series.
interpFlag	L5	If true, stress table will be time interpolated.
TIMHM.6		
timhm(i=1,npoint_HM)	4E14.7	Times in HM loading curve.
TIMHM.7		
nNodes	I5	Number of nodes associated with current stress time-series.
TIMHM.8		
stressNodes(i=1,nNodes)	4(A5,5X)	Nodes associated with current stress time-series.
TIMHM.9		

Parameter	Format	Description
stresshm(i=1,npoint_HM)	4E14.7	Loading rates for current stress time-series in Pa/s.
TIMHM.7 through TIMHM.9 are repeated n Stress times		

* Note that these parameters may be required under a different combination of flags (twoPhase, calcKsKphi and oneDCOM), and the requirements listed here are based on the recommended flag settings specified in this table. The echo of the input in the output record will specify which parameters are required for the current set of flags.

7.1.4   Time-Variable Permeability (TIMVK record)

The user can specify a time-variable permeability function for a specified set of nodes. Using the inputs from the TIMVK input record, specified in Table 7-5, the absolute permeability for the specified elements is multiplied by the time-interpolated scale factor vkvals.

Table 7-5: TIMVK Input Record

Parameter[+]	Format	Description
TIMVK	A5	First line of record. Once these characters have been read, the remaining record is read, containing the parameters detailed below.
ntptab_vk	*	number of nodes
vkelem(i=1, ntptab_vk)	*	node ids
npoint_vk	*	number of times in permeability function
Timvkv, vkvals	*	time, permeability scale factor
Repeat last line npoint_vk times.		

[+]Each parameter on a single line.
*Refers to free format.

7.1.5   Time-Variable Boundary Conditions (TIMBC record)

Based on the TOUGH2-MP implementation, the time-varying pressure, saturation and temperature Dirichlet boundary condition uses an input TIMBC record, outlined in Table 7-6, and updates the pressure, saturation and temperature at each boundary condition element at the beginning of each new time step. This type of boundary condition only works with large volume boundary conditions, not with negative volume boundary conditions.

Table 7-6: Time-varying Dirichlet Boundary Condition Input Record (TIMBC)

Parameter[+]	Format	Description
TIMBC	A5	First line of record. Once these characters have been read, the remaining record is read, containing the parameters detailed below.
version	I5	Version number is expected to be 2 with the inclusion of temperature.
npoint, ntptab	2I5	number of time points, number of nodes
timbcv(i=1,npoint)	4E14.7	Times
bcelem	A5	node id
pgbcel(i=1,npoint)	4E14.7	Gas pressures (Pa)
sgbcel(i=1,npoint)	4E14.7	Gas saturation (10+gas saturation, as in INCON) or air mass fraction
tgbcel(i=1,npoint)	4E14.7	Temperature
Repeat last four lines ntptab times.		

[+]Each parameter on a single line

Note that the interpolation routine for saturations assumes boundary condition at a single node is always two-phase or single phase i.e., a single node always has a gas saturation (values between 10 and 11), or an air mass fraction (values between 0 and 1).

7.1.6   Model Linking (MLINK record)

Model linking is invoked with the MLINK input block, detailed in Table 7-7.

Table 7-7: GFRES Input Record

Parameter	Format	Description
MLINK	A5	First line of record. Once these characters have been read, the remaining record is read, containing the parameters detailed below.
MLINK.1 (first line)		
version	I5	Current version is 1.
MLINK.2 (second line)		
NQELEM	I5	Number of flow nodes (FN) and connections (FC).
NPELEM	I5	Number of pressure nodes (PN).
NZONE	I5	Number of flow zones. Each flow zone has a common liquid and gas flow multiplier.

MLINK.3 (third line)		
positiveFlowOnly	L4	Only positive flows are applied to pressure nodes.
NAVG	I4	Averages flows from flow connections over the last NAVG time steps.
MLINK.4 – Repeat from i = 1, NZONE		
zoneLiqQMult(i)	E15.8	Zone liquid flow multiplier.
zoneGasQMult(i)	E15.8	Zone gas flow multiplier.
MLINK.5 – Repeat from i = 1, NQELEM		
qzoneElem(i)	A5,5X	Flow node element ID.
qzoneElemZone(i)	I5	Zone number associated with flow node.
MLINK.6 – Repeat from i = 1, NQELEM		
qzoneConnStart(i)	A5	Node ID for node at start of flow connection.
qzoneConnEnd(i)	A5	Node ID for node at end of flow connection.
qzoneConnZone(i)	I5	Zone number associated with flow connection.
qzoneFlowMult(i)	E10.3	Zone flow multiplier.
MLINK.7 – Repeat from i = 1, NPELEM		
pzoneElem(i)	A5,5X	Pressure node element ID.
pzoneElemZone(i)	I5	Zone number associated with pressure node.

7.1.7   Modified van Genuchten Capillary Pressure and Relative Permeability Functions

The modified van Genuchten capillary pressure and relative permeability functions are invoked using ICP and IRP = 14 in the ROCKS section. The inputs to the modified van Genuchten function are detailed in Table 7-8.

Table 7-8: ROCKS.1.2 and ROCKS.1.3 Input Record for Modified Van Genuchten Functions

Parameter	Format*	Description
ROCKS.1.2		
IRP	I5	Set to 14 to invoke the modified van Genuchten relative permeability model
RP(1)	E10.4/E15.9	S_{lrk} – residual liquid saturation for relative permeability functions.
RP(2)	E10.4/E15.9	Sgr – residual gas saturation
RP(3)	E10.4	Flag to determine relative gas permeability equation. If zero, use Luckner model (equation **4-17**), otherwise use 1-k_{rl}.

RP(4)	E10.4	Flag to determine relative gas permeability equation. If zero, use Luckner model (equation **4**-**17**), otherwise use Mualem model (equation **4**-**18**).
ROCKS.1.3		
ICP	I5	Set to 14 to invoke the modified van Genuchten capillary pressure model
CP(1)	E10.4/E15.9	n – analogous to pore size distribution index
CP(2)	E10.4/E15.9	$1/\alpha$ – analogous to gas entry pressure [Pa]
CP(3)	E10.4	if CP(3) = 0 then $P_{c,max} = 10^{50}$, $\varepsilon = -1$ if 0 < CP(3) < 1, then $P_{c,max} = 10^{50}$, $\varepsilon = CP(3)$ if CP(3) $\geq$ 1, then $P_{c,max} = CP(3)$, $\varepsilon = -1$ When ε is greater than 0, a linear P_c function is used when Sl < $S_{lr} + \varepsilon$
CP(4)	E10.4	if zero, then m = 1−1 n
CP(6)	E10.4	S_{lrc} – if zero, then $S_{lrc} = S_{lrk}$

*Two values are provided in the format for some variables. The first value is used for the standard ROCKS input record, the second is for the ROCKL input record, which provides extended precision for some variables.

7.1.8   Time Stepping Options (TSTEP record)

The time step input record (TSTEP) allows the modeller greater control over time-step changes. The input record is described in Table 7-9.

Table 7-9: Time Step Adjustment Input Record (TSTEP)

Parameter[+]	Format	Description
TSTEP	A5	First line of record. Once these characters have been read, the remaining record is read, containing the parameters detailed below.
TSTEP.1 (first row)		
version	I5	Current version is 2.
TSTEP.2 (second row)		
INCFACT	E10.5	Increment time step factor (time step multiplier), default 2. Time steps are only increased if the number of iterations is less than MOP(16) and MAXTSHOLD steps after the last time step reduction. Default TOUGH2 time stepping uses a time step multiplier of 2 whenever the number of iterations is less than MOP(16). It is suggested that a multiplier of 2 is aggressive and a smaller value be used (e.g. 1.5).
DECFACT	E10.5	Time step reduction factor, default 2. Default TOUGH2 time stepping reduces time steps by a factor of REDLT, which has a default value of 4.
DX0FACT	E10.5	Increment factor when DX=0.0. When the DX is zero for all primary variables, the solution is either at steady-state or the time step is too small to produce any changes. Numerous time steps at DX of zero can be a sign of model instability and create erroneous stead-state output. If the DX is zero for all primary variables, the time step is increased according to this factor. Must be greater than 1.
MAXTSHOLD	I5	After a time step decrease, the time step is not increased until MAXTSHOLD time steps have completed, default 5.

7.1.9   High Precision Output Times (TIMES record)

Higher precision times allows for more accurate output times, particularly for times greater than 25 k years. Higher precision times (5E15.10) in the standard TOUGH2 TIMES input record is invoked by setting the number of times (ITI) negative.

7.1.10 Convergence Failure Handling (GFRES record)

TOUGH2 simulations frequently terminate prematurely after a series of successive time step reductions are unable to resolve non-linear Newton-Raphson convergence issues. Typically this is addressed by restarting the simulation at a known good point with modified convergence criteria. The GFRES option detects incipient failure and performs an automatic restart with modified convergence strategies.

When a failure appears likely (e.g. after ten successive reductions in time step size) the simulation is restarted at a point a number of time-steps previously. Instead of just a reduction in the time step, an alternate numeric "strategy" would be used where a "strategy" is defined as a collection of appropriate numeric parameters. The selected strategy would replace current numeric parameters and the simulation restarted. Table 7-10 describes the GFRES input record.

Table 7-10: GFRES Input Record

Parameter	Format	Description
GFRES	A5	First line of record. Once these characters have been read, the remaining record is read, containing the parameters detailed below.
GFRES.1 (first line)		
version	I5	Current version is 2.
GFRES.2 (second line)		
NKEEP	I2	Number of previous time steps to keep.
NSTRAT	I2	Number of strategies to read.
NFAIL	I2	Number of consecutive time step reductions used to indicate incipient failure (max 25).
GFRES.3 (third line)		
OPTION	A30	Either REVERT or SEQUENTIAL.
		REVERT option restores original strategy (defined in PARAM and TSTEP records) after a specified number of successful time steps past the failure point.
		SEQUENTIAL option expects strategies in order of convergence. When the model is successful, it moves up the list allow for faster progression, when problems are detected it moves down the list to prevent failure.
GFRES.4 (fourth line) if REVERT specified as OPTION		
NREVERT	I5	Number of successful time steps past failure point before reverting to original strategy.
REVERTFACTOR	E5.2	Factor applied to NREVERT each time strategy is reverted. Prevents excessive strategy switching.

GFRES.4 (fourth line) if SEQUENTIAL specified as OPTION		
NREVERT	I5	Number of successful time steps before moving up the strategy list.
STRATINDEX	I2	The placement of the original strategy in the list.
GFRES.5		
RE1	*	Convergence criterion for relative error.
NOITE	*	Maximum number of Newtonian iterations per time step.
TMULT	*	Time step multiplier (INCFACT in TSTEP).
TREDU	*	Time step reduction factor (DECFACT in TSTEP).
THOLD	*	Minimum number of time steps before next increase (MAXTSHOLD in TSTEP).
DX0MULT	*	Increment factor when DX=0.0 (DX0FACT in TSTEP)
Repeat GFRES.5 line NSTRAT times.		

7.1.11 GPU Matrix Solver (GFGPU record)

Use of the GPU solver requires an appropriate NVIDIA graphics processing unit (GPU), with proper CUDA 6 drivers and DLLs (NVIDIA, 2014). The input record is detailed in Table 7-11. Note that the GPU matrix solver uses the RITMAX and CLOSUR parameters specified in the SOLVR input block. Also, O and Z preconditioning specified in the SOLVR input block is applied before the GPU solver is called. If no SOLVR input block is specified, TOUGH2 defaults will be used.

It should be noted that the GPU solver cannot be executed under Windows remote desktop, as the GPU is not activated. In this case, the output file will state, within the echo of the input: "Number of GPU devices in the system: 0". An alternative remote desktop application, LogMeIn, successfully ran the GPU solver.

Table 7-11: GFGPU Input Record

Parameter	Format	Description
GFGPU	A5	First line of record. Once these characters have been read, the remaining record is read, containing the parameters detailed below.
GFGPU.1 (first line)		
GSLV	I1,2x	Solver choice (default = 3): GSLV = 1: Conjugate Gradient (CG) GSLV = 2: Biconjugate Gradient Stabilized (BiCGSTAB) GSLV = 3: General Minimum Residual (GMRES) GSLV = 4: Induced Dimension Reduction (IDR) GSLV = 5: Conjugate Residual (CR)

GPRECOND	I1,2X	Preconditioner choice (GPRECOND) default = 4
		GPRECOND = 1: No Preconditioner
		GPRECOND = 2: Jacobi Preconditioner
		GPRECOND = 3: Multi-colored (Symmetric) Gauss-Seidel
		GPRECOND = 4: ILU(p)
		GPRECOND = 5: ILUT(t,m)
		GPRECOND = 6: ILU(p,q)
SOPT	I2,2X	Additional solver option (SOPT)
		if GPRECOND= 4 or 6, SOPT is the p value
		if GPRECOND=5, SOPT is the t value
		See the Paralution manual (2014) for details.
POPT	I2	Additional Preconditioner option (POPT)
		if GPRECOND=5, POPT is the m value
		if GPRECOND=6, POPT is the q value

7.1.12   Output Files (FILES record)

Binary output files, revised COFT/FOFT formats, and COFT/FOFT path for MP are invoked with the FILES keyword, as described in Table 7-12. Invoking the FILES keyword will also provide output times in years, rather than seconds, within the output listing file.

Table 7-12: FILES Input Record

Parameters	Format	Description
FILES	A5	First line of record. Once these characters have been read, the remaining record is read, containing the parameters detailed below.
FILES.1 (first line)		
version	I5	Current version is 1.
FILES.2 (second line)		
IBINOUT	I5	If greater than zero, binary output files are produced.
IFCOFT	I5	If greater than zero, writes revised FOFC/COFT output.
IGFDOUT	I5	If greater than zero, writes diffusion output in binary format to DOUT.
FILES.3 (third line)		

IPATHOUT	I5	IPATHOUT - if set to non-zero, MP FOFT and COFT output is written to a separate file by each processor.
FILES.4 (fourth line)		
GFPATH	A200	GFPATH - output path if IPATHOUT is non-zero

7.1.13 FLAC Integration

To call the TOUGH-FLAC algorithm, the TFLAC record must be included in the input file, as shown in Table 7-13. This record must be invoked after the ROCKS record, as it assigns geomechanical parameters on a material by material basis. Caution should be taken if invoking the poroelastic model and elasto-plastic permeability modification model for the same material group, as the assumptions inherent in these approaches are generally not compatible. The record uses unformatted input.

Table 7-13: TFLAC Input Record

Parameters	Format	Description
TFLAC	A5	First line of record. Once these characters have been read, the remaining record is read, containing the parameters detailed below.
TFLAC.1 (first line)		
Version	I5	Current version is 1.
TFLAC.2 (second line)		
waterC	*	Sets the water compressibility to be used in poroelastic equations. A reasonable value would be 4.55E-10 Pa^{-1}.
TFLAC.3 (third line)		
nFlac	*	An integer specifying the number of properties that are subject to hydromechanical coupling
TFLAC.4 – Repeat 4.1,4.2 and 4.3 from i = 1, nFlac		
TFLAC.4.1		
matName	*	Material name, must match a name in the ROCKS record.
poroFlag	*	Poroelastic flag (if this parameter equals 1 poroelastic coupling is turned on)
permFlag	*	This flag activates permeability modification. If it equals 1 then elasto-plastic coupling is activated, if it equals 3 then permeability is calculated in a problem specific function in FLAC3D.
TFLAC.4.2 - If poroFlag equals 1 (parameters for equations in section 4.4.1). This line is skipped if poroFlag does not equal 1 (no blank line is expected).		
bulkCOM	*	Bulk compressibility

skemptB	*	Skempton's B coefficient
TFLAC.4.3 - If permFlag equals 1 (parameters for equations in section 4.4.2). This line is skipped if permFlag does not equal 1 (no blank line is expected). If permFlag equals 3, this record is not required.		
paramA	*	Parameter A, Y-intercept of damaged permeability curve (stress = 0)
paramBs	*	Parameter B, slope of stress-permeability curve, single failure mode
paramBm	*	Parameter B, slope of stress-permeability curve, multiple failure modes
paramC	*	Parameter C, exponent multiplier of stress-permeability curve
paramD	*	Parameter D, swelling equation fitting parameter, rate of permeability decay

Before T2GGM can call FLAC3D, some setup is required for the FLAC3D part of the model. The purpose of this setup is to make a FLAC3D grid, set up FLAC3D material properties, set initial conditions, establish the undrained pressures and mechanical equilibrium. These goals are accomplished through a series of FLAC3D model calls which run specific FLAC3D scripts and then save the model state for use by the next script. To avoid having to specify the full path of input files, all scripts and their input files are currently kept in the same folder.

Table 7-14 describes the scripts, required input files and output files produced for the 1D consolidation example shown in Section 5.9.8.1. For a given problem the details of how the FLAC3D files are set up will differ, but all models will have three basic components:

1. Gridding – A grid can be generated in FLAC3D or imported from another program such as mView. The TOUGH2 and FLAC3D grids should be virtually identical, with the same number of TOUGH2 and FLAC3D elements. If the grids are generated separately a mapping algorithm must be run to match elements with the same coordinates, so that the i-th TOUGH2 element can be mapped to the j-th FLAC3D element (zone).

2. Initialization – A this stage properties, boundary conditions, and initial conditions must be specified, likely by using a FLAC3D script. The FLAC3D model must be run once to calculate a stable initial mechanical equilibrium. Required fish functions, especially *tough_flac.fis* should be loaded at this stage so that they are included in the project. The *tough_flac.fis* will not be run at this stage but should be loaded. This step should be performed in the GUI rather than the console version of FLAC3D. After the FLAC3D model has run and called necessary fish functions it saves the model state for later use (e.g. *initModel.sav*).

3. Running – A this stage the flac3d model is called from within T2GGM. Before T2GGM starts it is necessary to copy the saved FLAC3D model state (e.g. *initModel.sav*) to a file called *FLAC3D.sav*. Every time T2GGM calls FLAC3D it runs the script *flac3d.f3dat* which loads *FLAC3D.sav*. The *flac3d.f3dat* script then loads the pressure distribution from T2GGM (*tou_fla*), solves a new mechanical equilibrium, and writes the updated stress and damage information into the file *fla_tou* which is read by T2GGM at the start of the next iteration. After the FLAC3D model runs it saves the updated model state to *FLAC3D.sav* for use in the next TOUGH2 iteration.

Table 7-14: FLAC3D Setup for 1D Consolidation

Script	Description	Input	Output
Gridding 1-grid.f3dat This script must be run once at the start of modelling.	Reads a grid (and property distribution) currently produced by mView. This could also be generated using internal FLAC3D functions. Calculates functions to map the FLAC3D grid to the mView grid. This mapping function is more important if the grids are produced separately and therefore have different numbering. It needs the T2GGM element block, also produced by mView, with the header removed.	mView produced grids: *1-mViewGrid.f3grid* *mView_ELEM* Mapping algorithms: *geomReadWrite.fis* *makeMapFile.fis*	Saved model state: *1-grid.f3sav* Grid data: *first_layer_centroid.txt* *last_layer_centroif.txt* FT_MAP TF_MAP
Properties and Initialization 2-initModel.f3dat This script must be run after 1-grid.f3dat, once at the start of modelling.	Reads saved model state with gridding data. Sets material properties (there are many ways this could be accomplished). Calls and initializes mechanical model. Calls and initializes fluid flow model. Calculates initial undrained response. Calls tough-flac algorithm (to include the fish functions in the project). Saves initial model state. This becomes the initial condition for the TOUGH-FLAC model run.	Saved model state: *1-grid.f3sav* Fish functions: *2-materialConstants.fis* *tough_flac.fis*	Saved model state: *initModel.sav*
Running Flac3d.f3dat This script is called by T2GGM during each iteration.	Loads saved model state. Calls *tough_flac* fish function to read a file exported by T2GGM called tou_fla. This sends pressure, temperature, liquid saturation, capillary pressure. These are not all used currently. Calls *load_time* function to apply an external load which may change with time. Solves the new mechanical equilibrium, calls *flac_tough* fish function to write the file fla_tou, which will be read by T2GGM. This file contains average effective stress, shear strain increment, average principle stress, and failure state flag.	Saved model state: *FLAC3D. sav* (This is identical to initModel.sav the first time this function is called, the batch file calling T2GGM should have a line copying initModel.sav to FLAC3D.sav). T2GGM output: *tou_fla*	Saved model state: *FLAC3D. sav* (updated model state writes over previous state for start of next time step) T2GGM input: *fla_tou*

Script	Description	Input	Output
	These are not all used for all types of coupling.		

7.1.14   Pressure-dependent Permeability and Capillary Pressure

The pressure-dependent permeability and capillary pressure functions are specified through two records: the ROCKS record and LASGT record.

The ROCKS record includes an additional line (ROCKS.1.4) for each material type that allows pressure-dependent permeability and capillary pressure. This additional line is read if the GK parameter (Klinkenberg parameter in ROCKS1.1) is negative. The GK parameter also provides the value for the scaling factor f. Details of the inputs for the ROCKS1.4 line are provided in Table 7-15.

Table 7-15: ROCKS.1.4 Input Record

Parameter	Format*	Description
P1_L	E10.4/E15.9	Initial pressure at the onset of dilatant flow, or if LPMOD=3 P_r (pressure range over which the permeability is modified, equivalent to P2-P1), in Pa.
P2_L	E10.4/E15.9	Pressure corresponding to the maximum increase in permeability, in Pa.
L_GASONLY	I5	A flag that determines whether permeability modifications are conducted for the gas phase only, or both phases. A value less than zero modifies absolute permeability (both gas and liquid), and a value greater than or equal to zero modifies gas phase permeability only.
L_ICPEXT	I5	Determines method used for modifying capillary pressure. L_ICPEXT =1 – Leverett L_ICPEXT =2 – direct L_ICPEXT =3 – cubic law for fractures L_ICPEXT =4 – Leverett when k < k*f , 0 when k => k*f

*Two values are provided in the format for some variables. The first value is used for the standard ROCKS input record, the second is for the ROCKL input record, which provides extended precision for some variables.

The LASGT record includes additional inputs to define the method for pressure-dependent permeability and capillary pressure modification (either pressure threshold dependent, or total stress dependent), and defines the total stress on an element basis. If no total stress is defined for an element, then a total stress is calculated based on the initial pore pressure (saturation averaged pressure) plus P1_L. Details for the LASGT input record are provided in Table 7-16.

Table 7-16: LASGT Input Record

Parameter	Format	Description
LASGT.1 (first row)		
L_FD	I5	A flag that determines the directionality of fractures:
		L_FD = 0 – No fracture directionality, the permeability for all connections are modified.
		L_FD = 1 – Horizontal fractures only, the permeability for all connections in the XY plane are modified
		L_FD = 2 – vertical fractures only, the permeability for all connections in the XZ plane are modified
FS_L	E10.4	Fracture scaling factor. Permeability is additionally modified by multiplication by this scaling factor, only for the connections specified by L_FD.
LAS_VER	I5	Version number for LASGT input record.
		LAS_VER = 0 – Only first line of input record is read (LASGT.1)
		LAS_VER = 1 – Lines LASGT.1 through LASGT.3 are read.
LASGT.2 (second row)		
L_PMOD	I5	Determines method used for modifying permeability
		=1 is linear function as in equation (**4-26**)
		=2 is similar to (1), with a constant fracture permeability maintained
		=3 uses a spatial total stress input by the user, or calculated by the BSTAT functions. In this case P1 is equivalent to Pr, unless specified in the P1Lval below.
numTS	I8	Number of elements read in LASGT.3
LASGT.3 (rows 3 through (numTS+3))		
tselem	A5	Element ID
tsval	E10.6	Total stress in Pa.
P1Lval	E10.6	Pr (pressure range over which the permeability is modified, equivalent to P2-P1) in Pa.

The modified permeability is output to the nodal listing file in the GPERX column. The modified capillary pressure is output to the nodal listing file under the column titled PCX.

7.1.15   Bentonite States (BSTAT)

Bentonite states, where the permeability and capillary pressure of bentonite materials vary with water saturation (in addition to the relative permeability and capillary pressure curves), are specified in the BSTAT record, detailed in Table 7-17.

Table 7-17: BSTAT Input Record

Parameters	Format	Description
BSTAT	A5	First line of record. Once these characters have been read, the remaining record is read, containing the parameters detailed below.
BSTAT.1 (first line)		
version	I5	Current version is 1.
debug	A5	If equal to 'DEBUG', writes BSTATE output at each time step.
BSTAT.2 (second line)		
readTable	*	Logical (T or F) determining whether bentonite permeability is calculated, or interpolated from a saturation-permeability input table. If true, lines BSTAT.3 through BSTAT.6 are NOT read.
BSTAT.3 (third line) – Only if readTable is FALSE		
restartBSTAT	*	Logical (T or F) determines whether initial micro-porosities are read from the BSRES file in the case of a model restart. Initial micro-porosities are written to the BSRES file if the restartBSTAT flag is F. When restarting, the BSTAT code expects the same BSTAT input record (except for this flag is set to T) as well as the BSRES file from the simulation that started at time zero.
BSTAT.4 (third line) – Only if readTable is FALSE		
NBSMAT	*	Number of bentonite material types
BSTAT.5 – Repeat from i = 1, NBSMAT – Only if readTable is FALSE		
matName	*	5 characters equivalent to a MAT name specified in ROCKS record.
BS_BSW	*	Bound water saturation.
BS_ALPHA	*	Exponent in micro-porosity equation.

BS_BETA	*	Expansive bentonite fraction.
BS_MICROMAX	*	Maximum micro-porosity, must be less than total porosity specified in ROCKS.
BS_MEGAINIT	*	Initial mega-porosity.
BS_MEGAK	*	Initial mega-porosity permeability.
BSTAT.6 – Only if readTable is FALSE		
NBSZ	*	Number of zones.
BSTAT.7– Repeat from i = 1, NBSZ – Only if readTable is FALSE		
BSZ_GAPVOL	*	Gap volume.
BSZ_MSP	*	Maximum swelling pressure.
BSTAT.8		
NBSEL	*	Number of bentonite state elements. Cannot be a boundary element (large volume or negative volume).
BSTAT.9– Repeat from i = 1, NBSEL		
BSELID	A5	Element ID for bentonite state element.
BSELZ	I5	Zone associated with bentonite state element.
BSTAT.10 – Only if readTable is TRUE		
NBSZ	*	Number of zones.
Repeat BSTAT.10 and BSTAT.11 from i=1, NBSZ		
BTAT.11 – Only if readTable is TRUE		
numPts	*	Number of points in saturation-permeability table.
BTAT.12 – Repeat from i=1, numPts - Only if readTable is TRUE		
SLpts	*	Liquid saturation
Kpts	*	Permeability

At the start of each simulation with the BSTAT record, a BSRES file is written, containing the initial micro-porosities for each bentonite state node. To restart a simulation, this BSRES file is required, and the restartBSTAT flag turned on. The BSRES file is not written during a restarted simulation; only the initial micro-porosities at time zero are required for any restart.

If the readTable option is selected, permeabilities will be modified according to saturation based on the table read in the BSTAT input record. Calculations of component porosities are not

conducted in this case, so no changes to capillary pressure are conducted. As well, if dilatant flow is also considered (using the LASGT pressure-dependent permeability and capillary pressure), swelling pressures will not be calculated, and an alternate method of determining the total stress or threshold pressure is required.

7.2 GGM

GGM consists of a set of FORTRAN 77 subroutines that are compiled with TOUGH2. In order to drive the GGM module, in addition to configuring TOUGH2 to provide the necessary run-time information via subroutine arguments, files containing all input and solution control parameters must be prepared. Example input files are provided with the source code containing input data that is consistent with the relevant Data report (QUINTESSA and GEOFIRMA 2011b). A description of each of the input parameters is given in Table 7-21 and Table 7-22. GGM sends its output to various FORTRAN units with the format described in the Design Description. This output can be directed to file and analyzed as appropriate. Note that for extremely long runs very large output files (several gigabytes in size) may be produced if output is requested at every internal time step. The LOGTR input parameter can be used to control how often GGM sends output to the output file unit.

GGM can also be compiled and run in standalone mode for testing purposes. Compilation scripts that can be run in a Linux environment or on Windows using Cygwin are provided with the source code for this purpose. Further details can be found with the README file provided with the software.

7.2.1 Input Files

GGM requires two types of input file:

1. A single global input file defining global parameters and GGM configuration options (read from unit IGGMINPT); and
2. A per compartment input file defining compartment specific input parameters (read from unit IGGMINCO).

The general format employed by these fields is given in Table 7-18, with italicized text denoting user input. Here *filetype* is GLOBAL or COMPARTMENT, *value* is the data value, *name* is an alphanumeric code and *comment* is arbitrary text that is ignored by the GGM but which can be used to store information such as required units.

Table 7-18: General Format for Input Files

Line	Contents
1	# GGM_INPUT_FILE_FORMAT 1
2	# GGM_INPUT_FILE_TYPE *filetype*
subsequent	v*alue name comment*

The data required for the global and compartmental input files are given in Table 7-21 and Table 7-22, respectively.

The values used for these parameters in the postclosure safety assessment for OPG's proposed DGR for L&ILW are given in QUINTESSA and GEOFIRMA (2011b). The name,

description and units of each parameter are output to the console before it is read in. All input is echoed to file by GGM so that it can be checked that it has been read in and correctly converted to internal units. Note that GGM accepts as input the initial masses of the organic substrates (PIMORG1, PIMORG2 and PIMORG3) and effective molar masses (PMORG1, PMORG2, PMORG3) that define the mass per mole of the relevant functional group. This allows the total number of moles of each of the relevant functional groups to be calculated by GGM. GGM output file variables are listed in Table 7-23.

7.2.2   Output Files

GGM generates three types of output file:

1. A single global output file providing summed inventories and rates across all compartments (written to unit `IGGMCALC`);
2. A single output file containing compartment specific outputs (written to unit `IGGMOUCO`); and
3. Files with the input file format presented in Section 7.2.1 that can be used when restarting T2GGM.

7.2.2.1   Global Output File

The format of the global output file is given in Table 7-19 with italicized text denoting user input. The columns are formatted in a fixed width, space separated column format. Each column contains data padded with spaces to a width of 26 characters. All units and names fields are quoted so that, should any of these fields contain spaces, the file can still be read in to common packages as a space separated file format.

The global output file contains data summed or averaged over all compartments. The specific data output, together with units and method with which compartment data are processed to get the 'global' value are given in Table 7-23.

Table 7-19: Global Output File Format

Line	Contents
1	`# GGM_OUTPUT_FILE_FORMAT 1`
2	`# GGM_OUTPUT_FILE_TYPE GLOBAL`
3	`#` *array_index* *array_index* *array_index* ...
4	`#` "(*units*)" "(*units*)" "(*units*)" ...
5	"*name*" "*name*" "*name*" ...
subsequent	*value* *value* *value* ...

7.2.2.1.1   Compartment Output File

The file format used for the output file containing all compartment-based data is given in Table 7-20. The data to be output are the same as those specified in Table 7-23.

Table 7-20: Compartment Output File Format

Line	Contents
1	`GEOFIRMA FOFT 1`
2	*number of data types (d)*

Line	Contents
	Then one line per data type:
3	*name#1 units#1*
4	*name#2 units#2*
…	*...*
d+2	*name#d units#d*
d+3	*number of compartments (c)*
	Then a compartment id for each compartment:
d+4	*comp_id#1 comp_id#2 .... comp_id#c*
	Then one block per time step:
d+5	Time
	Within a time block include one line per compartment containing all data for that compartment
d+5+1	*comp#1 value#1, comp #1 value#2, ...*
d+5+2	*comp#2 value#1, comp #2 value#2, ...*
	...
d+5+c	*comp#c value#1, comp #2 value#2, ...*

7.2.2.1.2 Restart Output Files

As part of the restart facility, the code is required to generate output files that allow the code to be restarted. Only the compartment-based input files contain time dependent inventory data and so data in the same format but with up-to-date inventory data are written to file for each compartment on demand. The restart data are written to and read from files with the filestem GGMRES. The file format for the restart files is identical to that presented in Section 7.2.1.

Table 7-21: Specification of GGM Global Input Data

Name	Description/Category	Input Units	Internal Units
	Biomass Decay		
PD	Biomass decay rate	a^{-1}	s^{-1}
	Solubility constants		
PKCO2	CO_2	mol L^{-1} MPa^{-1}	mol m^{-3} Pa^{-1}
PKH2	H_2	mol L^{-1} MPa^{-1}	mol m^{-3} Pa^{-1}
PKH2S	H_2S	mol L^{-1} MPa^{-1}	mol m^{-3} Pa^{-1}
PKCH4	CH_4	mol L^{-1} MPa^{-1}	mol m^{-3} Pa^{-1}
PKO2	O_2	mol L^{-1} MPa^{-1}	mol m^{-3} Pa^{-1}
PKN2	N_2	mol L^{-1} MPa^{-1}	mol m^{-3} Pa^{-1}
	Effective molar mass of metals		
PM1	Mass of carbon and galvanized steel per mole of equivalent iron.	kg mol^{-1}	kg mol^{-1}
PM2	Mass of passivated carbon steel per mole of equivalent iron.	kg mol^{-1}	kg mol^{-1}
PM3	Mass of stainless steel and Ni-based alloys per mole of equivalent iron.	kg mol^{-1}	kg mol^{-1}
PM4	Mass of zirconium alloys per mole of equivalent zirconium.	kg mol^{-1}	kg mol^{-1}
	CO_2 Enhanced corrosion		
PPRCO2	Reference partial pressure of CO_2 for enhancement of corrosion	MPa	Pa
PE	Exponent for the enhancement of corrosion by CO_2	-	-
	L&ILW Corrosion rates		
PR111	carbon and galvanized steel corrosion rate aerobic conditions unsaturated conditions	μm a^{-1}	m s^{-1}
PR112	carbon and galvanized steel corrosion rate aerobic conditions saturated conditions	μm a^{-1}	m s^{-1}
PR121	carbon and galvanized steel corrosion rate anaerobic conditions unsaturated conditions	μm a^{-1}	m s^{-1}
PR122	carbon and galvanized steel corrosion rate anaerobic conditions saturated conditions	μm a^{-1}	m s^{-1}

Name	Description/Category	Input Units	Internal Units
PR211	passivated carbon steel corrosion rate aerobic conditions unsaturated conditions	μm a^{-1}	m s^{-1}
PR212	passivated carbon steel corrosion rate aerobic conditions saturated conditions	μm a^{-1}	m s^{-1}
PR221	passivated carbon steel corrosion rate anaerobic conditions unsaturated conditions	μm a^{-1}	m s^{-1}
PR222	passivated carbon steel corrosion rate anaerobic conditions saturated conditions	μm a^{-1}	m s^{-1}
PR311	stainless steel and Ni-based alloys corrosion rate aerobic conditions unsaturated conditions	μm a^{-1}	m s^{-1}
PR312	stainless steel and Ni-based alloys corrosion rate aerobic conditions saturated conditions	μm a^{-1}	m s^{-1}
PR321	stainless steel and Ni-based alloys corrosion rate anaerobic conditions unsaturated conditions	μm a^{-1}	m s^{-1}
PR322	stainless steel and Ni-based alloys corrosion rate anaerobic conditions saturated conditions	μm a^{-1}	m s^{-1}
PR411	Zr alloys corrosion rate aerobic conditions unsaturated conditions	μm a^{-1}	m s^{-1}
PR412	Zr alloys corrosion rate aerobic conditions saturated conditions	μm a^{-1}	m s^{-1}
PR421	Zr alloys corrosion rate anaerobic conditions unsaturated conditions	μm a^{-1}	m s^{-1}
PR422	Zr alloys corrosion rate anaerobic conditions saturated conditions	μm a^{-1}	m s^{-1}
	Used Fuel Corrosion Rates		
PD1	Basic rate of corrosion of carbon steel during Phase 1	μm a$^{-1/2}$	m s$^{-1/2}$
PD2	Basic rate of corrosion of carbon steel during Phase 2	μm a^{-1}	m s^{-1}
PD3	Basic rate of corrosion of carbon steel during Phase 3	μm a^{-1}	m s^{-1}
PD4	Basic rate of corrosion of carbon steel during Phase 4	μm a^{-1}	m s^{-1}
	Used Fuel Molar Activation Energies		
PE1	Activation energy of corrosion of carbon steel reaction during Phase 1	J mol^{-1}	J mol^{-1}
PE2	Activation energy of corrosion of carbon steel reaction during Phase 2	J mol^{-1}	J mol^{-1}
PE3	Activation energy of corrosion of carbon steel reaction during Phase 3	J mol^{-1}	J mol^{-1}

Name	Description/Category	Input Units	Internal Units
PE4	Activation energy of corrosion of carbon steel reaction during Phase 4	$J\ mol^{-1}$	$J\ mol^{-1}$
	Rate constants for organic degradation		
PVCA	cellulose under aerobic degradation	a^{-1}	s^{-1}
PVCB	cellulose under denitrification	a^{-1}	s^{-1}
PVCC	cellulose under ferric-ion reduction	a^{-1}	s^{-1}
PVCD	cellulose under sulphate reduction	a^{-1}	s^{-1}
PVCE	cellulose under methanogenesis	a^{-1}	s^{-1}
PVRA	IX resins under aerobic degradation	a^{-1}	s^{-1}
PVRB	IX resins under denitrification	a^{-1}	s^{-1}
PVRC	IX resins under ferric-ion reduction	a^{-1}	s^{-1}
PVRD	IX resins under sulphate reduction	a^{-1}	s^{-1}
PVRE	IX resins under methanogenesis	a^{-1}	s^{-1}
PVPA	plastics and rubbers under aerobic degradation	a^{-1}	s^{-1}
PVPB	plastics and rubbers under denitrification	a^{-1}	s^{-1}
PVPC	plastics and rubbers under ferric-ion reduction	a^{-1}	s^{-1}
PVPD	plastics and rubbers under sulphate reduction	a^{-1}	s^{-1}
PVPE	plastics and rubbers under methanogenesis	a^{-1}	s^{-1}
PVFES	Rate constant for the precipitation of FeS	s^{-1}	s^{-1}
PVFEOO	Rate constant for the reductive dissolution of FeOOH	s^{-1}	s^{-1}
PVMGO	Rate constant for the conversion of Magnesium Oxide to Magnesium Carbonate	s^{-1}	s^{-1}
	Rate constants for hydrogen kinetic reactions		
PVH1	Microbial oxidation of H_2 via iron reduction	a^{-1}	s^{-1}
PVH2	Microbial oxidation of H_2 via sulphate reduction	a^{-1}	s^{-1}
PVH3	Microbial generation of methane	a^{-1}	s^{-1}
	Biomass yield coefficients		
PYA	aerobic degradation	-	-
PYB	Denitrification	-	-
PYC	ferric-ion reduction	-	-
PYD	sulphate reduction	-	-
PYE	Methanogenesis	-	-

Name	Description/Category	Input Units	Internal Units
	Biomass recycling		
PKR	Fraction of dead biomass recycled as cellulose	-	-
	Densities of metals		
PRO1	carbon and galvanized steel	kg m^{-3}	kg m^{-3}
PRO2	passivated carbon steel	kg m^{-3}	kg m^{-3}
PRO3	stainless steel and Ni-based alloys	kg m^{-3}	kg m^{-3}
PRO4	Zr alloys	kg m^{-3}	kg m^{-3}
	Miscellaneous		
PRLIQ	Density of the water (saline) in the repository as modelled by GGM	kg m^{-3}	kg m^{-3}
PMLIQ	Molar mass of the water (saline) in the repository as modelled by GGM	kg mol^{-1}	kg mol^{-1}
PRLIQT2	Density of the geosphere water (fresh)	kg m^{-3}	kg m^{-3}
PMLIQT2	Molar mass of the geosphere water (fresh)	kg mol^{-1}	kg mol^{-1}
	Effective molar mass of the organic substrates		
PMORG1	Mass of actual cellulose substrate per mole equivalent cellulose	kg mol^{-1}	kg mol^{-1}
PMORG2	Mass of actual IX resins substrate per mole of equivalent styrene monomer.	kg mol^{-1}	kg mol^{-1}
PMORG3	Mass of actual plastics and rubbers substrate per mole of equivalent styrene monomer.	kg mol^{-1}	kg mol^{-1}
	Relative Humidity Dependence		
PHUM	T or F. (True or false) Specifies whether relative humidity dependent behaviour is enabled. When set to F it is assumed that the relative humidity is sufficiently high to allow all vapour phase processes to proceed.	-	-
PRHMIN	Relative Humidity value (fractional) below which all vapour phase corrosion and microbial reactions are modelled as having ceased	-	-
PRHMAX	Relative Humidity value (fractional) above which all vapour phase corrosion and microbial reactions are modelled as fully active.	-	-
PHTYPE	Type of relative humidity modulation function to use. An integer. Can currently be 1 = linear ramp, or 2 = smoothed linear ramp.	-	-
	Temperature Dependence		

Name	Description/Category	Input Units	Internal Units
PTMODE	The temperature mode to use. An integer. Can be 1 = isothermal, or 2 = non-isothermal. When non-isothermal, the temperature is taken from TOUGH2. When isothermal, each compartment can be given an independent temperature that is read in from the compartmental input files.	-	-
	Time step and output control		
PEPS	Specifies the maximum fractional change allowed in a differential variable per time step. Controls the maximum time step reported to TOUGH2.	-	-
PEPSC	Cut-off value below which differential variables are not used to control the suggested timestep.	mixed	mixed
PEPSR	Cut-off value below which the rate of a differential variable is not used to control the suggested time step.	mixed	mixed
LOGTR	Log base 10 of the ratio of times of subsequent writes to the output file. The next output time occurs at approximately (last output time)*10^(LOGTR), and allows output to be generated with a resolution suitable for plotting on a logarithmic scale, consistent with the way it is usually displayed.	-	-
PMINSAT	Saturation below which the water consuming reactions are controlled to prevent them from drawing water into the volume.	-	-

Table 7-22: Specification of GGM Compartment Specific Input Data

Name	Description	Input Units	Internal Units
	Surface areas of metals		
PA1	carbon and galvanized steel	m^2	m^2
PA2	passivated carbon steel	m^2	m^2
PA3	stainless steel and Ni-based alloys	m^2	m^2
PA4	Zr alloys	m^2	m^2
	Initial concentrations		
PIQNO3	Initial quantity of nitrates in volume	kg	mol
PICSO4	Initial concentration of sulphates in repository water	$kg\ m^{-3}$	$mol\ m^{-3}$
PICFEO	Initial concentration of Fe(III) in repository water	$mol\ m^{-3}$	$mol\ m^{-3}$
	Initial gas partial pressures		
PIPO2	O_2	MPa	Pa
PIPCO2	CO_2	MPa	Pa
PIPN2	N_2	MPa	Pa
PIPH2	H_2	MPa	Pa
PIPH2S	H_2S	MPa	Pa
PIPCH4	CH_4	MPa	Pa
	Initial masses of organic substrates		
PIMORG1	Cellulose	kg	kg
PIMORG2	IX resins (dry)	kg	kg
PIMORG3	Plastics and rubbers	kg	kg
	Initial quantities of metallic materials		
PIQ1	Carbon and galvanized steel	kg	mol
PIQ2	Passivated carbon steel	kg	mol
PIQ3	Stainless steel and Ni-based alloys	kg	mol
PIQ4	Zr alloys	kg	mol
	Initial amounts of biomass species		
PIXA	Aerobes	mol	mol
PIXB	Denitrifiers	mol	mol
PIXC	Iron reducers	mol	mol
PIXD	Sulphate reducers	mol	mol

Name	Description	Input Units	Internal Units
PIXE	Methanogens	mol	mol
PIXDIED	Total amount of biomass that has died	mol	mol
PIXDEAD	Total amount of dead (dehydrated) and non-recyclable biomass	mol	mol
	Properties used for tracking system across restarts		
PIICO2	Amount of CO_2 that has left the volume	mol	mol
PIIH2	Amount of H_2 that has left the volume	mol	mol
PIIH2S	Amount of H_2S that has left the volume	mol	mol
PIICH4	Amount of CH_4 that has left the volume	mol	mol
PIIO2	Amount of O_2 that has left the volume	mol	mol
PIIN2	Amount of N_2 that has left the volume	mol	mol
PINGH2O	Cumulative amount of water that has been generated by the gas generation reactions	mol	mol
	Initial amounts of other materials		
PIQFEC	$FeCO_3$	mol	mol
PIQFE3	Fe_3O_4	mol	mol
PIQFES	FeS	mol	mol
PIQMGO	MgO	mol	mol
PIQFE2	Fe_2O_3	mol	mol
PIQCO3	CO_3^{2-} (The amount of carbonate ions available for corrosion. This can be set to a very large number – larger than the total number of moles Fe present – if this is assumed to be effectively infinite.)	mol	mol
PIQZRO2	Total amount of ZrO_2		
	Temperature Dependence		
PT	Compartment temperature. Only used if the current temperature mode (PTMODE) is isothermal.	ºC	K
PTORIG	The time at which temperature dependent corrosion starts (the waste emplacement time). This is the time origin, t_1, for the Phase 1 corrosion rate.	y	s
	Compartment Dimensions		

Name	Description	Input Units	Internal Units
PBTS	The ratio of the expected bentonite wet-zone thickness to the ratio of the thickness of the compartment as measured away from the container wall. Alternatively, this can be thought of as the saturation above which water breaks through to the container wall. (Break-Through Saturation)	-	-

Table 7-23: Specification for GGM Global Output Data

Name	Description	Processing over compartments	Units
TIME	Time	None	s
DELTAT	The elapsed time since the last TOUGH2 time step.	None	s
QAIR	The rate of generation of bulk air component (or alternate gas). Includes vapour and dissolved phases of air.	Sum	kg s^{-1}
QLIQ	The rate of generation of geosphere water.	Sum	kg s^{-1}
DAIR	The discrepancy between the amount of gas generated by T2 and GGM over the last time step.	Sum	mol
DLIQ	The discrepancy between the amount of water generated by T2 and GGM over the last time step.	Sum	mol
IAS	Water saturation	Void volume weighted average	-
IAGWV	Saturated void volume	Sum	m^3
IAVAV	Unsaturated void volume	Sum	m^3
IATEAS	Terminal electron acceptor stage	Maximum	-
IACFEO	The effective concentration of FeOOH were it to be dissolved in the aqueous phase	Saturated volume weighted average	mol m^{-3}
IAPCO2	Partial pressure of CO_2	Gas volume weighted average	Pa
IAPH2	Partial pressure of H_2	Gas volume weighted average	Pa
IAPH2S	Partial pressure of H_2S	Gas volume weighted average	Pa
IAPCH4	Partial pressure of CH_4	Gas volume weighted average	Pa
IAPO2	Partial pressure of O_2	Gas volume weighted average	Pa
IAPN2	Partial pressure of N_2	Gas volume weighted average	Pa
IAPGAS	Total gas pressure	Gas volume weighted average	Pa

Name	Description	Processing over compartments	Units
IANGAS	Quantity of gas in the unsaturated phase (Sum of the number of moles of all the individual gases.)	Sum	mol
IAMAIR	Mass of bulk gas (IANGAS * the molar mass of bulk gas)	Sum	kg
IACCO2	Concentration of CO_2 in repository water	Saturated volume weighted average	mol m^{-3}
IACH2	Concentration of H_2 in repository water	Saturated volume weighted average	mol m^{-3}
IACH2S	Concentration of H_2S in repository water	Saturated volume weighted average	mol m^{-3}
IACCH4	Concentration of CH_4 in repository water	Saturated volume weighted average	mol m^{-3}
IACO2	Concentration of O_2 in repository water	Saturated volume weighted average	mol m^{-3}
IACN2	Concentration of N_2 in repository water	Saturated volume weighted average	mol m^{-3}
IANCO2	Total number of moles of CO_2 in the unsaturated phase	Sum	mol
IANH2	Total number of moles of H_2 in the unsaturated phase	Sum	mol
IANH2S	Total number of moles of H_2S in the unsaturated phase	Sum	mol
IANCH4	Total number of moles of CH_4 in the unsaturated phase	Sum	mol
IANO2	Total number of moles of O_2 in the unsaturated phase	Sum	mol
IANN2	Total number of moles of N_2 in the unsaturated phase	Sum	mol
IAQGAS	Gas component generation rate (rate of increase of number of moles of gas in both vapour and dissolved phases)	Sum	mol s^{-1}
IAQAIR	Bulk air component generation rate in both vapour and dissolved phases. (IAQGAS * the molar mass of bulk gas.)	Sum	kg s^{-1}
IAA11	Surface area of carbon and galvanized steel under unsaturated conditions	Sum	m^2

Name	Description	Processing over compartments	Units
IAA21	Surface area of passivated carbon steel under unsaturated conditions	Sum	m^2
IAA31	Surface area of stainless steel and Ni-based alloys under unsaturated conditions	Sum	m^2
IAA41	Surface area of Amount of Zr alloys under unsaturated conditions	Sum	m^2
IAA12	Surface area of carbon and galvanized steel under saturated conditions	Sum	m^2
IAA22	Surface area of passivated carbon steel under saturated conditions	Sum	m^2
IAA32	Surface area of stainless steel and Ni-based alloys under saturated conditions	Sum	m^2
IAA42	Surface area of Zr alloys under saturated conditions	Sum	m^2
IARH2O	Rate of generation of H_2O within the volume due to gas generation processes.	Sum	$mol\ s^{-1}$
IAQH2O	Amount of H_2O	Sum	mol
IAQLIQ	The water generation rate. (IARH2O times the molar mass of water.)	Sum	$kg\ s^{-1}$
IAGPSF	Gas pressure scaling factor.	Maximum	$kg\ kg^{-1}$
IARCDV	Rate controlling differential variable number	Zero	-
IARH	Relative humidity (fractional)	Gas volume weighted average	-
IAH	Relative humidity modulation factor h(RH) at the current relative humidity	h(gas volume weighted RH)	-
IAXTOT	Amount of live (hydrated) biomass	Sum	mol
IAWATEPS	Water consuming reaction rate scaling factor	Maximum	-
IADWDT	Rate of increase of amount of water	Sum	$mol\ s^{-1}$
IADCDT	Rate of consumption of water due to saturated phase reactions	Sum	$mol\ s^{-1}$
IADDDT	Rate of generation of water due to other reactions	Sum	$mol\ s^{-1}$
IADIDT	Rate at which water is entering	Sum	$mol\ s^{-1}$
IATEMP	The current temperature	Maximum	K

Name	Description	Processing over compartments	Units
IADELTA	The saturation breakthrough factor (delta) calculated on the basis of the average compartment water saturation. This increases from 0 to 1 as the average water saturation increases from the break-through saturation to 1. From v3.2 onwards, this parameter is not used in any calculations, it is just output.	Maximum	-
IAPHI1	The Phase 1 carbon steel consumption rate. This is defined as Φ_1 in Section 3.4.5.1.	Sum	mol s^{-1}
IAPHI2	The Phase 2 carbon steel consumption rate. This is defined as Φ_2 in Section 3.4.5.1.	Sum	mol s^{-1}
IAPHI3	The Phase 3 carbon steel consumption rate. This is defined as Φ_3 in Section 3.4.5.2.	Sum	mol s^{-1}
IAPHI4	The Phase 4 carbon steel consumption rate. This is defined as Φ_4 in Section 3.4.5.2.	Sum	mol s^{-1}
IADSDT	The rate of change of saturation	Void volume weighted average	s^{-1}
IADT	The internal GGM timestep	Minimum	s
IAZA	The compressibility factor, for use in the equation of state for gases. This is defined as Z in Section 3.7.	Gas volume weighted average	-
IAH12	An upscaled factor capturing relative-humidity heterogeneity for Phase 1 and Phase 2 of the Used Fuel corrosion model, as provided by TOUGH2.	Void volume weighted average	-
IAH3D3	An upscaled modulation factor capturing relative-humidity and saturation heterogeneity for Phase 3 of the Used Fuel corrosion model, as provided by TOUGH2.	Void volume weighted average	-
IAD4	An upscaled modulation factor capturing saturation heterogeneity for Phase 4 of the Used Fuel corrosion model, as provided by TOUGH2.	Void volume weighted average	-
IDCNO3	Concentration of NO_3	Saturated volume weighted average	mol m^{-3}
IDQFEO	Amount of FeOOH	Sum	mol
IDCSO4	Concentration of SO_4	Saturated volume weighted average	mol m^{-3}

Name	Description	Processing over compartments	Units
IDQC	Amount of cellulose monomer	Sum	mol
IDQR	Amount of styrene monomer	Sum	mol
IDQP	Amount of styrene monomer from plastics and rubber	Sum	mol
IDQ1	Amount of carbon and galvanized steel	Sum	mol
IDQ2	Amount of passivated carbon steel	Sum	mol
IDQ3	Amount of stainless steel and Ni-based alloys	Sum	mol
IDQ4	Amount of Zr alloys	Sum	mol
IDXA	Amount of aerobes	Sum	mol
IDXB	Amount of denitrifiers	Sum	mol
IDXC	Amount of iron reducers	Sum	mol
IDXD	Amount of sulphate reducers	Sum	mol
IDXE	Amount of methanogens	Sum	mol
IDQFEC	Amount of $FeCO_3$	Sum	mol
IDQFE3	Amount of Fe_3O_4	Sum	mol
IDQFES	Amount of FeS	Sum	mol
IDQMGO	Amount of MgO	Sum	mol
IDNCO2	Total number of moles of CO_2	Sum	mol
IDNH2	Total number of moles of H_2	Sum	mol
IDNH2S	Total number of moles of H_2S	Sum	mol
IDNCH4	Total number of moles of CH_4	Sum	mol
IDNO2	Total number of moles of O_2	Sum	mol
IDNN2	Total number of moles of N_2	Sum	mol
IDXDIED	Total amount of biomass that has died	Sum	mol
IDXDEAD	Total amount of dead (dehydrated) and non-recyclable biomass	Sum	mol
IDICO2	Amount of CO_2 that has left the volume	Sum	mol

Name	Description	Processing over compartments	Units
IDIH2	Amount of H_2 that has left the volume	Sum	mol
IDIH2S	Amount of H_2S that has left the volume	Sum	mol
IDICH4	Amount of CH_4 that has left the volume	Sum	mol
IDIO2	Amount of O_2 that has left the volume	Sum	mol
IDIN2	Amount of N_2 that has left the volume	Sum	mol
IDNGH2O	Cumulative amount of water that has been generated by the gas generation reactions	Sum	mol
IDQZRO2	Total amount of ZrO_2	Sum	mol
IDQFE2	Amount of Fe_2O_3	Sum	mol
IDQCO3	The amount of CO_3^{2-}	Sum	mol

REFERENCES

Akiyama, E., K. Matsukado, M. Wang, and K. Tsuzaki. 2010. Evaluation of Hydrogen Entry into High Strength Steel under Atmospheric Corrosion. Corrosion Science. 52, pp 2758-2765.

Alcolea, A., U. Kuhlmann, P. Marschall, A. Lisjak, G. Grasselli, O. Mahabadi, R. de La Vaissière, H. Leung, and H. Shao. 2015. A Pragmatic Methodology to Abstract the EDZ around Tunnels of a Geological Radioactive Waste Repository - Application to the HG-A experiment in Mont Terri. Clays in Natural and Engineered Barriers for Radioactive Waste Confinement, 6th International Conference, March 23-26, 2015. Brussels, Belgium.

ARC. 2010. Gas Transport and Geochemical Modelling. Alberta Research Council report for the Nuclear Waste Management Organization NWMO DGR-REP-03640-21109. Toronto, Canada.

ASM. 1987. Metals Handbook, Ninth Edition, Volume 13, Corrosion. American Society for Metals International. Metals Park, USA.

ASM. 2003. ASM Handbook, Volume 13A, Corrosion: Fundamentals, Testing, and Protection. American Society for Metals International. Metals Park, USA.

ASM. 2005. ASM Handbook, Volume 13B, Corrosion: Materials. American Society for Metals International. Metals Park, USA.

ASTM, 1996. ASTM Standard D 4546 – 96. Standard Test Methods for One-Dimensional Swell or Settlement Potential of Cohesive Soils, ASTM International, West Conshohocken, PA.

Barlaz, M. A. 1997. Microbial Studies of Landfills and Anaerobic Refuse Decomposition. Manual of Environmental Microbiology. Chapter 60, pp 541-557. ASM Press. Washington, USA.

Bate, F., D. Roberts, A. R. Hoch, C.P. Jackson. 2012. Gas migration calculations on the vault scale. Serco Assurance report SA/ENV-0924 Issue 3.1. Oxfordshire, UK.

Beadle, I., P.N. Humphreys, C. Pettit and J. Small. 2001. Integrating Microbiology into the Drigg Post-closure Radiological Safety Assessment. Materials Research Society Proceedings 663, pp 665-674.

Birgersson, M., M. Åkesson and H. Hökmark. 2008. Gas intrusion in saturated bentonite – A thermodynamic approach. Physics and Chemistry of the Earth, Parts A/B/C, 33, S248–S251. doi:10.1016/j.pce.2008.10.039

BNFL. 2002. Potential for the degradation of high molecular weight synthetic organic polymers. British Nuclear Fuel Limited Report DTP/90. United Kingdom.

Börgesson, L. 1984: water flow and swelling pressure in non-saturated bentonite-based clay barriers for isolation of toxic chemical waste. International Symposium, May 28-30, Stockholm, Sweden.

Bowerman, B.S., J.H. Clinton and S.R. Cowdery. 1988. Biodegradation of Ion Exchange Media. Brookhaven National Laboratory Report NUREG/CR-5221, BNL-NUREG-52163. New York, USA.

Bracke, G. and W. Muller. 2003. Modelling the gas generation of intermediate and low level radioactive wastes. Proceeding of ICEM '03, Oxford, United Kingdom.

Bracke, G., W. Muller, K. Kugel and D. Cologne. 2004. Derivation of gas generation rates for the Morsleben radioactive waste repository (ERAM). Proceedings of DisTec 2004. Berlin, Germany.

Brown, A.D. 1976. Microbial water stress. Bacteriological Reviews, 40(4), pp 803-846.

Calder, N. and J. Avis. 2015. Application of 1D Hydromechanical Coupling in TOUGH2 to a Deep Geologic Repository Glaciation Scenario. TOUGH Symposium 2015, Berkeley, CA, September 28-30.

Calder, N. 2014. FORGE Benchmark Modelling: Cell, Module and Repository Scale Gas Migration in a Hypothetical Repository. Nuclear Waste Management Organization Technical Report, NWMO TR-2014-06. Toronto, Canada.

Carman,P.D. 1941. Capillary size and capillary movement of moisture in fine sands, Soil Science, 52, 1-14.

Clayton, C.R. and I. Olefjord. 1995. Passivity of austenitic stainless steels. In Corrosion Mechanisms in Theory and Practice, pp 175-199. New York, USA.

Cohen, S. 2006. Preliminary Review of the Degradation of Cellulosic, Plastic, and Rubber Materials in the Waste Isolation Pilot Plant, and Possible Effects on Magnesium Oxide Safety Factor Calculations. S. Cohen & Associates Report. Vienna, Virginia. https://www.epa.gov/sites/production/files/2015-05/documents/epa_mgo_report _91107.pdf (accessed June 15, 2016).

CRC. 1995. Handbook of Chemistry and Physics, 76th edition. Chemical Rubber Company Press. Boca Raton, USA.

Cui, Y. J., A. M. Tang, C. Loiseau and P. Delage. 2008. Determining the unsaturated hydraulic conductivity of a compacted sand–bentonite mixture under constant-volume and free-swell conditions. Physics and Chemistry of the Earth, Parts A/B/C, 33, S462–S471. doi:10.1016/j.pce.2008.10.017

Davies, P.B. 1991. Evaluation of the Role of Threshold Pressure in Controlling Flow of Waste Generated Gas into Bedded Salt at the Waste Isolation Pilot Plant. Sandia Report SAND 90-3246, Sandia National Laboratory, Albuquerque, USA.

Debruyn, W. 1990. Corrosion of container materials under clay repository conditions. In Proceedings of Workshop on Corrosion of Nuclear Fuel Waste Containers, 1988, February 9 - 10. Winnipeg, MB. (Editor, D.W. Shoesmith). Atomic Energy of Canada Limited Report, AECL-10121, pp 175-186. Chalk River, Canada.

Desgranges, C., A. Abbas, and A. Terlain. 2003. Model for low temperature oxidation during long term interim storage. In Prediction of Long Term Corrosion Behaviour in Nuclear Waste Systems, D. Féron and D.D. Macdonald (eds.), European Federation of

Corrosion Publication Number 36 (Chapter 7, pp 194-207). Maney Publishing, London, UK.

de Waard, C. and U. Lotz. 1993. Prediction of CO_2 corrosion of carbon steel. In CORROSION/1993, Paper no. 69, NACE International, Houston, USA.

de Waard, C. and D.E. Milliams. 1976. Prediction of carbonic acid corrosion in natural gas pipelines. Industrial Finishing & Surface Coatings, pp 24-28.

de Waard, C., U. Lotz, and D.E. Milliams. 1991. Predictive model for CO_2 corrosion engineering in wet natural gas pipelines. Corrosion 47, pp 976-985.

de Waard, C., U. Lotz, and A. Dugstad. 1995. Influence of liquid flow velocity on CO_2 corrosion: a semi-empirical model. In CORROSION/1995, Paper no. 128, NACE International, Houston, USA.

EA. 2004. Guidance on the Management of Landfill Gas. UK Environment Agency Report LFTGN 03. United Kingdom.

EPRI. 1998. Preventing Gas Generation in Low Level Waste – Final Report. Electric Power Research Institute Technical Report EPRI TR-111019. Palo Alto, USA.

Finsterle, S. 1999. iTOUGH2 Command Reference, Version 4.0. Science Lawrence Berkeley National Laboratory Report LBNL-40041. Berkeley, USA.

Foct, F. and J.-M. Gras. 2003. Semi-empirical model for carbon steel corrosion in long term geological nuclear waste disposal. In Prediction of Long Term Corrosion Behaviour in Nuclear Waste Systems, D. Féron and D.D. Macdonald (eds.), European Federation of Corrosion Publication Number 36 Chapter 14, pp 91-102. Maney Publishing, London, UK.

FORGE. 2010. FORGE Milestone M15: Summary of Gas Generation and Migration. Current State-of-the-Art. Euratom 7th Framework Project, FORGE 2010. Deliverable D1.2-R.

Francis, A.J., J.B. Gillow and M.R. Giles. 1997. Microbial Gas Generation Under Expected Waste Isolation Pilot Plant Repository Conditions. Sandia National Labs Report SAND96-2582. Albuquerque, USA.

GEOFIRMA and QUINTESSA. 2011. Postclosure Safety Assessment: Gas Modelling. Geofirma Engineering Ltd. and Quintessa Ltd. report for the Nuclear Waste Management Organization NWMO DGR-TR-2011-31 R000. Toronto, Canada.

Graham, C. C., J. F. Harrington, R. J. Cuss and P. Sellin, 2012. Gas Migration Experiments in Bentonite: Implications for Numerical Modelling. Mineralogical Magazine, 76(8), 3279–3292.

Grant, W.D., G.J. Holtom, A. Rosevear and D. Widdowson. 1997. A Review of Environmental Microbiology Relevant to the Disposal of Radioactive Waste in a Deep Underground Repository. Nirex Report NSS R329. United Kingdom.

Gras, J.-M. 1996. Corrosion assessment of metal containers for the geological disposal of HLW. Part 1 : carbon steels, low alloy steels, cast iron. EDF Report No. HT-40/96/002/A, Electricité de France, Moret-sur-Loing, France.

Grey, M.G. 2002. Generation of Biogases in Sealed Containers of Low-Level Radioactive Waste. Canadian Radiation Protection Association Conference, Vancouver, Canada.

Halayko, K.S.G. 1998. Gas Flow in Compacted Clays. M.Sc. Thesis. Department of Civil and Geological Engineering University of Manitoba.

Harrington, J.F. and S.T. Horseman. 2003. Gas Migration in KBS-3 Buffer Bentonite: Sensitivity of Test Parameters to Experimental Boundary Conditions, SKB Technical Report TR-03-02, Swedish Nuclear Fuel and Waste Management Co, Stockholm, Sweden.

Hume, H. 1999. Gas Breakthrough in Compacted Avonlea Bentonite. M.Sc. thesis, University of Manitoba.

Itasca Consulting Group Inc. 2012. FLAC3D (Fast Lagrangian Analysis of Continua). Version 5.01.

IWA. 2002. Anaerobic digestion model No. 1 (ADM1). IWA Task Group for Mathematical Modelling of Anaerobic Digestion Processes. Scientific and Technical Report No. 13. IWA Publishing, London, United Kingdom.

J3. 2008. Fortran standards technical committee. http://www.j3-fortran.org/ (accessed June 15, 2016).

Jaeger, J., N. Cook and R. Zimmerman. 2007. Fundamentals of Rock Mechanics, Fourth Edition. Blackwell Publishing, Malden, USA.

Jobmann, M. 1988. Modification and application of the TOUGH2 code for modeling of water flow through swelling unsaturated sealing constructions. In TOUGH Workshop 1998. Berkeley, California: Lawrence Berkeley National Laboratory.

Kannen, H. and W. Muller. 1999. Gas Generation of Radioactive Wastes – Comparison Between Laboratory Experiments and Measurements on Real Wastes. ASME International. Proceedings of the 7th Radioactive Waste Management and Environmental Remediation Conference, Nagoya, Japan.

Karthikeyan, R., and A. Bhandari. 2001. Anaerobic biotransformation of aromatic and polycyclic aromatic hydrocarbons in soil microcosms: a review. Journal of Hazardous Substance Research 3, pp 1-19.

King, F. 2007. Overview of a carbon steel container corrosion model for a deep geological repository in sedimentary rock. Nuclear Waste Management Organization Technical Report, NWMO TR-2007-01. Toronto, Canada.

King, F. 2008. Corrosion of carbon steel under anaerobic conditions in a repository for SF and HLW in Opalinus Clay. Nagra Technical Report 08-12. Wettingen, Switzerland.

King, F. 2009. Hydrogen effects on carbon steel used fuel containers. Nuclear Waste Management Organization Technical Report, NWMO TR-2009-29. Toronto, Canada.

King, F., M. Kolar and D.W. Shoesmith. 1996. Modelling the effects of porous and semi-permeable layers on corrosion processes. In Proc. CORROSION/96, paper no. 380, NACE International, Houston, USA.

King, F., and S. Stroes-Gascoyne. 2000. An Assessment of the Long-term Corrosion Behaviour of C-steel and the Impact on the Redox Conditions Inside a Nuclear Fuel Waste Disposal Container. Ontario Power Generation Report 06819-REP-01200-10028. Toronto, Canada.

Kozeny, 1927. Uber kapillare Leitung des wassers im baden, Sitzungsberichte der Akadamie der Wissenschaften in Wien, Abteilung lla.

Kröhn, K. P. 2003. Investigation of uncertainties in the re-saturation model of bentonite as near-field buffer in a spent fuel repository in granite. In Proceedings of the GRS/IRSN conference EUROSAFE, seminar (Vol. 3).

Krumhansl, J.L., M.A. Molecke, H.W. Papenguth and L.H. Brush. 2000. A Historical Review of Waste Isolation Pilot Plant Backfill Development. Sandia National Laboratories Report SAND2000-1416C. Albuquerque, USA.

Larose, S. and R.A. Rapp. 1997. Review of low-temperature oxidation of carbon steels and low-alloy steels for use as high-level radioactive waste package materials. Center for Nuclear Waste Regulatory Analyses report, CNWRA 97-003. San Antonio, USA.

Lemieux, J-M, E. Sudicky, W. Peltier, L. Tarasov, 2008. Simulating the Impact of Glaciations on Continental Groundwater Flow Systems: 1. Relevant Processes and Model Formulation, Journal of Geophysical Research, 113, F03017, 12pp.

Leschine, S. B. 1995. Cellulose Degradation in Anaerobic Environments. Annual Review of Microbiology 49, pp 399-426.

Lovely, D.R. 2000. Anaerobic benzene degradation. Biodegradation 11, pp 107-116.

Marschall, P., M. Distinguin, H. Shao, P. Bossart, C. Enachescu and T. Trick. 2006. Creation and Evolution of Damage Zones around a Microtunnel in a Claystone Formation of the Swiss Jura Mountains. Conference Proceedings from the 2006 SPE International Symposium and Exhibition on Formation Damage Control held in Lafayette, L.A., 15–17 February 2006, SPE Paper 98537.

Martin, R. T. Adsorbed water on clay: a review. Massachusetts Institute of Technology, 1960.

McNab, W.W. and T.N. Narasimhan. 1994. Modelling reactive transport of organic compounds in groundwater using a partial redox disequilibrium approach. Water Resources Research 30, pp 2619-2635.

Mitchell, J. K. and K. Soga. Fundamentals of soil behavior. New York: Wiley, 2005.

Molnar, M., L. Palcsu, E. Svingor, Z. Szanto and I. Futo. 2000. Gas Formation in Drum Waste Packages of PAKS NPP. Proceedings of Nuclear Energy in Central Europe. Bled, Slovenia.

Molnar, M., L. Palcsu, E. Svingor, I. Futo, Z. Major and L. Rinyu. 2006. Isotope-Analytical Results of a Study of Gas Generation in L/ILW. Czechoslovak Journal of Physics 56, pp 637-644.

Mooney, A., P.G. Ward and K.E. O'Connor. 2006. Microbial degradation of styrene: biochemical, molecular genetics and perspectives for biotechnology applications. Applied Microbial Biotechnology 72, pp 1-10.

Nagra. 2008. Effects of post-disposal gas generation in a repository for low- and intermediate-level waste sited in the Opalinus Clay of Northern Switzerland. Nagra Technical Report 08-07. Wettingen, Switzerland.

Nasir, O., M. Fall, T.S. Nguyen and E. Evgin. 2011. Modelling of the Hydro-mechanical Response of Sedimentary Rocks of Southern Ontario to Past Glaciations. Engineering Geology, 123, pp 271-287

Neuzil, C. 2003. Hydromechanical Coupling in Geological Processes. Hydrogeology Journal, 11, pp 41-83.

Newman, R.C., S. Wang, and G. Kwong. 2010. Anaerobic corrosion studies of carbon steel used fuel containers. Nuclear Waste Management Organization Report, NWMO TR-2010-07. Toronto, Canada.

NVIDIA, 2014. https://developer.nvidia.com/cuda-toolkit (accessed June 15, 2016).

NWMO. 2010. Technical Computing Software. Nuclear Waste Management Organization Procedure NWMO-PROC-EN-0002 R001. Toronto, Canada.

NWMO. 2013. Postclosure Safety Assessment of a Used Fuel Repository in Sedimentary Rock: Pre-Project Report. NWMO TR-2013-07. Toronto, Canada.

Ollivier, B., P. Caumette, J-P. Garcia and R.A. Mah. 1994. Anaerobic Bacteria from Hypersaline Environments. Microbiological Reviews 58(1), pp 27-38.

Olsen, H. W. 1962. Hydraulic flow through saturated clays. Proceeding of the Ninth National Conference on Clays and Clay Minerals. Pergamon Press, West Lafayette, IN, PP 131-161.

Papillon, F., M. Jullien, and C. Bataillon. 2003. Carbon steel behaviour in compacted clay: two long term tests for corrosion prediction. In Prediction of Long Term Corrosion Behaviour in Nuclear Waste Systems. European Federation of Corrosion Publication No. 36 (Institute of Materials, Minerals and Mining, London), pp 439–454.

Paralution, 2014. Paralution User Manual Version 0.7.0. http://www.paralution.com (accessed June 15, 2016).

Pavlostathis, S.G. and E. Giraldo-Gomez. 1991. Kinetics of Anaerobic Treatment. Water Science and Technology 24 (8), pp 35-59.

Pedersen, K. 2000. Microbial Processes in Radioactive Waste Disposal. SKB Technical Report TR-00-04. Stockholm, Sweden.

Postma, D. and R. Jakobsen. 1996. Redox Zonation: Equilibrium Constraints on the Fe(III)/SO-reduction Interface. Geochimica et Cosmochimica Acta 60, pp 3169-3175.

Pourbaix, M. 1974. Atlas of Electrochemical Equilibria in Aqueous Solutions, Second Edition. NACE International. Houston, USA.

Pruess, K., C. Oldenburg and G. Moridis. 1999. TOUGH2 User's Guide, Version 2.0. Lawrence Berkeley National Laboratory Report LBNL-43134. Berkeley, USA.

QUINTESSA and GEOFIRMA. 2011a. T2GGM Version 2: Gas Generation and Transport Code. Quintessa Ltd. and Geofirma Engineering Ltd. report for the Nuclear Waste Management Organization Report NWMO DGR-TR-2011-33 R000. Toronto, Canada.

QUINTESSA and GEOFIRMA. 2011b. Postclosure Safety Assessment: Data. Quintessa Ltd. and Geofirma Engineering Ltd. report for the Nuclear Waste Management Organization NWMO DGR-TR-2011-32 R000. Toronto, Canada.

QUINTESSA, GEOFIRMA and SENES. 2011. Postclosure Safety Assessment. Quintessa Ltd., Geofirma Engineering Ltd. and SENES Consultants Ltd. report for the Nuclear Waste Management Organization NWMO DGR-TR-2011-25 R000. Toronto, Canada.

Reagan, M., G. Santos, and G.J. Moridis. 2005. WebGasEOS 2.0. http://lnx.lbl.gov/gaseos/gaseos.html (accessed June 15, 2016).

Reid, R.C., J.M. Prausnitz and B.E. Poling. 1987. The Properties of Gases and Liquids, Fourth Edition. McGraw-Hill, New York, USA.

Rittmann, B.E. and P.L. McCarty. 2001. Environmental Biotechnology: Principles and Applications. McGraw –Hill Higher Education. New York, USA.

Rutqvist J. and C.F. Tsang. 2003. Analysis of Thermal-hydrologic-mechanical Behavior near an Emplacement Drift at Yucca Mountain. Journal of Contaminant Hydrology, 62–63, pp 637–652.

Sedriks, A.J. 1996. Corrosion of Stainless Steels. Second Edition. John Wiley and Sons. New York, USA.

Shoesmith, D.W. and F. King. 1999. The effects of gamma radiation on the corrosion of candidate materials for the fabrication of nuclear waste packages. Atomic Energy of Canada Limited Report, AECL-11999, Whiteshell, Canada.

Shreir, L.L. 1976. Corrosion. Second Edition, Newnes-Butterworths. London, United Kingdom.

Sleijpen, G.L.G. and D. Fokkema. 1993. BiCGSTAB(m) for Linear Equations Involving Unsymmetric Matrices with Complex Spectrum, Electronic Transactions on Numerical Analysis, Vol. 1, pp. 11 - 32.

Small, J.S., M. Nykyri, N. Paaso, U. Hovi, M. Itavaara and T. Sarlin. 2005. Testing of a Near-Field Biogeochemical Model Against Data From a Large-Scale Gas Generation Experiment. Scientific Basis of Nuclear Waste Management, Ghent, Belgium.

Spormann, A.M. and F. Widdel. 2000. Metabolism of Alkylbenzes, Alkanes and other Hydrocarbons in Anaerobic Bacteria. Biodegradation 11, pp 85-105.

Stroes-Gascoyne, S., C.J. Hamon, C. Kohle and D.A. Dixon. 2006. The effects of dry density and porewater salinity on the physical and microbiological characteristics of highly

compacted bentonite. Ontario Power Generation, Nuclear Waste Management Division Report 06819-REP-01200-10016 R00. Toronto, Canada.

Stroes-Gascoyne, S., C.J. Hamon, D.A. Dixon, C. Kohle and P. Maak. 2007. The effects of dry density and porewater salinity on the physical and microbiological characteristics of highly compacted bentonite. In Scientific Basis for Nuclear Waste Management XXX, D. Dunn, C. Poinssot, B. Betg (eds.) Material Research Society Symposium Proceedings 985, Warrendale, PA, 2007, paper 0985-NN13-02.

Stroes-Gascoyne, S. and C.J. Hamon. 2008. The effect of intermediate dry densities (1.1-1.5 g/cm^3) and intermediate porewater salinities (60-90 g NaCl/L) on the culturability of heterotrophic aerobic bacteria in compacted 100% bentonite. Nuclear Waste Management Organization Technical Report NWMO TR-2008-11. Toronto, Canada.

Studer, J., W. Ammann, P. Meier, Ch. Muller, and E. Glauser. 1984. Verfullen und Versiegln von Stolen, Schachten und Bohrlochem, Band 2 Anhange, Nagra Technischer Bericht 84-33, Baden, Schweiz.

Talandier, J., G. Mayer and J. Croisé. 2006. Simulations of the Hydrogen Migration out of Intermediate-Level Radioactive Waste Disposal Drifts using TOUGH2. Proceedings, TOUGH Symposium 2006, Lawrence Berkley National Laboratory. Berkeley, USA.

Terlain, A., C. Desgranges, D. Féron, A. Galtayries, and P. Marcus. 2001. Oxidation of materials for nuclear waste canisters under long term disposal. CORROSION/2001, Paper No. 01119, NACE International, Houston, USA .

Terzaghi, K. 1943. Theoretical Soil Mechanics. John Wiley and Sons, New York, USA.

Therrien, R., R. G. McLaren, E. A. Sudicky, S.M. Panday, and, V. Guvanasen. 2010. FRAC3DVS-OPG: A Three-Dimensional Numerical Model Describing Subsurface Flow and Solute Transport. User's Guide. University of Waterloo, Waterloo, Canada.

Tsuru, T., Y. Huang, Md.R. Ali, and A. Nishikata. 2005. Hydrogen entry into steel during atmospheric corrosion process. Corrosion Science. 47, pp 2431-2440.

Villar G. M. 2002. Thermo-hydro-mechanical characterisation of a bentonite from Cabo de Gata. ENRESA Technical Publication, Madrid, Spain.

Walsh, R., N. Calder and J. Avis. 2012. A Simple Implementation of 1D Hydromechanical Coupling In TOUGH2. PROCEEDINGS, TOUGH Symposium 2012, Lawrence Berkeley National Laboratory, Berkeley, California, September 17-19, 2012.

Walsh, R., O. Nasir and N. Sgro. 2014. Modelling of the HG-A Experiment (FORGE WP4.3). Nuclear Waste Management Organization Technical Report NWMO TR-2014-07. Toronto, Canada

Wang, H., 2000. Theory of Linear Poroelasticity with Application to Geomechanics and Hydrology. Princeton University Press.   Princeton, USA.

Wang, Q., Y.J. Cui, A.M. Tang, J.D. Barnichon, S. Saba, and W.M. Ye. 2013. Hydraulic conductivity and microstructure changes of compacted bentonite/sand mixture during hydration. Engineering Geology, 164, 67-76.

Wang, Y. and A.J. Francis. 2005. Evaluation of Microbial Activity for Long-term Performance Assessments of Deep Geologic Nuclear Waste Repositories. Journal of Nuclear and Radiochemical Sciences 6(1), pp 43-50.

Wersin, P., M. Birgersson, S. Olsson, O. Karnland, and M. Snellman. 2007. Impact of corrosion-derived iron on the bentonite buffer within the KBS-3H disposal concept – the Olkiluoto site as case study. Posiva Oy Report, POSIVA 2007-11. Olkiluoto, Finland.

Williams, G.M., R.W. Pickup, S.F. Thornton, D.N. Lerner, H.E.H. Mallinson,Y. Moore and C. White. 2001. Biogeochemical Characterisation of a Coal Tar Distillate Plume. Journal of Contaminant Hydrology 53(3-4), pp 175-197.

Xie, M., S.S. Agus, T. Schanz and O. Kolditz. 2004. An upscaling method and a numerical analysis of swelling/shrinking processes in a compacted bentonite/sand mixture. International Journal for Numerical and Analytical Methods in Geomechanics, 28(15), 1479–1502. doi:10.1002/nag.396

Zehnder, A.J.B. and W. Stumm. 1988. Geochemistry and Biogeochemistry of Anaerobic Habitats. In: Biology of Anaerobic Micro-organisms, pp 1-38. John Wiley and Sons. New York, USA.

ABBREVIATIONS AND ACRONYMS

5CS	Fifth Case Study
DGR	Deep Geologic Repository
EDZ	Excavated Damage Zone
EOS	Equation-of-State
GGE	Gas Generation Experiment
GGM	Gas Generation Model
IFD	Integral Finite Difference
IX	Ion-Exchange
LBNL	Lawrence Berkeley National Laboratory
L&ILW	Low and Intermediate Level Waste
NE	Normal Evolution Scenario
NE-RC	Reference Case
NE-SBC	Simplified Base Case
NWL	Non-Water Limited
NWMO	Nuclear Waste Management Organization
OPG	Ontario Power Generation
RH	Relative Humidity
TEA	Terminal Electron Acceptor
UFC	Used Fuel Container
WI	Work Instruction
WIPP	Waste Isolation Pilot Plant
WL	Water Limited